



**HAL**  
open science

# Organized Organic Dye / Hole Transporting Materials for TiO<sub>2</sub>- and ZnO- based Solid-State Dye-Sensitized Solar Cells (s-DSSCs).

Annette Delices

► **To cite this version:**

Annette Delices. Organized Organic Dye / Hole Transporting Materials for TiO<sub>2</sub>- and ZnO- based Solid-State Dye-Sensitized Solar Cells (s-DSSCs).. Other. Université Sorbonne Paris Cité, 2017. English. NNT : 2017USPCC066 . tel-01931367

**HAL Id: tel-01931367**

**<https://theses.hal.science/tel-01931367v1>**

Submitted on 22 Nov 2018

**HAL** is a multi-disciplinary open access archive for the deposit and dissemination of scientific research documents, whether they are published or not. The documents may come from teaching and research institutions in France or abroad, or from public or private research centers.

L'archive ouverte pluridisciplinaire **HAL**, est destinée au dépôt et à la diffusion de documents scientifiques de niveau recherche, publiés ou non, émanant des établissements d'enseignement et de recherche français ou étrangers, des laboratoires publics ou privés.

Thèse de doctorat  
de l'Université Sorbonne Paris Cité  
Préparée à l'Université Paris Diderot  
**Ecole doctorale de Chimie Physique et de Chimie Analytique de Paris-  
Centre (ED 388)**

*Laboratoire Interfaces Traitements Organisation et Dynamique des Systèmes*

**Organized Organic Dye / Hole Transporting  
Materials for TiO<sub>2</sub> and ZnO based  
Solid-State Dye-Sensitized Solar Cells (s-DSSCs)**

Par Annette DELICES

Thèse de doctorat de Chimie

Dirigée par Pr. Mohamed JOUINI

Présentée et soutenue publiquement à L'Université Paris Diderot le 29/09/2017

- Président du Jury : **Pr. MAUREL François**, Professeur, Université Paris Diderot
- Rapporteurs : **Dr. FABRE Bruno**, Directeur de Recherche, Université de Rennes  
**Dr. GUILLEMOLES Jean-François**, Directeur de Recherche, IRDEP
- Examineurs : **Pr. LARTIGAU-DAGRON Christine**, Professeur, Université de Pau  
**Dr. MOINEAU-CHANE CHING Kathleen**, Directrice de Recherche,  
Université de Toulouse
- Co-directeur de thèse : **Pr. HAGFELDT Anders**, Professeur, Ecole Polytechnique Fédérale de  
Lausanne – Suisse
- Directeur de thèse : **Pr. JOUINI Mohamed**, Professeur, Université Paris Diderot



## **Abstract**

Due to instability problems of dye sensitized solar cells (DSSCs) in longtime uses, the iodine based liquid electrolyte has been replaced by several types of solid hole transporting materials (HTM) to perform solid state DSSCs (s-DSSCs). Among them, the substitution by conducting polymers (CP) has attracted considerable attention because of their good stability, high hole-conductivity and simple deposition within the mesoporous TiO<sub>2</sub> semiconductor. In this thesis work, several s-DSSCs based on CPs used as HTM have been developed in order to improve their photovoltaic performances taking into account the following two objectives: (i) the optimization of the interfacial charge transfer processes within the solar cell, and (ii) the optimization of the charge transport within the n-type oxide semiconductor. To reach these goals, each component that constitutes the device was varied in order to investigate its effect on the device's performances. As first attempt, an analytical study is carried out by varying the sensitizer in order to determine the fragments of the dyes structures, that have an important effect on the *in-situ* photo electrochemical polymerization process (PEP) both in organic and in aqueous media and hence on the performances of the s-DSSCs. Based on these results, a new concept of removing completely the interface between the dye and the HTM is developed. This is achieved by the synthesis of new dyes covalently linked to an electroactive monomer which is co-polymerized by *in-situ* PEP. The resulting co-polymer, used as HTM, is covalently linked to the dye. In addition, the nature of the chemical bond linking the triphenylamine residue TPA to the monomer is also investigated as a key factor in the s-DSSCs performances. Besides, and to optimize the charge transport processes within this type of s-DSSC, the elaboration of novel ZnO based s-DSSCs has been achieved and investigated.

**Keywords:** Solid-State Dye-Sensitized Solar Cells, *in-situ* Photo- Electrochemical Polymerization, donor-linker-acceptor organic dyes, covalent link, hole transporting material, conducting polymer, TiO<sub>2</sub>, ZnO.

## **Résumé**

En raison des problèmes d'instabilité à moyen termes des cellules solaires à colorant (DSSC), l'électrolyte liquide à base d'iodure a été remplacé par plusieurs types de matériaux solides transport de trous (HTM) pour obtenir des DSSCs à l'état solide (s-DSSCs). Parmi ces matériaux, l'utilisation des polymères conducteurs (PC) a attiré une attention considérable en raison de leur bonne stabilité, de leur haute conductivité et de la facilité de leur dépôt sur le semi-conducteur mésoporeux TiO<sub>2</sub>. Dans ce travail de thèse, plusieurs s-DSSCs basées sur des PC utilisés comme HTM ont été développés dans le but d'améliorer leurs performances photovoltaïques en tenant compte des deux objectifs suivants: (i) l'optimisation des processus de transfert inter facial de charge dans la cellule solaire, et (ii) l'optimisation du transport de charge dans le semi-conducteur d'oxyde de type n. Pour atteindre ces objectifs, chaque composant de la s-DSSC a été modifié afin d'étudier son effet sur les performances du dispositif final. En première tentative, une étude analytique est réalisée en faisant varier le sensibilisateur afin de déterminer les fragments de la structure du colorant, qui ont un effet important sur le processus de photopolymérisation électrochimique *in-situ* (PEP) à la fois en milieu organique et en milieu aqueux mais aussi sur les performances des s-DSSCs. Sur la base de ces résultats, un nouveau concept a été développé et consiste en la suppression totale de l'interface entre le colorant et le HTM. Ceci est obtenu par la synthèse de nouveaux colorants liés de façon covalente à un monomère électroactif qui est co-polymérisé par la PEP *in-situ*. Le copolymère résultant, utilisé comme HTM, est lié de manière covalente au colorant. En outre, la nature de la liaison chimique, reliant le résidu triphénylamine TPA au monomère, est également étudiée comme un facteur clé dans les performances de s-DSSC. En outre, et pour optimiser les processus de transport de charges dans ce type de s-DSSC, de nouvelles s-DSSC basées sur ZnO ont été réalisées et étudiées.

**Mots-clés:** Cellules solaires à colorant solide, photopolymérisation électrochimique *in-situ*, colorants organiques donneur-accepteur, liaison covalente, matériaux transporteur de trous, polymère conducteur, TiO<sub>2</sub>, ZnO.

---

---

# *Abbreviations*

---

---

ACN	Acetonitrile
ALD	atomic layer deposition
BL	blocking layer
CB	conduction band
CBZ	carbazole
CE	counter electrode
CP	conducting polymer
CV	cyclic voltammetry
CVD	chemical vapor deposition
DCM	dichloromethane
DEA	diethanolamine
DFT	density functional theory
DSSCs	dye-sensitized solar cells
D- $\pi$ -A	Donor – Linker – Acceptor
EDOT	3,4-ethylenedioxythiophene
$E_F$	Fermi level
$E_G$	Bandgap energy
$E_{\text{onset,ox}}$	onset of the oxidation potential
$E_{\text{ox}}(\text{dye})$	oxidation potential of the dye
EPD	electrochemical deposition
$E_{Q-F}$	quasi-Fermi level
ETM	electron transporting material
FF	fill factor
FTO	fluorine doped tin oxide
HRMS	High resolution mass spectrum
HTM	hole transporting material
$i_c$	capacitive current
ICT	intramolecular charge transfer
$i_f$	faradic current
IPCE	Incident Photon-to-Electron Conversion Efficiency
ITO	indium doped tin oxide
J	current density
$J_{sc}$	short-circuit current density
LCAO	linear combinations of atomic orbitals
LiTFSI	$\text{Li}(\text{CF}_3\text{SO}_2)_2\text{N}$
$L_n$	electron diffusion length
MLCT	metal-to-ligand charge transfer

Mtoe	Million Tonnes of Oil Equivalent
NR	nanorods
OFETs	organic field-effect transistors
OLEDs	organic light-emitting diodes
OPV	Organic Photovoltaic
PANI	polyaniline
PCE	power conversion efficiency
PEDOT	poly (3, 4-ethylenedioxythiophene)
PEN	polyethylene naphthalate
PEP	( <i>in-situ</i> ) photo-electrochemical polymerization
PET	polyethylene terephthalate
PIA	photoinduced absorption spectroscopy
$P_{in}$	the incoming power
PPy	polypyrrole
PVD	physical vapor deposition
$R_{CT}$	charge transfer resistance
RE	reference electrode
SCE	saturated calomel electrode
SCN	thiocyanato
s-DSSCs	solid-state DSSCs
SHE	standard hydrogen electrode
SNS	2,5-di(thiophen-2-yl)-1H-pyrrole
TBP	4-tert-butylpyridine
TCO	transparent conducting oxide
TDDFT	time dependent DFT
TPA	triphenylamine
VB	valence band
$V_{oc}$	open circuit potential
WE	working electrode
$\eta$	efficiency
$\sigma$	conductivity

---

---

# Contents

---

---

<b>General Introduction .....</b>	<b>1</b>
<b>Chapter I From Fossil Fuel to Renewable Energy: The Emergence of Solar Cells in Energy Transition.....</b>	<b>3</b>
I. 1. Photovoltaic effect: generalities .....	5
I. 1. a. The Sun: Primary Source of Energy .....	5
I. 1. b. Basic principle of photovoltaic .....	7
I. 1. c. Solar Cells: The Three Generations .....	12
I. 2. DSSC: Structure and components .....	16
I. 2. a. The photo-anode .....	17
I. 2. b. The photo-sensitizer.....	22
I. 2. c. The Hole Conducting Material .....	31
I. 2. d. The Counter Electrode .....	36
I. 3. Solid State-DSSC: operating principle and photovoltaic performances .....	37
I. 3. a. The Operating Principle .....	39
I. 3. b. Excitation, Electron Injection, Electron Transport and Charge Recombination .....	40
I. 3. c. Solar Cell Performances.....	43
I. 4. Aim of the thesis.....	47
I. 5. References .....	49
<b>Chapter II Influence of D-<math>\pi</math>-A Organic Dyes Structures on TiO<sub>2</sub> based s-DSSCs Performances .....</b>	<b>59</b>
II. 1. Generalities and Material used in s-DSSCs .....	60
II. 1. a. TiO <sub>2</sub> Photo-anode: Preparation Methods.....	60
II. 1. b. LEG4, D35, L1, BA504, BA741 and RK1 D- $\pi$ -A Organic Dyes Structure Overview and Sensitization Step .....	62
II. 1. c. Conducting Polymer as Hole Transporting Material.....	64

II. 1. d. The <i>In-situ</i> Photo-Electrochemical Polymerization Process of Conducting Polymers	.69
II. 1. e. Additives	73
II. 1. f. Counter-electrode	74
II. 2. Experimental Section	74
II. 2. a. Preparation of the TiO <sub>2</sub> Photo-anode	74
II. 2. b. Sensitization Step: Dye Adsorption	76
II. 2. c. The <i>In-situ</i> Photo-Electrochemical Polymerization Process of Conducting Polymers	76
II. 2. d. Additives and Counter Electrode	77
II. 3. Results and Discussion	78
II. 3. a. Characterization of the TiO <sub>2</sub> Photo-anode	78
II. 3. b. Properties of LEG4, D35, L1, BA504, and BA741 Dyes	80
II. 3. c. Study of <i>in-situ</i> PEP using L1, D35, LEG4, RK1, BA504 and BA741 organic dyes	87
II. 3. d. Characterization of PEDOT layer <i>in-situ</i> produced on the dyed photo-anode	92
II. 3. e. s-DSSCs devices performances	94
II.4. Conclusion	101
II. 5. References	102
<b>Chapter III Effect of the Dye-HTM Covalent Link on s-DSSCs Performances</b>	<b>106</b>
III. 1. Optimization of the Interfacial Charge Transfer	107
III. 1. a. General context	108
III. 1. b. Novel Organic Dyes Covalently Linked to the CP generated by <i>in-situ</i> PEP	109
III. 2. Experimental details	113
III. 2. a. ADCBZ and ADSNS Dyes Synthesis	113
III. 2. b. Characterization Techniques for Dyes Structure and Dye-Sensitized TiO <sub>2</sub> Substrates	114
III. 2. c. <i>In-situ</i> PEP process and s-DSSC performances	115
III. 3. Results and Discussion	115
III. 3. a. Characterization of Dye Molecules (ADCBZ and ADSNS)	115

III. 3. b. <i>In-situ</i> PEP deposition of PEDOT on the Sensitized TiO <sub>2</sub> Photo-anodes.....	120
III. 3. c. s-DSSCs devices performances.....	123
III. 3. d. Discussion .....	126
III. 3. e. Impact of the s-DSSCs aging process on photovoltaic performances.....	127
III. 4. Conclusion .....	128
III. 5. References.....	130
<b>Chapter IV Influence of the Nature of the Covalent Link between the Dye and the HTM on s-DSSCs Performances .....</b>	<b>132</b>
IV. 1. Modification of the covalent link between the dye and the HTM .....	133
IV. 1. a. General context: extension of electron donating in the donor part .....	134
IV. 1. b. Proposed organic dyes containing the electroactive monomer.....	135
IV. 2. Experimental details .....	137
IV. 2. a. Preparation of building blocks .....	137
IV. 2. b. Preparation of ADCBZ-1, ADSNS-1, ADCBZ-2 and ADSNS-2 dyes .....	138
IV. 3. Results and Discussion .....	139
IV. 3. a. Dyes syntheses and physico-chemical characterization.....	140
IV. 3. b. <i>In-situ</i> PEP deposition of PEDOT on the Sensitized TiO <sub>2</sub> Photo-anodes .....	148
IV. 3. c. s-DSSCs devices performances.....	150
IV. 3. d. Impact of the s-DSSCs aging process on photovoltaic performances .....	153
IV. 3. e. Discussion .....	154
IV. 4. Conclusion .....	155
IV. 5. References.....	156
<b>Chapter V Modification of the Oxide Semiconductor in s-DSSCs: Use of ZnO .....</b>	<b>157</b>
V. 1. Optimization of the Electron Transport Process within the Semiconductor .....	158
V. 1. a. General context.....	159
V. 1. b. s-DSSCs based ZnO using Conducting Polymers generated by <i>in-situ</i> PEP.....	162
V. 2. Elaboration of ZnO Photo-anode .....	163



V. 2. a. Preparation of ZnO blocking layer .....	163
V. 2. b. Preparation of ZnO mesoporous layer .....	165
V. 2. c. Sensitization Step: Dye Adsorption.....	166
V. 2. d. <i>In-situ</i> PEP process and additives .....	166
V. 2. e. Characterizations and s-DSSC performances.....	166
V. 3. Results and Discussion .....	167
V. 3. a. Electrochemical characterization of the ZnO blocking layer .....	167
V. 3. b. Structural characterization of ZnO blocking layer and ZnO mesoporous layer.....	170
V. 3. c. Characterization of D35 dye sensitized ZnO photo-anode.....	173
V. 3. d. <i>In-situ</i> PEP using D35 organic dye in organic medium .....	175
V. 3. e. SEM characterization of FTO/ZnO/D35/PEDOT photo-electrode .....	176
V. 3. f. ZnO based s-DSSCs devices performances .....	177
V. 3. g. Discussions .....	179
V. 4. Conclusion .....	180
V. 5. References.....	181
<b>General Conclusion and Perspectives .....</b>	<b>183</b>
<b>Annex I.....</b>	<b>187</b>
<b>Annex II.....</b>	<b>188</b>
<b>Annex III.....</b>	<b>194</b>
<b>Annex IV .....</b>	<b>199</b>



---

---

# *General Introduction*

---

---

Fossil fuels including coal, natural gas and oil are at present the world's primary energy sources which contribute to the greenhouse effect and thus to the global warming. This global warming is currently causing temperature and sea level rises, extreme weather phenomena (such as heavy rainfall, drought or storms) and a decline in agriculture yields, thus threatening mankind, biodiversity and our planet. With the objective to limit global warming below the 2 °C, agreement approved during the annual Conference of Parties - COP21, leaders from all parties progress toward a 100 % renewable energies future. The EU countries have already set themselves a target of 27 % final energy consumption from renewable sources by 2030.

Solar energy is the most promising renewable energy source since it is usable on the whole planet. Solar thermal energy and photovoltaics are two different technologies, both exploiting the sun as an energy source. The photovoltaic principle is the direct conversion of sunlight into electricity through modules known as solar cells. Photovoltaic technology has particularly attracted great interest as a sustainable, cost-effective device exhibiting high efficiency with much lower CO<sub>2</sub> emission. To date, the top-performing solar cell sits at 46 %: it is made of III-V compound semiconductor materials also known as multi-junction solar cells. Recently, researchers at the Fraunhofer Institute have successfully manufactured a silicon-based multi-junction solar cell with a record conversion efficiency of 30.2 %. Silicon is at present the basic component in conventional solar cells that currently dominates the world market. However, emerging photovoltaic technologies, such as perovskite, organic (OPV), tandem, quantum dots (QDSCs) and dye-sensitized solar cells (DSSCs), provide comparable efficiency both at low-cost manufacturing and using cost-effective starting materials, thus moving these technologies toward industrial production. They are becoming potentially competitive with silicon solar cells.

Classified in the third generation category of photovoltaics and known as "Grätzel cells", the interest for DSSCs began in 1991, since Michael Grätzel and Brian O'Regan reported the first cell: partially inspired by photosynthesis process, it recorded a solar efficiency at 7 %. The most powerful DSSC has been developed by K. Kakiage *et al.* in 2015 and now reaches 14 % efficiency. Despite their attractive properties and compared to the other emerging photovoltaic technologies, DSSCs are built from eco-friendly, colorful and semi-transparent constituent

elements suitable for a wide variety of applications. Typically, a conventional DSSC is composed of a photoanode, made of a mesoporous TiO<sub>2</sub> semiconductor coated with the dye, a counter-electrode and a liquid electrolyte, which contains triiodide and iodide redox shuttle (I<sub>3</sub><sup>-</sup>/ I<sup>-</sup>) used as hole transporting material (HTM) for the regeneration of the sensitizing dye molecule. Nowadays, most of the present researches on DSSCs are focused on optimizing each component, in order to further improve the device performances and durability.

Due to instability problems in longtime uses the iodine based liquid electrolyte has been replaced by several types of solid HTMs, namely in solid-state DSSCs (s-DSSCs). Among them, the substitution by a *p*-type conducting polymer (CP) has attracted considerable attention because of its good stability, high hole-conductivity and its simple deposition within the mesoporous TiO<sub>2</sub> semiconductor. In this thesis work, several s-DSSCs based on CPs used as HTM have been developed in order to improve their photovoltaic performances taking into account the following two objectives:

- (1) Optimizing the interfacial charge transfer processes within the solar cell
- (2) Optimizing the charge transport within the n-type oxide semiconductor.

Therefore, two different approaches were attempted in these s-DSSCs with the aim to give them a real sustainability and stability without neglecting the ecological and economic aspects. The first approach is the design of innovative organic donor-acceptor dyes with a new concept consisting in the total removal of the interface between the dye and the HTM, and the second is the substitution of the TiO<sub>2</sub> semiconducting material by ZnO.

## **Chapter I**

# **From Fossil Fuel to Renewable Energy: The Emergence of Solar Cells in Energy Transition**

With the rapid growth of the global population that will arise in very near future, the world energy demand is expected to increase to an unprecedented pace. Fossil fuels are at present the primary energy source supplying more than 80 % of the world energy consumption. However, these non-renewable resources are pollutants and becoming scarce. In fact, according to the International Energy Agency report<sup>[1,2]</sup>, the world energy production reached 13700 Million Tonnes of Oil Equivalent (Mtoe) in 2014 including oil (31 %), coal (29 %), natural gas (21 %) and nuclear (5 %). At this current rhythm of production, the world energy reserves are expected to be exhausted within 84 years on average<sup>[3]</sup>. In a world dependent on these resources for transport, industry, housing or electricity; safeguards become a primary concern for all States of the world at the economic and political levels (Kyoto Protocol, Energy Transition). This leads to the development of new and innovative technologies based on non-fossil sources, known as renewable energies, for a more-efficient and a more-carbon free energy production and consumption. Renewable energy technologies produce sustainable energy from sun, wind, water and plants, and presently amount to 14 % of the world energy production (Figure I-1).

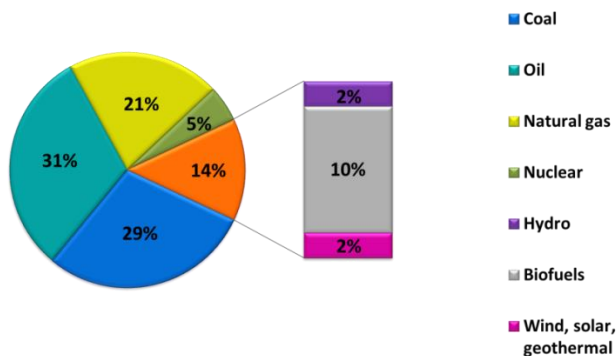


**Figure I-1:** Total primary energy supply by fuel in 2014 <sup>[2]</sup>

In recent years, the amount of energy produced by photovoltaic technology has increased considerably while the market price has diminished, enabling solar energy to be both more accessible for the realization of projects and increasingly competitive relative to other energy sources reaching progressively all countries of the world including emerging countries (China, India). The development prospects of solar energy industry are therefore promising and will play an essential role in the energy transition under the Kyoto Protocol. Chemistry is the heart of this technological breakthrough allowing the development of different types of novel solar cells from a variety of innovative materials.

## I. 1. Photovoltaic effect: generalities

The photovoltaic effect, “Photo” from the Greek meaning light and “voltaic” for the electric potential pioneered by Alessandro Volta, is a process in which two dissimilar materials in close contact produce an electrical voltage when struck by light or other radiant energy<sup>[4]</sup>. In most photovoltaic applications the radiant energy comes from the sunlight. It is therefore essential to understand the photovoltaic operating principle and to have an overview on the composition of the solar spectrum that drove researchers to develop a multitude of solar cells.

### I. 1. a. The Sun: Primary Source of Energy

The global world energy consumption, in 2014, amounts to 9425 Mtoe or approximately 109 613 TWh from all sources<sup>[5]</sup>. 19.2 % of our energy consumption originates from renewable energy and only 0.2 % of it, is generated by solar energy which translates in power into 190.8 TWh<sup>[6]</sup> that means  $10^6$  times less than the annual solar energy power received by the Earth ( $10^9$  TWh)<sup>[7]</sup>. Therefore the Sun is, in itself, a useable energy source. Indeed, knowing that the luminosity of the Sun is  $3.846 \times 10^{26}$  W and the distance from Earth to the Sun is 1 astronomical unit (A.U.) *i.e.*  $1.496 \times 10^{11}$  m, the solar constant *i.e.* the flux of solar radiation that receives a surface of  $1 \text{ m}^2$  at the top of the Earth in zero atmosphere, is roughly  $1360 \text{ W/m}^2$ . It should however be pointed out that this solar constant is estimated above Earth’s atmosphere exposed perpendicularly to Sun’s rays and varies +/- 3 % due to its elliptical orbit around the Sun.

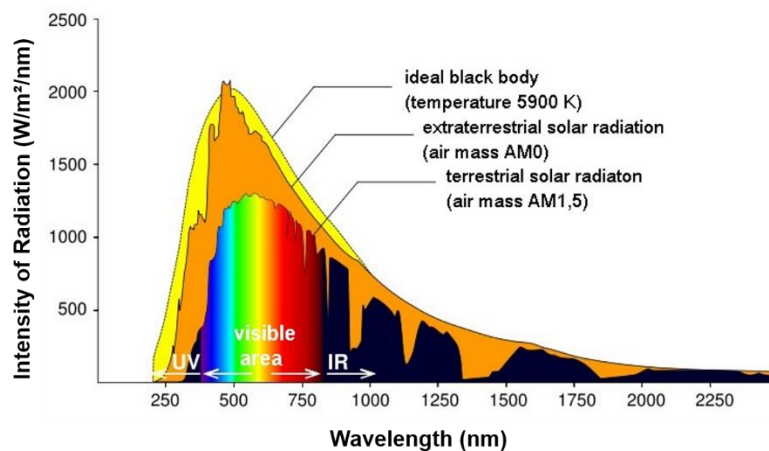


**Figure I-2:** Spectral distribution of solar radiation of an ideal black body, at the top of the Earth’s atmosphere on the 37° inclined surface and at sea level taken from ref. [8].

Solar radiation issued by the visible surface of the Sun, namely photosphere, refers to the electromagnetic radiation with a spectral distribution ranging from 0.2 $\mu\text{m}$  to 2.6  $\mu\text{m}$ , fairly similar to the black body radiation spectrum at a 5800 K<sup>[9]</sup> (Figure I-2). This electromagnetic radiation, including gamma rays, X-rays, Ultra-Violet, visible, Infra-Red, microwaves and radio waves, can be described (wave-particle duality) in terms of electromagnetic wave characterized by a frequency  $\nu$  and a wavelength  $\lambda$ , and also of massless stream of particles, known as photons, moving at speed of light in vacuum ( $c= 3.10^8 \text{ m.s}^{-1}$ ). The energy of this elementary particle is given by the Planck-Einstein relation:

$$E = h\nu = \frac{hc}{\lambda} \quad (\text{I-1})$$

With the Planck's constant  $h= 6.6 \times 10^{-34} \text{ J.s}$

However, not all of the electromagnetic radiation reaches the Earth's surface: some parts of this radiation are attenuated when it crosses the atmosphere. This electromagnetic radiation is, in fact, disturbed both by scattering and absorption processes due to gas molecules, aerosols, clouds that mainly constitutes the Earth's atmosphere. The solar spectrum at Earth's surface is therefore dependent of many atmospheric parameters as well as the path length through the atmosphere. It is characterized by an Air-Mass coefficient, "AM X", and defined as the optical path length  $L$  through Earth's atmosphere. When the Sun is directly at its zenith ( $\theta= 0^\circ$ ) the Air-Mass indicator is denoted AM 1, "1" for one atmosphere with a solar irradiance at Earth's surface (at sea level more precisely) reaching  $1040 \text{ W/m}^2$  in optimum conditions. This value is further reduced compared to the extraterrestrial solar radiation referred as

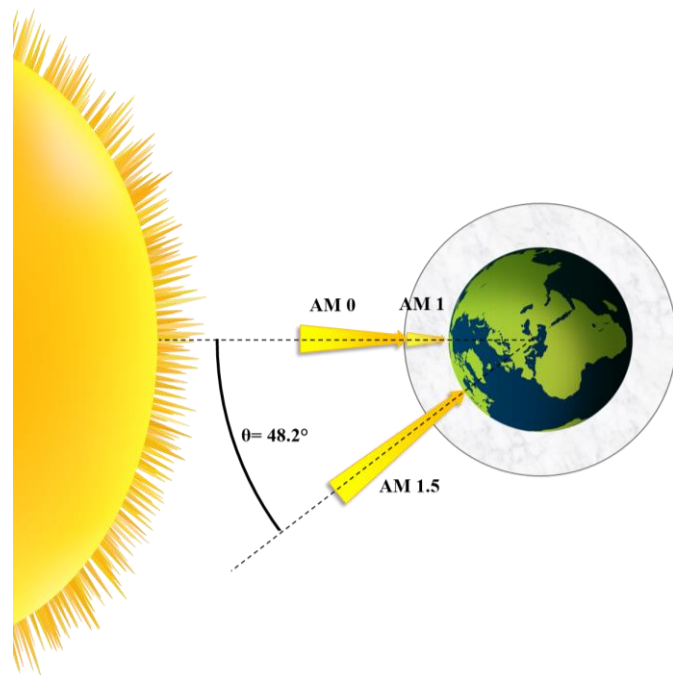


**Figure I-3: Air-Mass coefficient depiction at 0, 1, and 1.5 atmospheres.**



air mass zero, AM 0, meaning no atmosphere, and with a solar irradiance equivalent to the solar constant (Figure I-3).

For incident solar radiation at angle  $\theta$  relative to the normal to the Earth's surface  $L_0$ , the Air-Mass coefficient is expressed as:

$$AM X = \frac{L}{L_0} = \frac{1}{\cos \theta} \quad (I-2)$$

AM 1.5 is the standardized solar spectrum, established by the American Society for Testing and Materials (ASTM), corresponding to a zenith angle of  $\theta = 48.2^\circ$  (according to the tilt angle at  $37^\circ$  toward the equator) commonly used for terrestrial applications such photovoltaic solar cells. The power density related to AM 1.5G (G for a global radiation) is estimated at  $1000 \text{ W/m}^2$  at room temperature<sup>[10]</sup>, used as reference in this thesis work.

### **I. 1. b. Basic principle of photovoltaic**

The photovoltaic effect, discovered in 1839 by the French physicist Alexandre Edmond Becquerel, is a property that some materials exhibit to produce electricity when exposed to the light. From his experiments, A. E. Becquerel highlights the production of voltage and current, within an electrochemical cell consisting of silver chloride electrode connected to a counter platinum electrode dipping in an acidic electrolytic solution, when exposed to light<sup>[11]</sup>. During the following 100 years, research in photovoltaic field have intensified and mainly well described by Albert Einstein on his 1905 paper<sup>[12]</sup> behind “photoelectric effect” for which he won the Nobel Prize. Based on these works, in 1954 researchers from Bell Laboratories developed the first concrete solar cell, relatively efficient to convert enough solar energy into electric power with efficiency of 6 %. This principle is only based on semiconductor technology made from crystalline silicon, basic component that currently dominates the market. In fact, Russell Ohl from Bell Labs inadvertently discovered in 1940 that doped silicon, arising from the combination of a p-type semiconductor (p for positive charges) and an n-type semiconductor (n for negative charge), produced a flow of electricity under light irradiation. The resulting p-n junction is required to get an energy conversion from photons to electrons. To be able to explain the operating principle of a photovoltaic cell, we will first review the photovoltaic concept in

quantum chemistry and in solid-state physics. According to the valence bond theory, only electrons of the valence shell, the outermost shell from the nucleus, are engaged in a covalent bond in a molecule. The chemical bonding can also be described following the molecular orbital theory as linear combinations of atomic orbitals (LCAO). An orbital is a wave function  $\Psi$  describing the state of an electron depending on the distance from the nucleus ( $r$ ) and the angle ( $\theta, \phi$ ) which is the solution of the Schrödinger equation. The square modulus of this wave function  $|\Psi|^2$  is the probability of finding the electron in a space around a single atom (*i.e.* hydrogen). By solving  $|\Psi|^2$ , the wave function, described upon three quantum numbers:  $n$  (principle),  $l$  (angular), and  $m$  (magnetic), corresponds to the atomic orbital (1s for H) with an energy value determined exclusively from  $n$ . For a diatomic molecule,  $H_2$  for example, the covalent bond between two H atoms resulting from the overlap of 2 atomic orbitals (AO), following the LCAO leads to 2 coupled levels, 2 molecular orbitals (MO) with no more than 2 electrons per orbital, each distinguished by their spin (Pauli exclusion principle). One is referred to the “bonding” MO of lower energy (from the 2 AO constructive interference), and the other is called “anti-bonding” MO of higher energy (from the 2 AO destructive interference). Similarly, if we apply to larger molecules comprising  $N$  atoms, such as crystal lattice, each of their AO overlap with AO of the  $N-1$  other atoms leading to an infinite number of MOs at different energy levels. They are so close that they form a continuum of energy levels as an energy band (Figure I-4a)). The latter is equivalent to the electronic band structures in solid-state physics. Indeed, due to the periodic array of atoms, electrons feel the presence of other electrons through the periodic potential. Each of these new wave-functions ascribed to electrons by solving the Schrödinger equation is the Bloch’s wave introduced by the Physicist Felix Bloch during his doctoral thesis<sup>[13]</sup>. Similarly, each wave-function associated to an energy gives rise to a denumerable set of electron states as quasi-continuous bands known as “allowed bands” each separated by a “forbidden band”.

From this electronic band structure, materials can be classified upon their electrical conductivity. At 0 K, the energy levels are filled by electrons starting from the lowest. The levels that are filled by electrons constitute the valence band (VB). Beyond this band, the first lowest vacant band is the conduction band (CB). The Fermi level ( $E_F$ ), lying between the valence and the conduction band, refers to the chemical potential of electrons. For metals, the valence and conduction band overlap without any additional energy. Such metals contain a large number of free electrons and

hence are highly conductive (Figure I-4b)). When these two bands are separated by a forbidden band called “bandgap” ( $E_G$ ), the material is either an insulator or a semiconductor. In the case of insulator, the bandgap is high, thus it is impossible for an electron to jump from the VB to CB, even at room temperature (RT), and hence it cannot conduct. By contrast, for semiconductors the bandgap is sufficiently narrow to lift an electron from VB to CB at RT, leaving at the same time a hole in the VB. This hole in the VB is ultimately assimilated to positive charge that carries the current. They are thus conductive. These created electron-hole pairs are charge carriers corresponding to excitons<sup>[14]</sup>.

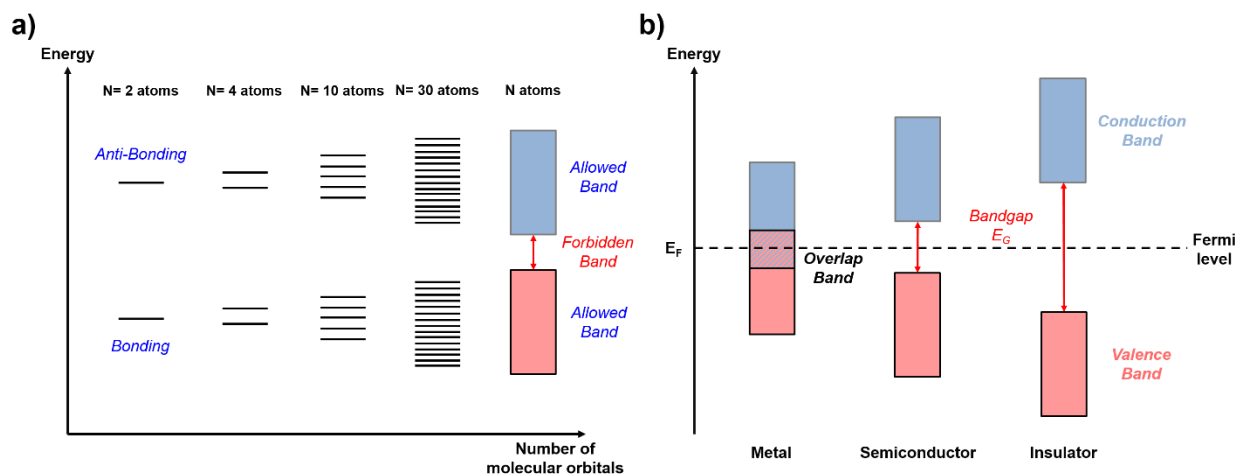


**Figure I-4:** a) Molecular orbital energy level diagram for 2, 4, 10, 30 and N atoms. b) Schematic band diagram for metal, semiconductor and insulator.

To make a semiconductor more conductive few electrons are included in the CB or, in an equivalent manner, some electrons from the VB are removed: this is the “doping” process. The terms used to specify a doped semiconductor (extrinsic) with an excess of electrons or holes, assimilated as impurities or defects, are n-type or p-type semiconductor respectively. Depending on the doping process, the Fermi level will be obviously impacted. For n-type semiconductor, the Fermi level shift toward the CB or toward the VB for the p-type semiconductor. When these two doped n-type and p-type semiconductors are joined, the p-n junction is formed. Some electrons from the n region diffuse across the junction to reach the p region leaving an ionized donor behind. Similarly, holes from the p region diffuse to n region leaving behind an ionized acceptor. Thus a new region, depleted on free charge carriers, is created in the vicinity of the junction resulting from the electrons-holes diffusion and recombination: this is the depletion zone. Furthermore, the presence of ions (negative in p region and positive in n region) generates an

electric field across the junction and causes the separation of electrons and holes and their transfer in the opposite direction to the diffusion process. When the electric field compensates the diffusion it leads to an equilibrium state. If an external field is applied by means of generator by connecting the + pole to the p region and – pole to the n region, it creates an electric field  $\xi$  in reverse direction to the internal field  $\xi_{int}$  (or built-in electric field), this is the forward bias and as a result the charge carriers flow and the current is obtained (Figure I-5a). The standard device having this configuration and relying on this operating principle is a diode.

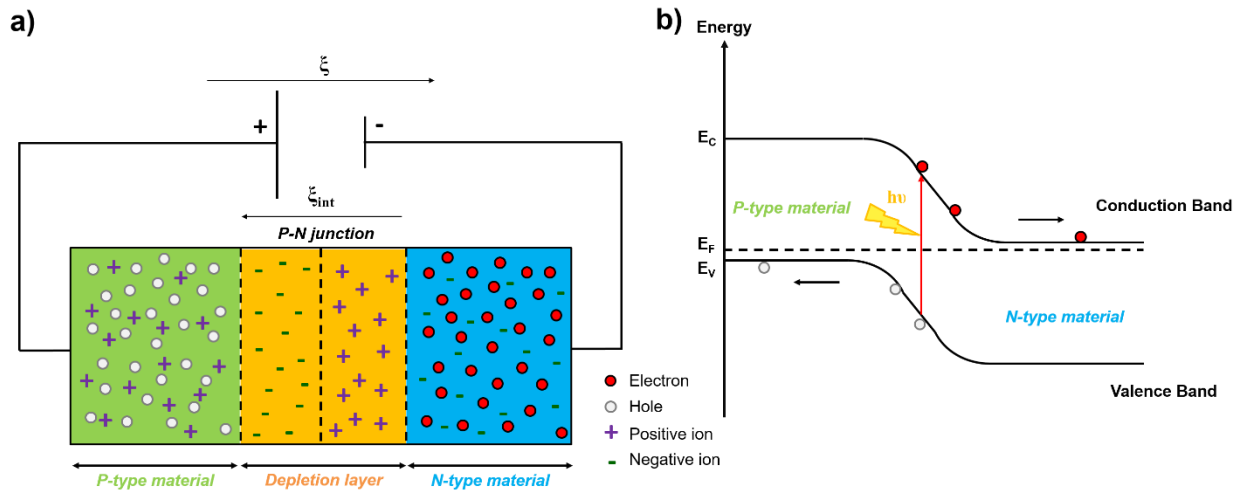


**Figure I-5:** a) P-N single junction diode under forward bias. b) Energy band diagram of a solar cell P-N junction.

The current flow is also obtained from the illumination of the p-n junction: this is the photovoltaic effect. When the junction is illuminated, a photon is absorbed by the semiconductor by stripping an electron from its VB to the CB provided that the energy of the photon is greater than the bandgap energy (Figure I-5b)). The generated exciton located in the depletion zone, where the internal electric field takes place, splits up and the electron moves toward the n side unlike the hole pushed toward the p side. The electron joins the hole through the external connection giving rise to a difference of potential: the electric current flows. The photovoltaic cells are then assembled to form modules.

As mentioned above, the most dominant semiconductor material used for photovoltaic technology is crystalline silicon. The choice of silicon (Si) atom is supported by the presence of 4 valence electrons (group IV) allowing to be covalently bonded with 4 neighboring Si atoms (tetravalent) resulting in a diamond cubic crystal structure in the crystal lattice. If one atom of Si is replaced by an atom of the group V, commonly phosphorous (P), the semiconductor is n-doped

due to the excess of free electrons. However, if Si is replaced by an atom of the group III, boron for example, the semiconductor is p-doped, due to the presence of holes.

Hence, the p-n junction is achieved. The energy bandgap as well as its light absorption ability of a semiconductor must be taken into consideration. The energy bandgap of semiconductors depends on the temperature following the relation proposed in 1967 by the physicist Y. P. Varshni<sup>[15]</sup> :

$$E_G(T) = E_G(0) - \frac{\alpha T^2}{T + \beta} \quad (\text{I-3})$$

Where  $E_G$  is the energy bandgap which may be direct (same crystal momentum  $\vec{p}$  for CB et VB) or indirect (different crystal momentum  $\vec{p}$  for CB et VB),  $E_G(0)$  is the energy bandgap at 0 K,  $\alpha$  and  $\beta$  are constants related to the material. Table I-1 provides the bandgap energy of homojunction (Si, Ge) and of heterojunction (GaAs) semiconductors<sup>[16,17]</sup>.

Material	Bandgap $E_G$ (0)	$\alpha$ (eV/K)	$\beta$ (K)	$E_G$ (300 K)
Si	1.170 eV	$4.73 \times 10^{-4}$	636	1.12 eV
Ge	0.7437 eV	$4.77 \times 10^{-4}$	235	0.66 eV
GaAs	1.519 eV	$5.41 \times 10^{-4}$	204	1.42 eV

**Table I-1:** Bandgap energy of Si, Ge, and GaAs semiconductors at 0K and 300K.

For Si the energy bandgap is 1.12 eV at RT, so the photons must have an energy value higher than 1.12 eV or  $1.79 \times 10^{-19}$  J. In wavelength, Si semiconductor will absorb a large portion of the spectrum till the cut-off wavelength  $\lambda_G$  from 1100 nm to 250 nm.

$$\lambda_G(nm) = \frac{h \times c}{E_G \times 1.6 \times 10^{-28}} = \frac{1242}{E_G} \quad (\text{I-4})$$

Beyond 1100 nm, photons are not absorbed and pass through the cell (18 %). This is one of the reason why Si solar cell is not 100 % efficient. Another reason is that almost the half of the sun irradiance is re-emitted as heat or light. Theoretically, 32 % of the sunlight can be converted as electricity with Si according to the “Shockley-Queisser limit” computations performed by W. Shockley and H.J. Queisser in 1961<sup>[18]</sup>. The predicted maximum efficiency is 33.7 % assuming single junction semiconductors with an energy bandgap of 1.34 eV (Figure I-6).

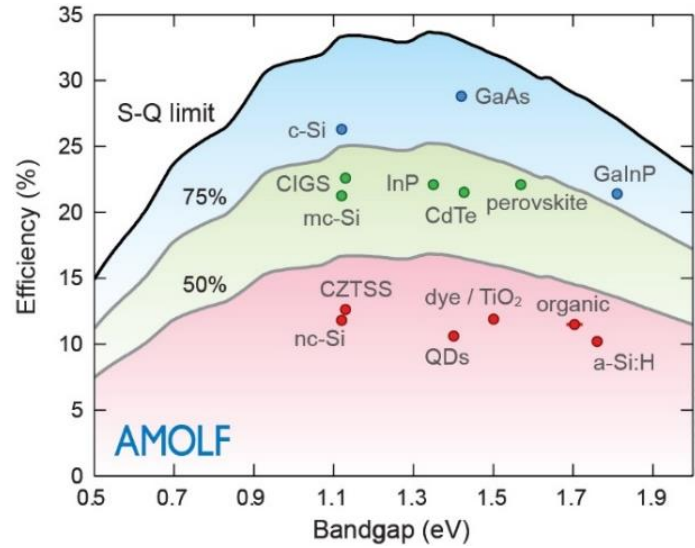


**Figure I-6:** Comparison between the most efficient single junction solar cells with the fundamental Shockley-Queisser limit (black line). The figure is taken from ref. [19] and AMOLF.

At present, the best efficiency for a single junction cell reaches 28.8 % close to the theoretical value. The cell was developed in 2012 by Alta Devices based on gallium arsenide (GaAs) which is an III-V heterojunction semiconductor<sup>[20]</sup>. Compared to Si and Ge, GaAs has the benefit of being a direct bandgap material. The nature of the gap has a fundamental role in the interaction of the semiconductor with electromagnetic radiation. In the case of a direct bandgap semiconductor, the electron characterized by a wave vector  $\vec{k}$  passes from the VB to the CB without changing the momentum ( $\vec{p} = \hbar \vec{k}$ ) and whose energy is equivalent to  $E_G$ . In the indirect bandgap semiconductor, the momentum is larger.

Remarkable progresses have been achieved in the field of photovoltaic, by the development of new solar cells such as multijunction cells, thin film technologies and emerging photovoltaics.

### **I. 1. c. Solar Cells: The Three Generations**

In the field of photovoltaic, research and development generally aims to provide higher efficiency and lower costs per watt of electricity generated for large scale application. In some countries, the production cost of electricity from solar energy is already lower than that of coal<sup>[21]</sup>. It is mainly produced by silicon solar cells classified in the first generation. Indeed, solar cells are usually identified in different "generations" according to the engineering of their architecture (Figure I-7).

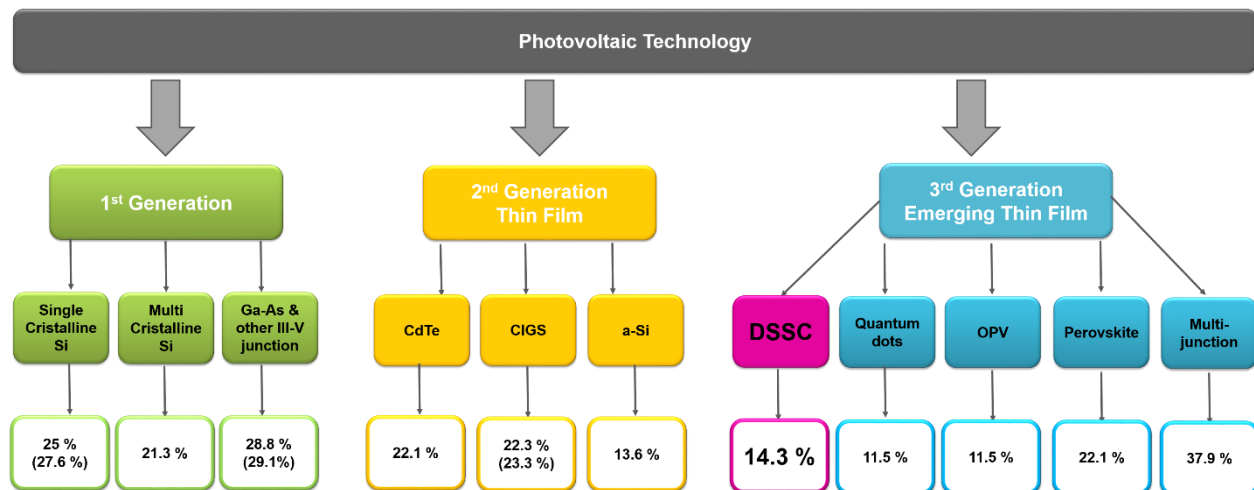


**Figure I-7:** The different photovoltaic technologies divided into three generations followed by their highest efficiency.

Generally the first generation includes crystalline Si cells (c-Si) made of wafers, as mentioned above, that provide the highest efficiency in single junction solar cells. They differ by their allotropic form. When wafers are derived from a single silicon crystal and structure of the crystal is perfectly homogeneous, they refer to monocrystalline solar cells. For wafers composed of several silicon crystals of various and varied sizes, they refer to polycrystalline solar cells (Figure I-8). The former is known to be efficient and the latter to be easy to produce. However, for both, the processes used to improve the purity of silicon are expensive.

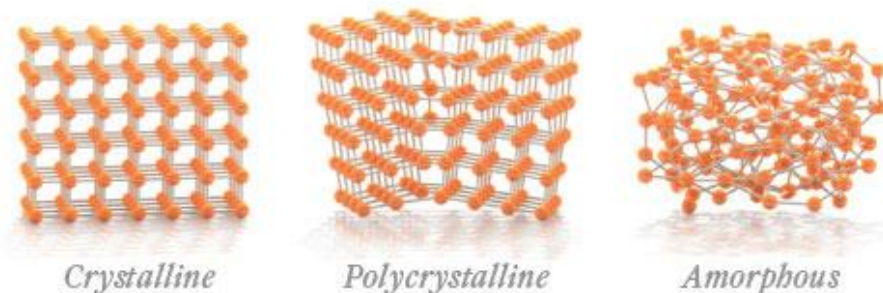


**Figure I-8:** Schematic representation of three allotropes of silicon (taken from the ref.[22]).

The purity is the limiting key factor that impact efficiency. Moreover the non-flexibility and the heaviness of silicon panels are two more issues that lead to the introduction toward thin-film technology.

Thin-film technology involves chemical vapor deposition technique and constitutes the second generation. The supporting substrate is made of cost-effective material such as glass, ceramic or plastic and it is thus lightweight. Thin-film solar cells are quite efficient and cheaper in

production to be sufficiently competitive to c-Si solar cells. The most successful thin-film technology is cadmium telluride (CdTe) solar cell patented by the American manufacturer First Solar<sup>[23]</sup>. CdTe belongs to the II-VI semiconductor group with a direct bandgap of 1.5 eV allowing to get a high absorption coefficient. At present, CdTe solar cells have the lowest energy payback time (1 year) which refers to the time, measured in years, required for any photovoltaic system to produce as much energy as was required in its manufacture<sup>[24]</sup>. According to the National Renewable Energy Laboratory (NREL) the best efficiency is up to 22 % that makes them the second most dominant photovoltaic technology in the market. However, these cells contain cadmium which is a highly toxic element and its disposal and recycling are both are both risky and costly. Amorphous silicon (a-Si) (Figure I-7) and copper, indium, gallium, selenide (CIGS) are two alternative materials that are environmental friendly. The best efficiency for CIGS solar cells is comparable to CdTe with 22.3 % obtained by Japanese producer from Solar Frontier<sup>[25]</sup>.

The third generation photovoltaics are the most promising technologies arising from the first generation and the second generation in terms of manufacture, flexibility, production cost, and toxicity. Devices are designed to overcome the Shockley-Queisser limit, for example by stacking multi-layers of single junction known as multi-junction solar cells. This is what Sharp Corporation achieved in 2009, by the development of a triple-junction solar cell combining three photo-absorption layers that have different bandgaps (Figure I-9).

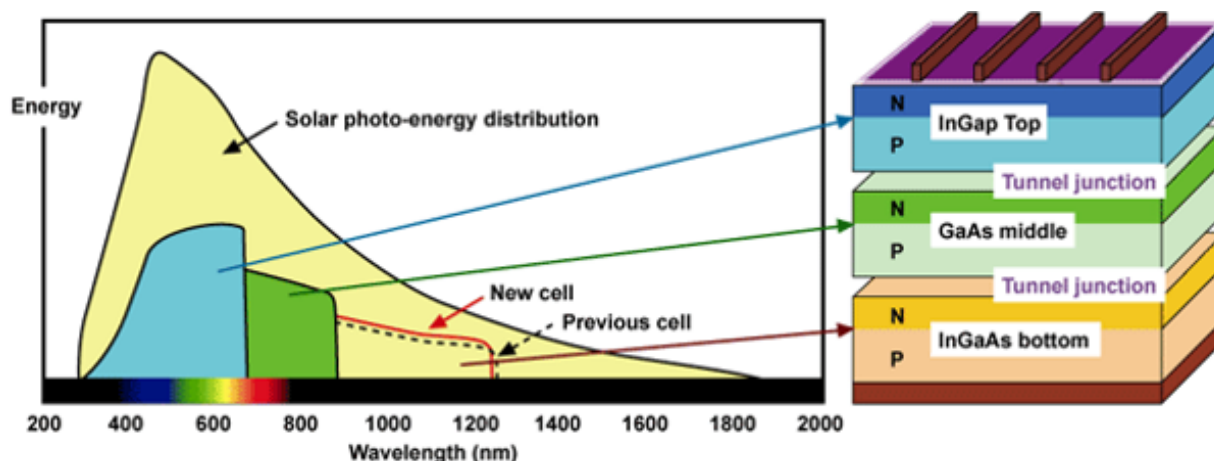


**Figure I-9:** Spectral distribution of solar radiation and wavelength sensitivity of the three photo-absorption layers (taken from the ref. [26]).



The bottom, middle and top layers of the solar cell are made of InGaAs (0.97-0.99 eV), GaAs (1.43 eV) and InGaP (1.88 eV) respectively yielding to 37.9 %<sup>[27]</sup>. Similarly, the limit can also be reached by stacking different solar cells so-called tandem solar cells that absorb optimally different part of the solar spectrum<sup>[28,29]</sup>. Researchers are also focused on innovative materials typically at nanoscale that deliver unique properties such as quantum dots<sup>[30,31]</sup> and yielded today at 11.5 %<sup>[32]</sup>. Quantum dots solar cells are part of emerging photovoltaic field<sup>[33]</sup> as well as plasmonic solar cells where the challenge is improving the light absorption due to the localized surface plasmon resonance<sup>[34]</sup>. The top performing of emerging photovoltaic is perovskite solar cell pioneered by the chemist T. Miyasaka in 2009<sup>[35]</sup>. Usually, a perovskite is in the form of  $ABX_3$  made of an organic cation (A), an inorganic cation (B) and an halogen anion (X) with a bandgap of nearly 1.5 eV: so an efficient light harvester<sup>[36]</sup>. In their first report, Miyasaka *et al.* employed two methylammonium lead trihalide as perovskite nanocrystals:  $CH_3NH_3PbBr_3$  and  $CH_3NH_3PbI_3$  with a bandgap of 2.02 eV and 1.44 eV respectively. Therefore  $CH_3NH_3PbI_3$  which is more light-sensitive yielded an efficiency of 3.8 %. Since then, extensive research have been achieved and the highest efficiency reaches 22.1 %<sup>[37,38]</sup>. Historically, perovskite solar cells emerged from Dye-Sensitized Solar Cells (DSSCs) where the adsorbed dye has been replaced progressively by the perovskite<sup>[39]</sup> (Figure I-10).

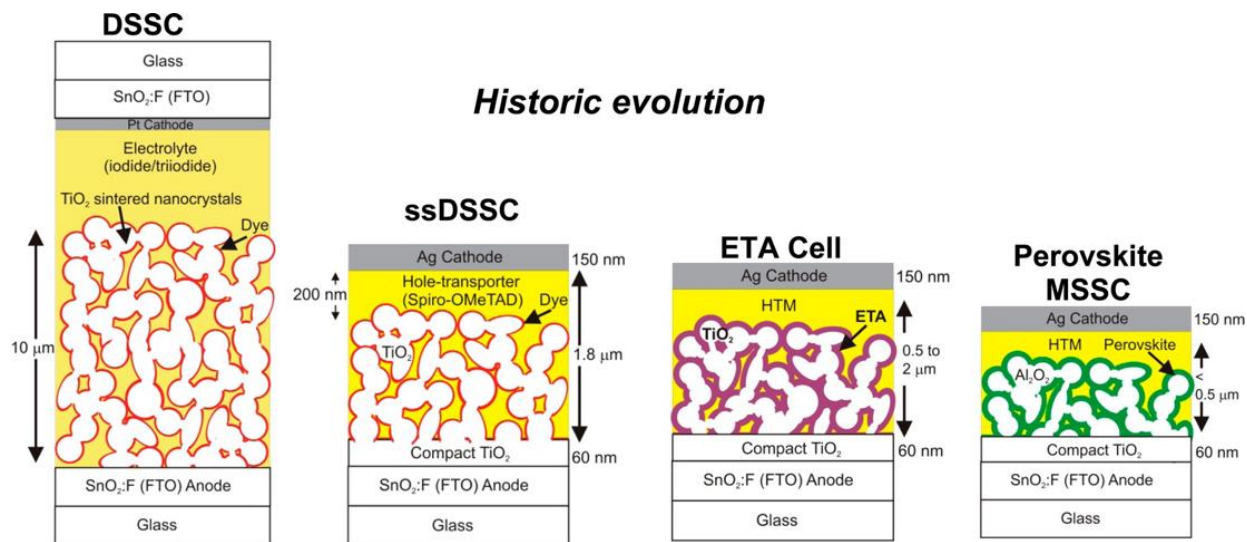


**Figure I-10:** Emergence of perovskite solar cells starting from liquid state DSSC, then the electrolyte was replaced by a hole transporting material (Spiro-OMeTAD) followed by the replacement of the dye by an extremely thin absorber (ETA). Finally ETA was replaced by perovskite absorber and  $TiO_2$  by  $Al_2O_3$ , figure taken from ref. [39].

DSSC is one of the most developed third generation solar cells since the first implementation, conducted by M. Grätzel and B. O'Regan in 1991<sup>[40]</sup>, has generated electricity from sunlight by means of photosensitizers. The chemical process in DSSCs partially follows the natural process of photosynthesis standing out by far from others photovoltaic cells. In addition, the materials used are inexpensive, lightweight, semi-flexible, semi-transparent, environmental friendly and colorful, essential criteria well suited for both indoor and outdoor applications. In terms of efficiency, DSSCs display currently 14.3 %<sup>[41]</sup> which is relatively high considering their short energy payback time and their ease of production. Moreover, they are also performant at lower insolation level and under diffuse light. Therefore, they are a promising alternative to the dominant technology of silicon solar panels.

## **I. 2.DSSC: Structure and components**

Conventionally, a DSSC is composed of four components: a photo-anode ①, a photoactive molecule ②, a hole conducting material ③ and a counter electrode ④ (Figure I-11). The photo-anode includes a metal semiconductor oxide layer deposited on a transparent conducting oxide (TCO) on a glass substrate or on plastic substrate. The photoactive molecule anchored to the mesoporous oxide semiconductor is a dye molecule which has the ability to harvest solar light. It is surrounded by a hole conducting material in the form of liquid electrolyte containing a redox shuttle or as a solid hole transporting material (HTM).

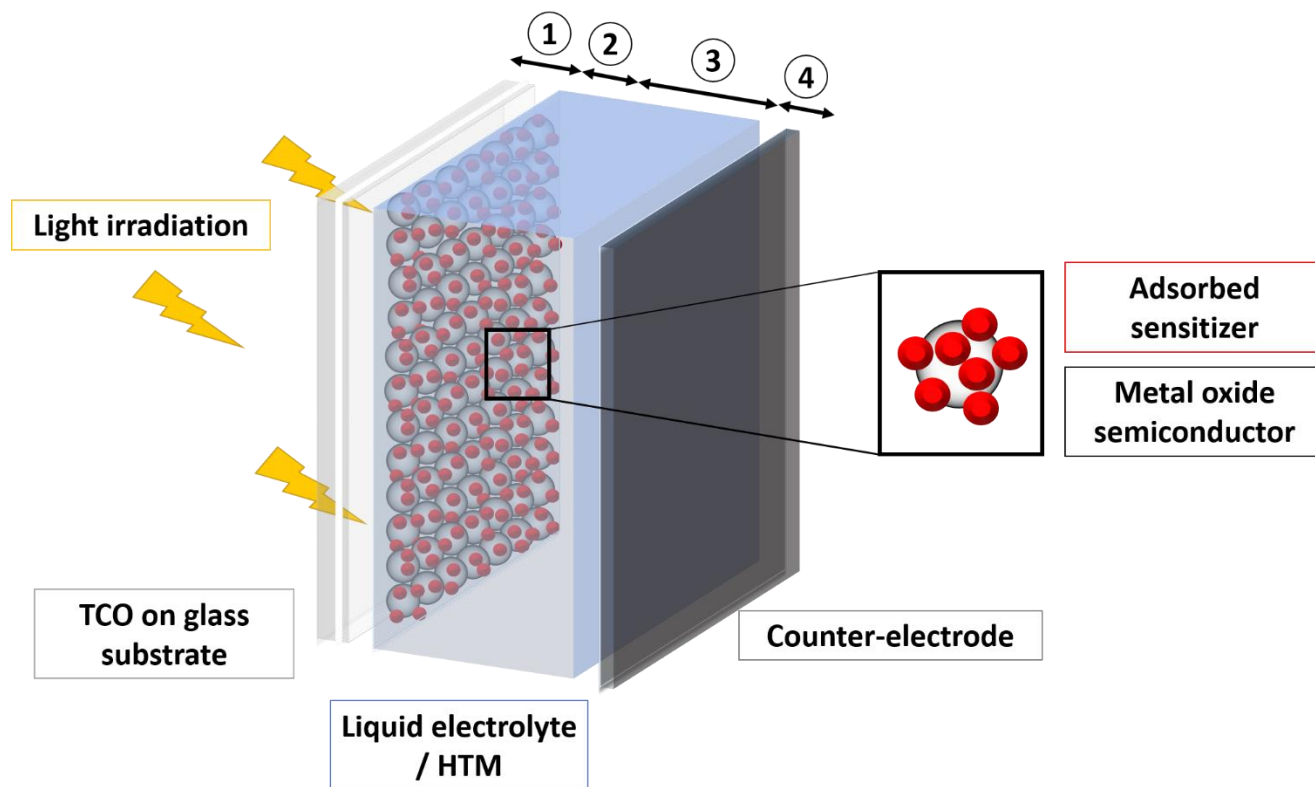


**Figure I-11:** Schematic representation of a dye-sensitized solar cell.

### I. 2. a. The photo-anode

The photo-anode is a fundamental starting material that impacts the DSSC overall performance. It must be highly transparent to allow the sunlight to reach the photoactive layer and must be highly conductive.

#### I.2.a.(i) Transparent Conducting Oxide

Among TCO supporting glass substrates in DSSC, fluorine doped tin oxide (FTO) is widely privileged compared to indium doped tin oxide (ITO), due to its electrical and optical properties, its stability at high temperature and its cost. This n-type semiconductor, characterized by a large direct bandgap of 4.1 eV, has a transmittance higher than 80 % in the visible range (Figure I-12b) with a low resistivity of approximately  $2 \times 10^{-4} \Omega \cdot \text{cm}$  and a carrier density of  $4 \times 10^{20} \text{ cm}^{-3}$ <sup>[42]</sup>. Thus, for a thickness of 200 nm the sheet resistance ( $R_s$ ) of FTO is around 12-15  $\Omega/\text{sq}$  and is independent of the temperature, in contrast to ITO in which the sheet resistance increases with the temperature as reported by F. Li *et al.*<sup>[43]</sup>. These two TCO were investigated on DSSCs by C. Sima *et al.* obtaining an efficiency of 2.24 % and 9.6 % for ITO and FTO respectively<sup>[44]</sup>.

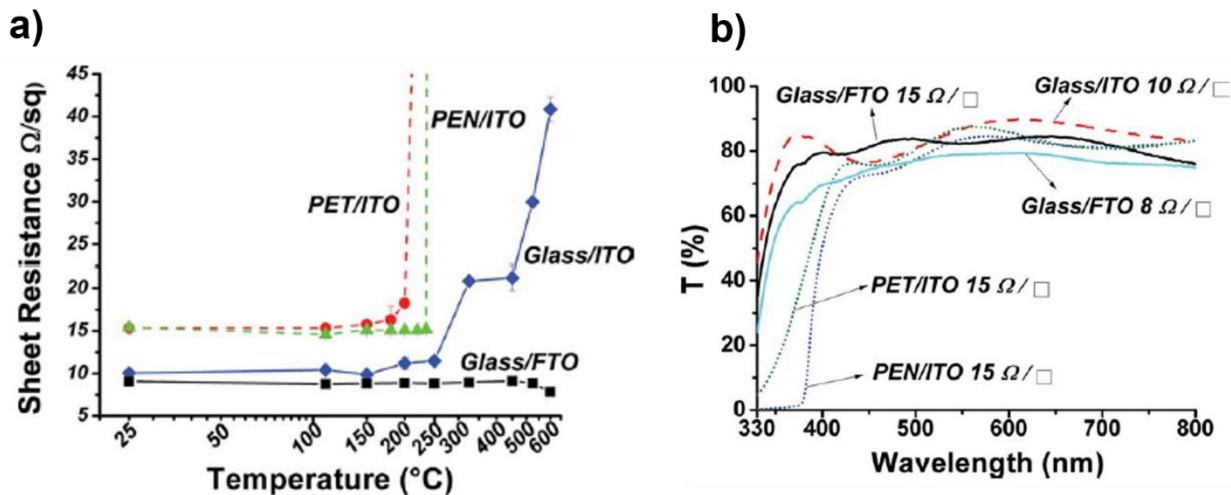


**Figure I-12:** (a) Sheet resistance at different temperature and (b) Transmittance as a function of wavelength of FTO, ITO, PEN/ITO and PET/ITO. Figures taken from ref. [45].

For more extensive DSSCs applications, flexible substrates such as plastic or metal have been developed. Usually for plastic substrate, polyethylene naphthalate (PEN) and polyethylene terephthalate (PET) coated on indium tin oxide (ITO) are used whereas titanium foils or stainless steel foils are applied for the preparation of metal substrate. Besides their flexibility, lightweight and production cost, plastic/ITO and metal substrates are not as conductive (Table I-2) and transparent as FTO and the sheet resistance decreases dramatically with the temperature<sup>[45]</sup> (see Figure I-12a).

Substrate	Work function (eV vs. vacuum)	Sheet resistance ( $\Omega/\text{sq}$ )	Highest efficiency (%)
FTO	- 4.7	8.5 to 15 <sup>[44,46]</sup>	14.3 % <sup>[41]</sup>
ITO	- 4.4 / - 4.5	8.5 (25°C) to 34.7 (450 °C) <sup>[47,48]</sup>	4.8 % <sup>[48]</sup>
ITO/PET		15 to 50 <sup>[45]</sup>	3.8 % <sup>[49]</sup>
ITO/PEN			8.1 % <sup>[50]</sup>
Ti		$10^{-3}$ <sup>[47]</sup>	9.2 % <sup>[51]</sup>

**Table I-2:** Electrical parameters of TCO and metal substrate and the highest efficiency obtained for DSSC using these materials as photo-anode substrate.

### I.2.a.(ii) Metal Oxide Semiconductor

For an effective photo-anode and hence a high charge collection efficiency ( $\eta_{\text{coll}}$ ), the metal oxide semiconductor that supports the photoactive molecules should fulfil the following criteria: it should be, at first, an n-type semiconductor to transport electrons toward the TCO with a wide bandgap ( $E_G > 3$  eV) and must be transparent to the major part of the solar spectrum and with a low light scattering effect. In order to act as an electron acceptor, the CB energy level of the semiconductor should match with respect to dyes excited state. The metal oxide semiconductor should have a large surface area for a maximum dye adsorption and should be highly porous and highly conductive<sup>[52]</sup>. Different metal oxide has been investigated such as  $\text{SnO}_2$ ,  $\text{Al}_2\text{O}_3$ ,  $\text{Nb}_2\text{O}_5$  and  $\text{SrTiO}_3$  which show a bandgap higher than 3 eV (Figure I-13). More details about semiconductor materials for DSSCs have been recently reviewed by Cavallo *et al.*<sup>[53]</sup>. Typically  $\text{TiO}_2$  and  $\text{ZnO}$  are the most investigated oxides owing to their attractive electronic properties depending on the morphology and the crystal structure.

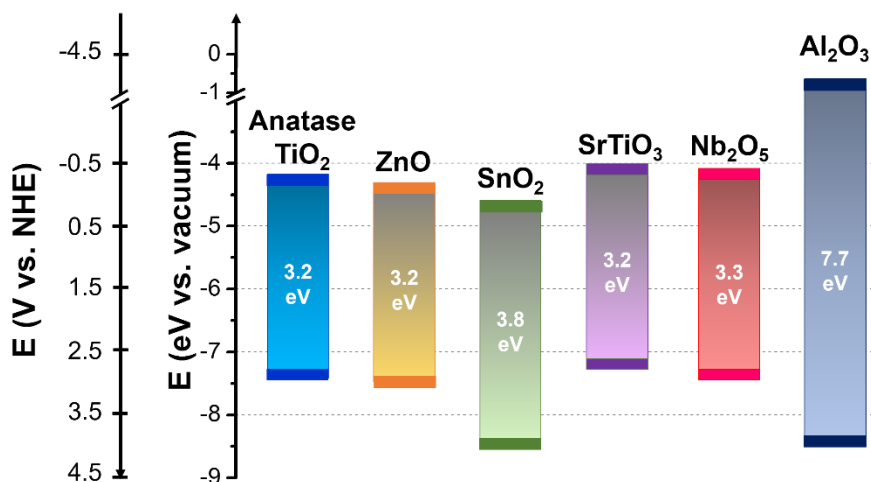


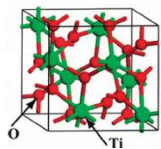
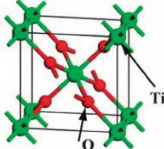
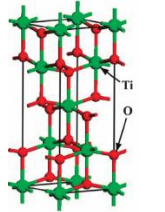
**Figure I-13:** Energy band diagram for various semiconductors used in DSSC.

#### ➤ $\text{TiO}_2$ :

Pure  $\text{TiO}_2$  is a colorless and a non-toxic oxide with a high refractive index and brightness. At nanoscale, it gives rise to a variety of applications such as white pigment in surface coating, toothpaste, food coloring and cosmetic or as self-cleaning function, as anti-fogging function and as photocatalyst<sup>[54]</sup>.  $\text{TiO}_2$  is found in nature essentially in three crystalline mineral forms: brookite, rutile and anatase. Brookite belongs to the orthorhombic crystal system built from  $\text{TiO}_6$  octahedra which share edges and corners with each other. Both rutile and anatase phases<sup>[55]</sup> adopt

a quadratic crystal system made from  $\text{TiO}_6$  octahedra which share two or four edges respectively. At high temperature ( $>550^\circ\text{C}$ ) anatase is transformed in rutile phase.  $\text{TiO}_2$  crystallographic characteristics and physical properties are given in Table I-3.

Among the three crystalline forms, rutile is the most thermodynamically stable form and the (100) plane is the most stable so the most exposed facet leading to a direct bandgap of 3.0 eV<sup>[56]</sup>. For anatase the (101) plane is the most stable leading to a higher indirect bandgap of 3.2 eV with a higher conduction band edge (-4.2 eV)<sup>[57]</sup>. Brookite  $\text{TiO}_2$  has the highest bandgap (3.4 eV) but even though its structure and its synthesis remain complex, few studies have been paid until now<sup>[58]</sup>. Therefore, for DSSCs applications anatase is the most favorable crystalline form.

<b>TiO<sub>2</sub> forms</b>	<b>Brookite</b>	<b>Rutile</b>	<b>Anatase</b>
<b>Crystalline structure</b>	Orthorhombic 	Tetragonal 	Tetragonal 
<b>Space group</b>	Pbca	$P4_2/mnm$	$I4_1/amd$
<b>Lattice parameters</b>	$a = 9.16 \text{ \AA}$ , $b = 5.43 \text{ \AA}$ $c = 5.13 \text{ \AA}$	$a = b = 4.58 \text{ \AA}$ $c = 2.96 \text{ \AA}$	$a = b = 3.78 \text{ \AA}$ $c = 9.51 \text{ \AA}$
<b>Bandgap</b> <sup>[56,59]</sup>	3.4 eV	3.0 eV	3.2 eV
<b>Refractive index</b> <sup>[60]</sup>	2.66	2.70	2.52
<b>Electrical Conductivity</b>			$10^5 \text{ S.m}^{-1}$ (at 300 K)
<b>Electron mobility</b> <sup>[61]</sup>		$0.1 \text{ cm}^2.\text{V}^{-1}.\text{s}^{-1}$	$4 \text{ cm}^2.\text{V}^{-1}.\text{s}^{-1}$

**Table I-3:**  $\text{TiO}_2$  crystallographic characteristics and physical properties

The transition from the  $\text{TiO}_2$  flat surface to mesoporous anatase has enhanced 1000 fold the internal surface area resulting in a high adsorption of the photo-sensitizer. It was initially introduced by Grätzel and O'Regan<sup>[40]</sup> who have employed  $\sim 10 \mu\text{m}$ -thick mesoporous layer of 20 nm  $\text{TiO}_2$  nanospheres for the first DSSC. Since then different morphologies of  $\text{TiO}_2$  nanomaterial have been developed to prepare the nanoporous layer such as nanorods<sup>[62]</sup>, nanowires<sup>[63]</sup>, tree-like nanostructure<sup>[64]</sup>, nanofibers<sup>[65]</sup>, nanosheet<sup>[66]</sup>, beads<sup>[67]</sup>, nanotubes<sup>[68]</sup> and nanoparticles (Figure I-14). The last three morphologies have the benefit to be prepared with (001) exposed facet, known to have a good potency for dye adsorption and charge transfer<sup>[66,69,70]</sup>. Different

mesoporous materials have also been developed including TiO<sub>2</sub> inverse opal structure<sup>[71]</sup> (Figure I-14). Jin *et al.* pointed out that the use of a mesoporous inverse photonic crystal TiO<sub>2</sub> film increases the amount of absorbed dye molecules and improves the overall photo-conversion efficiency<sup>[72]</sup>.

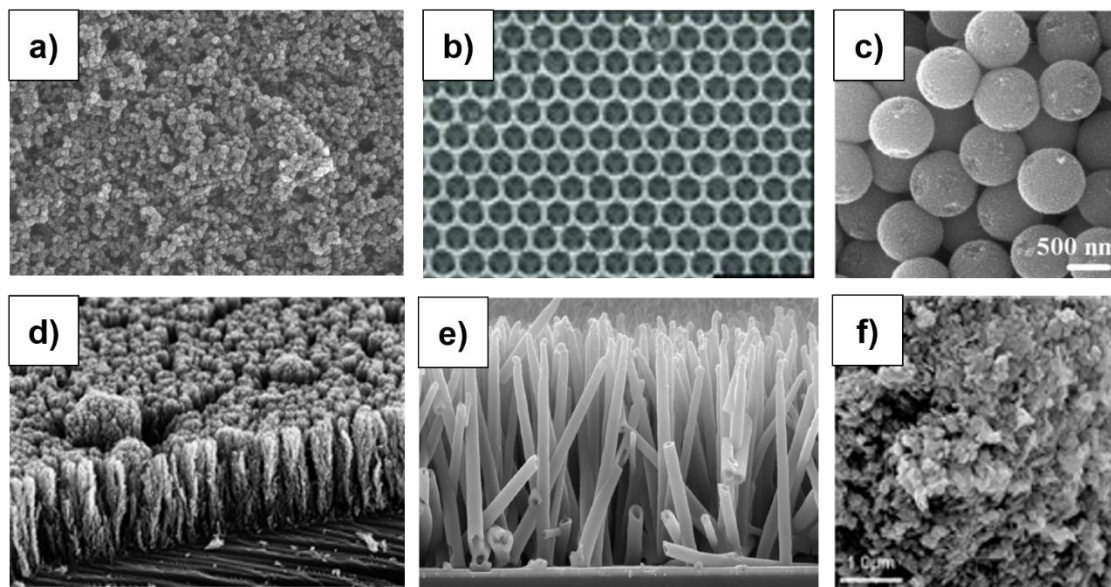


**Figure I-14:** Scanning electron microscopy images of TiO<sub>2</sub> (a) nanosphere<sup>[73]</sup>, (b) inverse opal<sup>[71]</sup>, (c) beads<sup>[67]</sup>, (d) tree-like nanostructure<sup>[64]</sup>, (e) nanotubes<sup>[68]</sup> and (f) nanosheet<sup>[66]</sup>

To date, films made of TiO<sub>2</sub> anatase nanoparticles with spherical shape are the most successful structure and morphology due to their porosity, dye absorption, charge transfer, and electron transport with a maximum efficiency of over 14%<sup>[41]</sup>. Therefore it will be used as semiconducting material in this project. However, ZnO appears to be a suitable alternative as photo-anode material.

#### ➤ ZnO :

As for TiO<sub>2</sub>, ZnO is a white pigment used in paint, food, ceramic, glass, cements ... It is also applied as n-type semiconductor (II-IV group) in DSSC as reported by Gerischer *et al.* in 1974 using a wurtzite-type crystalline structure, the most thermodynamically stable structure. Wurtzite belongs to a hexagonal crystal system where each Zn<sup>2+</sup> ion is surrounded by a tetrahedral of O<sup>2-</sup> ions<sup>[74]</sup>. ZnO can also be crystallized in face-centered cubic lattice as for rock-salt and zincblende structures (other main crystalline forms) but until now, they have not been synthesized except under very specific experimental conditions<sup>[75]</sup>. Wurtzite ZnO has a wide direct bandgap of 3.37 eV with a similar conduction band edge, work function (W) and refractive

index as compared to  $\text{TiO}_2$ , but with a higher carrier mobility allowing an efficient electron transport: key factor that impact the overall efficiency. For this reason research in ZnO semiconductor greatly intensified with the synthesis of 1D, 2D, and 3D anisotropic ZnO nanoparticles such as nanospheres, nanorods, nanotubes, nanosheet, nanoflowers, nanowires, nanobelts and tetrapods<sup>[76]</sup>. Furthermore, ZnO synthesis can be carried out under soft-chemistry conditions (low temperature). This opportunity offers promising prospects to flexible DSSC applications. Therefore ZnO will be also tested as semiconducting material in s-DSSCs.

➤ Blocking layer :

In both  $\text{TiO}_2$  and ZnO, a dense blocking layer or underlayer is required to prevent any contact between the TCO and the hole conducting material that diffuses through the semiconductor mesopores. The blocking layer is able (i) to reduce charge recombination<sup>[77]</sup> analyzed by Zhu *et al.* from intensity-modulated infrared transmittance, (ii) to enhance the suppression of leakage current<sup>[78]</sup> as reported by Cameron and Peter and (iii) to increase the open circuit potential ( $V_{oc}$ )<sup>[79]</sup> as underlined by Ito *et al.*<sup>[80]</sup> and Kavan and Grätzel<sup>[81]</sup> who first reported the use of nanocrystalline blocking layer. The thickness is well monitored to ensure the conductivity and not the resistivity. Usually the thickness is between 10-100 nm<sup>[82-84]</sup> which has demonstrated a significant improvement in device functional performances.

### **I. 2. b. The photo-sensitizer**

The photo-sensitizer or dye is a crucial component actively involved in light absorption, in light harvesting, in charge separation, and in the electron and hole injection into the oxide semiconductor and into the hole conducting material respectively. It should therefore (i) absorb all wavelengths extending from visible to NIR region *i.e.* panchromatic with a high molar extinction coefficient ( $\epsilon > 10^4 \text{ mol}^{-1} \cdot \text{L} \cdot \text{cm}^{-1}$ ). (ii) It should be stable under sunlight exposure. (iii) Its HOMO level, and more precisely its oxidized state energy level, must be at more positive potential with respect to the energy level of the hole conducting material for efficient dye regeneration, as explained in the next section. (iv) By contrast its LUMO level must be at more negative potential in comparison with the CB of the oxide semiconductor for an efficient electron injection. For this purpose, the photo-sensitizer is firmly grafted onto the mesoporous oxide semiconductor layer by means of anchoring group. There are two distinct photo-sensitizer categories: organometallic dyes and metal-free organic dyes.



I.2.b.(i) Organometallic dyes

Complex 1	N3	N719	N712
$E_{\text{HOMO}} = -4.98 \text{ eV}$ $E_{\text{LUMO}} = -2.88 \text{ eV}$ $\epsilon = 1.88 \cdot 10^4 \text{ M}^{-1} \cdot \text{cm}^{-1}$ (478 nm)	$E_{\text{HOMO}} = -4.98 \text{ eV}$ $E_{\text{LUMO}} = -2.88 \text{ eV}$ $\epsilon = 1.42 \cdot 10^4 \text{ M}^{-1} \cdot \text{cm}^{-1}$ (538 nm)	$E_{\text{HOMO}} = -5.34 \text{ eV}$ $E_{\text{LUMO}} = -3.43 \text{ eV}$ $\epsilon = 1.47 \cdot 10^4 \text{ M}^{-1} \cdot \text{cm}^{-1}$ (535 nm)	$\epsilon = 1.30 \cdot 10^4 \text{ M}^{-1} \cdot \text{cm}^{-1}$ (518 nm)
Z907	N749 (black dye)	C106	CYC-B11
$E_{\text{HOMO}} = -4.99 \text{ eV}$ $E_{\text{LUMO}} = -3.35 \text{ eV}$ $\epsilon = 1.20 \cdot 10^4 \text{ M}^{-1} \cdot \text{cm}^{-1}$ (526 nm)	$E_{\text{HOMO}} = -5.33 \text{ eV}$ $E_{\text{LUMO}} = -3.29 \text{ eV}$ $\epsilon = 0.75 \cdot 10^4 \text{ M}^{-1} \cdot \text{cm}^{-1}$ (605 nm)	$E_{\text{HOMO}} = -5.05 \text{ eV}$ $E_{\text{LUMO}} = -3.38 \text{ eV}$ $\epsilon = 1.87 \cdot 10^4 \text{ M}^{-1} \cdot \text{cm}^{-1}$ (550 nm)	$E_{\text{HOMO}} = -5.43 \text{ eV}$ $E_{\text{LUMO}} = -3.88 \text{ eV}$ $\epsilon = 2.42 \cdot 10^4 \text{ M}^{-1} \cdot \text{cm}^{-1}$ (554 nm)

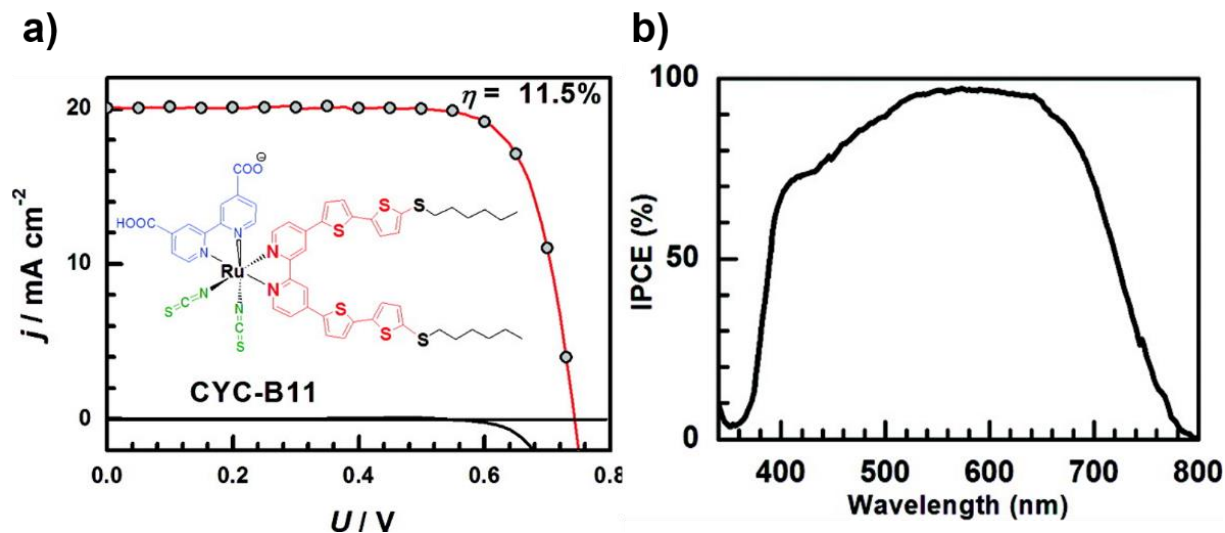
**Figure I-15:** Molecular structure of Ru-dyes with their related HOMO-LUMO levels and their extinction coefficient.

In their first DSSC<sup>[40]</sup>, Grätzel and O'Regan investigated Ruthenium (Ru) complex dye of the general structure  $[\text{RuL}_2(\mu\text{-(CN)Ru(CN)L}'_2)_2]$  where the L ligand is 2,2'-bipyridine-4,4'-dicarboxylic acid and the L' ligand is 2,2'-bipyridine known as "complex 1" previously synthesized by Nazeeruddin (pioneer of Ru complex dyes in DSSCs)<sup>[85]</sup>. This trinuclear Ru complex has the advantage of absorbing a very wide range in the visible with a molar extinction coefficient of  $1.88 \times 10^4 \text{ mol}^{-1} \cdot \text{L} \cdot \text{cm}^{-1}$  at 478 nm assigned to the electronic transition stemming from the metal to the L ligand, the well-known MLCT transition. The L ligand is structurally designed for grafting onto the oxide layer especially through the carboxylic functions. By cleaving the two cyano (CN) bridges in thiocyanato (SCN) derivatives, the trinuclear structure has been simplified by the design of novel mononuclear Ru complex dye,  $\text{cis-RuL}_2(\text{NCS})_2$ , coded as N3 dye<sup>[86]</sup>. The introduction of thiocyanate ligands extended the absorption to more than 800 nm with higher  $\epsilon$  (Figure I-15). However the open circuit potential ( $V_{\text{oc}}$ ) of the cell using this dye is similar to the complex 1 dye having the same anchoring group.

Indeed when, the carboxylic acid is substituted by the carboxylic salt tetra-*n*-butylammonium TBA<sup>+</sup>, the acidity is decreased affecting the energy level of the semiconductor conduction band to more positive potential so the V<sub>oc</sub> is increased. Such is the case with N719 and N712 dyes<sup>[87,88]</sup>.

Within this vision and in order to extent the spectral response into the NIR region, the switch from the two bipyridyl ligands to a fully deprotonated terpyridyl derivative and three thiocyanato ligands triggered the LUMO level of the “black dye” or N749 to more positive potential leading to the MLCT shift toward longer wavelengths and its absorption is extended to NIR region up to 920 nm<sup>[89]</sup>. For all these dyes the light harvesting capacity is large following the IPCE (the relation is given in the next section) of more than 80 % in particular for N3 and N749. However regarding their long-term stability, hydrophobic chains as electron donors are introduced in the molecular structure to prevent the dyes desorption of the anchoring group caused by water. The most familiar is Z907 dye<sup>[90-93]</sup> for its durability and thermal stability showing high photovoltaic performances. This 4,4'-Substituted 2,2'-Bipyridyl ancillary ligands based dye has led to a set of novel dyes containing either aliphatic groups such as K51<sup>[94]</sup>, K68<sup>[95]</sup>, A597<sup>[96]</sup> or aromatic groups such as K77-7<sup>[97]</sup>, IJ-1<sup>[98]</sup>, JJ-12<sup>[99]</sup> or both such as HRS-1<sup>[100]</sup>, TG6<sup>[101]</sup>, C106<sup>[102]</sup> (Annex I-1). Interestingly, using these dyes in DSSCs, the recombination has reduced considerably between the oxide semiconductor and the hole conducting material coming from the addition of hydrophobic side chains which minimize their contact. In the work conducted by Kroeze *et al.* the longest hydrocarbon chain length displays a fast charge separation and slow recombination in DSSCs<sup>[103]</sup>.

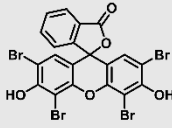
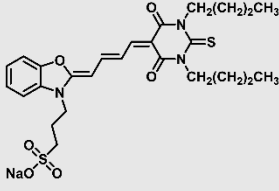
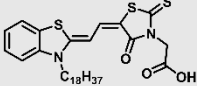
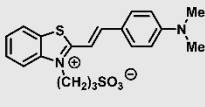
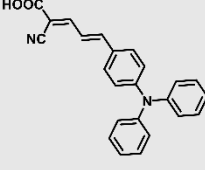
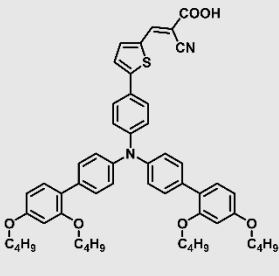
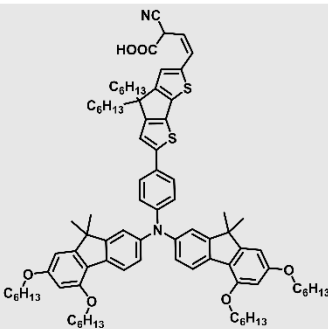
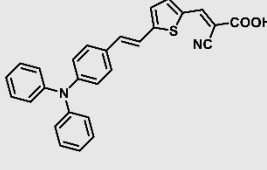
The last category of dyes combining aliphatic and aromatic groups has the best performances in DSSCs notably the CYC-B11 dye<sup>[104]</sup> (molecular structure quasi-similar to C106) reported by Chen *et al.* incorporating an electron-rich hexylthio-terminal chain showing the best  $\epsilon$  value ( $2.42 \times 10^4 \text{ mol}^{-1} \cdot \text{L} \cdot \text{cm}^{-1}$ ) when compared to all Ru based dyes with a top efficiency of 11.5 % (Figure I-16).



**Figure I-16:** (a) Photocurrent density–voltage characteristic curves of championship Ru-Dye, CYC-B11 and its molecular structure. (b) Incident photon-to-current conversion efficiency spectrum of CYC-B11.

All Ru based dyes have been well reviewed by Nazeeruddin<sup>[105]</sup>. Ru is actually targeted as  $d^6$  transition metal for photosensitizers due to its octahedral symmetry, and its interesting redox properties triggered by light inducing the MLCT. However, this noble Ru metal is expensive and is in limited supply and even toxic. Therefore other  $d^6$  metal photosensitizers have also been developed such as osmium (Os)<sup>[106]</sup>, rhenium (Re)<sup>[107]</sup> and iron (Fe)<sup>[108]</sup> resulting in a light absorption extension to higher wavelengths, in an interesting interfacial electron transfer behavior and in a high quantum yield respectively<sup>[109],[110]</sup>. Other organometallic complexes have been investigated based on  $d^8$  metal such as platinum (Pt)<sup>[111]</sup>, iridium (Ir)<sup>[112]</sup> and copper (Cu)<sup>[113]</sup>. Environmentally friendly photosensitizers extracted from flowers, vegetables, fruits and leaves have also been collected as alternative to Ru-complexes<sup>[114]</sup>. They are either in the form of metal-complex or metal-free dyes. Metal-complex chlorophyll based dyes are the most efficient natural pigments ( $\eta \sim 4.6\%$ )<sup>[115]</sup> followed by anthocyanin dyes ( $\eta \sim 2.9\%$ )<sup>[116]</sup>. Even though their preparation is easier and cost effective, they photodegraded because of the presence of free radical ions arising from excited electron from photocatalytic activity of  $\text{TiO}_2$  and moisture<sup>[117]</sup>. Therefore, DSSCs sensitized with organometallic dyes are unstable leading to low photovoltaic performances as compared to synthetic metal-free organic dyes.

I.2.b.(ii) Metal-free dyes

Eosin Y	Merocyanine 540	Mb(18)-N	BTS
$E_{\text{HOMO}} = -5.59 \text{ eV}$ $E_{\text{LUMO}} = -3.52 \text{ eV}$ $\epsilon = 1.12 \cdot 10^5 \text{ M}^{-1} \cdot \text{cm}^{-1}$ (538 nm)	$\epsilon = 9.86 \cdot 10^4 \text{ M}^{-1} \cdot \text{cm}^{-1}$ (558 nm)		$E_{\text{HOMO}} = -5.49 \text{ eV}$ $E_{\text{LUMO}} = -2.8 \text{ eV}$ $\lambda_{\text{max}} = 538 \text{ nm}$
			
Dye 2b	D35	JF419	D5 or L2
$\epsilon = 2.5 \cdot 10^5 \text{ M}^{-1} \cdot \text{cm}^{-1}$ (417 nm)	$E_{\text{HOMO}} = -5.53 \text{ eV}$ $E_{\text{LUMO}} = -3.09 \text{ eV}$ $\epsilon = 3.3 \cdot 10^5 \text{ M}^{-1} \cdot \text{cm}^{-1}$ (500 nm)	$E_{\text{HOMO}} = -4.92 \text{ eV}$ $E_{\text{LUMO}} = -2.82 \text{ eV}$ $\epsilon = 4.75 \cdot 10^5 \text{ M}^{-1} \cdot \text{cm}^{-1}$ (554 nm)	$E_{\text{HOMO}} = -5.57 \text{ eV}$ $E_{\text{LUMO}} = -3.09 \text{ eV}$ $\epsilon = 3.8 \cdot 10^4 \text{ M}^{-1} \cdot \text{cm}^{-1}$ (476 nm)
			

**Figure I-17:** Molecular structure of some organic dyes used in DSSCs.

Organic photosensitizers are the most attractive candidates as alternatives to Ru dyes owing to their high molecular extinction coefficient, their low production cost, their easy and versatile synthesis and their wide variety for the molecular structure design as well as their pleasing range of colors across the visible spectrum, from deep red to violet. In 1998, Arakawa and coworkers first reported DSSC based on organic dye, eosin Y (Figure I-17), leading to efficiency of up to 1.3 %<sup>[118]</sup>. Later and following the work done by Kamat using merocyanine dye for electrochemical cell<sup>[119]</sup>, the same group has studied a series of this dye, by modifying either the anchoring group, usually carboxyl group, or the alkyl chain type<sup>[120]</sup>. Obviously as mentioned earlier, the long hydrophobic chain based dye Mb(18)-N gave the highest efficiency (4.2 %). Since then they investigated different pure organic dyes such as mercurochrome<sup>[121]</sup>, and coumarin derivative<sup>[122]</sup>. Meanwhile, Wang *et al.* developed a DSSC based on hemicyanine dye with an overall yield of 2.1 % showing the highest short circuit photocurrent density ( $J_{\text{sc}} = 15 \text{ mA} \cdot \text{cm}^{-2}$ ) and the highest IPCE of nearly 100 %<sup>[123]</sup>. This hemicyanine photo-sensitizer

shows particularly a  $\pi$ -conjugated bridge between the methyl azolium propylsulfonate as electron acceptor (A) and the 4-[bis(methyl)-amino]benzyl as electron donor (BTS dye).

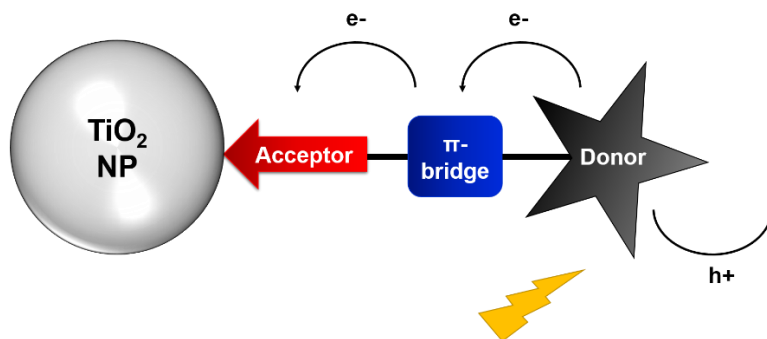


**Figure I-18:** Schematic representation of a donor- $\pi$ -conjugated bridge-acceptor dye

The introduction of the  $\pi$ -conjugated bridge into the D- $\pi$ -A framework (Figure I-18) enhances the intramolecular charge separation simultaneously toward the donor and the acceptor: this is called the “push-pull” effect<sup>[124]</sup>. Moreover it shifts the dye’s HOMO and LUMO frontiers energy levels affecting its intramolecular charge transfer (ICT) from the donor part to the electron acceptor part, and hence its absorption ability (in wavelength and/or in molecular extinction coefficient). For these reasons, the research work was directed toward the conception of novel fragments constituting the dye structure (donor,  $\pi$ -linker, and acceptor units) to optimize the overall yield<sup>[125]</sup>.

➤ Electron donor moiety (D) :

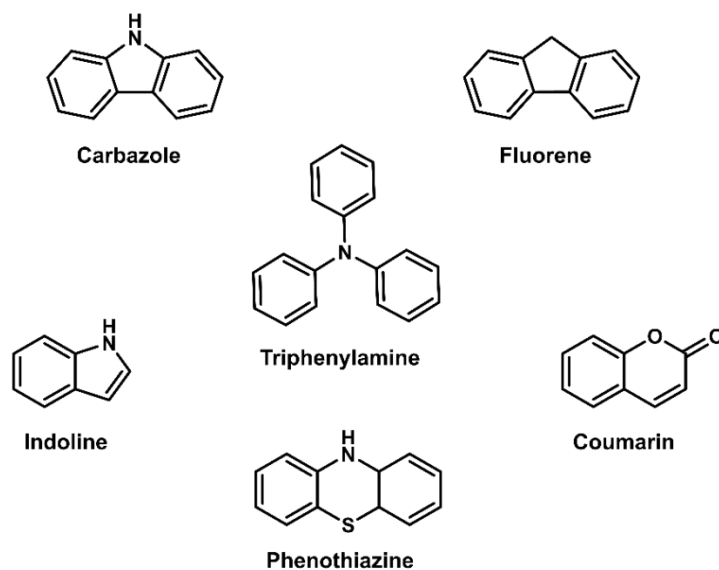


**Figure I-19:** Molecular structures of the different donor group

Typically the donor part of the dye is composed of an electron rich moiety where the HOMO energy level is lying on. Many efficient donor substituents were employed including indoline<sup>[126-128]</sup>, coumarin<sup>[129-131]</sup>, fluorene<sup>[132]</sup>, phenothiazine<sup>[133-135]</sup>, carbazole<sup>[41,136,137]</sup> and triphenylamine (TPA)<sup>[138,139]</sup>.

TPA, through its starburst-like structure containing a nitrogen atom center bonded by three neighboring aromatic rings (Figure I-19), is the most popularly used donor unit in view of its strong electron donor ability and hole mobility and its non-planar configuration preventing intermolecular aggregation<sup>[140]</sup>. TPA was first incorporated into organic light-emitting diodes (OLEDs) and into organic field-effect transistors (OFETs)<sup>[141]</sup> before Yanagida and coworkers initiated it as donor based dye ( $\epsilon = 2.5 \times 10^4 \text{ mol}^{-1} \cdot \text{L} \cdot \text{cm}^{-1}$ ) into DSSCs giving an efficiency of 5.3 %<sup>[142]</sup>. The reported IPCE is up to 80 % but is further improved for a novel type of TPA ( $\epsilon = 3.9 \times 10^4 \text{ mol}^{-1} \cdot \text{L} \cdot \text{cm}^{-1}$ ) in presence of fluorene (IPCE= 91 %) which gave an efficiency of nearly 8.1 %<sup>[143]</sup> with high  $J_{sc}$  and  $V_{oc}$ . Few years later, Feldt *et al.* highlighted the importance of alkyl bulky chain, here butoxy chain for D35 (Figure I-17), on TPA core used for reducing the charge recombination between the hole conducting material and the oxide semiconductor<sup>[144]</sup>. Considering this, Yella *et al.* combined both fluorene moiety and butoxyl chain to TPA core giving rise to an efficiency of 10.3 % under full sun<sup>[145]</sup>: the top efficiency for TPA based dyes (Figure I-20). In the following report, the study will be restricted to TPA donor based dyes.

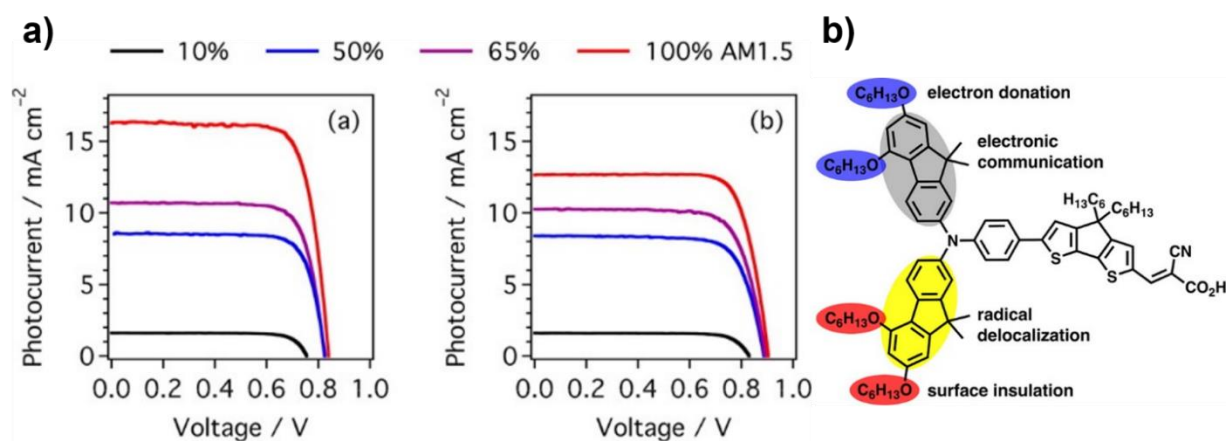


**Figure I-20:** (a) Photocurrent density–voltage characteristic curves of the TPA championship dye (JF419) in liquid DSSC device with 0.25 M (left) and 1 M (right) 4-tert-butylpyridine (TBP) at different light intensity (b) JF419 molecular structure.

➤ Electron acceptor as anchoring group (A):

The electron acceptor part is employed as electron withdrawing unit and as anchoring group to allow an optimal electron injection into the oxide semiconductor. Therefore the LUMO is spatially located in the anchoring group. A recent review, Zhang and Cole present anchoring groups in DSSCs<sup>[146]</sup> and they reported that cyanoacrylic group is more suitable for organic dyes than pyridine, perylene dicarboxylic acid anhydride, tetracyanate, 2-hydroxybenzotrile, etc. owing to its two strong negative mesomeric effects. However carboxylic group is exclusively bonded to the oxide semiconductor (TiO<sub>2</sub>) surface through mainly bidentate bridging<sup>[147]</sup> involving covalent bond (Figure I-21) between metal of the semiconductor and the dye in solution (chemisorption). So far, most of D- $\pi$ -A dyes hold the cyanoacrylic anchor<sup>[148–152]</sup>.

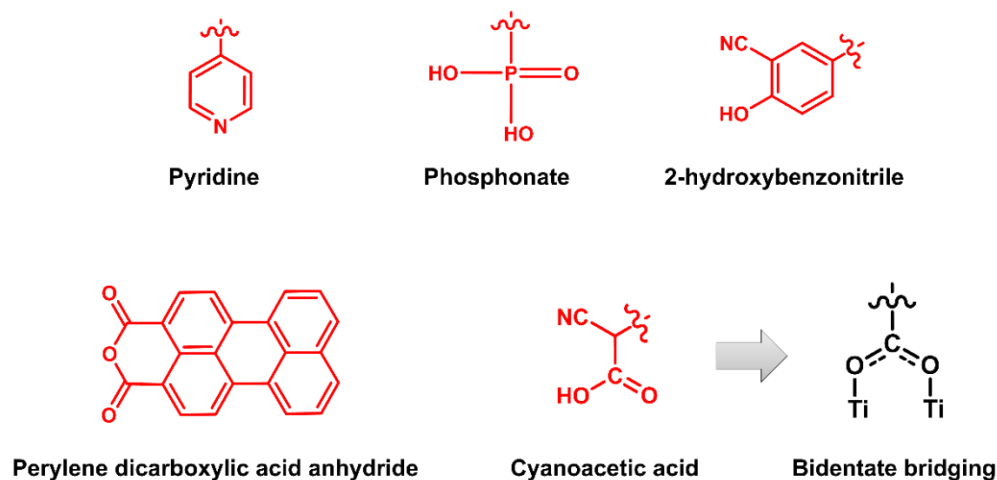


**Figure I-21:** Molecular structures of the different acceptor group.

➤ Conjugated bridge ( $\pi$ ):

Researchers attach great importance to the structural engineering of the  $\pi$ -conjugated bridge which considerably shifts the wavelength and the molecular extinction coefficient. Yanagida and coworkers were the first to promote the TPA and cyanoacrylic acid as electron donor and acceptor respectively<sup>[142]</sup>, using a conjugated oligoene spacer. They emphasize that extension of the conjugated chain impact the dyes spectral response due to the expansion of  $\pi$ -electron systems conjugated with a phenyl ring leading to higher efficiency.

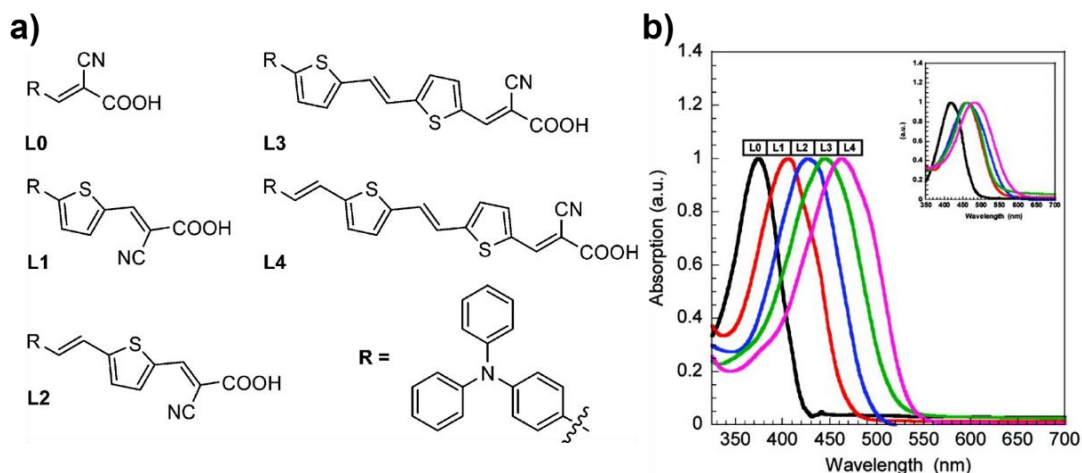


**Figure I-22:** (a) Molecular structure of series of dyes L0, L1, L2, L3, L4 and their (b) their normalized absorption spectra in ACN from ref. [124].

Hagberg *et al.* reported a D- $\pi$ -A dye with the thiophene as  $\pi$ -conjugated bridge, following the work conducted by Hara *et al.*<sup>[153]</sup>, yielding an efficiency of 5.1 %<sup>[154]</sup>. This dye coded as D5 and also as L2 (Figure I-22a) has been later compared to a series of chromophore by extending  $\pi$ -bridge with more than one thiophene unit<sup>[124]</sup>. As illustrated in Figure I-22b the absorption is coherently red-shifted with the conjugation increase, but the charge recombination is also increased due to the binding and orientation problems of the dye.

In addition to oligoene and thiophene or polythiophene<sup>[155]</sup>, other  $\pi$ -conjugated bridge have been developed such as benzothiadiazole<sup>[156,157]</sup>, benzotriazole<sup>[158,159]</sup>, and cyclopentadithiophene<sup>[145,160,161]</sup> (Figure I-23). The latter has the benefit to hold hydrophobic alkyl chains preventing the hole conducting material to reach the oxide semiconductor.

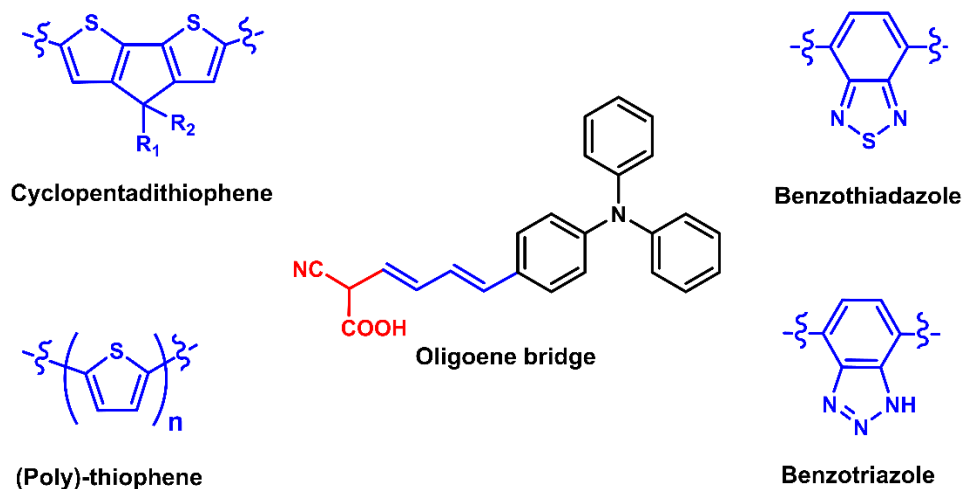


**Figure I-23:** Molecular structures of the first D- $\pi$ -A dye developed by Yanagida *et al.* and of the different  $\pi$ -conjugated bridge group.



### I. 2. c. The Hole Conducting Material

The photogenerated charge carriers, resulting from the dye absorption, are split away: the photo-excited electron is injected into the CB of the oxide semiconductor and the hole is transferred to the hole conducting material till it reaches the counter electrode. The hole conducting material can be considered as hole shuttle and as dye regenerator. Hence, the following criteria must be fulfilled: (i) the hole shuttle should not absorb the visible light, (ii) the energy level of the oxidized state of the hole conducting material must be higher than that of the HOMO of the dye, and (iii) the contact with the dye must be strong. Moreover the hole conducting material clearly determines the  $V_{oc}$  value (see the operating principle in the next section). To this day, three DSSCs types in different states can be distinguished: “liquid-state DSSCs” using a redox mediator as hole conducting material dissolved in a solution that constitute the liquid electrolyte, “solid-state DSSCs” (s-DSSCs) employing a hole transporting material (HTM) and “quasi-solid state DSSCs” for redox mediator as hole conducting material in ionic liquid and polymer gel. In the following, the two first will be detailed.

#### I.2.c.(i) The liquid electrolyte:

##### ➤ Redox mediator :

The standard redox mediator is the triiodide/iodide ( $I_3^-/I^-$ ) redox couple since it was used for the first time by Grätzel and O'Regan<sup>[40]</sup>. Its oxidation potential ( $E^{\circ}_{ox}=0.35V$  vs. NHE and  $E^{\circ}_{ox}=0.53V$  vs. NHE in ACN and in water respectively) is suitable as regard to the HOMO level of most dyes, it has a good solubility, the recombination kinetic is slow between this considered redox couple with  $TiO_2$ <sup>[162]</sup>, and it has been shown that the dye regeneration is faster indicating that the oxidized dye has been quickly reduced by  $I^-$  with high concentration of redox couple<sup>[163,164]</sup>. Most of liquid state DSSCs use the  $I_3^-/I^-$  redox shuttle yielding reasonable efficiencies 7.00 %<sup>[165]</sup>, 7.95 %<sup>[166]</sup>, 10.2 %<sup>[156]</sup> with the highest reported at  $\eta=10.3\%$ <sup>[167]</sup> from Wang *et al.*.

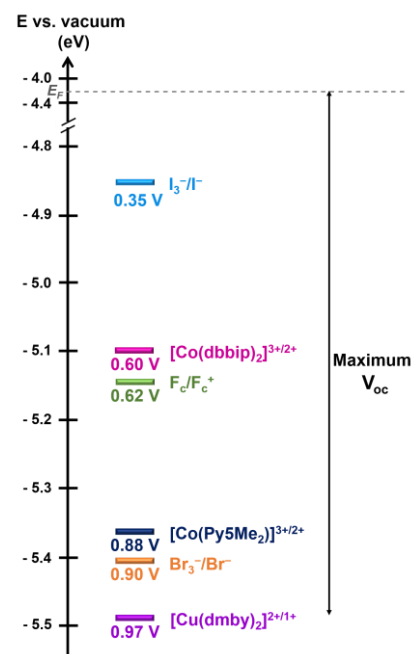


**Figure I-24:** Schematic energy diagram for redox shuttle used in DSSCs. The redox potentials are versus NHE.

However, despite the major advantages offered, it absorbs a portion of solar spectrum under 500 nm, the  $V_{oc}$  is low due to its low oxidation potential representing a large internal potential losses<sup>[168]</sup>. The generated  $I_3^-$ , as well as  $Br_3^-/Br^-$ <sup>[131]</sup>, needs two electrons to be reduced at the cathode that causes an overpotential, and easily corrodes metals.  $Fc/Fc^+$ <sup>[169]</sup>, quinone/hydroquinone,  $(SCN)_2/SCN^-$ , nickel Ni (III/IV), vanadium V (IV/V), copper Cu(I/II) and cobalt Co (II/III) coordination complexes<sup>[170]</sup>, and organic redox electrolytes<sup>[171]</sup> are often employed as alternative to  $I_3^-/I^-$  redox mediator, but Co (II/III) coordination complexes are considered as prospective candidates. Co(II) are mainly found in vitamin B12 as catalysts in photo redox reaction. They were then employed in DSSCs<sup>[172]</sup> and interestingly they exhibit many advantages: the visible absorption ability is weak, the reaction involves the transfer of one electron (no overpotential noticed), it has no corrosion effect and the photovoltage is improved due to its redox potential higher than that of  $I_3^-/I^-$ . The photovoltage increased from 0.67 V in 2001<sup>[172]</sup> to 1 V in 2012<sup>[173]</sup>. To date, the top efficiency for a DSSC is based on organic dye using Co (II/III) as redox shuttle with  $\eta = 14.3\%$ <sup>[41]</sup> and for a DSSC based on TPA organic dye (C257)  $\eta = 10\%$  is reached<sup>[174]</sup> using Co (II/III) as redox shuttle. For Cu(I/II) redox mediator, a yield of up to 10% has been successfully achieved because of its more positive redox potential (0.97V vs NHE)<sup>[175]</sup><sup>[176]</sup> (Figure I-24).

➤ Solvent :

Acetonitrile (ACN) is the most commonly used rather than valeronitrile, ethylene carbonate, N-methylpyrrolidone regarding organic solvent for redox mediator. However when the device is not carefully sealed, these solvents, classified as toxic or as volatile organic solvents, leak out and tend to corrode metals. Moreover they are temperature dependent: at low temperature, the solvent can freeze and as consequence the salts become insoluble, and at high temperature, the solvent quickly evaporates. As DSSCs based on these solvents cannot be exploited for long-term applications, the addition of ionic liquid or polymer gel which is more viscous have been proposed to prevent any solvent leakage<sup>[156,177]</sup> or to replace organic electrolyte to 100% aqueous electrolyte<sup>[178,179]</sup>. Another alternative is directed toward 100% solid materials such as HTM.

**I.2.c.(ii) The solid hole transporting material (HTM):**

Bach *et al.* elaborated a solid-state DSSC (s-DSSC) in 1998 by incorporating as solid organic HTM 2,2',7,7'-tetrakis(N,N-di-p-methoxyphenyl-amine)9,9'-spirobifluorene (spiro-

OMeTAD)<sup>[180]</sup>. Spiro-OMeTAD is a small single molecule (2 nm) containing four p-methoxyphenyl amine grafted on both sides of two fluorene rings linked via a tetrahedral carbon center (see Figure I-24). This most widely used HTM was first tested with Ru-complex dye yielding to 0.74 % and later with a metal-free organic dye (indoline) leading to a higher overall efficiency  $\eta = 4.1\%$ <sup>[181]</sup>. The photovoltage is up to 0.85 V due to the more positive redox potential with respect to  $I_3^-/I^-$ . But two physical parameters limit spiro-OMeTAD's application: the hole mobility ( $\mu$ ) and the conductivity ( $\sigma$ ). Indeed, the conductivity has been found to be relatively low, approximately  $2.10^{-5} \text{ S.cm}^{-1}$  reported by Snaith *et al.*<sup>[182]</sup> but has been optimized through the introduction of an oxidized form of spiro-OMeTAD. The different cationic salts used are spiro-OMeTAD<sup>2+</sup>(PF<sub>6</sub>)<sup>2-</sup>, spiro-OMeTAD<sup>+</sup>(CF<sub>3</sub>SO<sub>3</sub>)<sup>-</sup> and spiro-OMeTAD<sup>2+</sup>(TFSI)<sup>2-</sup>, and the latter gave the highest conductivity up to  $10^{-3} \text{ S cm}^{-1}$  with an efficiency of 3.09 %<sup>[183]</sup>. The conductivity has also been increased by doping spiro-OMeTAD in conjunction with cobalt complexes leading to an impressive s-DSSC efficiency of 7.2 %. At present the record efficiency reaches 7.8 % using an organic TPA blue dye denoted S5<sup>[184]</sup> (Figure I-25).

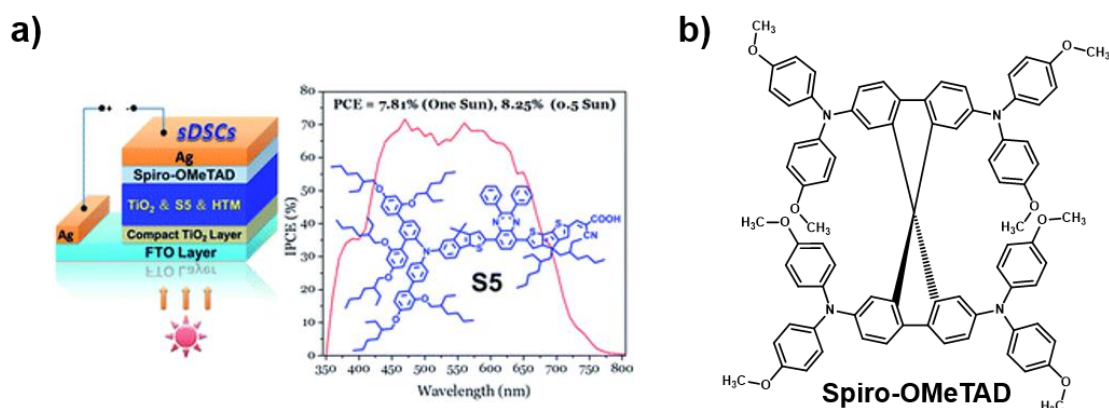


**Figure I-25:** Record efficiency obtained by Tian *et al.*<sup>[184]</sup> in (a) s-DSSC using S5 as dye and (b) Spiro-OMeTAD as HTM.

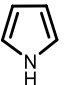
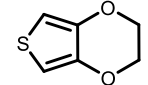
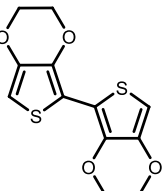
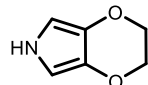
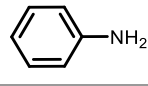
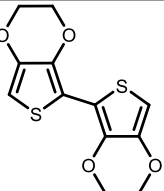
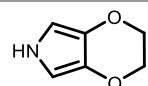
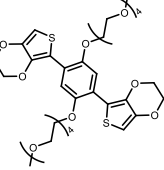
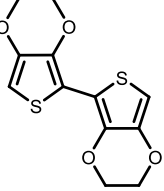
Regarding the charge carrier mobility, which is related to the conductivity, it has been reported to be low  $\mu = 10^{-4} \text{ cm}^2.\text{V}^{-1}.\text{s}^{-1}$ <sup>[182,185]</sup> which affects the photocurrent density and the charge recombination rate in solar cell<sup>[186]</sup>.

$$\mu = \frac{\sigma}{n e} \quad (\text{I-5})$$

In this respect, a major effort has been made to optimize the charge mobility preferably by varying the thickness of the oxide semiconductor (1.5  $\mu\text{m}$  - 3  $\mu\text{m}$ ) to reduce the charge recombination<sup>[181,185]</sup>, by the development of other small molecules such as AS44<sup>[187]</sup> or MeO-TPD<sup>[188]</sup> or even by the development of novel classes of HTM such as inorganic materials

(CuSCN<sup>[189]</sup>, CuI<sup>[190]</sup>) or conducting polymers (Poly(3-hexylthiophene-2,5-diyl) (P3HT)<sup>[191]</sup>, Poly(3-octylthiophene-2,5-diyl) (P3OT)<sup>[192]</sup>, Poly[2,6-(4,4-bis-(2-ethylhexyl)-4H-cyclopenta [2,1-b;3,4-b']dithiophene)-alt-4,7(2,1,3-benzothiadiazole)] (PCPDTBT)<sup>[193]</sup>). A number of methods have been investigated to prepare and to deposit the conducting polymer (CP) used as HTM (further details will be provided in the following Chapter). However, the poor pore filling *i.e.* the HTM penetration within the mesoporous oxide semiconductor still remains problematic. In fact, when the HTM is not in close contact to the dye infiltrated into the pores, it restrains the dye to be regenerated or the dye cannot transfer the photogenerated holes to the HTM.

In order to overcome the difficulty of filling the pores while maintaining the strong contact between the dye and the CP, the direct production of CP inside the mesoporous oxide semiconductor layer by *in-situ* photo-electrochemical polymerization (PEP) of the organic monomer has been implemented. Yanagida *et al.* achieved the first s-DSSCs in 1997 incorporating an *in-situ* produced conducting polymers, polypyrrole (PPy), as HTM<sup>[194]</sup>. But the absorption of this CP in the visible range compete with the Ru-dye absorption which mainly decreased the light harvesting efficiency of the cell leading to a low efficiency of  $\eta = 0.10\%$  (Table I-4). Similarly, polyaniline (PANI) absorbs in the visible part as well as polythiophene<sup>[195]</sup>. So Yanagida and coworkers investigated Poly(3,4-ethylenedioxythiophene) (PEDOT) as HTM. They used, at first, 3,4 ethylenedioxythiophene (EDOT) as PEP precursor in Ru-dye based s-DSSC<sup>[196]</sup> but shortly after they used Bis-EDOT as *in-situ* PEP precursor to generate the same conducting polymer. As result, they obtained a notable improvement of the efficiency from  $\eta < 0.01\%$  to  $\eta = 0.53\%$ <sup>[197]</sup>. This increase is due to the lower oxidation potential of the Bis-EDOT monomer with respect to that of the dye. This important factor has been taken into consideration for the subsequent research works in s-DSSCs using *in-situ* generated PEDOT such as Mozer *et al.* who found the optimal mesoporous TiO<sub>2</sub> layer of 5-6  $\mu\text{m}$  ( $\eta = 2.6\%$ )<sup>[198]</sup>. Moreover Xia *et al.* investigated the effect of the different doped anions on PEDOT among ClO<sub>4</sub><sup>-</sup>, CF<sub>3</sub>SO<sub>3</sub><sup>-</sup>, BF<sub>4</sub><sup>-</sup>, and (CF<sub>3</sub>SO<sub>2</sub>)<sub>2</sub>N<sup>-</sup> (abbreviated TFSI<sup>-</sup>) and the latter gave the highest efficiency  $\eta = 2.85\%$ <sup>[199]</sup>. The performance was further improved by the dye substitution from organometallic ( $\eta = 2.85\%$  for Z907) to organic ( $\eta = 6.1\%$  for D149) as reported firstly by Liu *et al.*<sup>[200]</sup>. Later Yang and coworkers were the first to apply D- $\pi$ -A configuration TPA dye for s-DSSC based on PEDOT generated by *in-situ* PEP both in organic medium and aqueous micellar medium.

Year	<i>In-situ</i> produced conducting polymer	Precursor	Sensitizer	Efficiency	Ref.
1997	Polypyrrole		N3	0.10 %	[194]
2002	Poly(3,4-ethylenedioxythiophene)		N719	0.01 %	[196]
2004	Poly(3,4-ethylenedioxythiophene)		N719	0.53 %	[197]
2006	Poly(3,4-ethylenedioxythiophene)		HRS-1	2.6 %	[198]
2008	Poly(3,4-ethylenedioxythiophene)		Z907	2.85 %	[199]
2008	Poly(3,4-ethylenedioxythiophene)		$[\text{Ru}(\text{H}_2\text{DCB})_2(\text{dnbpy})]^{2+}$	0.1 %	[201]
2009	Polyaniline			0.36 %	[202]
2010	Poly(3,4-ethylenedioxythiophene)		D149	6.1 %	[200]
2014	Poly(3,4-ethylenedioxythiophene)		Z907 D35	1.5 % 4.6 %	[203]
2014	Poly(3,4-ethylenedioxythiophene)		D21L6 D35	3.05 % 4.34 %	[204]
2015	Poly(3,4-ethylenedioxythiophene) derivative		D205	5.2 %	[205]
2016	Poly(3,4-ethylenedioxythiophene)		LEG4	7.11 %	[206]
2016	Poly(3,4-ethylenedioxythiophene)		DPP07	5.54 %	[207]

**Table I-4:** Reported efficiencies of s-DSSC based on conducting polymer produced by *in-situ* PEP using Ru-dyes (blue) and organic dyes (red)

For **LEG4** in aqueous medium the reported efficiency is 4.8 %<sup>[208]</sup> and later optimized to 5.2 %<sup>[203]</sup>. The implementation of the *in-situ* PEP in aqueous medium has shown faster dye regeneration due to the shorter polymer chains length. Regarding PEDOT generated in organic medium using **LEG4**, the s-DSSC displays remarkably 7.11 % reported by Zhang *et al.*<sup>[206]</sup>. To date, this is the top efficiency obtained for s-DSSCs based on conducting polymer produced by *in-situ* PEP. Other CPs have been developed such as PEDOT derivatives<sup>[205]</sup> or PEDOP<sup>[204]</sup>.

PEDOT differs from other conducting polymers and even from other HTM, owing of its advantages: (i) it is highly transparent in the visible range, (ii) the mobility is up to  $0.1 \text{ cm}^2 \cdot \text{s}^{-1}$ , (iii) the conductivity arising from the doped form is also high  $\sigma = 550 \text{ S} \cdot \text{cm}^{-1}$  (iv) the low solubility of the monomer in water ( $2.1 \text{ g} \cdot \text{L}^{-1}$  at  $20^\circ\text{C}$ ) is problematic for the polymerization reaction except in presence of surfactants<sup>[209–211]</sup> (v) can be generated easily by *in-situ* PEP in both media (organic/aqueous) which is a successful way to overcome the pore filling limit (vi) it is stable and (vii) its oxidation potential is lower than the HOMO level of almost all dyes. PEDOT is thus the most promising HTM for s-DSSCs.

#### **I. 2. d. The Counter Electrode**

The counter electrode (CE), adjacent to the redox mediator or to the HTM, is the last element that completes the internal electrical circuit of a DSSC or a s-DSSC. It must (i) inject electrons either into the electrolyte to reduce the redox mediator or into the HTM to regenerate the sensitizer. Dye regeneration is a fast process so (ii) a catalyst material is required to sufficiently generate reducing species. Moreover (iii) to ensure electronic conduction, the charge transfer resistance ( $R_{CT}$ ), which has an impact on the fill factor, must be low, with a maximum value of  $1 \text{ } \Omega \cdot \text{cm}^2$ <sup>[138]</sup>. Platinum (Pt) which was the first CE employed in the conventional DSSC, is one of the most favorite in view of its low  $R_{CT}$  reported to vary under  $1 \text{ } \Omega \cdot \text{cm}^2$  depending on the thickness, the deposition method<sup>[212]</sup> and the electrolyte used. However Pt is not an abundant element and hence it is expensive. In addition, for DSSC, the liquid electrolyte dissolves Pt CE limiting its large scale application. Therefore, different kind of materials have been investigated such as conducting polymers<sup>[213,214]</sup>, carbon<sup>[215]</sup>, metal sulfide<sup>[216]</sup>, metal oxide<sup>[217]</sup>, and natural material<sup>[218]</sup>.

For s-DSSC, the most suitable CE is noble metal including gold (Au) and silver (Ag). They are thermally evaporated in a vacuum chamber on the electrode surface and the resulting layers have

the benefit to reflect back the transmitted light. Snaith *et al.* studied the reflectivity of both metals and showed that the reflectivity from Au is 56 % whereas from Ag, it is 96 %<sup>[219]</sup>. Au is thus more dissipative than Ag. But interestingly Au is the most prominent for solid state DSSC using *in-situ* produced PEDOT since the work function (Wf) of Au, Wf= 4.9 eV<sup>[220]</sup>, closely matches with the HOMO level of PEDOT reported to be roughly around 4.9-5.1 eV<sup>[197]</sup> whereas for silver Wf is 4.3 eV. Moreover silver is not long term stable than gold and it quickly oxidizes.

We reviewed the four components that composed a DSSC or a s-DSSC, using either a liquid electrolyte containing the redox mediator or a solid HTM. For this research thesis, exclusively s-DSSC employing a conducting polymer will be considered. The operating principle and device characterization of these s-DSSCs will be detailed in the next section and as for the preparation method of s-DSSC materials will be found in the Chapter 2.

### **I. 3. Solid State-DSSC: operating principle and photovoltaic performances**

The operating principle of s-DSSC is quasi similar to that of the DSSC which was inspired from photosynthesis. It involves photo-electrochemical processes between the different components of this “sandwich” configuration device. And according to the kinetic of each reaction, the photovoltaic performances of the s-DSSC can be determined before rising to the power conversion efficiency.

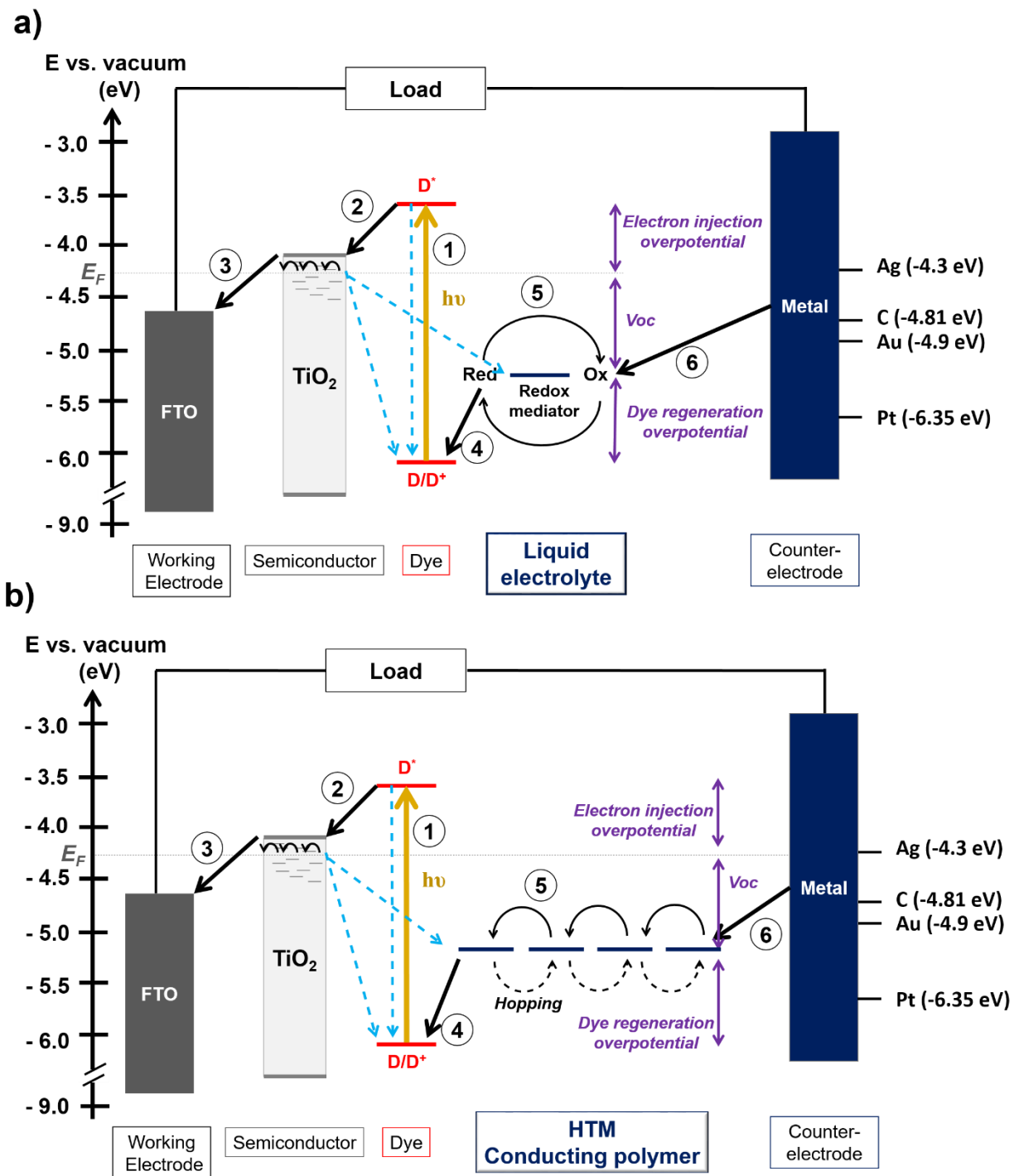


**Figure I-26:** Scheme of the operating principle of a liquid electrolyte DSSC and a solid-state DSSC based on *in-situ* conducting polymer.



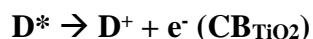
### I. 3. a. The Operating Principle

Typically in a photo-electrochemical solar cell, the working principle can be described through the energy level diagram including the energy levels of the different components as shown in the Figure I-26. The mechanism mainly occurs in 6 steps as the following:

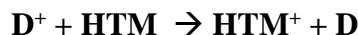
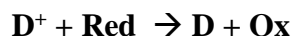
- (1) Light harvesting of dyes for charges carrier generation: from sunlight, the incident photon is absorbed by the photosensitizer and thus promotes an electron from the HOMO to the LUMO level: the dye which was initially in the ground state **D** is now in an excited state **D\***.



- (2) Electron transfer toward the oxide semiconductor: the photo-excited sensitizer **D\*** injects the electron into the conduction band of the semiconductor leaving behind a hole: the sensitizer is in oxidized state **D<sup>+</sup>**.

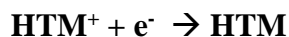


- (3) Electron transport across the photo-anode: the electron in the conduction band flows through the oxide semiconductor toward the TCO of the photo-anode and then conveyed to the external circuit until the cathode.
- (4) Regeneration of the oxidized dye by electron transfer: the oxidized dye **D<sup>+</sup>** returns back to its ground state **D** through the electron injection from the electron donor or reduced species of the redox mediator for liquid electrolyte DSSC, or from the HTM for s-DSSC. The reduced species are thus oxidized.



- (5) Hole transport across the hole transporting layer: in the case of liquid electrolyte DSSC, the oxidized species diffuse progressively toward the counter electrode whereas for HTM, the received hole from oxidized dye roams along the HOMO level as “hopping” process until the counter electrode.

- (6) Hole transfer or reduction at the cathode: the oxidized species are reduced back thanks to the counter electrode.



The cycle is therefore completed. However the device will operate only if the reaction kinetics takes place for the different interfacial electron transfers<sup>[138]</sup>.

### **I. 3. b. Excitation, Electron Injection, Electron Transport and Charge Recombination**

In the photo-electrochemical cell, the working principle relies predominantly on the energy level matching of each component and the reaction kinetics of electron injection and that of electron transport which occasionally led to charge recombination.

#### **I.3.b.(i) Excitation**

Upon illumination of the DSSC, the sensitizer is photo-excited and an electron is pulled from a lower to a higher energy level. The latter must be slightly higher than the CB of the oxide semiconductor *i.e.* higher than  $-4.0$  eV for  $\text{TiO}_2$  and  $-3.9$  eV for  $\text{ZnO}$ . Moreover the excited state lifetime ( $\tau_{\text{dye}}$ ) must be sufficiently long to inject an electron into the oxide semiconductor before dye relaxation. Typically, the electron lifetime of the photo-excited dye is about  $10^{-9}$ - $10^{-8}$  s for metal complex dyes and shorter for organic dyes  $\tau_{\text{dye}} < 10^{-9}$  s <sup>[221,222]</sup>.

#### **I.3.b.(ii) Electron injection**

##### ➤ Electron injection from dye to the semiconductor :

The interfacial charge transfer takes place at dye/oxide semiconductor and at dye/hole transporting layer interfaces. The electron injection from dye into the semiconductor CB takes place in an ultrafast timescale ranging from femtosecond to picosecond<sup>[223]</sup> depending on the experimental conditions but when it is close to the photo-excited dye lifetime, in that case, these two processes are in competition. The electron injection is faster for organic dyes than that for metal complex dye<sup>[222]</sup>.

➤ Electron injection from hole transporting layer to the dye :

For the dye regeneration process, electron injection from the redox mediator or from the HTM, is reported to be in the microsecond scale<sup>[224]</sup> and hence the lifetime of the oxidized dye should be higher than 100s<sup>[138]</sup>. In the case of liquid electrolyte, the redox potential  $E_{redox}$  is considered and the driving force should be at more negative potential than the dye's HOMO level for the electron injection. The electrochemical potential of the redox mediator is given by the Nernst expression:

$$E_{redox} = E^0 - \frac{RT}{nF} \times \ln\left(\frac{[Red]}{[Ox]}\right) \quad (I-6)$$

With  $E^0$  the standard potential, R the universal gas constant, T the temperature, F the Faraday constant,  $[Red]$  is the concentration of the reduced species and  $[Ox]$  is the concentration of the oxidized species.

For HTM in s-DSSC, the HOMO level is exclusively considered, and similarly its oxidation potential  $E_{(HTM^+/HTM)}$  must be at more negative potential than the potential of oxidized dye  $E_{(D^+/D)}$ . Indeed, Haque *et al.* found that this potential difference,  $\Delta G_{(Dye-HTM)}$ , must be at least of 0.2 eV to drive the photo-generated holes toward the HOMO of the HTM<sup>[225]</sup>. However, when the HOMO of the HTM is too high, the  $V_{oc}$  will decrease. So an effective balance must be struck.

$$\Delta G_{(Dye-HTM)} = E_{(HTM^+/HTM)} - E_{(D^+/D)} \quad (I-7)$$

Regarding the electron injection timescale, Mozer *et al.* observed that the dye regeneration occurs at 1 to 100  $\mu$ s for PEDOT produced by *in-situ* PEP<sup>[226]</sup> whereas for Spiro-OMeTAD it is estimated to nanosecond.

**I.3.b.(iii) Electron transport**

➤ Electron transport in the semiconductor :

Injected electrons are transported across the semiconductor toward the TCO back electrode by diffusion. The electrons are diffused by a multiple trapping/detrapping processes<sup>[227]</sup> onto the mesoporous semiconductor network. However when the porosity of the semiconductor increases, the electron pathway will be tricky and hence the electron transport will be slow<sup>[228]</sup>. It has been reported that the porosity should not be below 76 % for  $TiO_2$  with an average thickness of 10  $\mu$ m<sup>[229]</sup>. Light intensity and nanostructures are also parameters that influence the electron transport in the semiconductor. Therefore, for an efficient electron transport, the timescale must be short to

avoid the trapping process, and also other recombination processes. Generally, the timescale is about  $10^{-3}$  s.

Regarding the CB energy level, its potential energy ( $E_{CB}$ ) is similar to the quasi-Fermi level ( $E_{Q-F}$ ) under illumination caused by the injection of photo-excited electrons that shifts upwards the Fermi level ( $E_F$ ) with respect to the thermodynamic equilibrium in dark.

At equilibrium:

$$E_{CB} = E_F - \frac{RT}{nF} \times \ln\left(\frac{n_{CB}}{N_{CB}}\right) \quad (I-8)$$

Where  $n_{CB}$  and  $N_{CB}$  are the density of electrons in conduction band and the effective density of states in conduction band.

Outside the thermodynamic equilibrium, the quasi Fermi level potential is given by the equation I-9.

$$E_{CB} = E_{Q-F} - \frac{RT}{nF} \times \ln\left(\frac{n_{CB}}{N_{CB}}\right) \quad (I-9)$$

➤ Electron transport in the hole transporting layer :

In liquid electrolyte, the transport mechanism of oxidized species toward the CE is diffusion. The diffusion constant for  $I_3^-$  has been determined to be  $10^{-5}$   $\text{cm}^2.\text{s}^{-1}$ . In solid HTM, the charge transport is faster than redox mediator due to their high charge mobility. The holes are transported toward the counter electrode by hopping process or inversely the electrons are transported toward the oxidized dye to regenerate it. Conducting polymers display the best mobility ( $> 0.1 \text{ cm}^2.\text{s}^{-1}$ ) [186].

**I.3.b.(iv) Charge recombination**

The charge recombination processes, occurring mainly from the oxide semiconductor in two directions (blue dash lines in Figure I-26), induces a reduction in the photocurrent density. Indeed, the first corresponds to the injected electron that stands in the semiconductor CB which can recombine with a hole in the oxidized dye state resulting in the dye regeneration. This back electron transfer reaction occurs on microsecond to millisecond time scale. The second corresponds to the electron capture from the CB to the oxidized species of the redox mediator and occurs after several milliseconds, this current loss refers to the dark current.

### I. 3. c. Solar Cell Performances

Once the device is fitted, the solar cell is characterized by using different techniques: (i) to access power conversion efficiency such as current density-voltage (J-V) measurement, (ii) to determine the conversion rate from incident photon to electron such as incident photo to current conversion efficiency measurement (IPCE) and (iii) to study mechanisms occurring during its operation such as the photoinduced absorption spectroscopy (PIA).

#### I.3.c.(i) Current Density-Voltage (J-V) Measurement

The J-V measurement is fundamental to characterize a solar cell in order to access the power conversion efficiency of the device denoted  $\eta$  or PCE as mentioned previously. It is obtained by performing a voltage scan of the cell, with a defined surface, under a defined illumination typically 1 sun and from that, the flow of the photocurrent density is recorded (Figure I-27). In laboratory, 1 sun is simulated by xenon or halogen lamps and calibrated beforehand with a silicon diode used as reference to get a light power density of  $1000 \text{ W.m}^{-2}$  which represents AM1.5. The desired  $\eta$  is defined by the ratio of the maximum power delivered by the cell denoted  $P_{\max}$  and the incident light power  $P_{\text{in}}$ .

$$\eta (\%) = \frac{P_{\max}}{P_{\text{in}}} \times 100 \quad (\text{I-10})$$

$P_{\max}$  is obtained as the product of the fill factor (FF), the short-circuit current density ( $J_{\text{sc}}$ ) and the open circuit voltage ( $V_{\text{oc}}$ ).

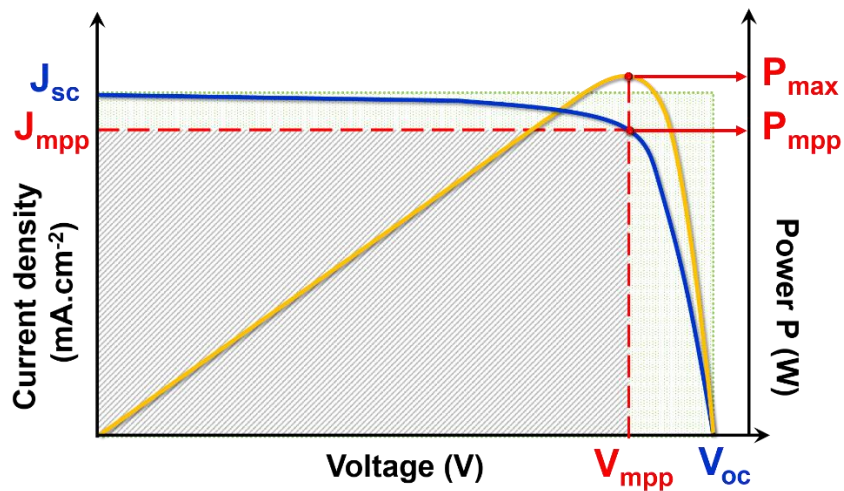


**Figure I-27:** Current density - Voltage (J-V) characteristics (blue) and the corresponding Power -Voltage (P-V) curve of a DSSC under illumination.

Due to the dependence of the short circuit current  $I_{sc}$  with respect to the solar cell area of, only  $J_{sc}$  has been considered. The  $J_{sc}$  corresponds to the current density of the cell's terminals at zero resistance load (*i.e.* when the electrodes of the solar cell is short circuited). This value is the maximum current density of the solar cell which varies with the photon flux incident and with the optical properties (absorption of the sensitizer and reflection of the counter electrode).

The  $V_{oc}$  corresponds to the voltage of the cell's terminals occurring at zero current density through the external circuit. This value is the maximum voltage of the solar cell which strongly varies with the amount of recombination. In the photo-electrochemical cell, the  $V_{oc}$  generated under illumination corresponds to the difference between the quasi-Fermi level of the electrons in the semiconductor and the equilibrium redox potential of the electrolyte (Figure I-26) and can be written as follows:

$$V_{oc} = \frac{E_{Q-F} - E_{redox}}{q} \quad (I-11)$$

$$V_{oc} = \frac{E_{CB}}{q} + \frac{RT}{nFq} \times \ln\left(\frac{n_{CB}}{N_{CB}}\right) - \frac{E_{redox}}{q} \quad (I-12)$$

The FF is defined as the ratio between the maximum power generated by the solar cell ( $P_{max} = J_{mpp} \times V_{mpp}$ ) and the product of  $V_{oc}$  and  $J_{sc}$ . In other words, this is the ratio of the small rectangle (in grey, Figure I-27) area having the maximum power point ( $J_{mpp}$  and  $V_{mpp}$ ) that fit the J-V curve to the largest rectangle (in green, Figure I-27). The FF of an ideal cell is 1 with a J-V curve that fit accurately the largest rectangular shape. It is expressed as:

$$FF = \frac{J_{mpp} \times V_{mpp}}{J_{sc} \times V_{oc}} \quad (I-13)$$

The efficiency is therefore described through the fundamental three parameters:

$$\eta (\%) = \frac{P_{max}}{P_{in}} \times 100 = \frac{FF \times J_{sc} \times V_{oc}}{P_{in}} \times 100 \quad (I-14)$$

In fact, the current density-voltage characteristic of an illuminated solar cell behaves as a diode<sup>[230]</sup>. The equivalent circuit model for DSSC is represented in the Figure I-28 and it consists of a diode that represents the electrical properties of the pn-junction, a constant current source ( $I_{ph}$ ) connected in parallel, a series resistance ( $R_s$ ) and a shunt resistance ( $R_{sh}$ ). The series resistance includes the resistance of the semiconductor and that of the liquid electrolyte or HTM.

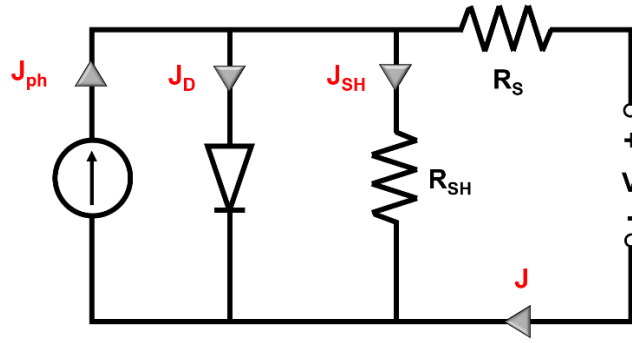


**Figure I-28:** Equivalent circuit of a DSSC

The current density ( $J$ ) can be expressed using Kirchhoff's law:

$$J = J_{ph} - J_{sh} - J_d \quad (\text{I-15})$$

$J_d$  represents the current density of the diode where the formula is modeled using the Shockley equation which is similar to the Butler-Volmer equation (the second exponential term is ignored):

$$J_d = J_0 \left( \exp\left(\frac{q V_d}{nkT}\right) - 1 \right) \quad (\text{I-16})$$

With  $V_d$  the voltage across the diode expressed as:

$$V_d = V + V_s = V + JAR_s \quad (\text{I-17})$$

$J_{sh}$  is the lost current density due to the direct recombination of the photo-injected electron (1) with the liquid electrolyte or HTM or (2) with the oxidized dye.

$$J_{sh} = \frac{(V + JAR_s)}{R_{sh}} \quad (\text{I-18})$$

By replacing  $J_{sh}$  and  $J_d$  in the Equation (I-15), the current density ( $J$ ) is described as follows:

$$J = J_{ph} - J_0 \left( \exp\left(\frac{q (V + JAR_s)}{nkT}\right) - 1 \right) - \frac{(V + JAR_s)}{R_{sh}} \quad (\text{I-19})$$

Where  $J_0$  is the exchange current density,  $k$  is the Boltzmann constant,  $T$  is the temperature,  $q$  is elementary charge,  $A$  is the illuminated device area,  $n$  is the ideality factor and  $V$  is the applied bias voltage<sup>[231]</sup>. From this Equation (I-19), the power conversion efficiency can be obtained by plotting  $J = f(V)$ . Moreover the dark J-V measurement determines the electrical parameters such as the  $R_s$ ,  $R_{sh}$ , and  $n$ .

### **I.3.c.(ii) Incident Photon-to-Electron Conversion Efficiency**

The Incident Photon-to-Electron Conversion Efficiency (IPCE) assesses the number of incident photon converted to electrons of the corresponding DSSC illuminated at different wavelengths performed with a monochromatic light. It is defined as the ratio between the number of

photogenerated electrons in the external circuit  $N_e$  and the number of incident photons  $N_v$  at a given incident wavelength ( $\lambda$ )<sup>[232]</sup> :

$$IPCE(\lambda) = \frac{N_e}{N_v} \quad (I-20)$$

$N_v$  and  $N_e$  can be expressed in terms of the incoming power ( $P_{in}$ ) and of the short circuit current density  $J_{sc}$  respectively and during a time  $t$  (s):

$$N_v = \frac{P_{in}(\lambda) \times t}{h\nu} \text{ and } N_e = \frac{J_{sc}(\lambda) \times t}{q} \quad (I-21)$$

Where  $h\nu$  is the photon energy and  $q$  is the elementary charge. So the Equation (I-20) can be rewritten as:

$$IPCE(\lambda) = \frac{J_{sc}(\lambda) \times hc}{P_{in}(\lambda) \times e \times \lambda} = 1240 \times \frac{J_{sc}(\lambda) [mA.cm^{-2}]}{P_{in}(\lambda) [mW.cm^{-2}] \times \lambda [nm]} \quad (I-22)$$

Moreover, the IPCE can also be formulated as a product of four yields including the light harvesting efficiency  $LHE(\lambda)$  of the dye, the quantum yield of electron injection from the excited dye into the  $TiO_2$  conduction band  $\Phi_{inj}$ , the quantum yield of the dye regeneration  $\Phi_{reg}$  and the charge collection efficiency  $\eta_{coll}$  by the FTO electrode:

$$IPCE(\lambda) = LHE(\lambda) \times \Phi_{inj} \times \Phi_{reg} \times \eta_{coll} \quad (I-23)$$

$LHE$  can be determined from the maximum absorption ( $A$ ) wavelength of the dye adsorbed on the oxide semiconductor<sup>[233]</sup> :

$$LHE(\lambda) = 1 - 10^{-A} \quad (I-24)$$

### **I.3.c.(iii) Photoinduced Absorption Spectroscopy**

The photoinduced absorption spectroscopy (PIA) measurement gives some information on the electron injection from dye into the oxide semiconductor after photo-excitation and from liquid electrolyte or HTM toward the oxidized dye and thus the charge separation and recombination processes can be investigated. In fact, it measures the absorption difference ( $\Delta A$ ) corresponding to the dye's oxidized state absorption when illuminated and the dye in its ground state in dark as a function of the wavelength. Usually if the oxidized dye state has a long lifetime,  $\Delta A$  is in order of  $10^{-4}$ <sup>[234]</sup>. The excitation is provided by a square-wave modulated (on/off) monochromatic light source (green 530 nm or blue 460 nm laser) and the transmitted signal is detected by a silicon photodiode. Interestingly, it has been reported that this method is a suitable method to study the quality of pore filling in case of solid hole conductors<sup>[235]</sup>.



## **I. 4. Aim of the thesis**

Although efficiencies up to 14 % have been reported for DSSCs, the use of liquid electrolyte has some disadvantages restraining the large production scale. The substitution of liquid electrolyte by a solid hole transporting material (HTM) offers a nice alternative for DSSCs stability improvement. Up to now, conducting polymers generated by *in-situ* PEP has demonstrated conclusive photovoltaic performances in s-DSSCs since it partially resolves the pore infiltration issue in the mesoporous TiO<sub>2</sub> and allows a strong contact with the dye. Despite these good performances, there are still opportunities to improve these devices, particularly the charge transport within the n-type semiconductor and the interfacial charge transfers which remain difficult because of the competition with the recombination processes.

Therefore the overall objectives of my thesis work are:

- (1) To understand and to find a way to minimize the energy barrier in two-tiered approach in these s-DSSCs: (i) at the dye/HTM interface and (ii) at the dye/semiconductor interface, in order to enable efficiently the charge transfer and to prevent their recombination within the s-DSSCs.
- (2) To find an alternative way to optimize the electron transport occurring within the semiconductor, in order to overcome the “trapping/detrapping” mechanism: the main cause of current losses in s-DSSCs.

These objectives are coupled with an important requirement *i.e.* to obtain economical, stable and environmentally friendly s-DSSCs.

To reach these goals, in Chapter II, we used several commercial dyes, based on the common D- $\pi$ -A configuration where D is a triphenylamine core, to prepare s-DSSCs and to study their photovoltaic performances. The commercial dyes have been selected based on their intrinsic properties in order to determine promising fragments constituting the dye structure (donor,  $\pi$ -linker, and acceptor) and to correlate their structure properties with: (i) the *in-situ* PEP process used to produce conducting polymer and (ii) the obtained s-DSSCs performances. In addition, the *in-situ* PEP process is carried out both in organic and in aqueous media when possible.

Based on these results, in the work presented in Chapter III and in Chapter IV, the pristine D- $\pi$ -A structure of L1 commercial dye is used as basic structure to design a new series of dyes for the development of unprecedented s-DSSCs with the new concept of removing the interface between the dye and the HTM. In order to remove this interface, the new dyes present, as an additional donor, a pre-functionalized electroactive monomer on the TPA core. The interface is removed by the fact that the dye, covalently linked to the electroactive monomer (*e.g.* carbazole, SNS), can be co-polymerized by *in-situ* PEP with a second monomer (*e.g.* Bis-EDOT, dissolved in the electrolytic solution): the resulting co-polymer, used as HTM, is inevitably covalently linked to the dye. In addition, the nature of the chemical bond formed to link the TPA to the monomer is important as it usually plays a key (structural, electronic) role in the s-DSSCs performances. Therefore, dyes with various connections (ester, alkene groups) of different rigidity have been synthesized, characterized and incorporated in s-DSSCs, in order to enhance the charge transfers processes.

Even though s-DSSCs based TiO<sub>2</sub> show high efficiencies, the interesting structural and electrical properties of nanostructured ZnO in addition to its abundance and relative low cost, make it a relevant substitute for TiO<sub>2</sub> in s-DSSCs. Indeed, an important issue corresponds to the charge transport, which can be further optimized in s-DSSCs due to the high charge transport properties of ZnO semiconductor. Therefore, and for the first time, s-DSSCs based on ZnO semiconductor as electron transport material, have been implemented in view of optimizing the charge transport within the oxide semiconductor which is the subject of the Chapter V. To achieve these devices, we used an efficient commercial organic dye (D35) as light harvesting material and a conducting polymer produced by *in-situ* PEP as HTM. These unprecedented ZnO based s-DSSCs have been successfully prepared and their preliminary photovoltaic performances are promising.

The overall conclusion summarize the promising results presented throughout this work namely those obtained from (i) the series of s-DSSCs based on TiO<sub>2</sub> with different organic commercial dyes structures, from (ii) the series of s-DSSCs based on TiO<sub>2</sub> with optimized TiO<sub>2</sub>/dye and dye/HTM interfaces and from (iii) the series of s-DSSCs based on ZnO with optimized photo-anode structure. In addition further possible ways to enhance the performances of s-DSSCs based on TiO<sub>2</sub> or ZnO will be discussed.

## I. 5. References

- (1) August: IEA data shows global energy production and consumption continue to rise <https://www.iea.org/newsroom/news/2016/august/iea-data-shows-global-energy-production-and-consumption-continue-to-rise.html>.
- (2) Publication: World Energy Balances - 2016 edition - excerpt - Key World Energy Trends <https://www.iea.org/publications/freepublications/publication/world-energy-balances---2016-edition---excerpt---key-world-energy-trends.html>.
- (3) Goldemberg, J.; Ferguson, C. D.; Prud'homme, A. *The World's Energy Supply: What Everyone Needs to Know*; Oxford University Press, 2015.
- (4) photovoltaic effect | physics <https://www.britannica.com/science/photovoltaic-effect>.
- (5) Publication: Key World Energy Statistics <https://www.iea.org/publications/freepublications/publication/key-world-energy-statistics.html>.
- (6) Statistical Review of World Energy | Energy economics | BP Global <http://www.bp.com/en/global/corporate/energy-economics/statistical-review-of-world-energy.html>.
- (7) Publication: Solar Energy Perspectives <https://www.iea.org/publications/freepublications/publication/solar-energy-perspectives.html>.
- (8) 1 Energy from the Sun [http://klimat.czn.uj.edu.pl/enid/Climate\\_Change\\_classes\\_ss/ss\\_Energy\\_from\\_the\\_Sun\\_6ev.html](http://klimat.czn.uj.edu.pl/enid/Climate_Change_classes_ss/ss_Energy_from_the_Sun_6ev.html).
- (9) *Springer Handbook of Electronic and Photonic Materials* | Safa Kasap | Springer.
- (10) Kumar, P. *Organic Solar Cells: Device Physics, Processing, Degradation, and Prevention*; CRC Press, 2016.
- (11) Becquerel, A.-E. *Comptes Rendus* **1839**, 9 (567), 1839.
- (12) Einstein, A. *Ann. Phys.* **1905**, 323 (13), 639–641.
- (13) Bloch, F. Z. *Für Phys. Hadrons Nucl.* **1929**, 52 (7), 555–600.
- (14) Sze, S. M.; Ng, K. K. *Physics of semiconductor devices*; John Wiley & sons, 2006.
- (15) Varshni, Y. P. *Physica* **1967**, 34 (1), 149–154.
- (16) Wolpert, D.; Ampadu, P. In *Managing Temperature Effects in Nanoscale Adaptive Systems*; Springer New York: New York, NY, 2012; pp 15–33.
- (17) Pässler, R. *Phys. Status Solidi B* **1999**, 216 (2), 975–1007.
- (18) Shockley, W.; Queisser, H. J. *J. Appl. Phys.* **1961**, 32 (3), 510–519.
- (19) Polman, A.; Knight, M.; Garnett, E. C.; Ehrler, B.; Sinke, W. C. *Science* **2016**, 352 (6283), aad4424-aad4424.
- (20) Kayes, B. M.; Nie, H.; Twist, R.; Spruytte, S. G.; Reinhardt, F.; Kizilyalli, I. C.; Higashi, G. S. In *2011 37th IEEE Photovoltaic Specialists Conference*; 2011; pp 000004–000008.
- (21) *Bloomberg.com*. January 3, 2017.
- (22) Hoffman, J. F. W. and R. Thin, Fast, and Flexible Semiconductors <https://spectrum.ieee.org/semiconductors/materials/thin-fast-and-flexible-semiconductors>.
- (23) First Solar Achieves Yet Another Cell Conversion Efficiency World Record (NASDAQ:FSLR) <http://investor.firstsolar.com/releasedetail.cfm?ReleaseID=956479>.

- (24) Bhandari, K. P.; Collier, J. M.; Ellingson, R. J.; Apul, D. S. *Renew. Sustain. Energy Rev.* **2015**, *47*, 133–141.
- (25) Significant progress in CIGS thin-film solar cell technology reported at IWCIGSTech7 <https://www.pv-tech.org/technical-papers/significant-progress-in-cigs-thin-film-solar-cell-technology-reported-at-iw>.
- (26) Sharp Develops Solar Cell with World’s Highest Conversion Efficiency of 37.9% | Press Releases | Sharp Global <http://www.sharp-world.com/corporate/news/130424.html>.
- (27) Takamoto, T.; Washio, H.; Juso, H. *IEEE*, 2014; pp 0001–0005.
- (28) You, J.; Dou, L.; Yoshimura, K.; Kato, T.; Ohya, K.; Moriarty, T.; Emery, K.; Chen, C.-C.; Gao, J.; Li, G.; Yang, Y. *Nat. Commun.* **2013**, *4*, 1446.
- (29) Albrecht, S.; Saliba, M.; Correa Baena, J. P.; Lang, F.; Kegelmann, L.; Mews, M.; Steier, L.; Abate, A.; Rappich, J.; Korte, L.; Schlattmann, R.; Nazeeruddin, M. K.; Hagfeldt, A.; Grätzel, M.; Rech, B. *Energy Env. Sci* **2016**, *9* (1), 81–88.
- (30) Santra, P. K.; Kamat, P. V. *J. Am. Chem. Soc.* **2012**, *134* (5), 2508–2511.
- (31) Yun, H. J.; Paik, T.; Diroll, B.; Edley, M. E.; Baxter, J. B.; Murray, C. B. *ACS Appl. Mater. Interfaces* **2016**, *8* (23), 14692–14700.
- (32) Peng, W.; Du, J.; Pan, Z.; Nakazawa, N.; Sun, J.; Du, Z.; Shen, G.; Yu, J.; Hu, J.-S.; Shen, Q.; Zhong, X. *ACS Appl. Mater. Interfaces* **2017**, *9* (6), 5328–5336.
- (33) Kamat, P. V. *J. Phys. Chem. Lett.* **2013**, *4* (6), 908–918.
- (34) Mandal, P.; Sharma, S. *Renew. Sustain. Energy Rev.* **2016**, *65*, 537–552.
- (35) Kojima, A.; Teshima, K.; Shirai, Y.; Miyasaka, T. *J. Am. Chem. Soc.* **2009**, *131* (17), 6050–6051.
- (36) *Organic-Inorganic Halide Perovskite Photovoltaics - From / Nam-Gyu Park / Springer.*
- (37) Saliba, M.; Matsui, T.; Seo, J.-Y.; Domanski, K.; Correa-Baena, J.-P.; Nazeeruddin, M. K.; Zakeeruddin, S. M.; Tress, W.; Abate, A.; Hagfeldt, A.; Grätzel, M. *Energy Env. Sci* **2016**, *9* (6), 1989–1997.
- (38) Yang, W. S.; Park, B.-W.; Jung, E. H.; Jeon, N. J.; Kim, Y. C.; Lee, D. U.; Shin, S. S.; Seo, J.; Kim, E. K.; Noh, J. H.; Seok, S. I. *Science* **2017**, *356* (6345), 1376–1379.
- (39) Snaith, H. J. *J. Phys. Chem. Lett.* **2013**, *4* (21), 3623–3630.
- (40) O’Regan, B.; Grätzel, M. *Nature* **1991**, *353* (6346), 737–740.
- (41) Kakiage, K.; Aoyama, Y.; Yano, T.; Oya, K.; Fujisawa, J.; Hanaya, M. *Chem Commun* **2015**, *51* (88), 15894–15897.
- (42) Cachet, H. In *Fluorinated Materials for Energy Conversion*; Nakajima, T., Groult, H., Eds.; Elsevier Science: Amsterdam, 2005; pp 513–534.
- (43) Li, F.; Chen, C.; Tan, F.; Li, C.; Yue, G.; Shen, L.; Zhang, W. *Nanoscale Res. Lett.* **2014**, *9* (1), 579.
- (44) Sima, C.; Grigoriu, C.; Antohe, S. *Thin Solid Films* **2010**, *519* (2), 595–597.
- (45) Zardetto, V.; Brown, T. M.; Reale, A.; Di Carlo, A. *J. Polym. Sci. Part B Polym. Phys.* **2011**, *49* (9), 638–648.
- (46) Noh, S. I.; Ahn, H.-J.; Riu, D.-H. *Ceram. Int.* **2012**, *38* (5), 3735–3739.
- (47) Wang, H.; Liu, Y.; Huang, H.; Zhong, M.; Shen, H.; Wang, Y.; Yang, H. *Appl. Surf. Sci.* **2009**, *255* (22), 9020–9025.
- (48) Noh, J. H.; Lee, S.; Kim, J. Y.; Lee, J.-K.; Han, H. S.; Cho, C. M.; Cho, I. S.; Jung, H. S.; Hong, K. S. *J. Phys. Chem. C* **2009**, *113* (3), 1083–1087.
- (49) Liu, X.; Luo, Y.; Li, H.; Fan, Y.; Yu, Z.; Lin, Y.; Chen, L.; Meng, Q. *Chem. Commun.* **2007**, No. 27, 2847.

- (50) Yamaguchi, T.; Tobe, N.; Matsumoto, D.; Nagai, T.; Arakawa, H. *Sol. Energy Mater. Sol. Cells* **2010**, *94* (5), 812–816.
- (51) Yun, H.-G.; Bae, B.-S.; Kang, M. G. *Adv. Energy Mater.* **2011**, *1* (3), 337–342.
- (52) Barbé, C. J.; Bartlett, J. R. In *Sol-Gel Technologies for Glass Producers and Users*; Aegerter, M. A., Mennig, M., Eds.; Springer US, 2004; pp 283–294.
- (53) Cavallo, C.; Di Pascasio, F.; Latini, A.; Bonomo, M.; Dini, D. *J. Nanomater.* **2017**, *2017*, 1–31.
- (54) Hashimoto, K.; Irie, H.; Fujishima, A. *Jpn. J. Appl. Phys.* **2005**, *44* (12R), 8269.
- (55) Hanaor, D. A. H.; Sorrell, C. C. *J. Mater. Sci.* **2011**, *46* (4), 855–874.
- (56) Koelsch, M.; Cassaignon, S.; Ta Thanh Minh, C.; Guillemoles, J.-F.; Jolivet, J.-P. *Thin Solid Films* **2004**, *451–452*, 86–92.
- (57) Park, N.-G.; van de Lagemaat, J.; Frank, A. J. *J. Phys. Chem. B* **2000**, *104* (38), 8989–8994.
- (58) Magne, C.; Cassaignon, S.; Lancel, G.; Pauporté, T. *ChemPhysChem* **2011**, *12* (13), 2461–2467.
- (59) Amtout, A.; Leonelli, R. *Phys. Rev. B* **1995**, *51* (11), 6842–6851.
- (60) Thomas, A. *Gemstones: Properties, Identification and Use*; New Holland Publishers, 2008.
- (61) Tang, H.; Prasad, K.; Sanjinès, R.; Schmid, P. E.; Lévy, F. *J. Appl. Phys.* **1994**, *75* (4), 2042–2047.
- (62) Wang, J.; Zhang, T.; Wang, D.; Pan, R.; Wang, Q.; Xia, H. *J. Alloys Compd.* **2013**, *551*, 82–87.
- (63) Wu, W.-Q.; Lei, B.-X.; Rao, H.-S.; Xu, Y.-F.; Wang, Y.-F.; Su, C.-Y.; Kuang, D.-B. *Sci. Rep.* **2013**, *3* (1).
- (64) Sauvage, F.; Di Fonzo, F.; Li Bassi, A.; Casari, C. S.; Russo, V.; Divitini, G.; Ducati, C.; Bottani, C. E.; Comte, P.; Graetzel, M. *Nano Lett.* **2010**, *10* (7), 2562–2567.
- (65) Zheng, D.; Xiong, J.; Guo, P.; Li, Y.; Gu, H. *J. Nanosci. Nanotechnol.* **2016**, *16* (1), 613–618.
- (66) Jiang, L.; Sun, L.; Yang, D.; Zhang, J.; Li, Y.-J.; Zou, K.; Deng, W.-Q. *ACS Appl. Mater. Interfaces* **2017**, *9* (11), 9576–9583.
- (67) Chen, D.; Huang, F.; Cheng, Y.-B.; Caruso, R. A. *Adv. Mater.* **2009**, *21* (21), 2206–2210.
- (68) Xu, C.; Shin, P. H.; Cao, L.; Wu, J.; Gao, D. *Chem. Mater.* **2010**, *22* (1), 143–148.
- (69) Wu, X.; Chen, Z.; Lu, G. Q. M.; Wang, L. *Adv. Funct. Mater.* **2011**, *21* (21), 4167–4172.
- (70) Chu, L.; Qin, Z.; Yang, J.; Li, X. *Sci. Rep.* **2015**, *5* (1).
- (71) Seo, Y. G.; Woo, K.; Kim, J.; Lee, H.; Lee, W. *Adv. Funct. Mater.* **2011**, *21* (16), 3094–3103.
- (72) Jin, M.; Kim, S. S.; Yoon, M.; Li, Z.; Lee, Y. Y.; Kim, J. M. *J. Nanosci. Nanotechnol.* **2012**, *12* (1), 815–821.
- (73) Makris, T.; Dracopoulos, V.; Stergiopoulos, T.; Lianos, P. *Electrochimica Acta* **2011**, *56* (5), 2004–2008.
- (74) Coleman, V. A.; Jagadish, C. In *Zinc Oxide Bulk, Thin Films and Nanostructures*; Elsevier, 2006; pp 1–20.
- (75) Özgür, ü.; Alivov, Y. I.; Liu, C.; Teke, A.; Reshchikov, M. A.; Doğan, S.; Avrutin, V.; Cho, S.-J.; Morkoç, H. *J. Appl. Phys.* **2005**, *98* (4), 041301.
- (76) Zhang, Q.; Dandeneau, C. S.; Zhou, X.; Cao, G. *Adv. Mater.* **2009**, *21* (41), 4087–4108.
- (77) Zhu, K.; Schiff, E. A.; Park, N.-G.; van de Lagemaat, J.; Frank, A. J. *Appl. Phys. Lett.* **2002**, *80* (4), 685–687.

- (78) Cameron, P. J.; Peter, L. M. *J. Phys. Chem. B* **2003**, *107* (51), 14394–14400.
- (79) Cameron, P. J.; Peter, L. M. *J. Phys. Chem. B* **2005**, *109* (15), 7392–7398.
- (80) Ito, S.; Ishikawa, K.; Wen, C.-J.; Yoshida, S.; Watanabe, T. *Bull. Chem. Soc. Jpn.* **2000**, *73* (11), 2609–2614.
- (81) Kavan, L.; Grätzel, M. *Electrochimica Acta* **1995**, *40* (5), 643–652.
- (82) Grätzel, M. *Acc. Chem. Res.* **2009**, *42* (11), 1788–1798.
- (83) Selopal, G. S.; Memarian, N.; Milan, R.; Concina, I.; Sberveglieri, G.; Vomiero, A. *ACS Appl. Mater. Interfaces* **2014**, *6* (14), 11236–11244.
- (84) Selopal, G. S.; Wu, H.-P.; Lu, J.; Chang, Y.-C.; Wang, M.; Vomiero, A.; Concina, I.; Diau, E. W.-G. *Sci. Rep.* **2016**, *6* (1).
- (85) Nazeeruddin, M. K.; Liska, P.; Moser, J.; Vlachopoulos, N.; Grätzel, M. *Helv. Chim. Acta* **1990**, *73* (6), 1788–1803.
- (86) Nazeeruddin, M. K.; Kay, A.; Rodicio, I.; Humphry-Baker, R.; Mueller, E.; Liska, P.; Vlachopoulos, N.; Graetzel, M. *J. Am. Chem. Soc.* **1993**, *115* (14), 6382–6390.
- (87) Nazeeruddin, M. K.; Zakeeruddin, S. M.; Humphry-Baker, R.; Jirousek, M.; Liska, P.; Vlachopoulos, N.; Shklover, V.; Fischer, C.-H.; Grätzel, M. *Inorg. Chem.* **1999**, *38* (26), 6298–6305.
- (88) Nazeeruddin, M. K.; Baranoff, E.; Grätzel, M. *Sol. Energy* **2011**, *85* (6), 1172–1178.
- (89) Nazeeruddin, M. K.; Péchy, P.; Grätzel, M. *Chem. Commun.* **1997**, No. 18, 1705–1706.
- (90) Wang, P.; Zakeeruddin, S. M.; Exnar, I.; Grätzel, M. *Chem Commun* **2002**, No. 24, 2972–2973.
- (91) Wang, P.; Zakeeruddin, S. M.; Moser, J. E.; Nazeeruddin, M. K.; Sekiguchi, T.; Grätzel, M. *Nat. Mater.* **2003**, *2* (6), 402–407.
- (92) Voitchovsky, K.; Ashari-Astani, N.; Tavernelli, I.; Tétreault, N.; Rothlisberger, U.; Stellacci, F.; Grätzel, M.; Harms, H. A. *ACS Appl. Mater. Interfaces* **2015**, *7* (20), 10834–10842.
- (93) Kwak, C. H.; Baeg, J. H.; Yang, I. M.; Giribabu, K.; Lee, S.; Huh, Y. S. *Sol. Energy* **2016**, *130*, 244–249.
- (94) Snaith, H. J.; Zakeeruddin, S. M.; Schmidt-Mende, L.; Klein, C.; Grätzel, M. *Angew. Chem. Int. Ed.* **2005**, *44* (39), 6413–6417.
- (95) Kuang, D.; Klein, C.; Snaith, H. J.; Humphry-Baker, R.; Zakeeruddin, S. M.; Grätzel, M. *Inorganica Chim. Acta* **2008**, *361* (3), 699–706.
- (96) Hallett, A. J.; Jones, J. E. *Dalton Trans* **2011**, *40* (15), 3871–3876.
- (97) Lu, S.; Wu, T.; Ren, B.; Geng, R. *J. Mater. Sci. Mater. Electron.* **2013**, *24* (7), 2346–2350.
- (98) Yum, J.-H.; Jung, I.; Baik, C.; Ko, J.; Nazeeruddin, M. K.; Grätzel, M. *Energy Env. Sci* **2009**, *2* (1), 100–102.
- (99) Kim, J.-J.; Yoon, J.; Kim, E. J.; Kim, B. R.; Yoon, Y.-J.; Kang, M. *Int. J. Photoenergy* **2012**, *2012*, 1–7.
- (100) Jiang, K.-J.; Masaki, N.; Xia, J.; Noda, S.; Yanagida, S. *Chem. Commun.* **2006**, No. 23, 2460.
- (101) Matar, F.; Ghaddar, T. H.; Walley, K.; DosSantos, T.; Durrant, J. R.; O'Regan, B. *J. Mater. Chem.* **2008**, *18* (36), 4246.
- (102) Cao, Y.; Bai, Y.; Yu, Q.; Cheng, Y.; Liu, S.; Shi, D.; Gao, F.; Wang, P. *J. Phys. Chem. C* **2009**, *113* (15), 6290–6297.
- (103) Kroeze, J. E.; Hirata, N.; Koops, S.; Nazeeruddin, M. K.; Schmidt-Mende, L.; Grätzel, M.; Durrant, J. R. *J. Am. Chem. Soc.* **2006**, *128* (50), 16376–16383.

- (104) Chen, C.-Y.; Wang, M.; Li, J.-Y.; Pootrakulchote, N.; Alibabaei, L.; Ngoc-le, C.; Decoppet, J.-D.; Tsai, J.-H.; Grätzel, C.; Wu, C.-G.; Zakeeruddin, S. M.; Grätzel, M. *ACS Nano* **2009**, 3 (10), 3103–3109.
- (105) Pashaei, B.; Shahroosvand, H.; Graetzel, M.; Nazeeruddin, M. K. *Chem. Rev.* **2016**, 116 (16), 9485–9564.
- (106) Kinoshita, T.; Fujisawa, J.; Nakazaki, J.; Uchida, S.; Kubo, T.; Segawa, H. *J. Phys. Chem. Lett.* **2012**, 394–398.
- (107) Zhang, T.-T.; Jia, J.; Wu, H.-S. *Theor. Chem. Acc.* **2012**, 131 (9).
- (108) Duchanois, T.; Etienne, T.; Cebrián, C.; Liu, L.; Monari, A.; Beley, M.; Assfeld, X.; Haacke, S.; Gros, P. C. *Eur. J. Inorg. Chem.* **2015**, 2015 (14), 2469–2477.
- (109) Wenger, O. S. *Coord. Chem. Rev.* **2009**, 253 (9–10), 1439–1457.
- (110) Polo, A. S.; Itokazu, M. K.; Murakami Iha, N. Y. *Coord. Chem. Rev.* **2004**, 248 (13–14), 1343–1361.
- (111) Geary, E. A. M.; Yellowlees, L. J.; Jack, L. A.; Oswald, I. D. H.; Parsons, S.; Hirata, N.; Durrant, J. R.; Robertson, N. *Inorg. Chem.* **2005**, 44 (2), 242–250.
- (112) Baranoff, E.; Yum, J.-H.; Graetzel, M.; Nazeeruddin, M. K. *J. Organomet. Chem.* **2009**, 694 (17), 2661–2670.
- (113) Bessho, T.; Constable, E. C.; Graetzel, M.; Hernandez Redondo, A.; Housecroft, C. E.; Kylberg, W.; Nazeeruddin, M. K.; Neuburger, M.; Schaffner, S. *Chem. Commun.* **2008**, No. 32, 3717.
- (114) Calogero, G.; Bartolotta, A.; Di Marco, G.; Di Carlo, A.; Bonaccorso, F. *Chem Soc Rev* **2015**, 44 (10), 3244–3294.
- (115) Wang, X.-F.; Zhan, C.-H.; Maoka, T.; Wada, Y.; Koyama, Y. *Chem. Phys. Lett.* **2007**, 447 (1–3), 79–85.
- (116) Li, Y.; Ku, S.-H.; Chen, S.-M.; Ali, M. A.; AlHemaid, F. M. *Int. J. Electrochem. Sci.* **2013**, 8 (1), 1237–1245.
- (117) Prabavathy, N.; Shalini, S.; Balasundaraprabhu, R.; Velauthapillai, D.; Prasanna, S.; Muthukumarasamy, N. *Int. J. Energy Res.* **2017**.
- (118) Sayama, K.; Sugino, M.; Sugihara, H.; Abe, Y.; Arakawa, H. *Chem. Lett.* **1998**, 27 (8), 753–754.
- (119) Khazraji, A. C.; Hotchandani, S.; Das, S.; Kamat, P. V. *J. Phys. Chem. B* **1999**, 103 (22), 4693–4700.
- (120) Sayama, K.; Hara, K.; Sugihara, H.; Arakawa, H.; Mori, N.; Satsuki, M.; Suga, S.; Tsukagoshi, S.; Abe, Y. *Chem. Commun.* **2000**, No. 13, 1173–1174.
- (121) Hara, K. *Sol. Energy Mater. Sol. Cells* **2000**, 64 (2), 115–134.
- (122) Hara, K.; Sayama, K.; Arakawa, H.; Ohga, Y.; Shinpo, A.; Suga, S. *Chem. Commun.* **2001**, No. 6, 569–570.
- (123) Wang, Z.-S.; Li, F.-Y.; Huang, C.-H. *Chem. Commun.* **2000**, No. 20, 2063–2064.
- (124) Hagberg, D. P.; Marinado, T.; Karlsson, K. M.; Nonomura, K.; Qin, P.; Boschloo, G.; Brinck, T.; Hagfeldt, A.; Sun, L. *J. Org. Chem.* **2007**, 72 (25), 9550–9556.
- (125) Mishra, A.; Fischer, M. K. R.; Bäuerle, P. *Angew. Chem. Int. Ed.* **2009**, 48 (14), 2474–2499.
- (126) Horiuchi, T.; Miura, H.; Sumioka, K.; Uchida, S. *J. Am. Chem. Soc.* **2004**, 126 (39), 12218–12219.
- (127) Ito, S.; Miura, H.; Uchida, S.; Takata, M.; Sumioka, K.; Liska, P.; Comte, P.; Péchy, P.; Grätzel, M. *Chem. Commun.* **2008**, No. 41, 5194.

- (128) Suzuka, M.; Hayashi, N.; Sekiguchi, T.; Sumioka, K.; Takata, M.; Hayo, N.; Ikeda, H.; Oyaizu, K.; Nishide, H. *Sci. Rep.* **2016**, *6* (1).
- (129) Wang, Z.-S.; Cui, Y.; Hara, K.; Dan-oh, Y.; Kasada, C.; Shinpo, A. *Adv. Mater.* **2007**, *19* (8), 1138–1141.
- (130) Hara, K.; Wang, Z.-S.; Sato, T.; Furube, A.; Katoh, R.; Sugihara, H.; Dan-oh, Y.; Kasada, C.; Shinpo, A.; Suga, S. *J. Phys. Chem. B* **2005**, *109* (32), 15476–15482.
- (131) Kakiage, K.; Osada, H.; Aoyama, Y.; Yano, T.; Oya, K.; Iwamoto, S.; Fujisawa, J.; Hanaya, M. *Sci. Rep.* **2016**, *6* (1).
- (132) Justin Thomas, K. R.; Baheti, A. *Mater. Technol.* **2013**, *28* (1–2), 71–87.
- (133) Tian, H.; Yang, X.; Chen, R.; Pan, Y.; Li, L.; Hagfeldt, A.; Sun, L. *Chem. Commun.* **2007**, No. 36, 3741.
- (134) Huang, Z.-S.; Meier, H.; Cao, D. *J Mater Chem C* **2016**, *4* (13), 2404–2426.
- (135) Chiykowski, V. A.; Lam, B.; Du, C.; Berlinguette, C. P. *Chem Commun* **2017**, *53* (15), 2367–2370.
- (136) Venkateswararao, A.; Thomas, K. R. J.; Lee, C.-P.; Li, C.-T.; Ho, K.-C. *ACS Appl. Mater. Interfaces* **2014**, *6* (4), 2528–2539.
- (137) Teng, C.; Yang, X.; Yuan, C.; Li, C.; Chen, R.; Tian, H.; Li, S.; Hagfeldt, A.; Sun, L. *Org. Lett.* **2009**, *11* (23), 5542–5545.
- (138) Hagfeldt, A.; Boschloo, G.; Sun, L.; Kloo, L.; Pettersson, H. *Chem. Rev.* **2010**, *110* (11), 6595–6663.
- (139) Mahmood, A. *Sol. Energy* **2016**, *123*, 127–144.
- (140) Ning, Z.; Tian, H. *Chem. Commun.* **2009**, No. 37, 5483.
- (141) Roncali, J.; Leriche, P.; Cravino, A. *Adv. Mater.* **2007**, *19* (16), 2045–2060.
- (142) Kitamura, T.; Ikeda, M.; Shigaki, K.; Inoue, T.; Anderson, N. A.; Ai, X.; Lian, T.; Yanagida, S. *Chem. Mater.* **2004**, *16* (9), 1806–1812.
- (143) Kim, S.; Lee, J. K.; Kang, S. O.; Ko, J.; Yum, J.-H.; Fantacci, S.; De Angelis, F.; Di Censo, D.; Nazeeruddin, M. K.; Grätzel, M. *J. Am. Chem. Soc.* **2006**, *128* (51), 16701–16707.
- (144) Feldt, S. M.; Gibson, E. A.; Gabrielsson, E.; Sun, L.; Boschloo, G.; Hagfeldt, A. *J. Am. Chem. Soc.* **2010**, *132* (46), 16714–16724.
- (145) Yella, A.; Humphry-Baker, R.; Curchod, B. F. E.; Ashari Astani, N.; Teuscher, J.; Polander, L. E.; Mathew, S.; Moser, J.-E.; Tavernelli, I.; Rothlisberger, U.; Grätzel, M.; Nazeeruddin, M. K.; Frey, J. *Chem. Mater.* **2013**, *25* (13), 2733–2739.
- (146) Zhang, L.; Cole, J. M. *ACS Appl. Mater. Interfaces* **2015**, *7* (6), 3427–3455.
- (147) Anselmi, C.; Mosconi, E.; Pastore, M.; Ronca, E.; De Angelis, F. *Phys. Chem. Chem. Phys.* **2012**, *14* (46), 15963.
- (148) Sun, H.; Liu, D.; Wang, T.; Lu, T.; Li, W.; Ren, S.; Hu, W.; Wang, L.; Zhou, X. *ACS Appl. Mater. Interfaces* **2017**, *9* (11), 9880–9891.
- (149) Prachumrak, N.; Sudyoasuk, T.; Thangthong, A.; Nalaoh, P.; Jungsuttiwong, S.; Daengngern, R.; Namuangruk, S.; Pattanasattayavong, P.; Promarak, V. *Mater Chem Front* **2017**.
- (150) Ciou, Y.-S.; Lin, P.-H.; Li, W.-M.; Lee, K.-M.; Liu, C.-Y. *J. Org. Chem.* **2017**, *82* (7), 3538–3551.
- (151) Teng, C.; Yang, X.; Yang, C.; Li, S.; Cheng, M.; Hagfeldt, A.; Sun, L. *J. Phys. Chem. C* **2010**, *114* (19), 9101–9110.
- (152) Jiang, X.; Marinado, T.; Gabrielsson, E.; Hagberg, D. P.; Sun, L.; Hagfeldt, A. *J. Phys. Chem. C* **2010**, *114* (6), 2799–2805.



- (153) Hara, K.; Kurashige, M.; Dan-oh, Y.; Kasada, C.; Shinpo, A.; Suga, S.; Sayama, K.; Arakawa, H. *New J. Chem.* **2003**, 27 (5), 783–785.
- (154) Hagberg, D. P.; Edvinsson, T.; Marinado, T.; Boschloo, G.; Hagfeldt, A.; Sun, L. *Chem. Commun.* **2006**, No. 21, 2245.
- (155) Tian, H.; Yang, X.; Chen, R.; Zhang, R.; Hagfeldt, A.; Sun, L. *J. Phys. Chem. C* **2008**, 112 (29), 11023–11033.
- (156) Joly, D.; Pellejà, L.; Narbey, S.; Oswald, F.; Chiron, J.; Clifford, J. N.; Palomares, E.; Demadrille, R. *Sci. Rep.* **2015**, 4 (1).
- (157) Lee, D. H.; Lee, M. J.; Song, H. M.; Song, B. J.; Seo, K. D.; Pastore, M.; Anselmi, C.; Fantacci, S.; De Angelis, F.; Nazeeruddin, M. K.; Grätzel, M.; Kim, H. K. *Dyes Pigments* **2011**, 91 (2), 192–198.
- (158) Ni, J.-S.; Yen, Y.-C.; Lin, J. T. *Chem Commun* **2015**, 51 (96), 17080–17083.
- (159) Yen, Y.-S.; Lee, C.-T.; Hsu, C.-Y.; Chou, H.-H.; Chen, Y.-C.; Lin, J. T. *Chem. - Asian J.* **2013**, 8 (4), 809–816.
- (160) Ellis, H.; Eriksson, S. K.; Feldt, S. M.; Gabriellsson, E.; Lohse, P. W.; Lindblad, R.; Sun, L.; Rensmo, H.; Boschloo, G.; Hagfeldt, A. *J. Phys. Chem. C* **2013**, 117 (41), 21029–21036.
- (161) Gabriellsson, E.; Ellis, H.; Feldt, S.; Tian, H.; Boschloo, G.; Hagfeldt, A.; Sun, L. *Adv. Energy Mater.* **2013**, 3 (12), 1647–1656.
- (162) Boschloo, G.; Hagfeldt, A. *Acc. Chem. Res.* **2009**, 42 (11), 1819–1826.
- (163) Pelet, S.; Moser, J.-E.; Grätzel, M. *J. Phys. Chem. B* **2000**, 104 (8), 1791–1795.
- (164) Nasr, C.; Hotchandani, S.; Kamat, P. V. *J. Phys. Chem. B* **1998**, 102 (25), 4944–4951.
- (165) Li, G.; Jiang, K.-J.; Li, Y.-F.; Li, S.-L.; Yang, L.-M. *J. Phys. Chem. C* **2008**, 112 (30), 11591–11599.
- (166) Li, H.; Fang, M.; Hou, Y.; Tang, R.; Yang, Y.; Zhong, C.; Li, Q.; Li, Z. *ACS Appl. Mater. Interfaces* **2016**, 8 (19), 12134–12140.
- (167) Zeng, W.; Cao, Y.; Bai, Y.; Wang, Y.; Shi, Y.; Zhang, M.; Wang, F.; Pan, C.; Wang, P. *Chem. Mater.* **2010**, 22 (5), 1915–1925.
- (168) Nusbaumer, H.; Zakeeruddin, S. M.; Moser, J.-E.; Grätzel, M. *Chem. - Eur. J.* **2003**, 9 (16), 3756–3763.
- (169) Daeneke, T.; Kwon, T.-H.; Holmes, A. B.; Duffy, N. W.; Bach, U.; Spiccia, L. *Nat. Chem.* **2011**, 3 (3), 213–217.
- (170) Apostolopoulou, A.; Vlasiou, M.; Tziouris, P. A.; Tsiakoulis, C.; Tsipis, A. C.; Rehder, D.; Kabanos, T. A.; Keramidis, A. D.; Stathatos, E. *Inorg. Chem.* **2015**, 54 (8), 3979–3988.
- (171) Wang, M.; Chamberland, N.; Breau, L.; Moser, J.-E.; Humphry-Baker, R.; Marsan, B.; Zakeeruddin, S. M.; Grätzel, M. *Nat. Chem.* **2010**, 2 (5), 385–389.
- (172) Nusbaumer, H.; Moser, J.-E.; Zakeeruddin, S. M.; Nazeeruddin, M. K.; Grätzel, M. *J. Phys. Chem. B* **2001**, 105 (43), 10461–10464.
- (173) Kashif, M. K.; Axelson, J. C.; Duffy, N. W.; Forsyth, C. M.; Chang, C. J.; Long, J. R.; Spiccia, L.; Bach, U. *J. Am. Chem. Soc.* **2012**, 134 (40), 16646–16653.
- (174) Zhang, M.; Wang, Y.; Xu, M.; Ma, W.; Li, R.; Wang, P. *Energy Environ. Sci.* **2013**, 6 (10), 2944.
- (175) Saygili, Y.; Söderberg, M.; Pellet, N.; Giordano, F.; Cao, Y.; Muñoz-García, A. B.; Zakeeruddin, S. M.; Vlachopoulos, N.; Pavone, M.; Boschloo, G.; Kavan, L.; Moser, J.-E.; Grätzel, M.; Hagfeldt, A.; Freitag, M. *J. Am. Chem. Soc.* **2016**, 138 (45), 15087–15096.

- (176) Freitag, M.; Teuscher, J.; Saygili, Y.; Zhang, X.; Giordano, F.; Liska, P.; Hua, J.; Zakeeruddin, S. M.; Moser, J.-E.; Grätzel, M.; Hagfeldt, A. *Nat. Photonics* **2017**, *11* (6), 372–378.
- (177) Wu, J. H.; Lan, Z.; Lin, J. M.; Huang, M. L.; Hao, S. C.; Sato, T.; Yin, S. *Adv. Mater.* **2007**, *19* (22), 4006–4011.
- (178) Bella, F.; Gerbaldi, C.; Barolo, C.; Grätzel, M. *Chem Soc Rev* **2015**, *44* (11), 3431–3473.
- (179) Ellis, H.; Jiang, R.; Ye, S.; Hagfeldt, A.; Boschloo, G. *Phys Chem Chem Phys* **2016**, *18* (12), 8419–8427.
- (180) Bach, U.; Lupo, D.; Comte, P.; Moser, J. E.; Weissörtel, F.; Salbeck, J.; Spreitzer, H.; Grätzel, M. *Nature* **1998**, *395* (6702), 583–585.
- (181) Schmidt-Mende, L.; Bach, U.; Humphry-Baker, R.; Horiuchi, T.; Miura, H.; Ito, S.; Uchida, S.; Grätzel, M. *Adv. Mater.* **2005**, *17* (7), 813–815.
- (182) Snaith, H. J.; Grätzel, M. *Adv. Mater.* **2007**, *19* (21), 3643–3647.
- (183) Nguyen, W. H.; Bailie, C. D.; Unger, E. L.; McGehee, M. D. *J. Am. Chem. Soc.* **2014**, *136* (31), 10996–11001.
- (184) Shen, Z.; Xu, B.; Liu, P.; Hu, Y.; Yu, Y.; Ding, H.; Kloo, L.; Hua, J.; Sun, L.; Tian, H. *J Mater Chem A* **2017**, *5* (3), 1242–1247.
- (185) Schmidt-Mende, L.; Grätzel, M. *Thin Solid Films* **2006**, *500* (1–2), 296–301.
- (186) Docampo, P.; Guldin, S.; Leijtens, T.; Noel, N. K.; Steiner, U.; Snaith, H. J. *Adv. Mater.* **2014**, *26* (24), 4013–4030.
- (187) Leijtens, T.; Ding, I.-K.; Giovenzana, T.; Bloking, J. T.; McGehee, M. D.; Sellinger, A. *ACS Nano* **2012**, *6* (2), 1455–1462.
- (188) Yang, L.; Xu, B.; Bi, D.; Tian, H.; Boschloo, G.; Sun, L.; Hagfeldt, A.; Johansson, E. M. *J. J. Am. Chem. Soc.* **2013**, *135* (19), 7378–7385.
- (189) O'Regan, B.; Lenzmann, F.; Muis, R.; Wienke, J. *Chem. Mater.* **2002**, *14* (12), 5023–5029.
- (190) Meng, Q.-B.; Takahashi, K.; Zhang, X.-T.; Sutanto, I.; Rao, T. N.; Sato, O.; Fujishima, A.; Watanabe, H.; Nakamori, T.; Urugami, M. *Langmuir* **2003**, *19* (9), 3572–3574.
- (191) Yang, L.; Cappel, U. B.; Unger, E. L.; Karlsson, M.; Karlsson, K. M.; Gabrielsson, E.; Sun, L.; Boschloo, G.; Hagfeldt, A.; Johansson, E. M. *J. Phys Chem Chem Phys* **2012**, *14* (2), 779–789.
- (192) Chevrier, M.; Richeter, S.; Surin, M.; Ahmad, M.; Lazzaroni, R.; Dubois, P.; Bouclé, J.; Clément, S. 2016.
- (193) Grancini, G.; Santosh Kumar, R. S.; Abrusci, A.; Yip, H.-L.; Li, C.-Z.; Jen, A.-K. Y.; Lanzani, G.; Snaith, H. J. *Adv. Funct. Mater.* **2012**, *22* (10), 2160–2166.
- (194) Murakoshi, K.; Kogure, R.; Wada, Y.; Yanagida, S. *Chem. Lett.* **1997**, *26* (5), 471–472.
- (195) Senadeera, G. K. ; Kitamura, T.; Wada, Y.; Yanagida, S. *J. Photochem. Photobiol. Chem.* **2004**, *164* (1–3), 61–66.
- (196) Saito, Y.; Kitamura, T.; Wada, Y.; Yanagida, S. *Synth. Met.* **2002**, *131* (1–3), 185–187.
- (197) Saito, Y. *Electrochem. Commun.* **2004**, *6* (1), 71–74.
- (198) Mozer, A. J.; Wada, Y.; Jiang, K.-J.; Masaki, N.; Yanagida, S.; Mori, S. N. *Appl. Phys. Lett.* **2006**, *89* (4), 043509.
- (199) Xia, J.; Masaki, N.; Lira-Cantu, M.; Kim, Y.; Jiang, K.; Yanagida, S. *J. Am. Chem. Soc.* **2008**, *130* (4), 1258–1263.
- (200) Liu, X.; Zhang, W.; Uchida, S.; Cai, L.; Liu, B.; Ramakrishna, S. *Adv. Mater.* **2010**, *22* (20), E150–E155.

- (201) Caramori, S.; Cazzanti, S.; Marchini, L.; Argazzi, R.; Bignozzi, C. A.; Martineau, D.; Gros, P. C.; Beley, M. *Inorganica Chim. Acta* **2008**, *361* (3), 627–634.
- (202) Kim, Y.; Lim, J.; Sung, Y.-E.; Xia, J.; Masaki, N.; Yanagida, S. *J. Photochem. Photobiol. Chem.* **2009**, *204* (2–3), 110–114.
- (203) Zhang, J.; Yang, L.; Shen, Y.; Park, B.-W.; Hao, Y.; Johansson, E. M. J.; Boschloo, G.; Kloo, L.; Gabrielsson, E.; Sun, L.; Jarbou, A.; Perruchot, C.; Jouini, M.; Vlachopoulos, N.; Hagfeldt, A. *J. Phys. Chem. C* **2014**, *118* (30), 16591–16601.
- (204) Zhang, J.; Häggman, L.; Jouini, M.; Jarbou, A.; Boschloo, G.; Vlachopoulos, N.; Hagfeldt, A. *ChemPhysChem* **2014**, *15* (6), 1043–1047.
- (205) Song, I. Y.; Kim, M.; Park, T. *ACS Appl. Mater. Interfaces* **2015**, *7* (21), 11482–11489.
- (206) Zhang, J.; Vlachopoulos, N.; Jouini, M.; Johansson, M. B.; Zhang, X.; Nazeeruddin, M. K.; Boschloo, G.; Johansson, E. M. J.; Hagfeldt, A. *Nano Energy* **2016**, *19*, 455–470.
- (207) Zhang, J.; Vlachopoulos, N.; Hao, Y.; Holcombe, T. W.; Boschloo, G.; Johansson, E. M. J.; Grätzel, M.; Hagfeldt, A. *ChemPhysChem* **2016**, *17* (10), 1441–1445.
- (208) Yang, L.; Zhang, J.; Shen, Y.; Park, B.-W.; Bi, D.; Häggman, L.; Johansson, E. M. J.; Boschloo, G.; Hagfeldt, A.; Vlachopoulos, N.; Snedden, A.; Kloo, L.; Jarbou, A.; Chams, A.; Perruchot, C.; Jouini, M. *J. Phys. Chem. Lett.* **2013**, *4* (23), 4026–4031.
- (209) Lagrost, C.; Jouini, M.; Tanguy, J.; Aeiya, S.; Lacroix, J. ; Chane-Ching, K. ; Lacaze, P. . *Electrochimica Acta* **2001**, *46* (26–27), 3985–3992.
- (210) Heinze, J.; Frontana-Urbe, B. A.; Ludwigs, S. *Chem. Rev.* **2010**, *110* (8), 4724–4771.
- (211) Poly(3,4-ethylenedioxythiophene) and Its Derivatives: Past, Present, and Future [https://www.researchgate.net/publication/237360890\\_Poly34-ethylenedioxythiophene\\_and\\_Its\\_Derivatives\\_Past\\_Present\\_and\\_Future](https://www.researchgate.net/publication/237360890_Poly34-ethylenedioxythiophene_and_Its_Derivatives_Past_Present_and_Future).
- (212) Murakami, T. N.; Grätzel, M. *Inorganica Chim. Acta* **2008**, *361* (3), 572–580.
- (213) Park, B.; Pazoki, M.; Aitola, K.; Jeong, S.; Johansson, E. M. J.; Hagfeldt, A.; Boschloo, G. *ACS Appl. Mater. Interfaces* **2014**, *6* (3), 2074–2079.
- (214) Ellis, H.; Vlachopoulos, N.; Häggman, L.; Perruchot, C.; Jouini, M.; Boschloo, G.; Hagfeldt, A. *Electrochimica Acta* **2013**, *107*, 45–51.
- (215) Wang, H.; Sun, K.; Tao, F.; Stacchiola, D. J.; Hu, Y. H. *Angew. Chem.* **2013**, *125* (35), 9380–9384.
- (216) Li, Y.; Chang, Y.; Zhao, Y.; Wang, J.; Wang, C. *J. Alloys Compd.* **2016**, *679*, 384–390.
- (217) Wang, H.; Wei, W.; Hu, Y. H. *Top. Catal.* **2014**, *57* (6–9), 607–611.
- (218) Maiaugree, W.; Lowpa, S.; Towannang, M.; Rutphonsan, P.; Tangtrakarn, A.; Pimanpang, S.; Maiaugree, P.; Ratchapolthavisin, N.; Sang-aroon, W.; Jareenboon, W.; Amornkitbamrung, V. *Sci. Rep.* **2015**, *5*, 15230.
- (219) Snaith, H. J.; Moule, A. J.; Klein, C.; Meerholz, K.; Friend, R. H.; Grätzel, M. *Nano Lett.* **2007**, *7* (11), 3372–3376.
- (220) Anderson, P. A. *Phys. Rev.* **1959**, *115* (3), 553–554.
- (221) Vamvounis, G.; Glasson, C. R.; Bieske, E. J.; Dryza, V. *J Mater Chem C* **2016**, *4* (26), 6215–6219.
- (222) Hara, K.; Sato, T.; Katoh, R.; Furube, A.; Ohga, Y.; Shinpo, A.; Suga, S.; Sayama, K.; Sugihara, H.; Arakawa, H. *J. Phys. Chem. B* **2003**, *107* (2), 597–606.
- (223) Ghadiri, E.; Zakeeruddin, S. M.; Hagfeldt, A.; Grätzel, M.; Moser, J.-E. *Sci. Rep.* **2016**, *6* (1).
- (224) Ardo, S.; Meyer, G. J. *Chem Soc Rev* **2009**, *38* (1), 115–164.
- (225) Haque, S. A.; Park, T.; Holmes, A. B.; Durrant, J. R. *ChemPhysChem* **2003**, *4* (1), 89–93.

- (226) Mozer, A. J.; Panda, D. K.; Gambhir, S.; Winther-Jensen, B.; Wallace, G. G. *J. Am. Chem. Soc.* **2010**, *132* (28), 9543–9545.
- (227) Boschloo, G.; Hagfeldt, A. *J. Phys. Chem. B* **2005**, *109* (24), 12093–12098.
- (228) Liang, L.; Dai, S.; Hu, L.; Kong, F.; Xu, W.; Wang, K. *J. Phys. Chem. B* **2006**, *110* (25), 12404–12409.
- (229) Benkstein, K. D.; Kopidakis, N.; van de Lagemaat, J.; Frank, A. J. *J. Phys. Chem. B* **2003**, *107* (31), 7759–7767.
- (230) Koide, N.; Islam, A.; Chiba, Y.; Han, L. *J. Photochem. Photobiol. Chem.* **2006**, *182* (3), 296–305.
- (231) Piotrwiak, P. *Solar Energy Conversion: Dynamics of Interfacial Electron and Excitation Transfer*; Royal Society of Chemistry, 2013.
- (232) Fulay, P. P.; Lee, J.-K. *Electronic, Magnetic, and Optical Materials, Second Edition*; CRC Press LLC, 2016.
- (233) Wang, Z.-S.; Yamaguchi, T.; Sugihara, H.; Arakawa, H. *Langmuir* **2005**, *21* (10), 4272–4276.
- (234) Kiebooms, R.; Menon, R.; Lee, K. In *Handbook of Advanced Electronic and Photonic Materials and Devices*; Nalwa, H. S., Ed.; Academic Press: Burlington, 2001; pp 1–102.
- (235) Boschloo, G.; Hagfeldt, A. *Inorganica Chim. Acta* **2008**, *361* (3), 729–734.

## **Chapter II**

**Influence of D- $\pi$ -A Organic Dyes Structures on TiO<sub>2</sub>**

**based s-DSSCs Performances**

Recently, the influence of molecular structures of different dyes on the photovoltaic performances of s-DSSCs was investigated<sup>[1]</sup>, more precisely on the *in-situ* PEP process used to produce the HTM performed in organic medium. In this chapter, a series of commercially available D- $\pi$ -A organic dyes including **LEG4**, **D35**, **L1**, **BA504**, **BA741** and **RK1** are studied in order to determine the promising fragment of the dye structure: *i.e.* donor, linker, and acceptor residues that have an efficient contribution on the *in-situ* PEP process to produce conducting polymer (CP) used as HTM both in organic and in aqueous media and hence on the performances of the s-DSSCs. Some of these dyes were previously used in s-DSSCs. Indeed, **L1** dye was first used in DSSC<sup>[2]</sup> based on liquid electrolyte yielding 2.75 % and thereafter was included in s-DSSC based spiro-OMeTAD<sup>[3]</sup> where efficiency was 2.1 %. For **LEG4** dye, the maximum efficiencies are reported to be 7.11 % and 5.2 % for s-DSSCs based on PEDOT as HTM generated by *in-situ* PEP in organic and aqueous media respectively<sup>[1,4]</sup>. Regarding **D35**, the devices yielded to 4.6 % and to 3.8 % for the same HTM produced in organic and aqueous media respectively<sup>[4]</sup>. To date, none of the other three dyes were investigated in s-DSSCs even in conventional DSSCs, except **RK1**. Indeed, **RK1** dye was recently included in DSSC based on liquid and ionic liquid and gave a high power conversion efficiency of 10.2 % and 7.36 % respectively<sup>[5]</sup>.

Therefore, these dyes will be tested in s-DSSCs based on *in-situ* generated PEDOT in two different media: organic and aqueous one. Prior to report on s-DSSCs results based on these different dyes, we will present in detail the techniques used and the components that constitutes the s-DSSCs studied in this thesis work.

## **II. 1. Generalities and Material used in s-DSSCs**

### **II. 1. a. TiO<sub>2</sub> Photo-anode: Preparation Methods**

As mentioned in the previous Chapter, the photo-anode includes a transparent conducting oxide (FTO) and a metal semiconductor oxide, here TiO<sub>2</sub>, deposited at first as blocking layer on which a second as mesoporous layer is lying. In the literature, different methods have been developed to prepare the mesoporous and the blocking layers, and the most commonly employed are: the

chemical spray pyrolysis deposition technique for blocking layer and doctor blade technique for the mesoporous one.

### **II.1.a.(i) TiO<sub>2</sub> blocking layer**

To minimize the current loss caused by charge carrier recombination between the FTO conducting substrate and the HTM, a compact layer of TiO<sub>2</sub> is deposited as a blocking layer on top of FTO glass substrate. TiO<sub>2</sub> blocking layer can be made either by physical methods including dip coating<sup>[6]</sup>, spin coating<sup>[7]</sup>, and physical vapor deposition (PVD)<sup>[8]</sup> or by chemical methods including chemical vapor deposition (CVD)<sup>[9]</sup>, sol-gel coating<sup>[10]</sup>, atomic layer deposition (ALD)<sup>[11]</sup>, electrochemical deposition (EPD)<sup>[12]</sup> and spray pyrolysis method<sup>[13,14]</sup>. The last three methods were compared and each of the resulting TiO<sub>2</sub> blocking layer films were characterized by cyclic voltammetry (CV) and by electrochemical impedance spectroscopy<sup>[15]</sup>. The film prepared by spray pyrolysis was found to be more competitive than ALD and EPD in s-DSSCs, therefore it is claimed that this method is the most effective. In s-DSSCs based on *in-situ* produced CP, the blocking layer is generally deposited by spray pyrolysis<sup>[4,16–18]</sup>. In this technique, pioneered by Chamberlin and Skarman in 1966<sup>[19]</sup>, a precursor solution is pulverized by means of spray pen with nitrogen gas flow on the substrate subjected to high temperature. Hence, the solution droplets react with the substrate resulting in the direct solvent evaporation and the formation of the desired nanoporous metal oxide<sup>[20]</sup>. This method will be applied to prepare the blocking layer in our studies (see experimental section II.2.a).

### **II.1.a.(ii) TiO<sub>2</sub> mesoporous layer**

The crystalline mesoporous TiO<sub>2</sub> layer is the framework supporting a monolayer of photosensitive dye. Therefore the following parameters of the mesoporous layer must be taken in consideration: (i) the active layer thickness, (ii) the particle size, (iii) the pore size (iv) the surface area and (v) the roughness. Typically TiO<sub>2</sub> mesoporous layer consists of spherical particles with diameter of 20 nm and the optimal thickness was reported to be 10  $\mu$ m for DSSC<sup>[21–23]</sup> in order to have simultaneously a maximum absorption from the dye and a high charge collection efficiency ( $\eta_{\text{coll}}$ ). Indeed when the thickness increases from 2  $\mu$ m to 10  $\mu$ m, the amount of light absorbed increases from 55 % to 98 % considering the absorption coefficient at 520 nm<sup>[24]</sup>. To get an excellent charge collection efficiency  $\eta_{\text{coll}}$  the electron diffusion length ( $L_n$ ) must be larger than the TiO<sub>2</sub> film thickness ( $d$ ) and knowing that  $L_n$  is approximately 100  $\mu$ m, the charge collection

efficiency is approximately 1 [25,26], in other words, the electron transport lifetime ( $\tau_n$ ) must be larger than the electron transport time ( $\tau_{tr}$ ):

$$\eta_{coll} = \frac{1}{1 + \tau_{tr}/\tau_n} \quad (\text{II-1})$$

$$L_n = \left(\frac{D_n}{\tau_n}\right)^{\frac{1}{2}} \quad (\text{II-2})$$

$D_n$  is the chemical diffusion coefficient expressed as:

$$D_n = \frac{d^2}{C \times \tau_{tr}} \quad (\text{II-3})$$

C is a constant on average equal to  $2.5 \pm 0.2$  [25,27] depending on the absorption coefficient of the film and on the illumination direction [28]. The pore size is about 20 nm [23,29].

TiO <sub>2</sub> mesoporous layer	Active layer thickness ( $\mu\text{m}$ )	Particle size (nm)	Pore size (nm)	Surface area ( $\text{m}^2 \cdot \text{g}^{-1}$ )
DSSC	10	20	20	80
s-DSSC	7	20	24	60

**Table II-1:** Optimal mesoporous TiO<sub>2</sub> properties to get an efficient DSSC or s-DSSC.

For s-DSSCs based CP obtained by *in-situ* PEP process, the thickness of the mesoporous layer is below 7  $\mu\text{m}$  [18,30,31] and the pore size is 24 nm [32] in order to have an effective pore filling (Table II-1). Various processes have been used to deposit the mesoporous layer in order to control the morphology, the size and the uniformity. Among them, the doctor-blade coating similar to slot die coating has emerged as the most suitable method. Therefore, doctor-blade technique will be used for the preparation of the mesoporous layer used in our s-DSSCs.

## **II. 1. b. LEG4, D35, L1, BA504, BA741 and RK1 D- $\pi$ -A Organic Dyes Structure Overview and Sensitization Step**

### **II.1.b.(i) Organic Dyes Structure**

All these organic dyes have the common feature to hold the triphenylamine (TPA) core as electron donating group on their D- $\pi$ -A structure. The non-planarity of TPA avoids the aggregation of dyes generally attributed to the disturbance of the  $\pi$ - $\pi$  stacking. The molecular structures of the dyes used in this work are shown in Figure II-1.



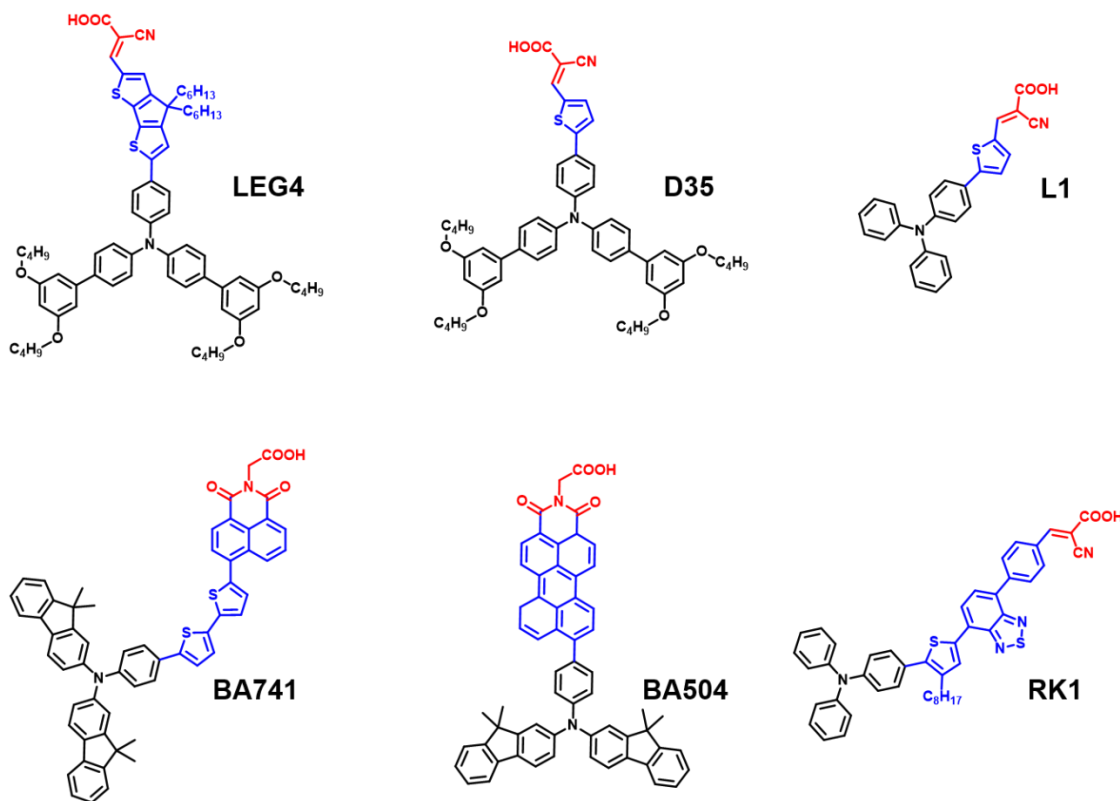


**Figure II-1:** Molecular structure of LEG4, D35, L1, BA741, BA504, and RK1 organic dyes consisting of a donor (black), a bridge (blue), and an acceptor (red).

The molecular structure of **L1** is constituted of the three basic moieties: TPA as donor, thiophene as linker and cyanoacrylic acid as acceptor. **D35** is obtained by *para*-substituted the 1,3-dibutoxy-5-methylbenzyl side chains on each of the two phenyl rings of TPA core. In this dye the butoxyl chains are used for reducing the charge recombination between the hole transport material (HTM) and the oxide semiconductor<sup>[33]</sup> on which the dye is adsorbed. **LEG4** has a similar structure to **D35** except that the thiophene linker is replaced by a cyclopentadithiophene derivative. As mentioned in Chapter 1, the hydrophobic alkyl chains on this linker prevent the close contact between the HTM and the oxide semiconductor.

In **RK1** dye, the thiophene linker of **L1** is replaced by a dissymmetric linker that embeds an alkylthiophene, a phenyl ring and a benzothiadiazole. As reported by Haid *et al.*<sup>[34]</sup> benzothiadiazole acts as electron withdrawing unit which should stabilize the dye radical cation and decrease recombination rate. Moreover the presence of phenyl ring between the anchoring group and the benzothiadiazole resulted in a higher photocurrent.

All these four dyes possess a carboxylic acid group as anchoring moiety and the nitrile functional group as electron withdrawing unit.

In **BA504** and **BA741** dyes, the electron withdrawing unit is a dicarboximide. For both, the presence of fluorene moiety in each side of the TPA constitutes the donor part. For **BA741** dye the linker is a 2,2'-bithiophene-5-naphthalene; whereas for **BA504**, the linker is a perylene moiety. These two dyes have the benefit to hold an extended conjugated linker and fluorene groups in the donor part, therefore they should absorb at high wavelength region with a high molar extinction coefficient.

### II.1.b.(ii) Sensitization Step: Dye-loading

The sensitization of the TiO<sub>2</sub> film by the organic dyes is usually carried out through dipping process to ensure an efficient adsorption of dye molecules by means of the anchoring group. The dye-loading time ranges from 30 min to 20 h depending on the dye structure.

### II. 1. c. Conducting Polymer as Hole Transporting Material

	Conducting polymer	Conductivity in doped state (S.cm <sup>-1</sup> )	E <sub>g</sub> (eV)
<b>No heteroatom</b>	Trans-Polyacetylene	10 <sup>5</sup> [35]	1.5
	Poly(p-phenylenevinylene)	3-5 × 10 <sup>3</sup>	2.5
<b>Nitrogen containing</b>	Polypyrrole	400	3.1
	Polycarbazole	1.3 × 10 <sup>-3</sup> [36]	3.65 [37]
	Polyaniline	200	3.2
<b>Sulfur containing</b>	Polythiophene	10 <sup>3</sup>	2.04 [38]
	Poly(3,4- ethylenedioxythiophene)	550 [39]	1.6 - 1.7
<b>Oxygen containing</b>	Polyfuran	1 [40]	2.4 [40]

**Table II-2:** Electrical properties of some of conducting polymer.

Since Shirakawa *et al.* discovered the unusual properties of polyacetylene, derived from the combination of metallic and polymeric properties<sup>[41]</sup>, a new field of material science has emerged: the organic conducting polymers (CPs) field recognized by the Nobel committee in 2000<sup>[42]</sup>. At present, more than 25 CPs have been synthesized (Table II-2) and most of them have

been tailored in a variety of devices such as batteries, supercapacitors, light emitting diodes, sensors, and solar cells, according to their specificities. Generally, CPs are highly conductive, they exhibit very good optical properties, they are flexible, they can be made biocompatible, biodegradable and porous<sup>[43]</sup> and they are easy to produce. Indeed, they can be synthesized by different methods, among them, the chemical and the electrochemical methods are the most widely employed. The latter has the advantage to produce the electroactive film directly on the conductive electrode surface with a good adhesion; therefore it is suitable for solar cells application.

### II.1.c.(i) Conducting polymers properties

In a  $\pi$ -conjugated polymer, the carbon chain must have a conjugated structure ( $\sigma$ - $\pi$  or/and  $\sigma$ -n alternations). The  $\pi$ -electrons are highly delocalized, through the continuous p-orbital overlap along the polymer backbone, resulting in good electrical behavior. The electrical conductivity of a CP can be further improved by the presence of a heteroatom as for polythiophene, polyaniline or PEDOT.

To become intrinsically conductive, the CP is doped leading to higher conductivity. In case of polyacetylene, when it is not doped, the electrical conductivity is reported to be at  $10^{-9}$  S.cm<sup>-1</sup> (in *trans* configuration)<sup>[44]</sup> similarly to the conductivity of insulators. Whereas in doped form the conductivity reaches  $10^5$  S.cm<sup>-1</sup> <sup>[41]</sup> a value reported for metals (see Figure II-2).

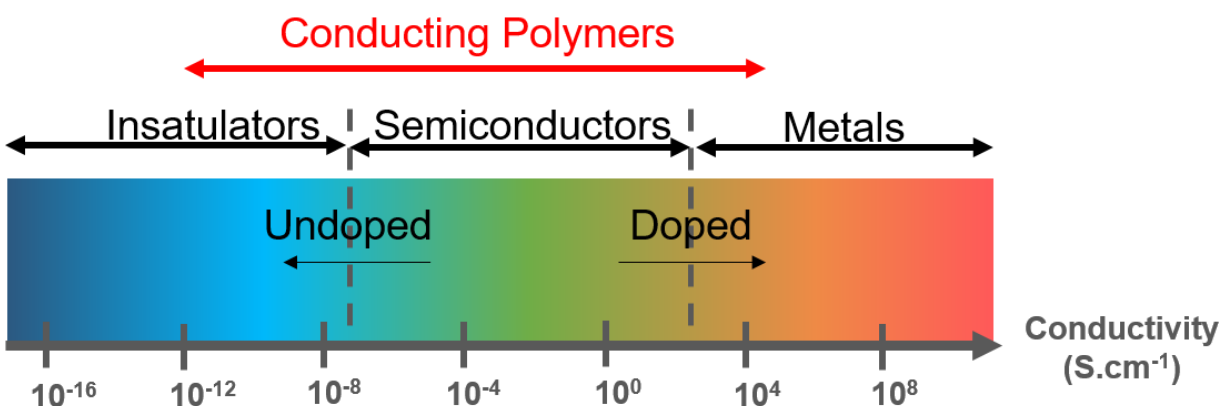


**Figure II-2:** Conductivity range of conducting polymer.

The doping process for CPs is different with respect to the doping process of inorganic materials. It introduces free charges carriers (electrons or holes) and subsequently introduces counter ions known as dopants to maintain the electroneutrality of the system.

The electrical properties of these CPs are determined by their electronic structures according to the valence band theory, as explained in Chapter 1. The interactions between the p-orbitals of the atoms constituting the polymer chain lead to binding MO at lower energy state and anti-bonding MO at higher energy state. As the polymer contains a large number of linked monomer, the energy levels merge into continuous bands known as VB and CB. Since the energy distance between HOMO and LUMO does not disappear completely, the band structure of the conjugated polymers is similar to the intrinsic semiconductor having a narrow bandgap. Moreover the more the system is conjugated the lower the energy bandgap  $E_G$  will be. In contrast, conventional polymers have a wide bandgaps as for insulators.

For conducting polymers, the doping process introduces additional energy levels changing the energy bandgap and the dopant can either takes electrons from HOMO (p-doping) or adds electrons to the LUMO (n-doping). These conducting polymers having these charge defects are assimilated to:

- polaron (radical cation/anion) when an electron is removed or added, this configuration corresponds to two new electronic states in the forbidden band.
- bipolaron (carbocation, carboanion) when an additional electrons is removed or added;
- soliton (free radical, carbanion, carbocation) when a single electronic state located in the middle of the forbidden band appears (Figure II-3).

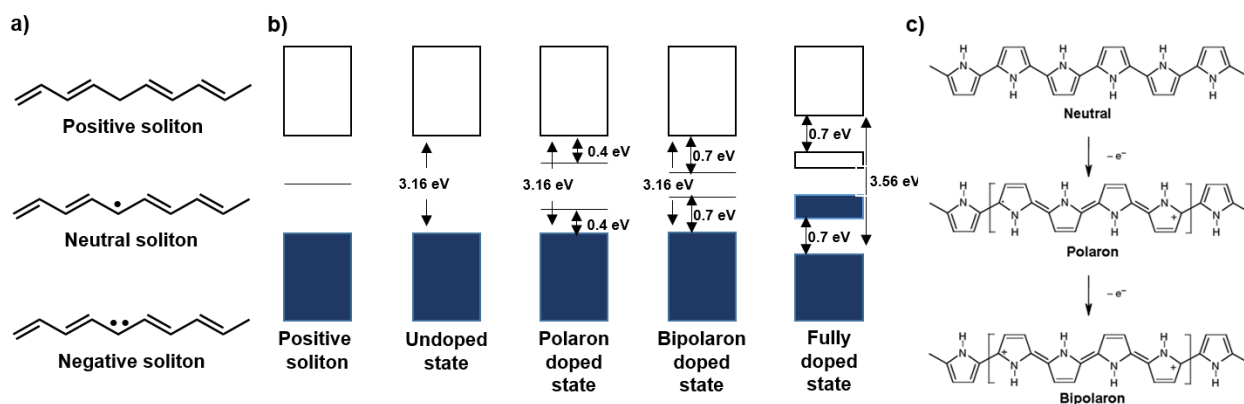


**Figure II-3:** Structure of the (a) trans-polyacetylene (c) polypyrrole taken from ref. [45] in different doped state and (c) their relative schematic electronic energy diagram.

Therefore, when CPs are doped, the charge carriers density and mobility are increased and finally the conductivity is improved (Equation I-5, Chapter I).

Regarding their optical properties, the  $E_G$  values of most undoped and doped conjugated polymers are in the range 1.5-3.0 eV<sup>[46]</sup> so they behave as semiconductors. The optical absorption is red-shifted for polymers having a lower bandgap. Interestingly, in doped form, this absorption band has a lower intensity in the visible region as shown in Figure II-4.

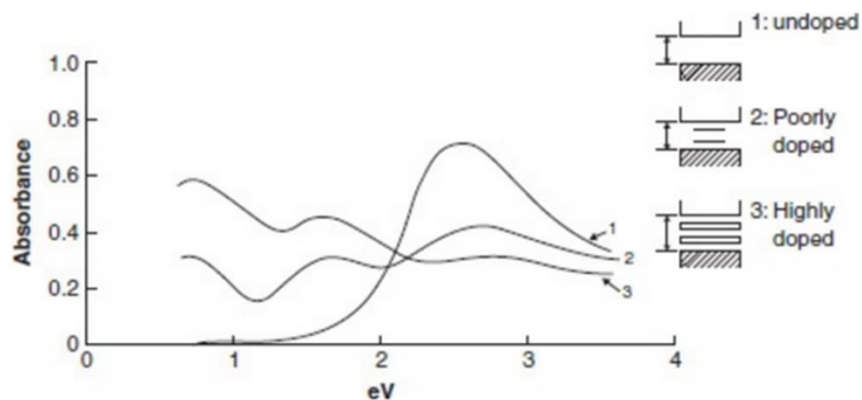


**Figure II-4:** Optical absorption spectra of polythiophene doped with different amount of ClO<sub>4</sub><sup>-</sup> compared to the same undoped polymer form. Figure taken from ref. [47].

This intensity can be further decreased either by increasing the amount of dopant or by modifying the nature of dopant<sup>[48]</sup>. Moreover, new absorption bands appear in the NIR region owing to the electronic transitions from the HOMO to the new state within the bandgap created by doping process. Therefore CPs in doped form are lightly colored and large part of them are transparent<sup>[49]</sup>.

The doping process occurs during the conjugated polymer synthesis and can be carried out chemically or electrochemically. In this work, only the electrochemical methods are considered where the doping process corresponds to oxidation in case of p-doping or reduction in the case of n-doping. In s-DSSCs, when the dye sensitizer is excited, the charge carriers are generated, electrons are transferred in the n-type oxide semiconductor, *e.g.* TiO<sub>2</sub>, and holes are transferred in p-type material, *e.g.* HTM, to enable the regeneration of the dye (cf. Chapter I). Therefore, the CP used as HTM will be produced by anodic electropolymerized through oxidation process of organic monomers.

### II.1.c.(ii) Anodic Electropolymerization

The electrochemical polymerization, first developed by Diaz *et al.* <sup>[50,51]</sup>, is carried out in a single compartment electrochemical cell where the polymer precursor (organic monomer) and the doping agent are dissolved in the solvent, constituting the electrolytic solution. The film

preparation can be performed either potentiostatically (*i.e.* constant voltage condition) or galvanostatically (*i.e.* constant current). In both conditions, the resulting conducting polymer is deposited on the working electrode (WE) surface and the dopant anions compensate the positive charges of the polymer produced during the electrochemical oxidation. The electropolymerization reaction starts by producing, at first, monomer radical cations followed by the formation of dimers through the radical-radical coupling reaction. Then the electrochemical oxidation of dimers results in the formation of oligomers after the radical-radical coupling reaction. This is followed by the growth process leading to oligomers with higher molecular weight. The solubility decreases progressively with the increase of the chain length which drives the polymer to be deposited on the WE. The conducting polymer properties depend on the deposition charge, time, temperature, solvent, doping agent and the electrode system<sup>[43]</sup>.

### **II.1.c.(iii) Charge transport**

The obtained polymer chains form a cross-linked network, so the charge carriers diffuse inside the polymer network in two directions:

- along the polymer intrachain called charge propagation
- between neighboring polymer chains, known as charge hopping as explained by Chan *et al.*<sup>[52]</sup>

The second mechanism is the most dominant for charge transport<sup>[53]</sup> process in CPs and further enhances the conductivity of the CP due to the higher mobility of charge carriers within the polymer network.

### **II.1.c.(iv) PEDOT**

Remarkably PEDOT polymer material, first synthesized electrochemically in the late 80s by Jonas and coworkers from Bayer company<sup>[54]</sup>, ranks among the top performing CPs. Indeed, this CP offers the advantages of being highly conductive, highly stable, optically transparent, having a lower energy bandgap (1.6-1.7 eV) and a low oxidation potential<sup>[55-58]</sup>. The influence of the dopants in PEDOT has been investigated and it was shown that the conductivity decreases with the following anion sequence  $\text{ClO}_4^- > \text{BF}_4^- > \text{CF}_3\text{SO}_3^- > \text{PF}_6^-$ <sup>[59]</sup>. Moreover PEDOT, which is formed from EDOT, has been also produced from Bis-EDOT monomer<sup>[57]</sup>. The latter oxidizes at lower potential so the electropolymerization is easier on the WE.

Thanks to its unique properties, PEDOT is used in various devices. In our s-DSSCs, PEDOT will be used as HTM and it will be generated by *in-situ* photo-electrochemical polymerization of EDOT and Bis-EDOT.

## II. 1. d. The *In-situ* Photo-Electrochemical Polymerization Process of Conducting Polymers

### II.1.d.(i) *In-situ* PEP Operating Principle

Fujishima *et al.*<sup>[60]</sup> produced the first CP by photo-electrochemical polymerization. The system setup is similar to electrochemical polymerization except that, by means of light, the monomer in solution is polymerized. Based on this work, the group of Yanagida developed a new variant technique called *in-situ* photo-electrochemical polymerization to form the CP directly on the dyed electrode surface<sup>[61]</sup>. The main driving force of this process is the photosensitizer which is adsorbed on the oxide semiconductor surface: it has a high capacity to harvest light and it may have the ability to oxidize the polymer precursors.

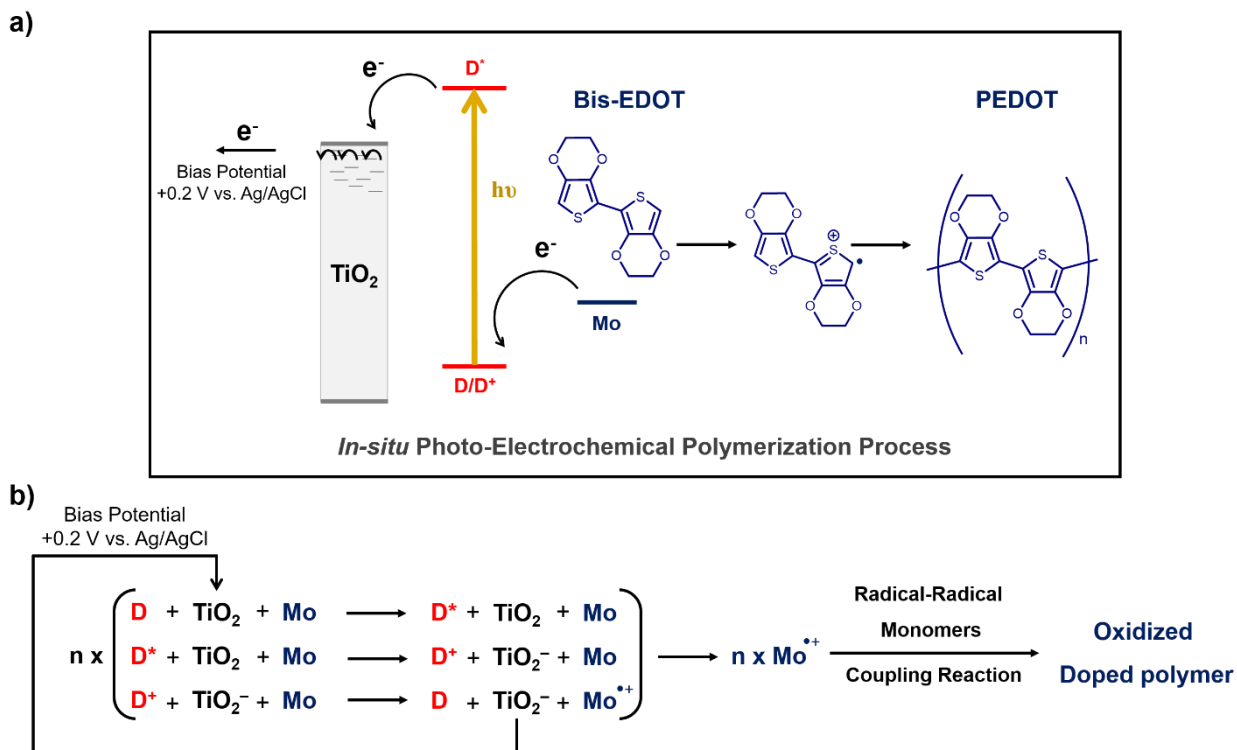


**Figure II-5:** (a) Schematic representation of the operating principle of the *in-situ* PEP process and (b) the associated reaction mechanism.

The operating principle described in Figure II-5 relies on charge transfer processes starting from the (i) excitation of the dye under light irradiation resulting in the formation of an electron-hole pair. (ii) The electron is then injected into the conduction band of the semiconductor leaving behind a hole: the sensitizer is in oxidized state. (iii) The potential of the oxidized dye is sufficiently high to oxidize the monomer in solution leading to a radical cation monomer. (iv) As for anodic electropolymerization, the coupling reaction of the generated radical cations occurs to produce oligomers and polymers on the electrode surface. (v) An external potential is applied, typically between 0.2 V to 0.3 V vs. Ag/AgCl<sup>[30]</sup>, in order to drain the injected electrons from the oxide semiconductor. When the applied potential is too high, the polymerization of the monomer occurs on the substrate even in dark as reported by Yanagida<sup>[62]</sup>. The external potential is one of the factors impacting the *in-situ* PEP. These factors include the type of the monomer precursor's, the dye, the solvent, the type of dopant, and the light irradiation intensity. Each of these factors must be optimized and controlled to achieve highly efficient PEP and hence an efficient s-DSSCs.

#### II.1.d.(ii) *In-situ* PEP Conditions and Optimization

The primary condition to initiate the *in-situ* PEP is the matching of potentials between the oxidation potential ( $E_{ox}(dye)$ ) of the dye and the onset oxidation potential ( $E_{onset,ox}(monomer)$ ) of the monomer precursor. Indeed, the  $E_{ox}(dye)$  must be at more positive potential than the  $E_{onset,ox}(monomer)$  to enable the dye to oxidize the monomer. The variation of the free energy  $\Delta G$  related to this difference of potential, determines the rate of polymerization process and the pore filling inside the mesoporous TiO<sub>2</sub> as reported by Zhang *et al.*<sup>[4]</sup>. Interestingly, compared to the  $E_{onset,ox}$  of common monomers used for *in-situ* PEP, the  $E_{onset,ox}$  of Bis-EDOT is low and the s-DSSCs based on PEDOT obtained with this monomer gave the highest performances<sup>[1]</sup>. However, for other monomers, their polymerization is restricted to few dyes because of their high oxidation potential in organic solvent. To solve this problem, the organic electrolyte, generally used medium for the *in-situ* PEP, has been substituted by an aqueous electrolyte. Indeed, in aqueous solvent and when the monomer is dissolved by means of a surfactant, the oxidation potential of the organic monomers is largely decreased which relies on the work done by the group of Lacaze<sup>[63-65]</sup>. Therefore, the organic electrolyte, generally used for the *in-situ* PEP, has been substituted by aqueous electrolyte when possible. This new approach of PEP developed by



Yang *et al.*<sup>[17]</sup> and Zhang *et al.*<sup>[4]</sup> enables the use of commercial monomers due to the decrease of their oxidation potential value and allows the production of CPs in aqueous medium.

Regarding the dye, it should have a high extinction coefficient and a broad light absorption. This may lead to good contact of the dye with the polymer and to the decrease of interfacial recombination in s-DSSC<sup>[66]</sup>. Another consideration is the nature of the doping anion on the CP which affects the *in-situ* PEP process. It was observed by Xia and coworkers that the *in-situ* PEP is efficient for PEDOT doped with TFSI<sup>-</sup>, and the polymer gave a higher conductivity and higher cell performances compared to PEDOT doped with ClO<sub>4</sub><sup>-</sup><sup>[16]</sup>. This higher conductivity is explained by the higher negative charge delocalization in the TFSI<sup>-</sup> which induces preferred stacking through the transverse PEDOT ring<sup>[67,68]</sup>. The same group has investigated the effect of the length of TFSI derivatives as doping anion<sup>[69]</sup>. They concluded that the pristine TFSI<sup>-</sup> remains the most performant both in the *in-situ* PEP and in s-DSSC. Moreover, the *in-situ* PEP has been studied<sup>[70]</sup> at different light intensities. During the *in-situ* PEP process, when the applied light intensity is high, ( $\geq 0.3$  Sun), less regular PEDOT is produced with shorter chains compared to PEDOT generated under light intensity of  $\leq 0.1$  Sun. Therefore, 0.1 Sun is usually applied to get good quality and highly conductive polymer film.

#### II.1.d.(iii) Analysis

The current-time transient recorded by potentiostatic technique during the *in-situ* PEP process gives information on the nucleation and growth mechanism in contrast to potentiodynamic technique<sup>[71]</sup>. The nucleation can be instantaneous or progressive and there are three types of growth, namely one (1D), two (2D), and three dimensional (3D) processes. For PEDOT the electropolymerization followed the instantaneous nucleation meaning that the number of nuclei is constant and they grow without the formation of further nuclei; the growth followed the 2D and 3D processes meaning that the nuclei preferably grow parallel to the electrode (2D) or both perpendicular and parallel to the electrode (3D) as described by Randriamahazaka *et al.*<sup>[72]</sup>. In the Figure II-6, the current-time transient can be divided in three sections.

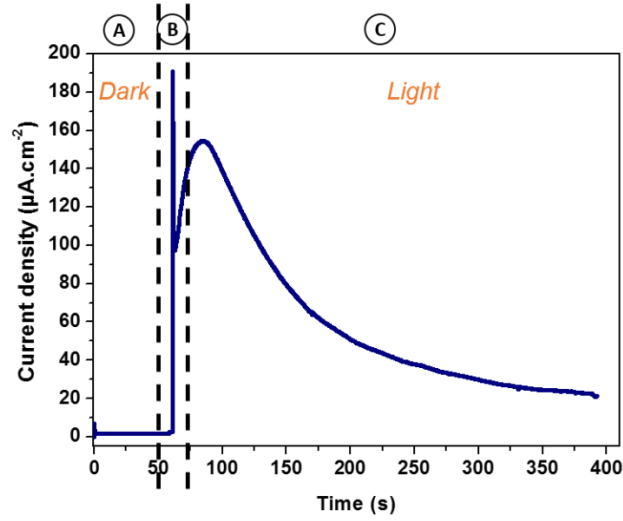


**Figure II-6:** Example of a current-time transient during *in-situ* PEP.

- In the first section A, having imposed a positive potential of 0.2V vs Ag/AgCl with no light at the WE, implies the existence of a potential difference in the WE/solution interface, sufficiently low for the non-oxidation of the monomer and there is no current leakage from the WE as observed previously due to the TiO<sub>2</sub> blocking layer. Therefore, the charge from the WE are only compensated by the Li<sup>+</sup> charges contained in the electrolyte solution which constitutes a double layer capacitance. The interface behaves like a capacitor which induces a capacitive current ( $i_c$ ) (no electron transfer) following an exponential decay:

$$i_c = ke^{-t/RC} \quad (\text{II-4})$$

Where k is a constant, R is the solution resistance, C is the capacitance and t is the time.

- In the section B, when the light is on, an electrochemical reaction occurs, therefore the measured current is a faradic current ( $i_f$ ) (the capacitive current is negligible) governed by the Cottrell equation:

$$i_f = nFAC_m^0 \sqrt{\frac{D_m}{\pi t}} \quad (\text{II-5})$$

Where n is the number of electrons, F is the Faraday constant, A is the area of the electrode,  $C_m^0$  is the initial concentration of the monomer and  $D_m$  is the diffusion

coefficient of monomers. The electrochemical reaction corresponds to the oxidation of monomers. Indeed, the molecules of monomers diffuse from the solution to the pores and to the surface of the dyed TiO<sub>2</sub> electrode and once they are oxidized they return back to the solution.

- Then, in the section C, the measured current corresponds to the nucleation and growth mechanisms. The radical cation monomers couple together until the oligomer reaches a critical size namely nuclei: this is the nucleation or the oligomerization process where the current increases. Then beyond this size, the growth process occurs, and the current decreases progressively until it reaches a current plateau.

### II. 1. e. Additives

The PEDOT/dye/TiO<sub>2</sub>/FTO substrate is treated with some additives to modulate the energetics of the cell components particularly the TiO<sub>2</sub> CB edge in order to enhance the s-DSSC device performances. Adsorption of Li<sup>+</sup> ions from the electrolyte (LiTFSI) to the TiO<sub>2</sub> surface increases the charge injection efficiency of the dye's excited state due to the TiO<sub>2</sub> CB edge to more positive potential<sup>[73–75]</sup>. Therefore the photocurrent density ( $J_{sc}$ ) and IPCE are enhanced. With 4-tert-butyl pyridine (tBP), it was found that the CB edge shift to more negative potential (Figure II-7), which increases the  $V_{oc}$  of the device<sup>[76,77]</sup>.

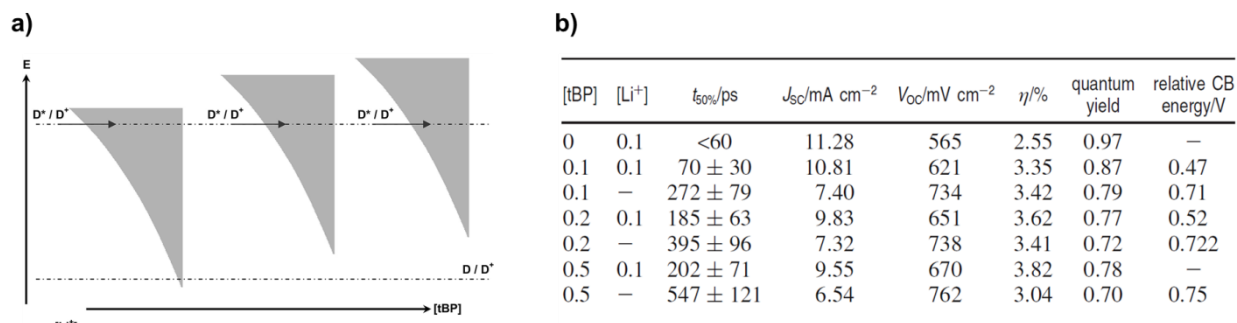


**Figure II-7:** (a) Influence of the additives (tBP and Li<sup>+</sup>) on the energetics of the density of TiO<sub>2</sub> conduction band and (b) photovoltaic performances obtained for a DSSC with different concentration of tBP and Li<sup>+</sup> additives. Figures are taken from ref. [77].

## II. 1. f. Counter-electrode

To complete the s-DSSC, the metallic counter-electrode is deposited through thermal resistance evaporation to get a thin and a homogeneous layer of the CP film. For such devices, the thickness is usually in the range of 30-100 nm for gold and 100-200 nm for silver, in order to reflect back the transmitted light. Gold is preferably used for our s-DSSCs.

## II. 2. Experimental Section

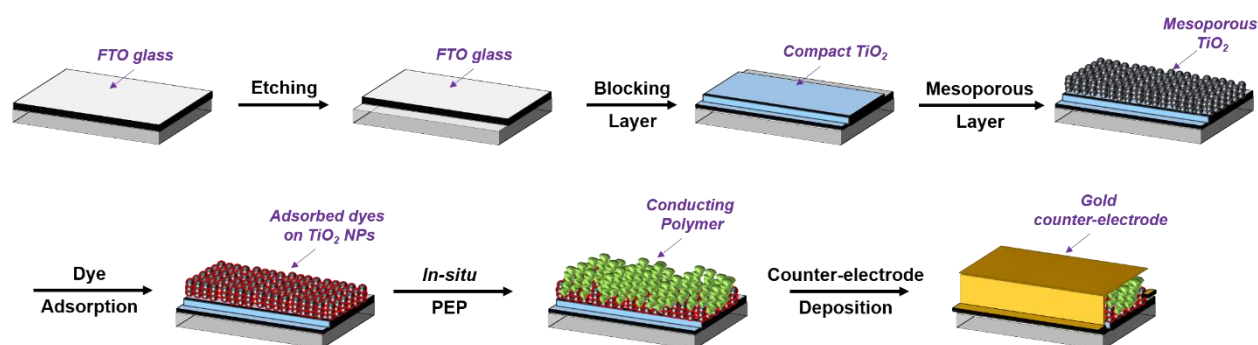


**Figure II-8:** Schematic representation of the different procedural steps to produce a s-DSSC.

Before proceeding to the preparation of TiO<sub>2</sub> electrodes (Figure II-8), the commercial FTO substrates (15  $\Omega$ /sq) were etched to form the desired electrodes pattern with zinc powder and HCl 10 %. Then the substrates were cleaned by successive sonication with soap water, deionized water, acetone, ethanol for 20 min.

### II. 2. a. Preparation of the TiO<sub>2</sub> Photo-anode

#### II.2.a.(i) Blocking layer

The TiO<sub>2</sub> the blocking layer was prepared following the procedure implemented by Cameron and Peter<sup>[78]</sup> and Zhang *et al.*<sup>[4]</sup>. The solution contains the TiO<sub>2</sub> precursors: 0.2 M of titanium isopropoxide and 2 M of acetylacetonate in isopropanol which was sprayed onto the pre-cleaned FTO substrate on the hot plate brought to 500°C (Figure II-9). The thickness should range from 10 nm to 200 nm with an optimum thickness reported to be around 100 nm. Thicker than 100 nm, an additional series resistance is introduced hindering a good electron transport within the TiO<sub>2</sub> layer<sup>[81]</sup>. Thinner than 50 nm, the film is subjected to the formation of cracks allowing charges

recombination. Therefore, to obtain approximately a thickness of 100 nm, 10 cycles of spray pyrolysis have been performed (at spray distance of 5 cm). The coated substrate was heated in air for 20 min and then cooled progressively to room temperature.

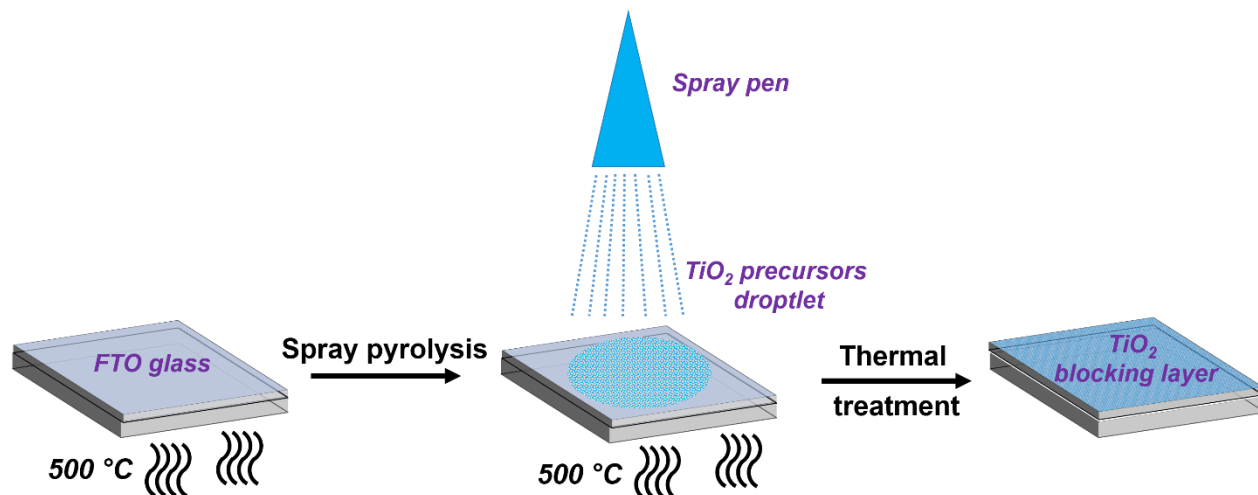


Figure II-9: Schematic representation of spray-pyrolysis technique on FTO substrate.

The film is characterized by the profilometer and SEM; its conductivity is checked by CV. For CV, the measurements are carried out in a single compartment electrochemical cell having three electrodes configuration (a working electrode, WE; a counter electrode, CE; a reference electrode, RE) and containing 0.5 mM K<sub>4</sub>Fe(CN)<sub>6</sub> · 3H<sub>2</sub>O, 0.5 mM K<sub>3</sub>Fe(CN)<sub>6</sub> and 0.5 M KCl in distilled water. The FTO without and with TiO<sub>2</sub> underlayer electrodes are used as WE, saturated calomel electrode (SCE) is the RE and stainless steel grid is the CE. The applied scan rate is 50 mV.s<sup>-1</sup>.

### II.2.a.(ii) Mesoporous layer deposited by doctor-blade technique

A colloidal TiO<sub>2</sub> paste is applied near the top edge of the substrate and by means of a squeegee the slurry is spread along the substrate uniformly as illustrated in Figure II-10.



Figure II-10: Schematic representation of doctor-blade technique on TiO<sub>2</sub> (blocking layer)/FTO substrate.

The thickness of the mesoporous layer is controlled by the scotch tape thickness. The layer is then sintered in an oven with a heating ramp control at up to 500°C: 180°C for 10 min, 320°C for

10 min, 400°C for 10 min, 500°C for half of an hour in air atmosphere, to evaporate and to burn organic compounds (terpineol, ethyl cellulose beads) providing a suitable porosity and to afford a suitable interconnection between TiO<sub>2</sub> particles. The resulting TiO<sub>2</sub> films are subsequently soaked in TiCl<sub>4</sub> aqueous solution at 70°C for 30 min in order to enhance the roughness factor and, consequently, to get a large number of dyes adsorbed on the surface resulting in higher photocurrent<sup>[29]</sup>. The film was characterized by the profilometer, SEM, and by XRD.

### **II. 2. b. Sensitization Step: Dye Adsorption**

For dye sensitization, the TiO<sub>2</sub> electrode films, rinsed with deionized water and ethanol, are annealed by following the same heating ramp procedure detailed above and then were immersed into the 0.2 mM dye solution overnight. The annealing process of the TiO<sub>2</sub> films results in grain growth and hence an increase in crystallinity. Thus, the charge transport is improved. To remove the excess of dye molecules physically adsorbed, the films were rinsed with the respective solvent and dried by a N<sub>2</sub> gas flow. Cyclic voltammetry (CV) experiments for dyes were performed in a one compartment cell where a stainless steel grid is used as CE and Ag/AgCl (3.5 M KCl) as RE. The WE is the dye chemisorbed at mesoporous TiO<sub>2</sub>/FTO without blocking layer (area of 1 cm<sup>2</sup>) to ensure the flow of electrons. These three electrodes were immersed in 0.1 M LiClO<sub>4</sub> in acetonitrile and the applied scan rate is 50 mV.s<sup>-1</sup>. For Bis-EDOT and EDOT monomer, a 3 mm diameter glassy carbon disk with was used as working electrode.

### **II. 2. c. The *In-situ* Photo-Electrochemical Polymerization Process of Conducting Polymers**

In this work, the *in-situ* PEP was carried out in an electrochemical cell where the dye sensitized TiO<sub>2</sub> electrode is used as working electrode, Ag/AgCl (3.5 M KCl) as the reference electrode and stainless steel grid as the counter electrode (see Figure II-11). Two different electrochemical techniques are performed to generate the polymer by *in-situ* PEP: the potentiostatic and the galvanostatic techniques in order to determine the best approach which leads to the best performances in s-DSSCs. The potentiostatic approach has been performed at 0.2 V vs Ag/AgCl in two different media:

- 5 mM Bis-EDOT and 0.1 M LiTFSI in acetonitrile

- 5 mM Bis-EDOT and 0.1 M LiTFSI in 0.05 M Triton X-100 in distilled water

Regarding the galvanostatic approach, the applied current density is fixed at  $15 \mu\text{A}\cdot\text{cm}^{-2}$  and the polymerization lasted for 1300 s to reach total charge of  $20\text{mC}\cdot\text{cm}^{-2}$  (Annex II-1) in the same organic or aqueous micellar media.

Simultaneously, the back side of the working electrode was subjected to an illumination of 0.1 sun by means of a white light provided by a LED lamp (ELFA Distrelec, Light Injector, White, 6000K-6°, 3 W, 4.5 V, 700 mA). The total photo-electrochemical polymerization charge was fixed at  $20 \text{mC}\cdot\text{cm}^{-2}$  in order to make an accurate comparison. The films were washed carefully with acetonitrile and then dried with N<sub>2</sub> flow.

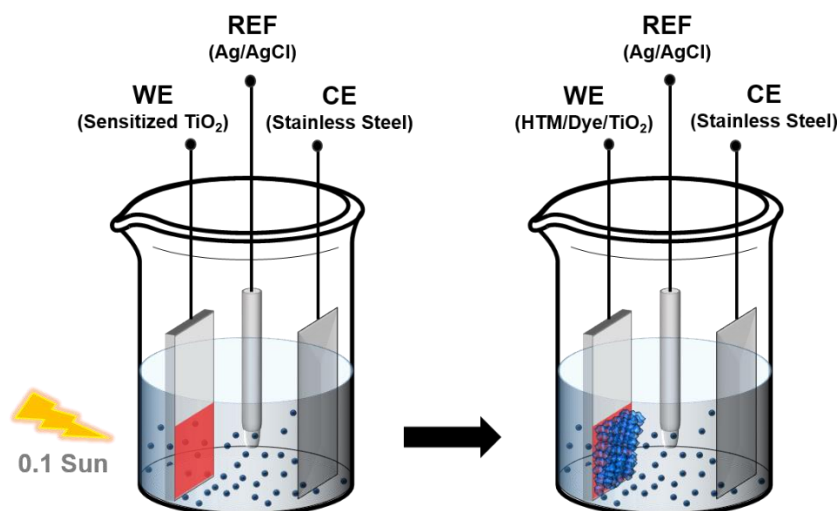


**Figure II-11:** Setup of an electrochemical cell for *in-situ* PEP.

#### II. 2. d. Additives and Counter Electrode

After polymerization, the *in-situ* generated PEDOT films are spin coated with 50  $\mu\text{L}$  of an ionic liquid additive containing tBP:LiTFSI (5:1) in acetonitrile. To complete the s-DSSC device, a 100 nm thick Au counter electrode was deposited onto the PEDOT layer covering the dye sensitized TiO<sub>2</sub> electrode, by thermal evaporation in a vacuum chamber (Leica EM MED020) with a base pressure of about  $10^{-5}$  mbar and with a control coating rate.

## II. 3. Results and Discussion

### II. 3. a. Characterization of the TiO<sub>2</sub> Photo-anode

#### II.3.a.(i) Blocking layer

The thickness of the blocking layer, measured by the profilometer is 100 nm (see Annex II-2) which is in accordance with the analysis obtained by SEM (see Figure II-15 in the next section). The surface morphology depicted by SEM in the Figure II-12 shows clearly the compactness of the TiO<sub>2</sub> NPs aggregates with uniform size.

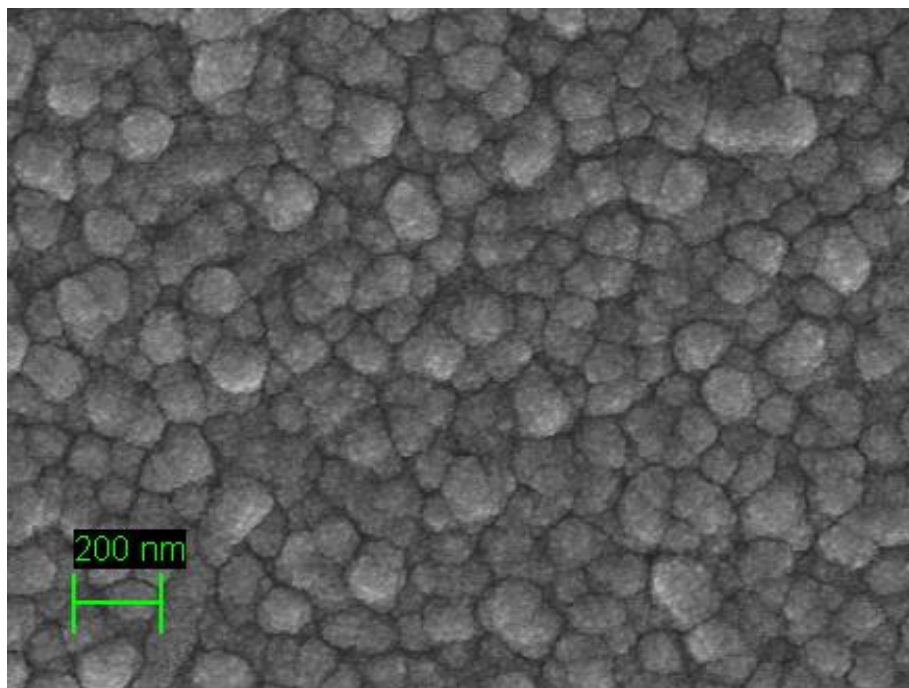


**Figure II-12:** SEM top views of the TiO<sub>2</sub> blocking layer surface deposited on FTO substrate.

To ensure whether this underlayer acts as blocking layer, electrochemical measurements have been performed.



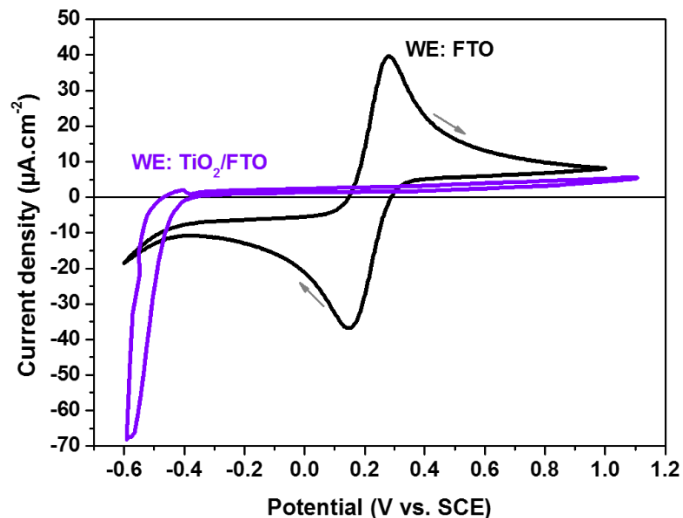


**Figure II-13:** Cyclic voltammograms of the FTO without and with TiO<sub>2</sub> blocking layer.

The Figure II-13 clearly illustrates that in presence of TiO<sub>2</sub> blocking layer, almost no current is detected, compared to pristine FTO surface where the current originates from the oxidation of Fe(CN)<sub>6</sub><sup>4-</sup> and the reduction of Fe(CN)<sub>6</sub><sup>3-</sup>.

### II.3.a.(ii) Mesoporous layer

The annealing process after spreading the TiO<sub>2</sub> paste on the TiO<sub>2</sub> blocking layer/FTO substrate, results in a good mesoporous layer with an aesthetically pleasing white layer as shown in the Figure II-14.

By profilometer (Annex II-2), the measured thickness of the mesoporous layer is approximately 6-7  $\mu\text{m}$ . This is highly consistent with the SEM images (Figure II-15). The doctor blade technique provided a layer of homogenous thickness layer composed of 20nm TiO<sub>2</sub> NPs and the thermal treatment provided a good porosity.

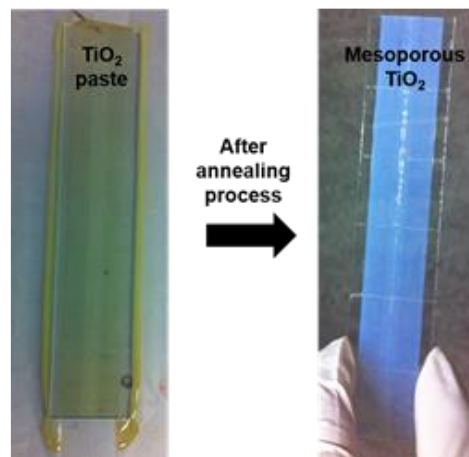


**Figure II-14:** Photographs of the mesoporous TiO<sub>2</sub> layer before (left) and after (right) the annealing process.

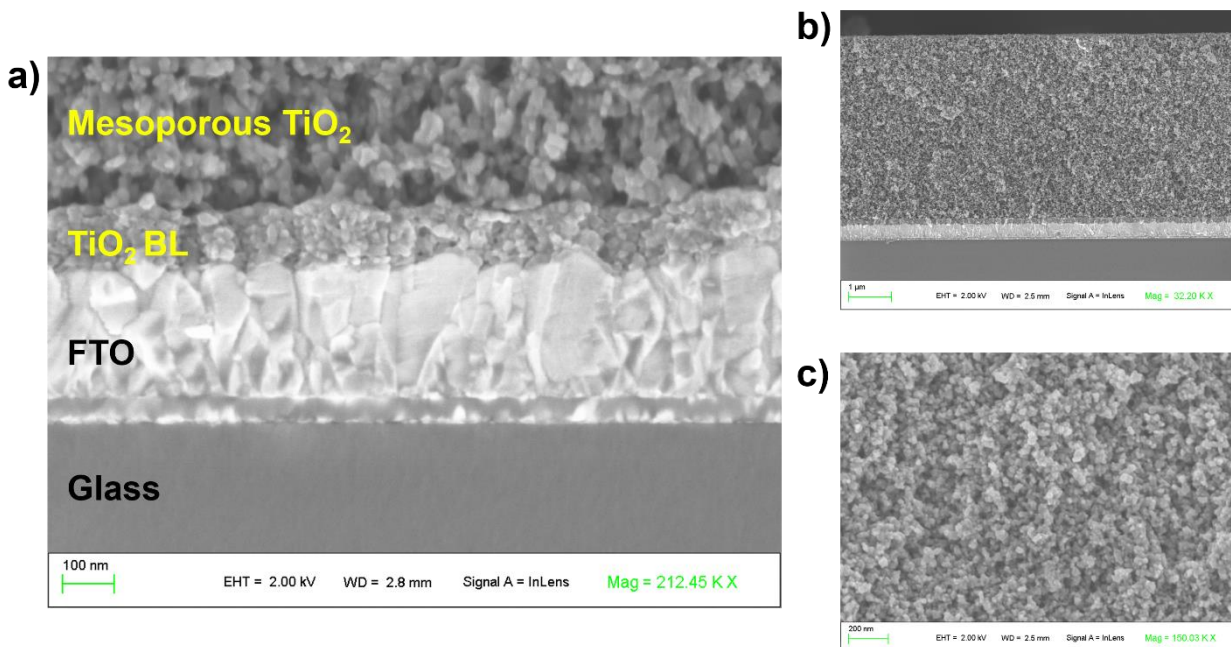


**Figure II-15:** Cross sectional SEM views of TiO<sub>2</sub> (blocking layer + mesoporous layer) deposited on the FTO substrate (a) with 100  $\mu\text{m}$  scale bar (b) with 1  $\mu\text{m}$  scale bar. And (c) top-view of the mesoporous TiO<sub>2</sub> layer.

The cross-section view of the substrate of TiO<sub>2</sub> (blocking layer + mesoporous layer) on FTO highlights the difference between the two TiO<sub>2</sub> layers: for the underlayer, TiO<sub>2</sub> NPs are more compact than that for the mesoporous layer (Figure II-15). The pores size has been determined to be approximately 30 nm by XRD, suitable for s-DSSC (see Annex II-3).

### II. 3. b. Properties of LEG4, D35, L1, BA504, and BA741 Dyes

#### II.3.b.(i) UV-Visible spectroscopy in solution

The UV-Vis absorption spectra of dyes are measured in DCM ( $C = 2.7 \times 10^{-5} \text{M}$ ) over a range of 350 to 750 nm as shown in the Figure II-16. Generally, the absorption bands of dyes located in the UV region are assigned to the  $\pi$ - $\pi^*$  transition of the conjugated system. The UV-Vis spectrum of **L1** shows one band at 432 nm, which is assigned to the intramolecular charge transfer (ICT), from the TPA to the cyanoacrylic acid acceptor. This ICT band is significantly red-shifted in the case of **D35** and the extinction coefficient is enhanced ( $\epsilon = 45000 \text{ mol}^{-1} \cdot \text{L} \cdot \text{cm}^{-1}$ ) by a factor of 2 with respect to that of **L1** ( $\epsilon = 23000 \text{ mol}^{-1} \cdot \text{L} \cdot \text{cm}^{-1}$ ), owing to the alkoxy side chains para-substituted onto the TPA core ( $\lambda_{\text{max}} = 491 \text{ nm}$ ). For **LEG4**, the ICT band is further

red-shifted ( $\lambda_{\text{max}} = 532 \text{ nm}$ ) and shows the highest  $\epsilon$  value of  $49438 \text{ mol}^{-1} \cdot \text{L} \cdot \text{cm}^{-1}$  compared to other dyes, owing to the more extended conjugation system in the linker part. This value is fairly similar to that reported in the literature<sup>[3]</sup>. Similarly the extended conjugation in the  $\pi$ -spacer of **RK1** causes the red-shift of the ICT band to  $478 \text{ nm}$  with an increase in  $\epsilon$  value (about 1.3 fold) compared to **L1**. However these values are slightly lower than those for **D35** both in wavelength and in intensity. The steric hindrance of alkoxy side chains in the donor part of **D35**, limits dyes aggregation and hence affects strongly the ICT band. This steric hindrance seems to play a more important role in the red shift of the ICT band than the conjugation extends in the spacer.

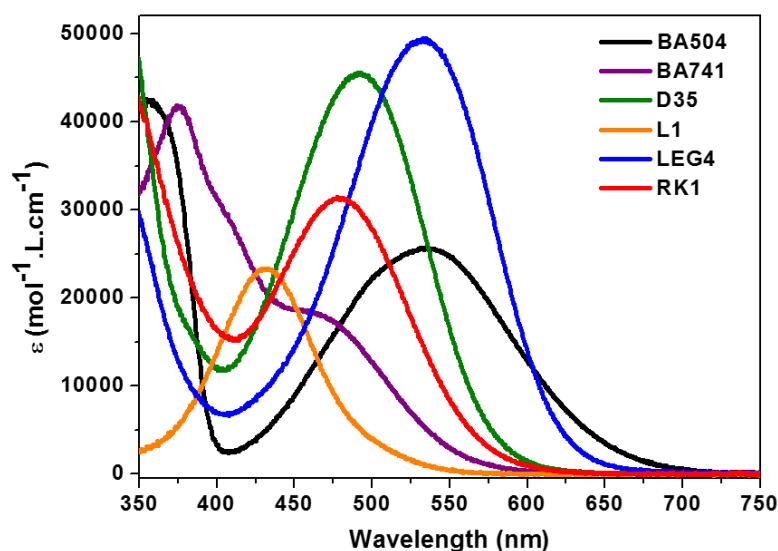


**Figure II-16:** UV-Visible absorption spectra of the organic dyes in DCM ( $C = 2.7 \times 10^{-4} \text{ M}$ ).

For **BA504**, a broad band is recorded from 400 to 700 nm which may rise from the high conjugated perylene  $\pi$ -spacer and the ICT band emerges at  $\lambda = 538 \text{ nm}$  which is the highest maximum wavelength. This high absorption wavelength originates from the electronic push from the strong conjugated fluorene donor to the dicarboximide withdrawing unit within the D- $\pi$ -A structure. For **BA741** the ICT band is dramatically blue-shifted ( $\lambda_{\text{max}} = 466 \text{ nm}$ ) and appears as a broad shoulder. In this dye the linker is weakly conjugated with respect to **BA504** and the measured  $\epsilon$  is 1.4 lower.

The molar extinction coefficients at the maximum absorbance for the different dyes are in the following order:

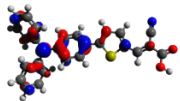
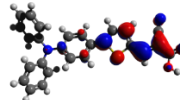
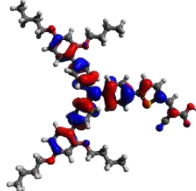
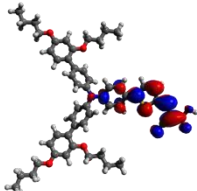
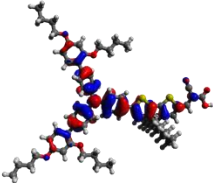
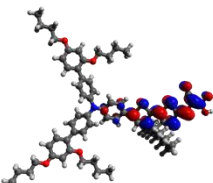
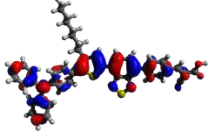
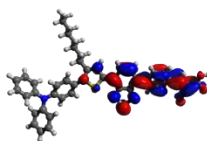
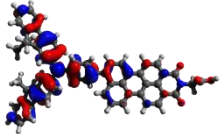
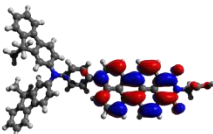
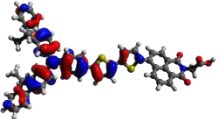
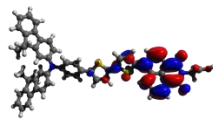
$$\epsilon(\text{LEG4}) > \epsilon(\text{D35}) > \epsilon(\text{RK1}) > \epsilon(\text{BA504}) > \epsilon(\text{L1}) > \epsilon(\text{BA741})$$

whereas their ability to absorb at high wavelength is as follows:

$$\lambda_{\max}(\text{BA504}) > \lambda_{\max}(\text{LEG4}) > \lambda_{\max}(\text{D35}) > \lambda_{\max}(\text{RK1}) > \lambda_{\max}(\text{BA741}) > \lambda_{\max}(\text{L1})$$

These results show that, with a broader spectral response and higher molar absorption coefficient **LEG4** is able to harvest more light.

### II.3.b.(ii) Theoretical characterization of dyes properties

Dye	HOMO	LUMO
L1		
D35		
LEG4		
RK1		
BA504		
BA741		

**Table II-3:** Frontiers orbitals involved in the main electronic transition calculated from DFT.

The experimental values of the dyes are compared to the theoretical calculations using density functional theory (DFT) at the CAM-B3LYP/6-31G(d) level<sup>[79]</sup> in DCM solution using a conductor-like polarizable continuum model (C-PCM)<sup>[80]</sup>. The first lowest excited states were characterized by time dependent DFT (TDDFT) at the same level. All calculations were performed with the Gaussian 09 software<sup>[81]</sup>. From the TDDFT calculations, the HOMO→LUMO single electronic transition is responsible of the absorption band in the visible region where the corresponding maximum wavelength, for each dye, is in compliance with the experimental value. These results are summarized in the Annex II-4. The electron density distribution of frontiers orbitals of all organic dyes is determined from DFT. As shown in the Table II-3, the HOMO is mainly localized on the triphenylamine core for all dyes, slightly extended to the conjugated spacer for **L1**, **D35** and **LEG4** and highly extended for **RK1**. Regarding the LUMO, it is mainly localized on the acceptor part. Therefore the HOMO→LUMO transition is the result of a good overlap on the  $\pi$ -conjugated bridge between acceptor and donor groups which suggests an efficient ICT during excitation of dyes that allows electron injection into TiO<sub>2</sub>.

### II.3.b.(iii) Fluorescence spectroscopy

The emission spectra (Annex II-5) are recorded in the same polar solvent (dichloromethane, DCM) at the same concentration ( $C = 2.7 \times 10^{-6}$  M) and the emission wavelength maxima of **L1**, **D35**, **LEG4**, **RK1** and **BA504** are located at 622, 558\*, 686, 691 and 586 nm respectively. For **BA741**, no emission signal is detected when the excitation wavelength is applied in the visible region. However when the excitation is performed at 354 nm, an emission spectrum is measured. The fluorescence measurements provide also information on the  $E_{0-0}$  which represents the frontiers orbital HOMO-LUMO energy bandgap of dyes. For each dye, the energy bandgap is determined from the intercept ( $\lambda_{int}$ ) of the dye excitation and emission spectra, and is calculated as follows<sup>[82]</sup> :

$$E_{0-0} (eV) = \frac{1240}{\lambda_{int}} \quad (\text{II-6})$$

The HOMO is determined from electrochemical measurements. As a consequence the LUMO level is calculated from:

$$E_{LUMO} = E_{HOMO} - E_{0-0} \quad (\text{II-7})$$

The energy bandgap of the dyes increases as follows:

$$E_{0-0}(\text{LEG4}) < E_{0-0}(\text{D35}) = E_{0-0}(\text{RK1}) < E_{0-0}(\text{BA504}) < E_{0-0}(\text{L1}) < E_{0-0}(\text{BA741})$$

This order corresponds to the increase of the dye's molar extinction coefficient.

The corresponding absorption and emission data as well as thermodynamic parameters obtained from electrochemical measurements are listed in the Table II-4.

Dye	$\lambda_{\text{max, abs}}$ (nm)	$\epsilon_{\text{max}}$ (M <sup>-1</sup> .cm <sup>-1</sup> )	$\lambda_{\text{max, exc}}$ (nm)	$\lambda_{\text{max, em}}$ (nm)	$E_{\text{ox}}$ (V vs. Ag/AgCl)	HOMO (eV)	LUMO (eV)	$E_{0-0}$ (eV)
L1	432	23300	448	622	1.25	-5.5	-3.15	2.35
D35	491	45600	500*	658*	0.96	-5.35	-3.17	2.18*
LEG4	532	49400	526	686	0.84	-5.29	-3.25	2.04
RK1	478	31400	475	691	0.98	-5.41	-3.23	2.18
BA504	538	25000	500	586	0.94	-5.36	-3.10	2.26
BA741	466	18100	354	414	0.88	-5.31	-2.08	3.23

Table II-4: Optical and electrochemical properties of organic dyes. \*For D35 it is taken from ref. [83].

### II.3.b.(iv) Electrochemical characterization in organic medium

The CVs display reversible redox behavior for each dye as shown in Figure II-17 and from the onset of the oxidation potential ( $E_{\text{onset,ox}}$ ), ascribed to the oxidation of the dye ( $D \rightarrow D^+ + e^-$ ), the HOMO level energy is determined. With  $E_{\text{onset,ox}} = 0.85\text{V vs. Ag/AgCl}$ , L1 has the highest onset oxidation potential with a corresponding HOMO energy value is  $E_{\text{HOMO, L1}} = -5.5\text{ eV}$ . The conversion from the voltage to electron-volt is given by the following relation:

$$E_{\text{HOMO}} = -(E_{\text{ref}}^{\text{SHE}} + E_{\text{abs}}^{\text{SHE}} + E_{\text{onset,ox vs.ref}}) \quad (\text{II-8})$$

Where  $E_{\text{onset,ox vs.ref}}$  is the onset of the oxidation potential (in V) with respect to the reference electrode,  $E_{\text{ref}}^{\text{SHE}}$  is the potential (in V) of the reference electrode with respect to the standard hydrogen electrode (SHE) and  $E_{\text{abs}}^{\text{SHE}}$  refers to the absolute potential (in eV at vacuum) of the standard hydrogen electrode at 298K described by Trasatti from IUPAC<sup>[84]</sup> and equal to:

$$E_{\text{abs}}^{\text{SHE}} = 4.44 \pm 0.02 \quad (\text{II-9})$$

For Ag/AgCl as reference,  $E_{\text{Ag/AgCl}}^{\text{SHE}} = + 0.21 \text{ V}$ .

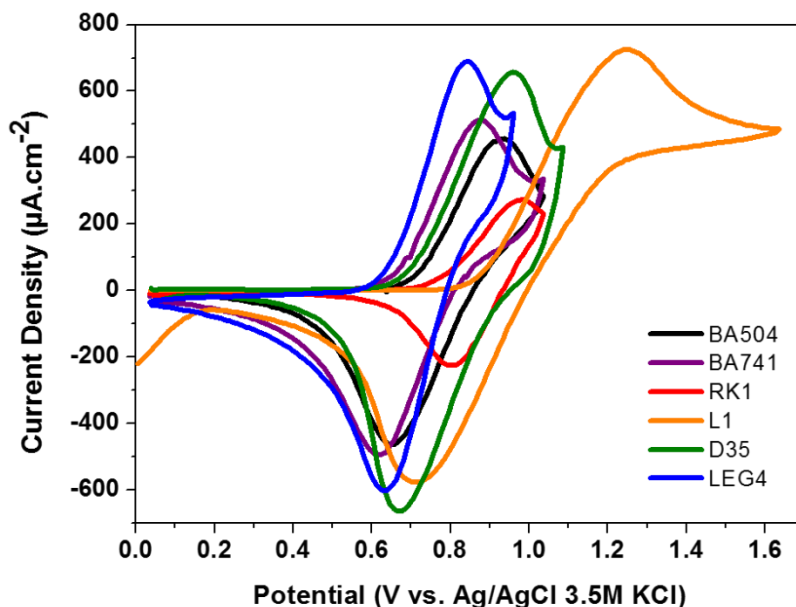


**Figure II-17:** Cyclic voltammograms of the different D- $\pi$ -A dyes sensitized on TiO<sub>2</sub> photo-anode in organic electrolyte.

With respect to **L1**, the presence of the electron-donating alkoxy chains in **D35** and **LEG4** dyes induces their oxidation at lower potential, with a HOMO level at more positive energy (in absolute scale). Interestingly, the HOMO energy level of **LEG4** dye is shifted to more positive values ( $E_{\text{HOMO, LEG4}} = -5.29 \text{ eV}$ ) due to the fluorene residue in the  $\pi$ -spacer. When cyclic voltammetry is considered, and in accordance with the shift of the ICT band in UV-Vis spectra, the bulky alkoxy side chains of **D35** have a higher impact than the conjugated spacer of **RK1** resulting in an easier oxidation of **D35** ( $E_{\text{onset,ox}} = 0.70 \text{ V vs. Ag/AgCl}$ ) than **RK1** dye ( $E_{\text{onset,ox}} = 0.76 \text{ V vs. Ag/AgCl}$ ). For **BA504** and **BA741** dyes, their LUMO level, calculated from the Equation (II-7), are shifted to more negative values which should result from the weaker electron acceptor property of the dicarboximide group compared to the cyanoacrylic acid group. However, the fluorene donor substituent on TPA lowers their oxidation potential as well as that of **D35** and **LEG4**, which might be a result of the strong conjugation and large electronic delocalization across the D- $\pi$ -A system in these dyes.

The onset of the oxidation potential of the different dyes decreases as follows:

$$E_{\text{onset,ox}}(\text{L1}) > E_{\text{onset,ox}}(\text{RK1}) > E_{\text{onset,ox}}(\text{BA504}) > E_{\text{onset,ox}}(\text{D35}) > E_{\text{onset,ox}}(\text{BA741}) > E_{\text{onset,ox}}(\text{LEG4})$$

From this observation, it is worth to highlight the importance of the donor substituent on the TPA core inducing the decrease of the  $E_{\text{onset,ox}}$ . Therefore, **RK1** and **L1** which does not contain any donor side group on the TPA are oxidized at higher potentials.

For organic dyes, the determination of the energy of frontier orbitals HOMO-LUMO are crucial in order to get an indication of the effectiveness of the charge transfers processes occurring from the LUMO of the dye to the TiO<sub>2</sub> CB and from the HOMO of the dye to the HTM VB. Indeed, to ensure an efficient electron injection into the TiO<sub>2</sub>, the LUMO level of dyes must be at higher energy than the CB of TiO<sub>2</sub> ( $E_{\text{CB,TiO}_2} = -4.2$  eV). For all the studied dyes, the LUMO level lies above the conduction band. As regard the HOMO level, it must be located at lower energy to collect the electrons from the HTM and subsequently to transfer the holes. In this study the HTM used to build the s-DSSC is PEDOT and its work function is reported to be at  $-5.2$  eV<sup>[85]</sup> so all dyes are concerned.

The schematic energy level diagram of organic dyes used in s-DSSC with PEDOT as HTM is represented in the Figure II-18.

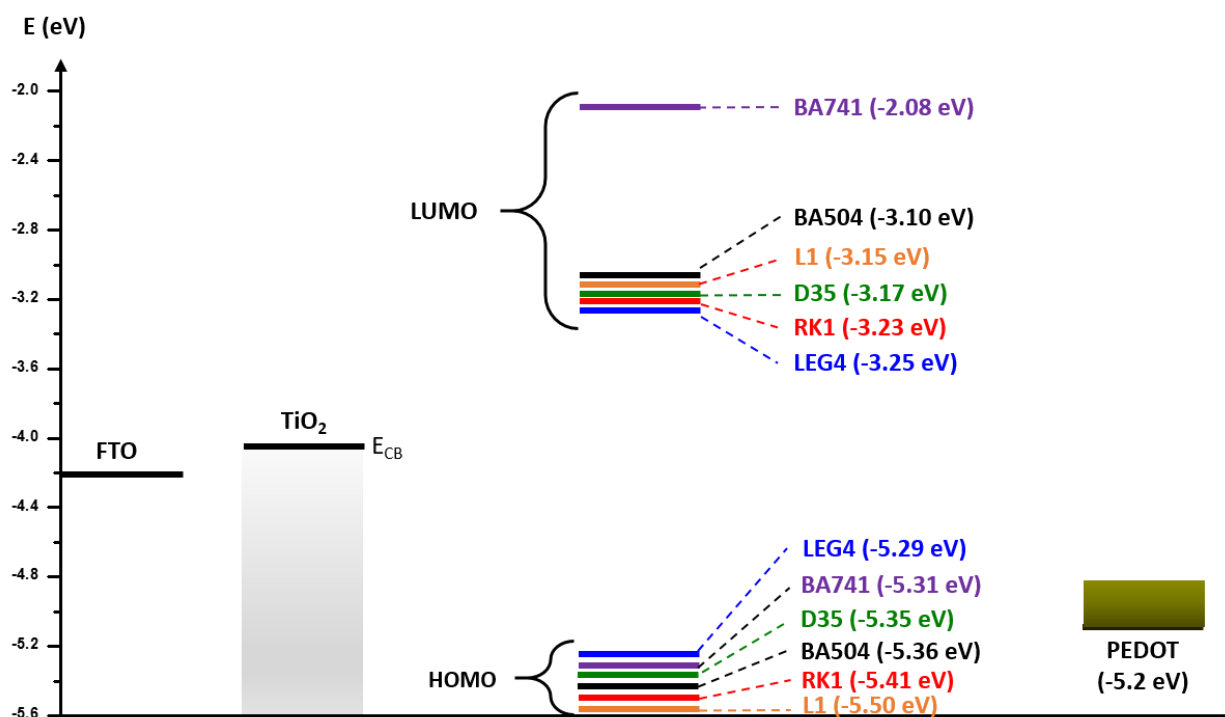


**Figure II-18:** Schematic energy diagram for dyes used in s-DSSCs with PEDOT as HTM.



### II. 3. c. Study of *in-situ* PEP using L1, D35, LEG4, RK1, BA504 and BA741 organic dyes

#### II.3.c.(i) *In-situ* PEP deposition of HTM on Sensitized TiO<sub>2</sub> Photo-anodes

The different dyes are firstly adsorbed on substrates to generate by *in-situ* PEP the HTM into the dyed mesoporous TiO<sub>2</sub> substrate. To perform the *in-situ* PEP in each media used in this work (organic or aqueous medium), the oxidation potential of the dye and the onset oxidation potential,  $E_{\text{onset,ox}}$  of the monomer (EDOT or Bis-EDOT) must match.

Therefore the CV of monomers are measured and compared to the CVs of dyes both in organic and aqueous solution as shown in the Figure II-19 and Figure II-21. The electrochemical data obtained in each medium are reported in the Table II-5.

Component	$E_{\text{ox}}$ (dye) (V vs. Ag/AgCl) in organic medium	$E_{\text{ox}}$ (dye) (V vs. Ag/AgCl) in aqueous medium	$E_{\text{onset, ox}}$ (monomer) (V vs. Ag/AgCl) in organic medium	$E_{\text{onset, ox}}$ (monomer) (V vs. Ag/AgCl) in aqueous medium
L1	1.25	1.00		
D35	0.96	0.95		
LEG4	0.84	0.88		
RK1	0.98	1.04		
BA504	0.94	0.98		
BA741	0.88	0.89		
Bis-EDOT			0.57	0.54
EDOT			1.21	0.96

**Table II-5:** Oxidation potential for dyes adsorbed on TiO<sub>2</sub> substrates and onset oxidation potential for monomers in organic and aqueous medium obtained from CVs.

#### II.3.c.(ii) *In-situ* PEP in organic medium

According to the voltammograms (Figure 46), Bis-EDOT displays a lower  $E_{\text{onset,ox}} = 0.57$  V vs. Ag/AgCl compared to  $E_{\text{onset,ox}}$  of EDOT (1.21 V vs. Ag/AgCl). Moreover, all  $E_{\text{ox}}$  of studied dyes match with the  $E_{\text{onset,ox}}$  of Bis-EDOT in contrast to the  $E_{\text{onset,ox}}$  of EDOT (see Table II-5).

Therefore when using these dyes for *in-situ* PEP, Bis-EDOT can exclusively be used as precursor.

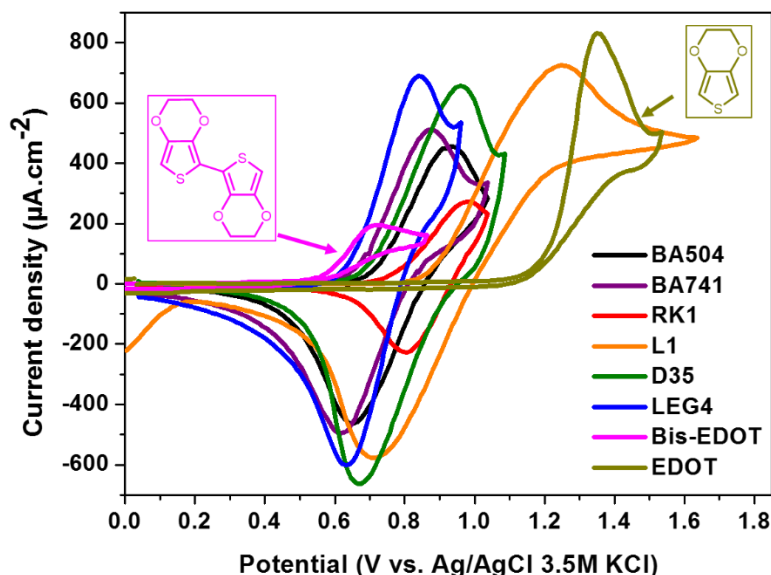


**Figure II-19:** Cyclic voltammograms of the different D- $\pi$ -A dyes and monomers in organic electrolyte.

Due to its higher  $E_{ox}$ , **L1** dye may oxidize EDOT monomer. However since none of the other dyes can be used for EDOT oxidation which prohibits the comparison of their efficiencies, only PEP using Bis-EDOT as precursor is carried out which allows the comparison of the efficiency of these different dyes.

Among the two electrochemical techniques (potentiostatic and galvanostatic) to implement the *in-situ* PEP, the performances obtained for s-DSSCs based on PEDOT produced by potentiostatic method gave the best efficiencies (Annex II-2b). Therefore for the following s-DSSCs the HTM will be produced exclusively by potentiostatic technique according to the aforementioned procedure in the section II.2.c. In all cases, the same amount of polymer is deposited on the dyed photo-anode corresponding to a total charge of about 20 mC.cm<sup>-2</sup>. The Figure II-20 illustrates the current-time transients during the *in-situ* PEP process using each of these dyes.

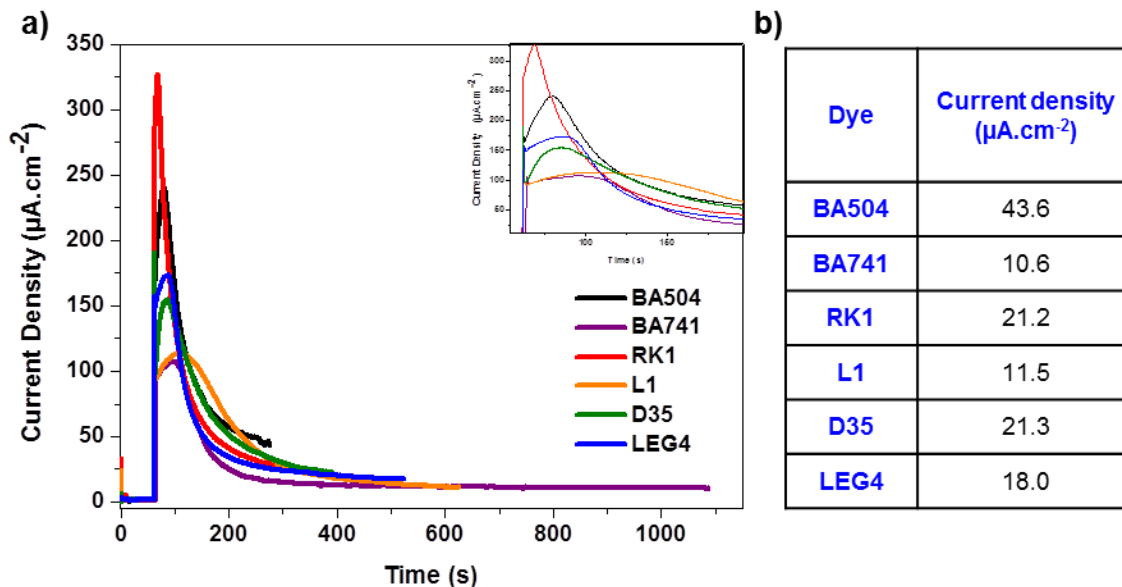


**Figure II-20:** Photocurrent variation during the *in-situ* PEP process of Bis-EDOT in organic medium on the electrode surface using organic dyes by applying a potential of 0.20 V vs. Ag/AgCl under 0.1 Sun.

The observed current is clearly light induced. Indeed, when light is off the curves show zero current indicating no PEP response; in contrast, under light illumination a current increase is observed indicating that the PEP process takes place. The trend is the classical behavior observed when electropolymerization (without light induction) of organic monomers is performed and it has the same behavior for all chronoamperograms. Only the nucleation process is slightly different depending on the dye used. Initially there is an increase in current which reflects to the nucleation, followed by a progressive current decrease where the growth process occurs to finally reach a constant current indicating a homogeneous polymerization.

For **BA741**, it seems that the process is quite slow since it has a lower current plateau. This can be explained by low ability of the dye to harvest light.

In contrast, for **BA504** the process is more efficient supported by the higher polymerization current plateau and reaching rapidly a total charge of 20 mC.cm<sup>-2</sup> during the growth process.

For the other four dyes **RK1**, **D35**, **LEG4** and **L1** the chronoamperograms are comparable indicating that the *in-situ* PEP process for these dyes is comparable.

### II.3.c.(iii) *In-situ* PEP in aqueous medium

The procedure to measure CVs is similar to that of the previous section, except that the organic electrolyte solution is replaced by an aqueous micellar solution containing 0.1M LiTFSI and 50 mM of Triton X-100 as solubilization surfactant.

Interestingly, the oxidation of EDOT is dramatically shifted ( $\Delta E = 230$  mV) to lower potential when the aqueous solvent is used instead of the organic one (see Figure II-21). However, this potential decrease is not sufficient to oxidize EDOT by each of the dyes. Indeed, the *in-situ* PEP process is restricted to **L1**, **RK1** and **BA504** owing to their high oxidation potential. However, we anyway performed *in-situ* PEP using each of the three remaining dyes **LEG4**, **BA741** and **D35** to ensure that when there is no match between  $E_{\text{onset,ox}}$  of EDOT precursor and the  $E_{\text{ox}}$  of these dyes ( $E_{\text{onset,ox}} > E_{\text{ox}}$ ) the *in-situ* PEP is not efficient.

As observed for EDOT in aqueous medium, the onset potential  $E_{\text{onset,ox}}$  of Bis-EDOT in the same medium is decreased. When compared to the voltammogram of Bis-EDOT in organic solvent, the  $E_{\text{onset,ox}}$  in aqueous medium is lowered by  $\Delta E = 30$  mV. Moreover, when this voltammogram is compared to those of dyes (Figure II-21) carried out in the same medium, it shows a good match between  $E_{\text{onset,ox}}$  of the precursor and the  $E_{\text{ox}}$  of each of the dyes. Thus, the Bis-EDOT precursor can be undoubtedly employed as *in-situ* PEP precursor using anyone of these dyes.

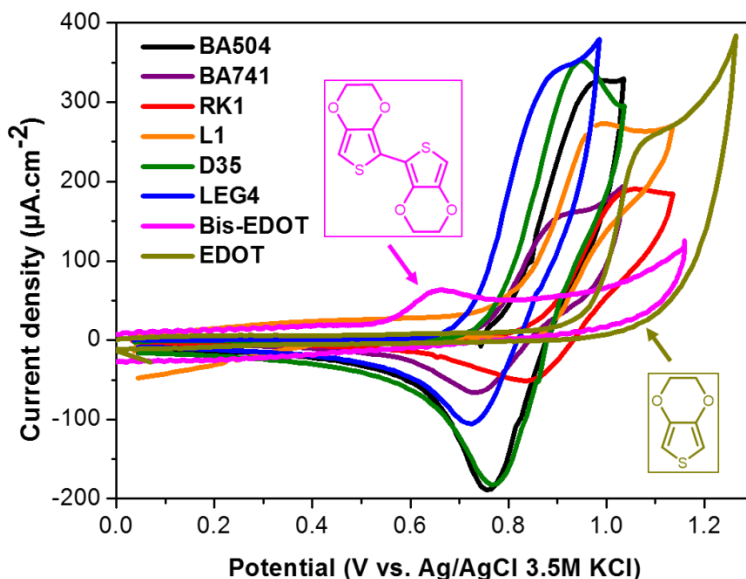


**Figure II-21:** Cyclic voltammograms of the different D- $\pi$ -A dyes and monomers in organic electrolyte.

➤ Bis-EDOT as *in-situ* PEP precursor in aqueous medium:

When using the same precursor, the current recorded during *in-situ* PEP in aqueous medium, is much lower ( $2\text{--}25 \mu\text{A}\cdot\text{cm}^{-2}$ ) than the current recorded in organic medium ( $10\text{--}50 \mu\text{A}\cdot\text{cm}^{-2}$ ). Thus the corresponding time to get a total charge of  $20\text{mC}\cdot\text{cm}^{-2}$  is much longer (Figure II-22). The **D35** dye shows a more efficient and more stable polymerization with high current plateau, probably due to the bulky side chains of **D35** that prevent aggregation of the dye on TiO<sub>2</sub> surface. Whereas

for **L1** dye as well as for **RK1** dye where no additional donor side chain is present on phenyl rings of TPA residue, the current drastically decreases, indicating that the presence of (alkyl or alkoxy) side chains is important when the aggregation of the TPA residues of the dye must be avoided. For **LEG4**, the current peak, where the monomer's oxidation occurs at first, is considerably high owing to its high light-harvesting ability. But even if **LEG4** bears the same bulky chains in the donor part, the current plateau is lower than **D35**. One possible reason is the negative shift of its oxidation potential (0.88 V) compared to **D35** (0.95 V) with respect to the onset of the oxidation potential of the monomer which induces a lower driving force  $\Delta G$ . The time duration of *in-situ* PEP to obtain the same charge when **BA741** is used, is much longer than that for **BA504**. This result was also obtained in organic medium and can similarly be attributed to the low light harvesting ability of the **BA741** dye when compared to the light harvesting ability of **BA504** dye.

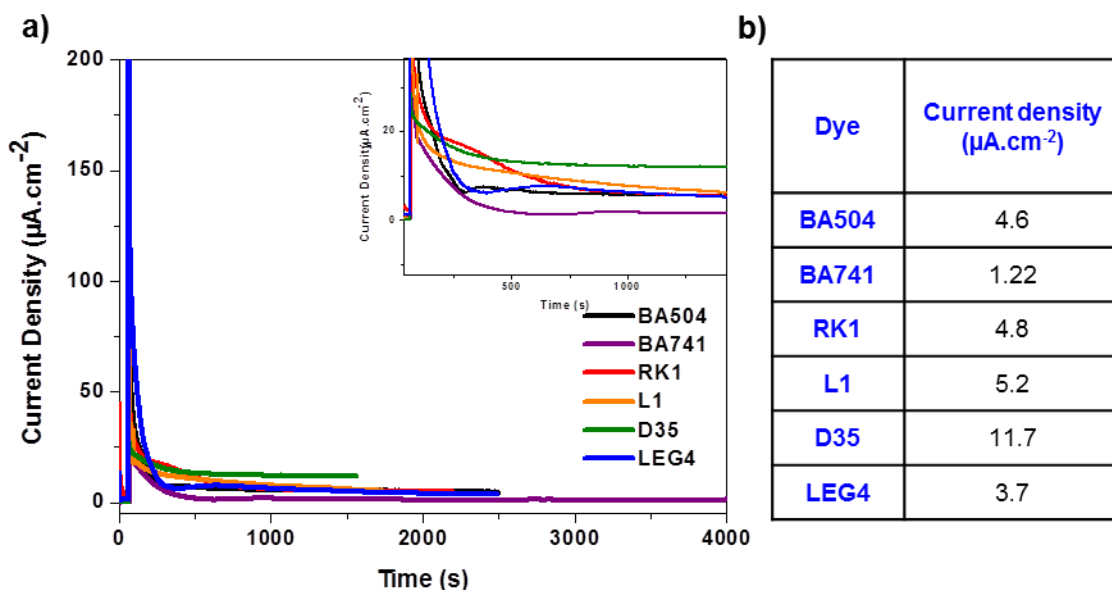


**Figure II-22:** Photocurrent variation during the *in-situ* PEP process of Bis-EDOT in aqueous medium on the electrode surface using organic dyes by applying a potential of 0.20 V vs. Ag/AgCl under 0.1 Sun.

➤ EDOT as *in-situ* PEP precursor:

When using EDOT as precursor for *in-situ* PEP process, the behaviors of chronoamperograms are all comparable. A main difference observed is, that the polymerization growth process occurs at different current densities (Figure II-23). **RK1** shows a higher current plateau than **L1**, and

**BA504.** This is due to difference between the onset oxidation of EDOT and the oxidation potential of these dyes. Indeed, the oxidation potential of **RK1** is about 80 mV higher than the onset oxidation of EDOT whereas this difference is of about 40 mV and 20 mV for respectively **L1** and **BA504**. For **LEG4** and **D35** dyes, despite their lower oxidation potential when compared to the onset oxidation potential of EDOT, a current is obtained when PEP is achieved indicating that the EDOT polymerization occurs anyway. However to get a total charge of 20 mC.cm<sup>-2</sup>, the time duration is more than 3000 s. For **BA741** the current is not really significant (2  $\mu$ A.cm<sup>-2</sup>) as observed previously.

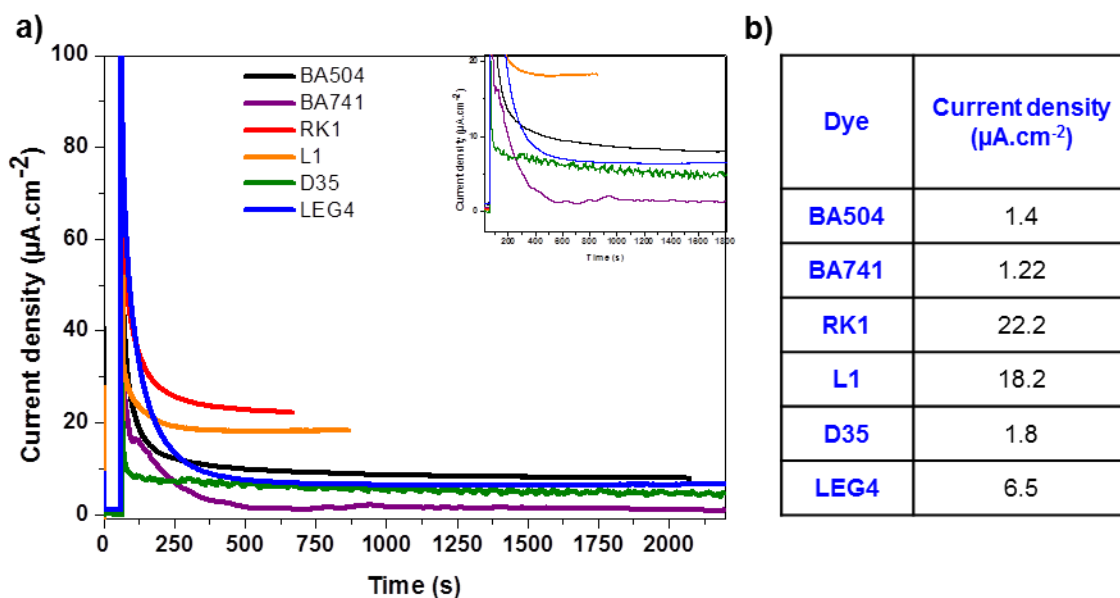


**Figure II-23:** Photocurrent variation during the *in-situ* PEP process of EDOT in organic medium on the electrode surface using organic dyes by applying a potential of 0.20 V vs. Ag/AgCl under 0.1 Sun.

### II. 3. d. Characterization of PEDOT layer *in-situ* produced on the dyed photo-anode

The PEDOT layer deposited on sensitized TiO<sub>2</sub> substrates are characterized by SEM in order to check the adequate contact between sensitizer and HTM and to be ensure that the pores of TiO<sub>2</sub> are filled with the polymer which is a key factor to improve photovoltaic performances.

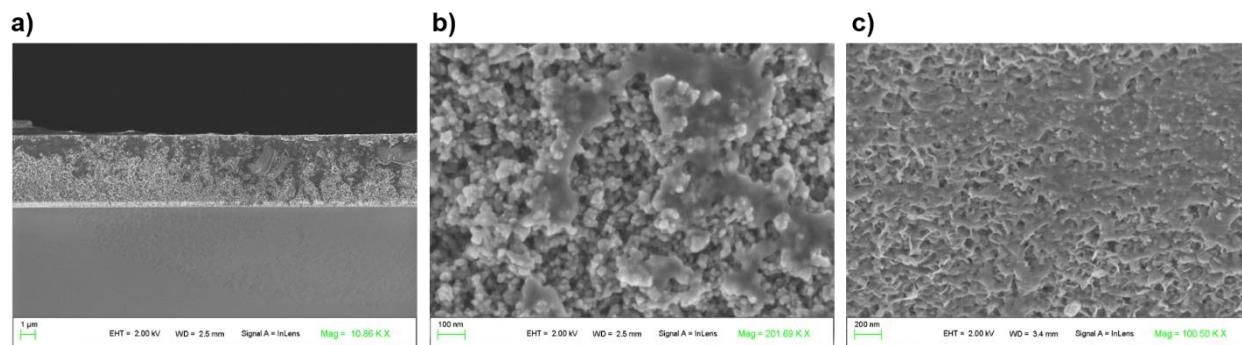


**Figure II-24:** SEM images of PEDOT layer *in-situ* produced on the dyed photo-anode with (a) cross-sectional view, (b) top view, and (c) with tilt angle

From a SEM image of the cross-section of the whole device (Figure II-24a) it can be seen that the PEDOT polymer penetrates uniformly into the 6.5 $\mu$ m-thick porous TiO<sub>2</sub> film. This is supported by the magnification of the SEM images (Figure II-24b and c) where it is clearly shown that the PEDOT polymer material is homogeneously distributed into the pores of mesoporous film of TiO<sub>2</sub> after polymerization. These results indicate clearly that when using *in-situ* PEP, an efficient incorporation of the HTM film on the supporting mesoporous TiO<sub>2</sub> layer is obtained which may lead to efficient s-DSSCs.

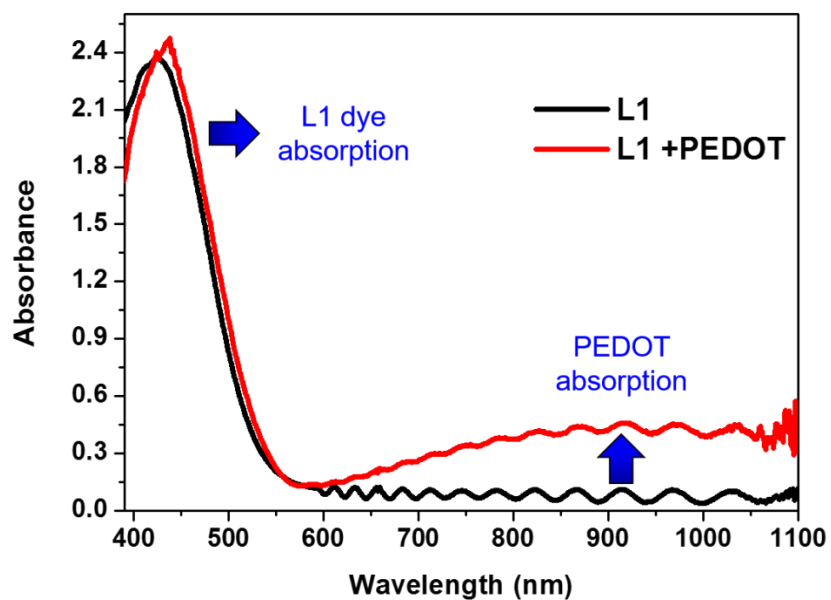


**Figure II-25:** Solid-state UV-Visible-IR spectra investigated for the dyed TiO<sub>2</sub> photo-anode before (black) and after the *in-situ* PEP (red) for L1 dye.

The solid-state UV-Visible-IR measurement is investigated for the dyed TiO<sub>2</sub> photo-anode before and after the *in-situ* PEP for each dye. In Figure II-25, the UV-Visible-IR spectrum of the TiO<sub>2</sub>

photo-anode sensitized with **L1** is illustrated and superimposed on the spectrum of the same substrate after the PEDOT deposition. Clearly, for **L1** dye adsorbed on the TiO<sub>2</sub> surface the intense absorption band located in the visible region, at 424 nm, is assigned to the dye absorption corresponding to the ICT band. However, this absorption is 8 nm blue shifted with respect to that carried out in solution for **L1**. This hypsochromic shift is generally attributed to H-aggregates occurring in solid-state and has been explained in terms of molecular exciton coupling theory<sup>[86]</sup>. The broad absorption band in the IR region is attributed to the absorption of the p-doped PEDOT in polaron and bipolaron states, as mentioned in the section (II.1). These two bands are observed for each dyes therefore the formation of PEDOT with different doping levels could be expected for different dyes based devices.

### **II. 3. e. s-DSSCs devices performances**

After gold counter-electrode deposition, the complete s-DSSCs based on different organic dyes are obtained and they are denominated as follows: **FTO/TiO<sub>2</sub>/Dye/PEDOT/Au**. The overall efficiency of a s-DSSC is determined under full sun illumination and in dark. This overall efficiency is calculated from three parameters: V<sub>oc</sub>, J<sub>sc</sub>, and FF, as reported in chapter 1, which vary upon the components that constitute the device:

- The oxide semiconductor
- The HTM
- The dye sensitizer

The oxide semiconductor component is the same for all s-DSSCs, therefore, it will not be discussed in this work.

The HTM is PEDOT polymer prepared from two different monomers (EDOT or Bis-EDOT). The experiments were carried out using two different media and two different electrochemical techniques. The results concerning the s-DSSCs performances will be reported and discussed according to each monomer using the different experimental procedures as follows:

- s-DSSCs using Bis-EDOT:
  - o in organic medium
  - o in aqueous micellar medium
- s-DSSCs using EDOT in aqueous medium. We must underline that for EDOT we only used aqueous medium to perform *in-situ* PEP. Since none of oxidation potentials of dyes



match with the onset of the oxidation potential of EDOT, the *in-situ* PEP of EDOT in organic medium is not thermodynamically feasible.

In each case, the results are exclusively discussed as regards to the dye sensitizer properties (optical and electrochemical) related to the dye structure which is one of the largest factors influencing the photovoltaic parameters that determine the efficiency of the s-DSSC.

### II.3.e.(i) s-DSSCs performances based PEDOT generated from Bis-EDOT in organic medium

The photovoltaic performances of FTO/TiO<sub>2</sub>/Dye/PEDOT/Au cells obtained for each dyes are listed in the Table II-6.

Dye	V <sub>oc</sub> (V)	J <sub>sc</sub> (mA/cm <sup>2</sup> )	FF (%)	Efficiency $\eta$ (%)
L1	0.43	3.7	57	0.91
D35*	0.83	8.19	68	4.6
LEG4*	0.91	10.8	57	5.6
RK1	0.45	5.6	57	1.42
BA504	0.57	3.2	64	1.14
BA741	0.50	3.1	52	0.8

**Table II-6:** Photovoltaic Parameters of s-DSSCs based PEDOT produced in organic medium from Bis-EDOT illuminated 100 mW cm<sup>-2</sup> (AM 1.5G). \*For D35 and LEG4 based s-DSSCs, the results are taken from ref.[4].

For the device based on L1 corresponding to the most simple dye structure (TPA connected to the cyanoacrylic acid acceptor through a thiophene bridge), the V<sub>oc</sub> is 430 mV, the FF is 57 % and the J<sub>sc</sub> is up to 3.7 mA/cm<sup>2</sup>, yielding an efficiency of 0.91 %. With **RK1**, the obtained V<sub>oc</sub> (450 mV) and the FF (57 %) are quite similar to those of **L1**. But **RK1** shows a much higher J<sub>sc</sub> (5.6 mA/cm<sup>2</sup>). The similarity of the V<sub>oc</sub> for both dyes may originate from the lack of side chains on the TPA core in the donor part. Indeed, the presence of alkoxy chains in the dye structure, as for **D35** and **LEG4**, increases significantly the V<sub>oc</sub>: 530 mV and 660 mV for **D35** and **LEG4** respectively. The V<sub>oc</sub> is determined by the difference between the quasi Fermi level correlated to the CB of TiO<sub>2</sub> and the VB of the PEDOT. Theoretically, the V<sub>oc</sub> should be up to 1 V, therefore since it is lower, some recombination occurs at TiO<sub>2</sub>/PEDOT interface. But it has

been reported that in presence of hydrophobic chains in the dye structure, the recombination process is minimized (cf. Chapter 1).

Regarding the photocurrent, s-DSSCs sensitized with **RK1**, **D35** and **LEG4**, show the highest values: 5.6, 7.7 and 9.5 mA/cm<sup>2</sup> respectively. It is intended that a high photocurrent value can be related to the following parameters: (i) to the high extinction coefficient of the dye, (ii) to the position of the HOMO-LUMO level of the dye with respect to the TiO<sub>2</sub> CB and PEDOT VB and (iii) to the absorption at higher wavelengths. **RK1**, **D35** and **LEG4** dyes which have the same anchoring group, show high extinction coefficients when compared to  $\epsilon$  of **L1** ( $> 3\text{-}4 \times 10^4 \text{ M}^{-1} \cdot \text{cm}^{-1}$ ), their absorption maxima are all red shifted relatively to that of **L1**. Therefore for these three dyes, the electron injection processes from dye to TiO<sub>2</sub> and from PEDOT to the dye are efficient compared to those of **L1**.

**BA504** and **BA741** supports an anchoring group different from that of the **L1**, the resulting LUMO is pulling away with respect to the CB of TiO<sub>2</sub>, therefore the electron injection process at this interface is ineffective illustrated by low  $J_{sc}$  values. In addition, the low  $J_{sc}$  values can be explained by the ineffective dye regeneration process due to the HOMO level which is far from the PEDOT VB level for both dyes. However, the benefit to hold the fluorene moiety in each side of the TPA partially avoids the charge recombination at TiO<sub>2</sub>/PEDOT interface resulting in a quite good  $V_{oc}$ : 570 mV and 500 mV for **BA504** and **BA741** respectively. In brief, the obtained efficiency follows this order:

$$\eta(\text{BA741}) < \eta(\text{L1}) < \eta(\text{BA504}) < \eta(\text{RK1}) < \eta(\text{D35}) < \eta(\text{LEG4})$$

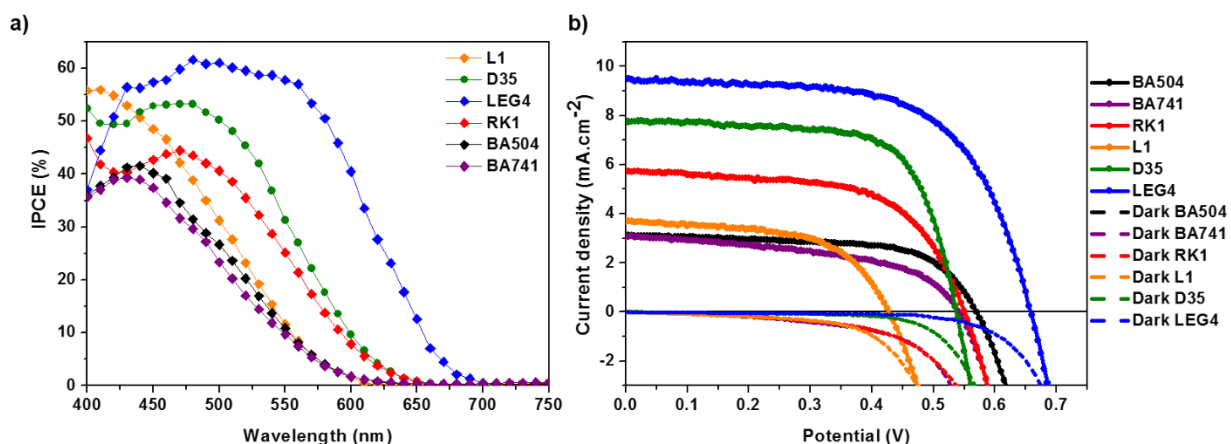


**Figure II-26:** (a) IPCE spectra and (b) J-V characteristics under the AM 1.5G illumination of the simulated sunlight (100mW/cm<sup>2</sup>), of the s-DSSCs photosensitized with the different organic commercial dyes using PEDOT as HTM generated from Bis-EDOT in organic medium.

As regards the IPCE presented in Figure II-26a, the highest value is obtained for **LEG4** based s-DSSC with maximum IPCE of 60 % followed by **L1** (56 at 410 nm), **D35** (53 % at 480 nm), and **RK1** (45 % at 470 nm) based s-DSSCs. For both **BA504** and **BA741** based devices, the IPCE is below 41 %. As mentioned in Chapter I, the resulting IPCE values reflect the  $J_{sc}$  of s-DSSCs sensitized with the different dyes according to the Equation (I-22). Indeed in the wavelength range, the integrated current values obtained from the IPCE are in accordance with the trend of  $J_{sc}$ :

$$\text{IPCE}(\text{BA741}) < \text{IPCE}(\text{BA504}) < \text{IPCE}(\text{L1}) < \text{IPCE}(\text{RK1}) < \text{IPCE}(\text{D35}) < \text{IPCE}(\text{LEG4})$$

### II.3.e.(ii) s-DSSCs performances based PEDOT generated in aqueous medium

➤ PEDOT produced from Bis-EDOT precursor

Dye	$V_{oc}$ (V)	$J_{sc}$ (mA/cm <sup>2</sup> )	FF (%)	Efficiency $\eta$ (%)
<b>L1</b>	0.21	1.22	41	<b>0.11</b>
<b>D35*</b>	0.78	8.6	68	<b>3.8</b>
<b>LEG4*</b>	0.84	10.94	56	<b>5.2</b>
<b>RK1</b>	0.41	0.8	41	<b>0.14</b>
<b>BA504</b>	0.62	2.47	53	<b>0.82</b>
<b>BA741</b>	0.54	0.85	33	<b>0.15</b>

**Table II-7: Photovoltaic Parameters of s-DSSCs based PEDOT produced in aqueous medium from Bis-EDOT illuminated 100 mW cm<sup>-2</sup> (AM 1.5G). \* D35 and LEG4 based s-DSSCs, the results are taken from ref.[4].**

The s-DSSCs using PEDOT generated in aqueous medium give quite good efficiencies (Table II-7). But when compared by pairs based on the same dye, they are lower than those obtained with PEDOT generated from the same precursor in organic medium (Table II-6). The only difference lies on the preparation of PEDOT which was performed in aqueous medium. In the literature, it was stated that PEDOT polymerized *in-situ* in aqueous medium results mainly in large amount of shorter chains<sup>[4]</sup> where the electron mobility is lower than PEDOT produced in organic medium. The large amount of low conductive shorter PEDOT chains within the device leads to a faster charge recombination between the TiO<sub>2</sub> electrons and the hole of the HTM holes and hence a lower  $V_{oc}$ . Moreover, the FF is dramatically decreased compared to the devices when

PEDOT is produced in organic medium. The reason of lower FF is due to the possible inclusion of Triton-X-100, used as surfactant during the *in-situ* PEP process, into the polymer layer which contributes to the higher resistance in the hole-conducting film<sup>[17]</sup>. In addition the resistivity of the HTM prevents an efficient electron injection from the HTM to the oxidized dye.

Interestingly the resulting efficiencies of the complete devices based on the different dyes slightly follow the same order to that obtained for s-DSSCs with PEDOT produced in organic medium:

$$\eta(\mathbf{L1}) < \eta(\mathbf{RK1}) < \eta(\mathbf{BA741}) < \eta(\mathbf{BA504}) < \eta(\mathbf{D35}) < \eta(\mathbf{LEG4})$$

Surprisingly, the overall efficiency of FTO/TiO<sub>2</sub>/RK1/PEDOT/Au collapses when PEDOT is produced in aqueous medium ( $\eta = 0.14\%$ ) with respect to the device using the same CP produced in organic medium ( $\eta = 1.42\%$ ). The same observation can be done for FTO/TiO<sub>2</sub>/RK1/PEDOT/Au device overall efficiency (0.11% for PEDOT produced in aqueous electrolyte whereas 0.91% for PEDOT produced in organic electrolyte). The common point between these two dyes is the absence of a supplementary donor on TPA core which induces the decrease of the  $V_{oc}$  as noted above. Indeed, for both **L1** and **RK1** dyes, the  $V_{oc}$  is low: 210 mV and 410 mV respectively, in contrast to **LEG4** and **D35** where the  $V_{oc}$  is higher than 780 mV due to the presence of alkoxy chains. The presence of fluorene moiety in the donor part of the dye structure (**BA504** and **BA741**) seems to be more efficient to minimize the recombination between TiO<sub>2</sub> and the HTM since the devices based on these dyes display a high  $V_{oc}$ . However the photocurrent density at short circuit condition is low, mainly for s-DSSCs based on **BA741**, **L1** and **RK1** dyes owing to their lower wavelength absorption and their higher oxidation potential inducing a higher  $\Delta G$ . This is one reason of their low IPCE measured which below 20% (Figure II-27). Whereas in case of **D35**, **BA504** and **LEG4** based s-DSSCs, their  $J_{sc}$ , and hence, their IPCE are higher.

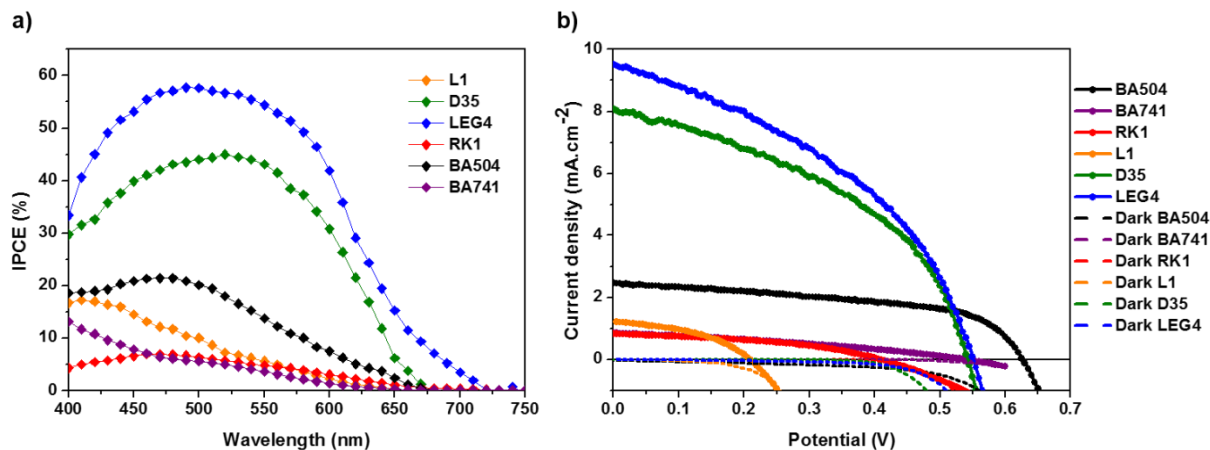


**Figure II-27:** (a) IPCE spectra and (b) J-V characteristics under the AM 1.5G illumination of the simulated sunlight (100mW/cm<sup>2</sup>), of the s-DSSCs photosensitized with the different organic commercial dyes using PEDOT as HTM generated from Bis-EDOT in aqueous medium.

➤ PEDOT produced from EDOT precursor

Dye	V <sub>oc</sub> (V)	J <sub>sc</sub> (mA/cm <sup>2</sup> )	FF (%)	Efficiency $\eta$ (%)
L1	0.25	2.0	54	0.28
D35*	0.82	6.2	60	3.00
LEG4*	0.68	6.51	64	2.80
RK1	0.50	4.0	56	1.11
BA504	0.48	1.9	41	0.38
BA741	0.12	0.35	27	0.01

**Table II-8:** Photovoltaic parameters of s-DSSCs based PEDOT produced in aqueous medium EDOT illuminated 100 mW cm<sup>-2</sup> (AM 1.5G). D35 and LEG4 based s-DSSCs, the results are taken from ref. [87].

Since the *in-situ* PEP of EDOT was only possible in aqueous medium, the comparison with the *in-situ* PEP of Bis-EDOT in aqueous medium will be done. According to the Table II-8, the efficiencies of s-DSSCs based on PEDOT obtained by the *in-situ* PEP of EDOT in aqueous medium are lower than those of s-DSSCs based on the same HTM produced by the *in-situ* PEP of Bis-EDOT in same aqueous medium. This was expected owing to the higher is the driving force ( $\Delta G$ ) between the onset potential  $E_{\text{onset,ox}}$  of EDOT aqueous medium with respect to the  $E_{\text{ox}}$  of dyes compared to the  $\Delta G$  between the  $E_{\text{onset,ox}}$  of Bis-EDOT in aqueous medium and the  $E_{\text{ox}}$  of the dye. Indeed, as mentioned above, the lower the  $E_{\text{onset,ox}}$  of the monomer is, the more efficient

*in-situ* PEP is and hence the more performant the s-DSSC is. Interestingly when taking into consideration the  $\Delta G$  for each organic dye with respect to EDOT which follows this order:

$$\Delta G (\text{RK1}) > \Delta G (\text{L1}) > \Delta G (\text{BA504}) > \Delta G (\text{D35}) > \Delta G (\text{BA741}) > \Delta G (\text{LEG4})$$

the *in-situ* PEP is coherently successful. Nevertheless, it is not sufficient to lead to a performant s-DSSC device. Indeed the order of the resulting efficiencies is as follows:

$$\eta (\text{D35}) > \eta (\text{LEG4}) > \eta (\text{RK1}) > \eta (\text{BA504}) > \eta (\text{L1}) > \eta (\text{BA741})$$

The parameters that control the anodic polymerization process of a monomer at the active surface of a working electrode (for better polymer homogeneity, regularity, long chain lengths and thus high conductivity) are: (i) the working potential which corresponds to the thermodynamic control of the polymerization reaction and depends on the oxidation potential of the dye; and (ii) the radical-radical coupling reaction rate, which controls the kinetics of the polymerization reaction and is largely dependent on the amount of radicals produced at the electrode surface when the monomer is oxidized. For *in-situ* PEP, the working potential is fixed by the dye oxidation potential in the electrolytic medium. Whereas when the amount of radicals produced at the electrode surface is high, the radical-radical coupling reactions may produce more polymer of shorter chains, which does not lead to highly conductive HTM. As a consequence less efficient s-DSSC based on this type of polymer is leading<sup>[88]</sup>. This is probably the case of **RK1** dye, which shows the highest oxidation potential but a less performant s-DSSC corresponding to a less conductive polymer when compared to **LEG4**.

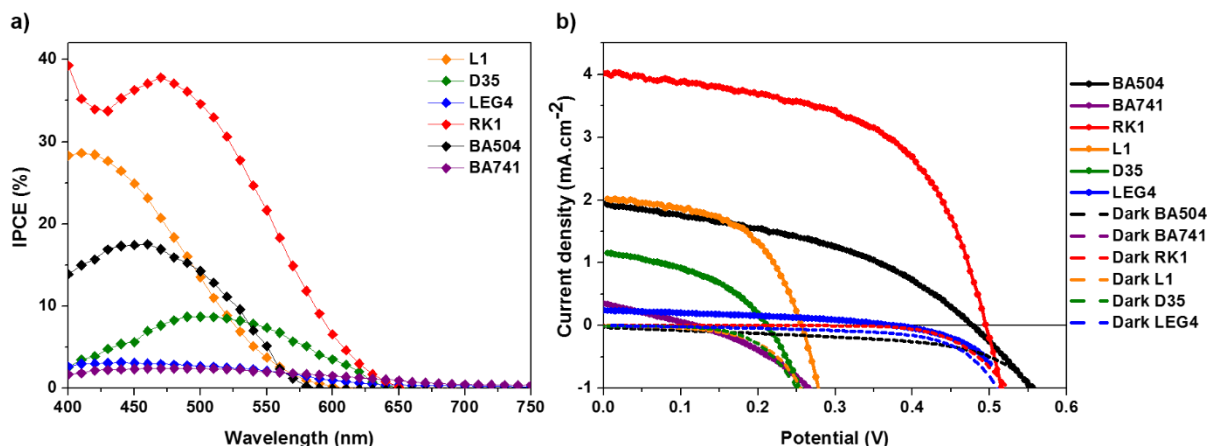


**Figure II-28:** (a) IPCE spectra and (b) J-V characteristics under the AM 1.5G illumination of the simulated sunlight (100mW/cm<sup>2</sup>), of the s-DSSCs photosensitized with the different organic commercial dyes using PEDOT as HTM generated from EDOT in aqueous medium.

## II. 4. Conclusion

In order to determine the best fragments *i.e.* donor, linker, and acceptor units, constituting the dye structure, that have an efficient contribution on the *in-situ* PEP process to produce conducting polymer (CP) used as HTM both in organic and in aqueous media and hence on the performances of the s-DSSCs, a series of commercially available organic dyes including **L1**, **D35**, **LEG4**, **RK1**, **BA504** and **BA741** were systematically investigated. All these organic dyes share the same TPA core, as donor, on their D- $\pi$ -A structure configuration and the molecular structure was varied at the level of the linker, the acceptor and the supplementary donor imbedded on the TPA. The optical and electrochemical properties of the dyes were studied and the *in-situ* PEP was carried out using each of these dyes adsorbed on the TiO<sub>2</sub> mesoporous surface. The *in-situ* PEP experiments were carried out using two different electrolytic media aqueous or organic. The as-obtained modified electrodes were used to set up s-DSSCs devices. The results show that when the **L1** pristine dye structure is modified with the alkoxy side chains, such as **D35** and **LEG4** dyes, the s-DSSCs based on these dyes show efficient light conversion even though the *in-situ* PEP obtained using each of these dyes does not show the highest polymerization reaction yield. **D35** based s-DSSC show exceptionally good and stable photovoltaic performances whatever the medium and the monomer used for the *in-situ* PEP. When the carboxylic anchoring group is used (**BA504** and **BA741**) instead of cyanoacrylic acid one, the efficiency is low when the dye is used for *in-situ* PEP and when the dye is introduced in s-DSSC. This clearly supports that the use of (i) cyanoacrylic acid as anchoring group on the TiO<sub>2</sub> semiconductor, (ii) the thiophene as  $\pi$ -conjugated bridge and (iii) the additional donating residues on the TPA core are recommended to obtain the promising organic dye structure which may improve the s-DSSC efficiency.

## II. 5. References

- (1) Zhang, J.; Vlachopoulos, N.; Jouini, M.; Johansson, M. B.; Zhang, X.; Nazeeruddin, M. K.; Boschloo, G.; Johansson, E. M. J.; Hagfeldt, A. *Nano Energy* **2016**, *19*, 455–470.
- (2) Hagberg, D. P.; Marinado, T.; Karlsson, K. M.; Nonomura, K.; Qin, P.; Boschloo, G.; Brinck, T.; Hagfeldt, A.; Sun, L. *J. Org. Chem.* **2007**, *72* (25), 9550–9556.
- (3) Tian, H.; Soto, A.; Xu, B.; Sun, L.; Hagfeldt, A.; Fabregat-Santiago, F.; Mora-Sero, I.; Kang, Y. S.; Bisquert, J.; Barea, E. M. *Nano* **2014**, *09* (05), 1440005.
- (4) Zhang, J.; Yang, L.; Shen, Y.; Park, B.-W.; Hao, Y.; Johansson, E. M. J.; Boschloo, G.; Kloo, L.; Gabrielsson, E.; Sun, L.; Jarboui, A.; Perruchot, C.; Jouini, M.; Vlachopoulos, N.; Hagfeldt, A. *J. Phys. Chem. C* **2014**, *118* (30), 16591–16601.
- (5) Joly, D.; Pellejà, L.; Narbey, S.; Oswald, F.; Chiron, J.; Clifford, J. N.; Palomares, E.; Demadrille, R. *Sci. Rep.* **2015**, *4* (1).
- (6) Yu, H.; Zhang, S.; Zhao, H.; Will, G.; Liu, P. *Electrochimica Acta* **2009**, *54* (4), 1319–1324.
- (7) Lee, J. G.; Cheon, J. H.; Yang, H. S.; Lee, D. K.; Kim, J. H. *J. Nanosci. Nanotechnol.* **2012**, *12* (7), 6026–6030.
- (8) Kim, H.-J.; Jeon, J.-D.; Kim, D. Y.; Lee, J.-J.; Kwak, S.-Y. *J. Ind. Eng. Chem.* **2012**, *18* (5), 1807–1812.
- (9) Ikeue, K.; Yamashita, H.; Anpo, M. *Chem. Lett.* **1999**, *28* (11), 1135–1136.
- (10) Saelim, N.; Magaraphan, R.; Sreethawong, T. *Energy Convers. Manag.* **2011**, *52* (8–9), 2815–2818.
- (11) Chandiran, A. K.; Yella, A.; Stefiik, M.; Heiniger, L.-P.; Comte, P.; Nazeeruddin, M. K.; Grätzel, M. *ACS Appl. Mater. Interfaces* **2013**, *5* (8), 3487–3493.
- (12) Jang, K.-I.; Hong, E.; Kim, J. H. *Korean J. Chem. Eng.* **2012**, *29* (3), 356–361.
- (13) Kavan, L.; Grätzel, M. *Electrochimica Acta* **1995**, *40* (5), 643–652.
- (14) Fabregat-Santiago, F.; Bisquert, J.; Cevey, L.; Chen, P.; Wang, M.; Zakeeruddin, S. M.; Grätzel, M. *J. Am. Chem. Soc.* **2009**, *131* (2), 558–562.
- (15) Kavan, L.; Tétreault, N.; Moehl, T.; Grätzel, M. *J. Phys. Chem. C* **2014**, *118* (30), 16408–16418.
- (16) Xia, J.; Masaki, N.; Lira-Cantu, M.; Kim, Y.; Jiang, K.; Yanagida, S. *J. Am. Chem. Soc.* **2008**, *130* (4), 1258–1263.
- (17) Yang, L.; Zhang, J.; Shen, Y.; Park, B.-W.; Bi, D.; Häggman, L.; Johansson, E. M. J.; Boschloo, G.; Hagfeldt, A.; Vlachopoulos, N.; Snedden, A.; Kloo, L.; Jarboui, A.; Chams, A.; Perruchot, C.; Jouini, M. *J. Phys. Chem. Lett.* **2013**, *4* (23), 4026–4031.
- (18) Saito, Y. *Electrochem. Commun.* **2004**, *6* (1), 71–74.
- (19) Chamberlin, R. R.; Skarman, J. S. *J. Electrochem. Soc.* **1966**, *113* (1), 86.
- (20) Patil, P. S. *Mater. Chem. Phys.* **1999**, *59* (3), 185–198.
- (21) Huang, C.-Y.; Hsu, Y.-C.; Chen, J.-G.; Suryanarayanan, V.; Lee, K.-M.; Ho, K.-C. *Sol. Energy Mater. Sol. Cells* **2006**, *90* (15), 2391–2397.
- (22) Xu, F.; Zhu, K.; Zhao, Y. *RSC Adv* **2016**, *6* (100), 98167–98170.
- (23) Wang, P.; Zakeeruddin, S. M.; Comte, P.; Exnar, I.; Grätzel, M. *J. Am. Chem. Soc.* **2003**, *125* (5), 1166–1167.
- (24) Zhu, K.; Jang, S.-R.; Frank, A. J. *J. Phys. Chem. Lett.* **2011**, *2* (9), 1070–1076.
- (25) Wang, Q.; Moser, J.-E.; Grätzel, M. *J. Phys. Chem. B* **2005**, *109* (31), 14945–14953.



- (26) Ghadiri, E.; Taghavinia, N.; Zakeeruddin, S. M.; Grätzel, M.; Moser, J.-E. *Nano Lett.* **2010**, *10* (5), 1632–1638.
- (27) Nakade, S.; Kanzaki, T.; Wada, Y.; Yanagida, S. *Langmuir* **2005**, *21* (23), 10803–10807.
- (28) Hagfeldt, A.; Boschloo, G.; Sun, L.; Kloo, L.; Pettersson, H. *Chem. Rev.* **2010**, *110* (11), 6595–6663.
- (29) Ito, S.; Murakami, T. N.; Comte, P.; Liska, P.; Grätzel, C.; Nazeeruddin, M. K.; Grätzel, M. *Thin Solid Films* **2008**, *516* (14), 4613–4619.
- (30) Yanagida, S.; Yu, Y.; Manseki, K. *Acc. Chem. Res.* **2009**, *42* (11), 1827–1838.
- (31) Zhang, J.; Häggman, L.; Jouini, M.; Jarboui, A.; Boschloo, G.; Vlachopoulos, N.; Hagfeldt, A. *ChemPhysChem* **2014**, *15* (6), 1043–1047.
- (32) Zhang, J.; Pazoki, M.; Simiyu, J.; Johansson, M. B.; Cheung, O.; Häggman, L.; Johansson, E. M. J.; Vlachopoulos, N.; Hagfeldt, A.; Boschloo, G. *Electrochimica Acta* **2016**, *210*, 23–31.
- (33) Feldt, S. M.; Gibson, E. A.; Gabrielsson, E.; Sun, L.; Boschloo, G.; Hagfeldt, A. *J. Am. Chem. Soc.* **2010**, *132* (46), 16714–16724.
- (34) Haid, S.; Marszalek, M.; Mishra, A.; Wielopolski, M.; Teuscher, J.; Moser, J.-E.; Humphry-Baker, R.; Zakeeruddin, S. M.; Grätzel, M.; Bäuerle, P. *Adv. Funct. Mater.* **2012**, *22* (6), 1291–1302.
- (35) Basescu, N.; Liu, Z.-X.; Moses, D.; Heeger, A. J.; Naarmann, H.; Theophilou, N. *Nature* **1987**, *327* (6121), 403–405.
- (36) Abthagir, P. S.; Saraswathi, R. *Thermochim. Acta* **2004**, *424* (1–2), 25–35.
- (37) Gupta, B.; Prakash, R. *Synth. Met.* **2010**, *160* (5–6), 523–528.
- (38) Zade, S. S.; Bendikov, M. *Org. Lett.* **2006**, *8* (23), 5243–5246.
- (39) Pettersson, L. A. A.; Carlsson, F.; Inganäs, O.; Arwin, H. *Thin Solid Films* **1998**, *313–314*, 356–361.
- (40) Sheberla, D.; Patra, S.; Wijsboom, Y. H.; Sharma, S.; Sheynin, Y.; Haj-Yahia, A.-E.; Barak, A. H.; Gidron, O.; Bendikov, M. *Chem Sci* **2015**, *6* (1), 360–371.
- (41) Shirakawa, H.; Louis, E. J.; MacDiarmid, A. G.; Chiang, C. K.; Heeger, A. J. *J. Chem. Soc. Chem. Commun.* **1977**, No. 16, 578.
- (42) The Nobel Prize in Chemistry 2000 [http://www.nobelprize.org/nobel\\_prizes/chemistry/laureates/2000/](http://www.nobelprize.org/nobel_prizes/chemistry/laureates/2000/).
- (43) Balint, R.; Cassidy, N. J.; Cartmell, S. H. *Acta Biomater.* **2014**, *10* (6), 2341–2353.
- (44) Chiang, C. K.; Fincher, C. R.; Park, Y. W.; Heeger, A. J.; Shirakawa, H.; Louis, E. J.; Gau, S. C.; MacDiarmid, A. G. *Phys. Rev. Lett.* **1977**, *39* (17), 1098–1101.
- (45) Camurlu, P. *RSC Adv* **2014**, *4* (99), 55832–55845.
- (46) *Organic optoelectronic materials*; Li, Y., Ed.; Lecture notes in chemistry; Springer: Cham, 2015.
- (47) Kar, P. In *Doping in Conjugated Polymers*; John Wiley & Sons, Inc., 2013; pp 81–96.
- (48) Manzoli, A.; Steffens, C.; Paschoalin, R. T.; Correa, A.; Alves, W.; Leite, F.; Herrmann, P. *Sensors* **2011**, *11* (12), 6425–6434.
- (49) Skotheim, T. A.; Reynolds, J. *Handbook of Conducting Polymers, 2 Volume Set*; CRC Press, 2007.
- (50) Diaz, A. F.; Castillo, J. I.; Logan, J. A.; Lee, W.-Y. *J. Electroanal. Chem. Interfacial Electrochem.* **1981**, *129* (1–2), 115–132.
- (51) Genies, E. M.; Bidan, G.; Diaz, A. F. *J. Electroanal. Chem. Interfacial Electrochem.* **1983**, *149* (1–2), 101–113.
- (52) Chance, R. R.; Brédas, J. L.; Silbey, R. *Phys. Rev. B* **1984**, *29* (8), 4491–4495.

- (53) *Conductive Polymers and Plastics* / James Margolis / Springer.
- (54) Jonas, F.; Heywang, G.; Schmidtberg, W.; Heinze, J.; Dietrich, M.; Jonas, F.; Heywang, G.; Schmidtberg, W.; Heinze, J.; Dietrich, M.; Aktiengesellschaft, B.; Gmbh, H. C. S.; Gmbh, H. C. S. Z. C.; Gmbh, H. C. S. C.; Gmbh, H. C.; Kg, H. P. M. G. & C. *Polythiophenes, process for their preparation and their use*; 1989.
- (55) Jonas, F.; Schrader, L. *Synth. Met.* **1991**, *41* (3), 831–836.
- (56) Heywang, G.; Jonas, F. *Adv. Mater.* **1992**, *4* (2), 116–118.
- (57) Sotzing, G. A.; Reynolds, J. R.; Steel, P. J. *Adv. Mater.* **1997**, *9* (10), 795–798.
- (58) Winter, I.; Reese, C.; Hormes, J.; Heywang, G.; Jonas, F. *Chem. Phys.* **1995**, *194* (1), 207–213.
- (59) Aubert, P.-H.; Groenendaal, L.; Louwet, F.; Lutsen, L.; Vanderzande, D.; Zotti, G. *Synth. Met.* **2002**, *126* (2–3), 193–198.
- (60) Okano, M. *J. Electrochem. Soc.* **1987**, *134* (4), 837.
- (61) Murakoshi, K.; Kogure, R.; Wada, Y.; Yanagida, S. *Chem. Lett.* **1997**, *26* (5), 471–472.
- (62) Saito, Y.; Azechi, T.; Kitamura, T.; Hasegawa, Y.; Wada, Y.; Yanagida, S. *Coord. Chem. Rev.* **2004**, *248* (13–14), 1469–1478.
- (63) Bazzaoui, E. A.; Aeiyaeh, S.; Lacaze, P. C. *Synth. Met.* **1996**, *83* (2), 159–165.
- (64) Sakmeche, N.; Aeiyaeh, S.; Aaron, J.-J.; Jouini, M.; Lacroix, J. C.; Lacaze, P.-C. *Langmuir* **1999**, *15* (7), 2566–2574.
- (65) Sakmeche, N.; Aaron, J.-J.; Aeiyaeh, S.; Lacaze, P.-C. *Electrochimica Acta* **2000**, *45* (12), 1921–1931.
- (66) Liu, X.; Zhang, W.; Uchida, S.; Cai, L.; Liu, B.; Ramakrishna, S. *Adv. Mater.* **2010**, *22* (20), E150–E155.
- (67) Salomon, M. *J. Solut. Chem.* **1993**, *22* (8), 715–725.
- (68) Djellab, H.; Armand, M.; Delabouglise, D. *Synth. Met.* **1995**, *74* (3), 223–226.
- (69) Xia, J.; Masaki, N.; Lira-Cantu, M.; Kim, Y.; Jiang, K.; Yanagida, S. *J. Phys. Chem. C* **2008**, *112* (30), 11569–11574.
- (70) Park, B.; Yang, L.; Johansson, E. M. J.; Vlachopoulos, N.; Chams, A.; Perruchot, C.; Jouini, M.; Boschloo, G.; Hagfeldt, A. *J. Phys. Chem. C* **2013**, *117* (44), 22484–22491.
- (71) Heinze, J.; Frontana-Urbe, B. A.; Ludwigs, S. *Chem. Rev.* **2010**, *110* (8), 4724–4771.
- (72) Randriamahazaka, H.; Noël, V.; Chevrot, C. *J. Electroanal. Chem.* **1999**, *472* (2), 103–111.
- (73) Liu, Y.; Hagfeldt, A.; Xiao, X.-R.; Lindquist, S.-E. *Sol. Energy Mater. Sol. Cells* **1998**, *55* (3), 267–281.
- (74) Park, N.-G.; Chang, S.-H.; van de Lagemaat, J.; Kim, K.-J.; Frank, A. J. *Bull.-KOREAN Chem. Soc.* **2000**, *21* (10), 985–988.
- (75) Kopidakis, N.; Benkstein, K. D.; van de Lagemaat, J.; Frank, A. J. *J. Phys. Chem. B* **2003**, *107* (41), 11307–11315.
- (76) Schlichthörl, G.; Huang, S. Y.; Sprague, J.; Frank, A. J. *J. Phys. Chem. B* **1997**, *101* (41), 8141–8155.
- (77) Koops, S. E.; O'Regan, B. C.; Barnes, P. R. F.; Durrant, J. R. *J. Am. Chem. Soc.* **2009**, *131* (13), 4808–4818.
- (78) Cameron, P. J.; Peter, L. M. *J. Phys. Chem. B* **2003**, *107* (51), 14394–14400.
- (79) Yanai, T.; Tew, D. P.; Handy, N. C. *Chem. Phys. Lett.* **2004**, *393* (1–3), 51–57.
- (80) Scalmani, G.; Frisch, M. J. *J. Chem. Phys.* **2010**, *132* (11), 114110.
- (81) Frisch, M. J.; Trucks, G. W.; Schlegel, H. B.; Scuseria, G. E.; Robb, M. A.; Cheeseman, J. R.; Scalmani, G.; Barone, V.; Mennucci, B.; Petersson, G. A.; Nakatsuji, H.; Caricato, M.;

- Li, X.; Hratchian, H. P.; Izmaylov, A. F.; Bloino, J.; Zheng, G.; Sonnenberg, J. L.; Hada, M.; Ehara, M.; Toyota, K.; Fukuda, R.; Hasegawa, J.; Ishida, M.; Nakajima, T.; Honda, Y.; Kitao, O.; Nakai, H.; Vreven, T.; Montgomery, J. A., {Jr.}; Peralta J.E.; Ogliaro, F.; Bearpark, M.; Heyd, J. J.; Brothers, E.; Kudin, K. N.; Staroverov, V. N.; Kobayashi, R.; Normand, J.; Raghavachari, K.; Rendell, A.; Burant, J. C.; Iyengar, S. S.; Tomasi, J.; Cossi, M.; Rega, N.; Millam, J. M.; Klene, M.; Knox, J. E.; Cross, J. B.; Bakken, V.; Adamo, C.; Jaramillo, J.; Gomperts, R.; Stratmann, R. E.; Yazyev, O.; Austin, A. J.; Cammi, R.; Pomelli, C.; Ochterski, J. W.; Martin, R. L.; Morokuma, K.; Zakrzewski, V. G.; Voth, G. A.; Salvador, P.; Dannenberg, J. J.; Dapprich, S.; Daniels, A. D.; Farkas, Ö.; Foresman, J. B.; Ortiz, J. V.; Cioslowski, J.; Fox, D. J. *///*.
- (82) Kitamura, T.; Ikeda, M.; Shigaki, K.; Inoue, T.; Anderson, N. A.; Ai, X.; Lian, T.; Yanagida, S. *Chem. Mater.* **2004**, *16* (9), 1806–1812.
- (83) Organic DSSC dyes | Dyenamo [http://www.dyenamo.se/dyenamo\\_dyes.php](http://www.dyenamo.se/dyenamo_dyes.php).
- (84) *J. Electroanal. Chem. Interfacial Electrochem.* **1986**, *209* (2), 417–428.
- (85) Docampo, P.; Guldin, S.; Leijtens, T.; Noel, N. K.; Steiner, U.; Snaith, H. J. *Adv. Mater.* **2014**, *26* (24), 4013–4030.
- (86) Eisfeld, A.; Briggs, J. S. *Chem. Phys.* **2006**, *324* (2–3), 376–384.
- (87) Zhang, J.; Jarboui, A.; Vlachopoulos, N.; Jouini, M.; Boschloo, G.; Hagfeldt, A. *Electrochimica Acta* **2015**, *179*, 220–227.
- (88) Zhang, J.; Ellis, H.; Yang, L.; Johansson, E. M. J.; Boschloo, G.; Vlachopoulos, N.; Hagfeldt, A.; Bergquist, J.; Shevchenko, D. *Anal. Chem.* **2015**, *87* (7), 3942–3948.

## **Chapter III**

# **Effect of the Dye-HTM Covalent Link on s-DSSCs Performances**

As shown in the Chapter II, the *in-situ* PEP process leads to a close contact between the sensitizer, adsorbed on the mesoporous TiO<sub>2</sub> photo-anode, and the conducting polymer used as HTM. In the present chapter, we are focusing on the charge transfer occurring at dye/HTM interface for a better dye regeneration process in s-DSSCs. For this purpose, we put forward the idea of completely removing this interface and to set new s-DSSCs based on covalently linked dye to the CP used as HTM. Therefore two metal-free organic dyes are first synthesized containing electroactive monomers as pendant groups. The monomer, covalently linked to the dye, is used as initiator for co-polymerization with a second monomer used as precursor in the *in-situ* PEP process to ensure the covalent linkage between the light active center and the generated copolymer used as HTM. After dyes syntheses, the mesoporous TiO<sub>2</sub> photo-anodes are sensitized by the novel dyes containing the electroactive groups and the resulting dyed photo-anodes are used to set up s-DSSC devices corresponding to the FTO/TiO<sub>2</sub>/dye-HTM/Au cells. The first photovoltaic performances of s-DSSCs based on these novels dyes are determined.

### III. 1. Optimization of the Interfacial Charge Transfer

The interfacial charge transfer processes are the key issues impacting the photovoltaic performances of a s-DSSC. After the electron injection from the photo-excited dye into the CB of the TiO<sub>2</sub>, the resulting oxidized dye returns back to ground state through the hole injection of a hole in the HTM. The dye regeneration process must be faster than each of the following two back electron transfer processes (Figure III-1): ① from TiO<sub>2</sub> to the oxidized dye in order to achieve a high photocurrent density of the device; and ② from TiO<sub>2</sub> to the HTM in order to have a high photovoltage of the device. In s-DSSCs based on CP produced by *in-situ* PEP, the dye regeneration process is faster than in conventional DSSCs based on liquid electrolyte. This is

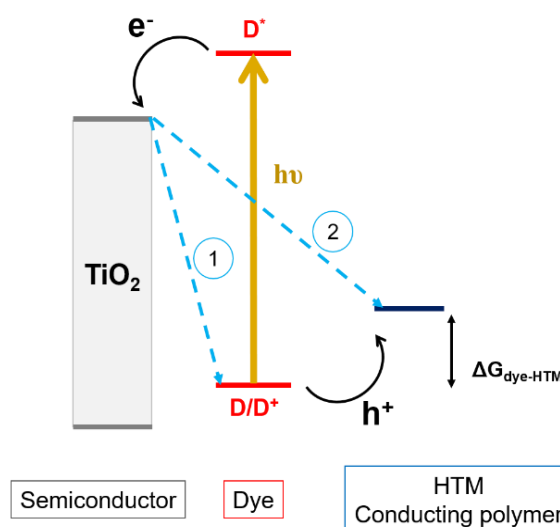


**Figure III-1:** Schematic diagram of charge transfer processes occurring in s-DSSC

attributed to the fast charge transport within the CP and hence to the direct electron transfer into the oxidized state of the dye. However the interfacial charge recombination are still present especially due to the large volume into the mesoporous TiO<sub>2</sub> unoccupied by the HTM, reported to be 80 %<sup>[1]</sup> of the total volume of the pores. Indeed, this poor pore filling can be explained by the inefficient monomer penetration during the *in-situ* PEP process in thick TiO<sub>2</sub> mesoporous layers.

### III. 1. a. General context

To solve the pore filling problem, some researchers have investigated the effect of the thickness which is limited to 7 μm, as explained in chapter 2, in order to have optimal monomer diffusion during the *in-situ* PEP<sup>[2,3]</sup>. The pore size has also been investigated as reported by Chen *et al.*<sup>[4]</sup> varying the pore size from 20 nm to about 40 nm in s-DSSC based on CP. Larger pore size leads to great improvement of the device. To further optimize the pore filling, Fukuri *et al.* proposed to perform the *in-situ* PEP with an illumination from the cathode side<sup>[1]</sup>. It results in slightly higher improvement of the photovoltaic performances ( $J_{sc}$ ,  $V_{oc}$  and FF) indicating that the back-electron transfer from TiO<sub>2</sub> to both HTM and dye is reduced.

To tackle interfacial recombination issues, a novel approach has been proposed and consists to remove the physical interface between the dye and the HTM by designing new photosensitizer dyes covalently bonded to the HTM in s-DSSC. Indeed, Odobel's group reported a P3OT chain covalently wired to a ruthenium bis-terpyridine complex acting as the sensitizer<sup>[5]</sup>. The molecular wiring of the sensitizer to the HTM significantly improves the FF and the  $V_{oc}$  indicating an enhancement of the charge transfer between the dye and the HTM. The substitution of the P3OT chain by P3HT in the Ru dye results in higher photovoltaic performances<sup>[6]</sup> with higher  $J_{sc}$ . Therefore the hole injection from the oxidized dye to the polymer chain is raised. This increase of charge transfer between the dye and HTM was highlighted by Durrant *et al.* who found that the  $J_{sc}$  is directly proportional to the hole transfer yield<sup>[7]</sup>. Similarly, another group has reported s-DSSCs based on a thiophene conjugated polymer covalently linked to a zwitterionic ruthenium complex dye deposited on the TiO<sub>2</sub> anatase electrode<sup>[8]</sup>. This s-DSSC configuration provides efficient charge carrier separation and injection into the TiO<sub>2</sub> conduction band. In both reports, the covalently linked dye/HTM compounds were the result of tedious synthetic routes. The as-obtained supermolecules were subsequently spin coated on the supporting oxide nanomaterial layer by solution process. However, it has been disclosed that spin coating of pre-synthesized

polymers on the mesoporous oxide material is not suitable<sup>[9]</sup>; the high molecular weight of these macromolecules may prevent their penetration within the TiO<sub>2</sub> mesopores providing a low surface contact between the HTM and the dye, and hence resulting to a poor charge transfer at this interface.

In the present chapter, in order to simultaneously solve interfacial recombination and pore filling issues and hence to improve the efficiency of s-DSSCs devices based on *in-situ* generated CP used as HTM, we are focusing on the decrease of the energy barrier of charge transfer between the dye and the HTM. In this respect, we report the synthesis and characterization of highly absorbing new metal-free organic dyes covalently linked to an electroactive side monomer. These electrochemically active groups are used as initiators for *in-situ* PEP in order to covalently bond the generated hole conducting CP after adsorption of the dye molecules on the mesoporous TiO<sub>2</sub>. The photovoltaic performances of the s-DSSCs obtained using this strategy are determined.

### **III. 1. b. Novel Organic Dyes Covalently Linked to the CP generated by *in-situ* PEP**

#### **III.1.b.(i) New dyes**

The new two dyes (Figure III-2), bis(2-(9H-carbazol-9-yl)ethyl)4,4'-(4-(5-(2-cyano-2-carboxyethenyl)thiophene-2-yl)phenylazanediyl)dibenzoate, denoted **ADCBZ**, and bis(2-(2,5-di(thiophene-2-yl)-1H-pyrrole)ethyl)4,4'-(4-(5-(2-cyano-2-carboxyethenyl)thiophene-2-yl)phenylazanediyl)dibenzoate denoted **ADSNS** are both designed as D- $\pi$ -A configuration based on the electron-rich TPA moiety similarly to **L1** dye, studied in the previous Chapter. The structure of **L1** would be an interesting starting configuration for further chemical structure modification.

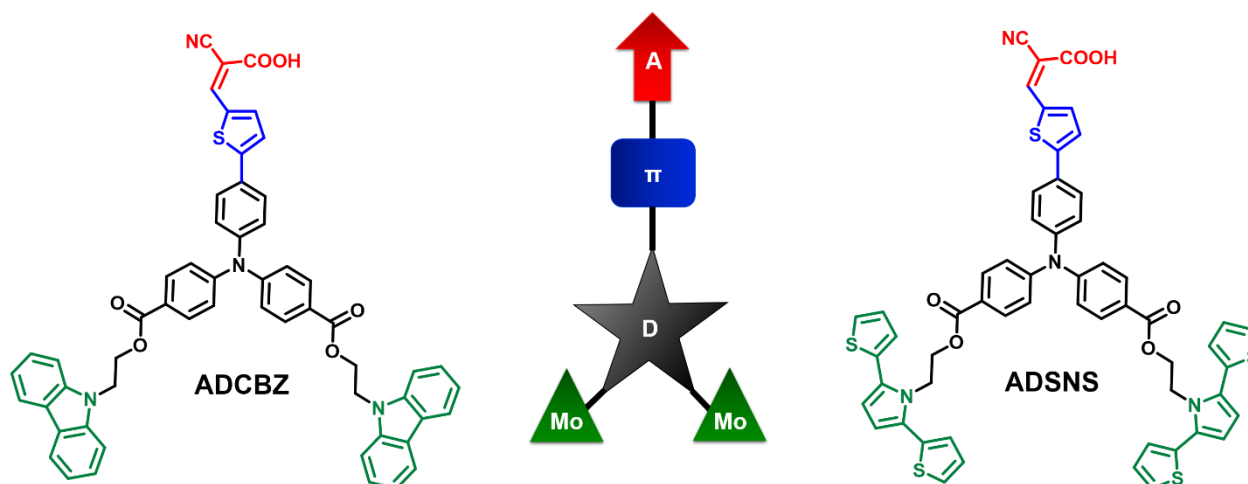


**Figure III-2:** Molecular structure of the novel organic D- $\pi$ -A dyes covalently linked to the monomer (Mo) highlighted in green.

In these dyes structures, the TPA building block holds a thiophene as  $\pi$ -conjugated bridge with a cyanoacrylic acid anchoring group as electron acceptor, and each of the two remaining phenyl groups are para-substituted with a monomer group either carbazole (denoted CBZ) or 2,5-di(thiophen-2-yl)-1H-pyrrole (denoted SNS). After adsorption of each of the new dyes on the  $\text{TiO}_2$  semiconductor, carbazole or SNS unit may undergo co-polymerization with the monomer precursor in solution, here Bis-EDOT, solubilized in organic electrolyte. This approach should produce, inside the  $\text{TiO}_2$  mesopores, a copolymer of Bis-EDOT and carbazole or SNS units covalently linked to the dye (Figure III-3).

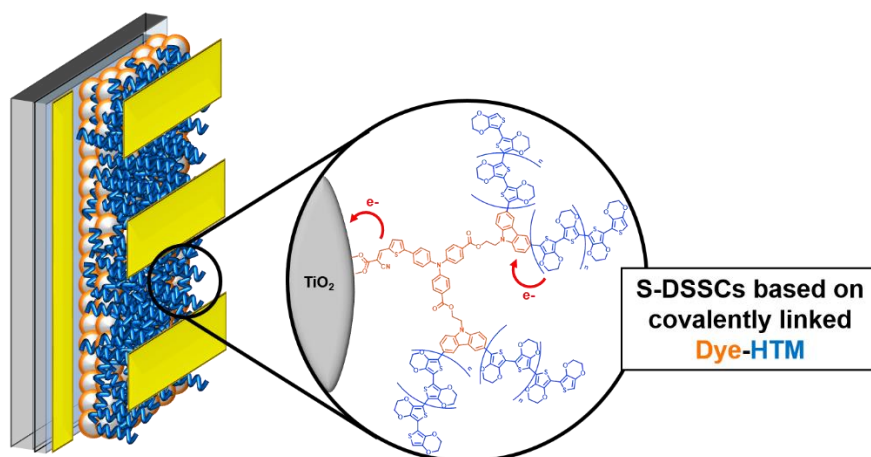


**Figure III-3:** Schematic representation of a s-DSSC based on covalently linked ADCBZ-PEDOT.

Carbazole units have been used recently as electron donor antennas<sup>[10]</sup> or as  $\pi$ -conjugated bridge<sup>[11]</sup> in organic dyes for efficient and stable DSSCs. Similarly, SNS units have



been introduced as electron donor in Ru dyes<sup>[12]</sup>. As a consequence, both monomers were neither act as electropolymerizable linkers to the HTM.

### III.1.b.(ii) Electroactive groups

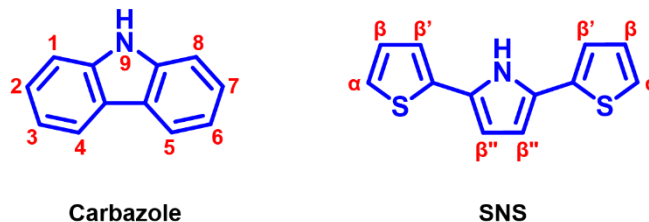


**Figure III-4:** Designation of hydrogen on carbazole and SNS monomers.

Carbazole moiety has the advantages (i) to be a cheap material, (ii) to have an excellent electron donating character, (iii) the nitrogen group can be easily substituted, (iv) different substituents can be introduced, (v) exhibits high thermal and photochemical stability, and (vi) can be easily electropolymerized. The oxidation of carbazole gave rise to a relatively stable radical cations to provide the poly(3,6-carbazole) where the repeat units in the polymer chain are linked at the 3- and 6-positions of the ring (see Figure III-4). However, the resulting polymer is in fact a dimer due to the stability of the biscarbazylum radical cations. Therefore different approaches have been proposed to get a higher molecular weight poly(3,6-carbazole). In this work, a co-polymerization of Carbazole/Bis-EDOT has been performed. This combination can give rise to interesting properties with respect to the corresponding homopolymers as reported by the Sotzing group<sup>[13]</sup>.

Similarly, the SNS moiety consisting of thiophene and pyrrole units, has also attracted considerable interest due to (i) ease of monomer synthesis, (ii) ease of electrochemical polymerization reported for the first time by Otero *et al.*<sup>[14]</sup> then proceeded by Ferraris *et al.*<sup>[15,16]</sup>, Toppare *et al.*<sup>[17,18]</sup>, Cihaner *et al.*<sup>[19,20]</sup>, and Chams *et al.*<sup>[21]</sup> especially for the N-substituted SNS derivatives. (iii) The resulting polymer is highly stable (iv) it exhibits good electrical conductivity and (v) acts as a good electron donating group if the N-functional substituent has an electron donating character. The anodic polymerization of SNS provides the poly(SNS) and occurs preferentially at  $\alpha$ -C atoms (see Figure III-4). In this work, as for carbazole, the co-polymerization has been performed between SNS and Bis-EDOT. Some works have been done on the co-polymerization of SNS and EDOT and the resulting properties are promising in various applications<sup>[22,23]</sup>.

### **III.1.b.(iii) N-functional substituent**

The N-functional substituent, linking the dye to the monomer, is a non-conjugated alkyl ester chain. This configuration is used in order to maintain the electronic properties of the dye and of the electroactive group as demonstrated by Houarner-Rassin *et al.*<sup>[24]</sup>.

In order to support our results obtained using these two new dyes, the analogous pristine dye **L1** is studied under the same conditions.

## III. 2. Experimental details

### III. 2. a. ADCBZ and ADSNS Dyes Synthesis

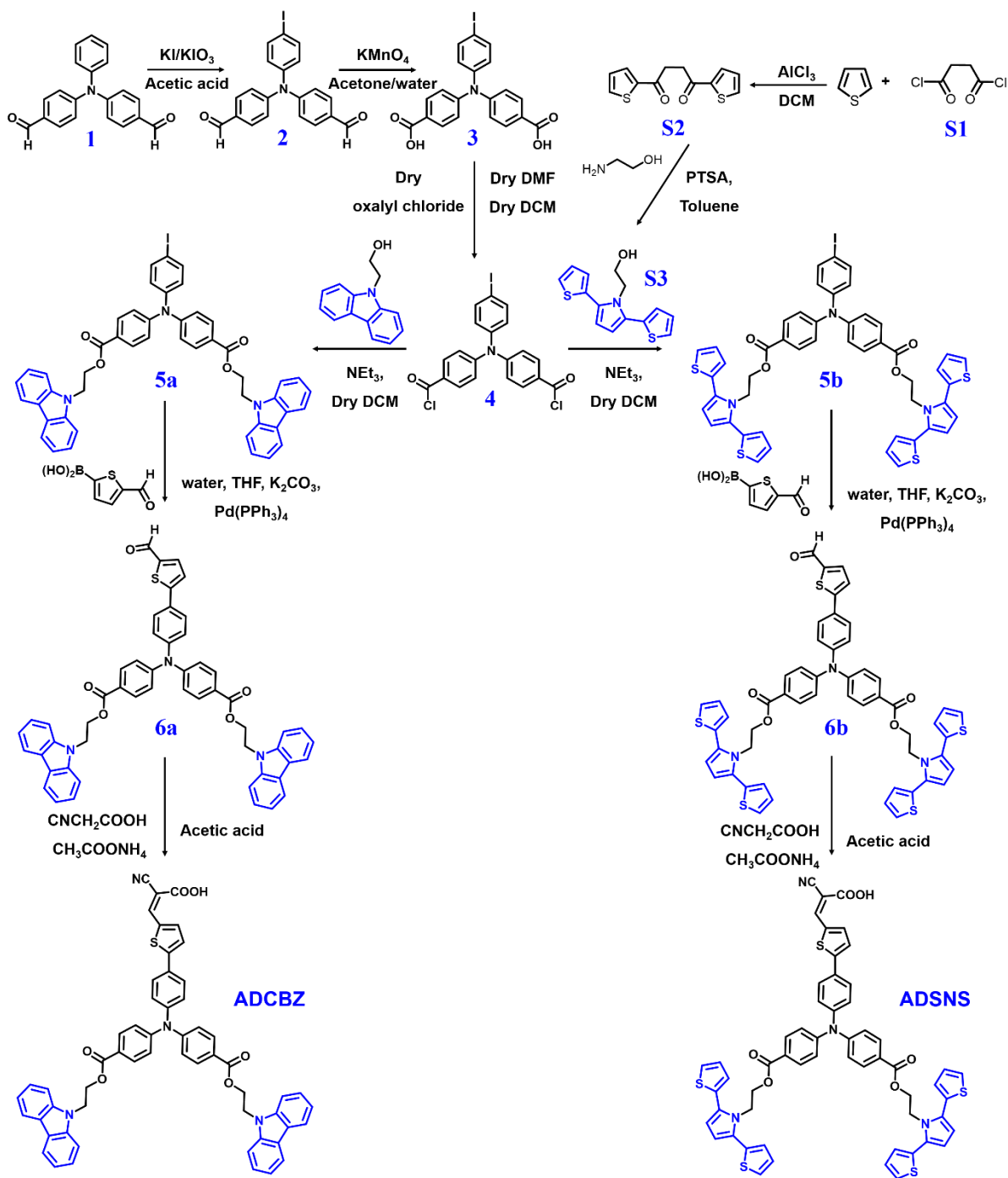


Figure III-5: Synthetic route of ADCBZ and ADSNS dyes

The commercial 4,4'-diformyltriphenylamine **1** was first iodinated in presence of potassium iodide and potassium iodate in acidic medium following the procedure recently published<sup>[25]</sup> (Figure III-5). From the desired 4,4'-(4-iodophenylazanediy) dibenzaldehyde **2**, the two aldehyde groups were oxidized with KMnO<sub>4</sub>, giving the carboxylic acid groups **3**<sup>[26]</sup>. The diacid chloride **4** was then obtained by the addition of dry oxalyl chloride catalyzed by DMF<sup>[26]</sup>. It was then condensed with the commercial 9H-carbazole-9-ethanol, giving the ester **5a**. Then, the Suzuki coupling reaction<sup>[27]</sup> has been implemented to synthesize the compound **6a** from commercial 5-formylthiophen-2-ylboronic acid and **5a**. The cyanoacrylic acid anchoring group is obtained by the Knoevenagel condensation reaction in the presence of cyanoacetic acid and ammonium acetate. The desired **ADCBZ** dye was successfully achieved.

In order to obtain **ADSNS** dye, the intermediate **S3** was first synthesized.

**S3** has been synthesized as follows (Figure III-5): within the main routes leading to the 4-di(2-thienyl)-1,4-butanedione **S2**, the double Friedel and Crafts reaction has been employed, firstly introduced by Merz and Ellinger<sup>[28]</sup>. It involves in the acylation of thiophene **S1** on succinyl chloride in the presence of Lewis acid, AlCl<sub>3</sub>. Then **S3** has been obtained from the condensation of 1,4-dicarbonyl compound with 2-aminoethanol in presence of a catalytic amount of PTSA: this reaction is referred to the Paal-Knorr synthesis<sup>[29]</sup>. The next steps follow the same procedure used to obtain **ADCBZ** to afford the compounds **5b**, **6b** and the desired **ADSNS**. Further details on dyes syntheses (reagents and conditions) have been given in Annex III-1.

### **III. 2. b. Characterization Techniques for Dyes Structure and Dye-Sensitized TiO<sub>2</sub> Substrates**

The chemical structures of the new dyes are elucidated by:

- <sup>1</sup>HNMR measured on a Bruker AVANCE III 400 MHz NMR spectrometer using CDCl<sub>3</sub> or DMSO as solvent and chemical shifts were reported as δ (ppm) values.
- High resolution mass spectrum (HRMS) was measured with Waters LCT Premier Mass Spectrometer in the Small Molecule Mass Spectrometry platform of ICSN.

Details concerning the intermediate products are given in Annex III-2.

The optical properties of dyes were investigated by fluorescence spectroscopy in ACN ( $C = 2.7 \times 10^{-6}$  M), by UV-Vis spectroscopy in ACN ( $C = 2.7 \times 10^{-5}$  M). These experimental results were compared to the theoretical results obtained using the DFT.

The electrochemical properties of **ADCBZ**, **ADSNS**, and **L1** dyes are investigated by cyclic voltammetry in acetonitrile containing 0.1 M LiClO<sub>4</sub>. To measure UV-Vis-NIR absorption spectra in solid state, dye-sensitized TiO<sub>2</sub> electrodes, with and without PEDOT are prepared. The measurements were performed on a Cary 5000 UV-Vis-NIR spectrophotometer (VARIAN, photometric accuracy is  $\leq 0.00025$  Abs., photometric range is 8 Abs.). The TiO<sub>2</sub>/FTO substrate signal was used as calibration background. Analyses of surface morphology dye-sensitized TiO<sub>2</sub> electrodes, with and without PEDOT, have been done by SEM.

### **III. 2. c. In-situ PEP process and s-DSSC performances**

The *in-situ* PEP process was carried out by chronoamperometry (see the experimental section in chapter 2) in organic medium using Bis-EDOT as monomer precursor. s-DSSCs are assembled following the procedure detailed in the previous chapter. The photovoltaic performances of s-DSSCs are determined from the I-V curves and from IPCE measurements.

## **III. 3. Results and Discussion**

### **III. 3. a. Characterization of Dye Molecules (ADCBZ and ADSNS)**

#### **III.3.a.(i) <sup>1</sup>H NMR and FTIR analyses**

The preparation **ADCBZ** and **ADSNS** described in Figure III-5 leads to an overall yield of 11 % after 6 steps and of 10 % for 8 steps respectively.

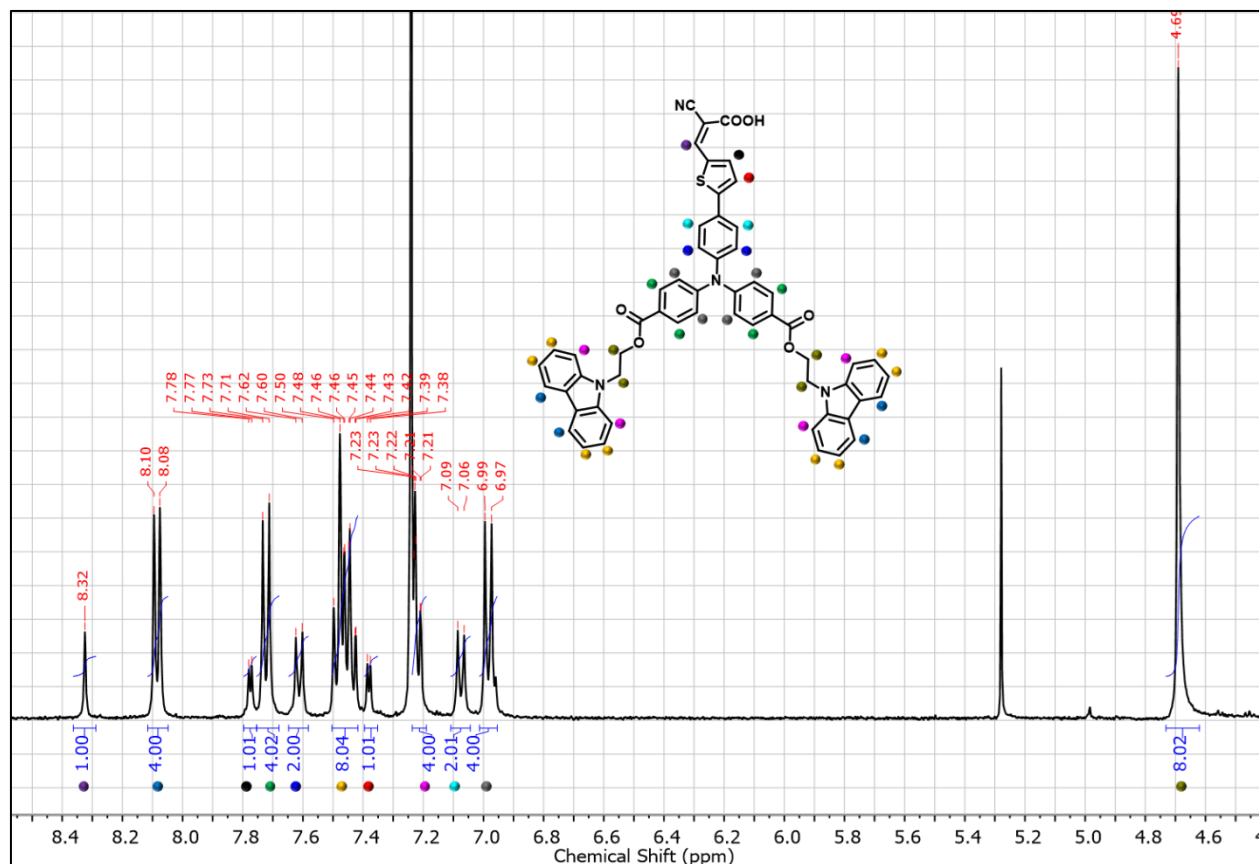


**Figure III-6:** NMR  $^1\text{H}$  spectrum of the ADCBZ dye in  $\text{CDCl}_3$  with proton assignment.

For both, the preparation yield resulting from the Suzuki coupling reaction is low; this reaction is the major limiting step of the synthesis. The final dyes structures are confirmed by  $^1\text{H}$  NMR (see Figure III-6 and Figure III-7) where the main characteristic peaks are observable at about 8.32 ppm assigned to the proton from the acceptor group, at 7.77 ppm and 7.38 ppm associated to the protons of the thiophene. Surprisingly, for ADCBZ protons providing from two distinct carbons of the alkyl ester substituent display the same chemical shift as a single peak  $\delta = 4.69$  ppm in contrast to ADSNS where two triplet are observed. This difference is due to the higher donating property of carbazole compared to SNS.

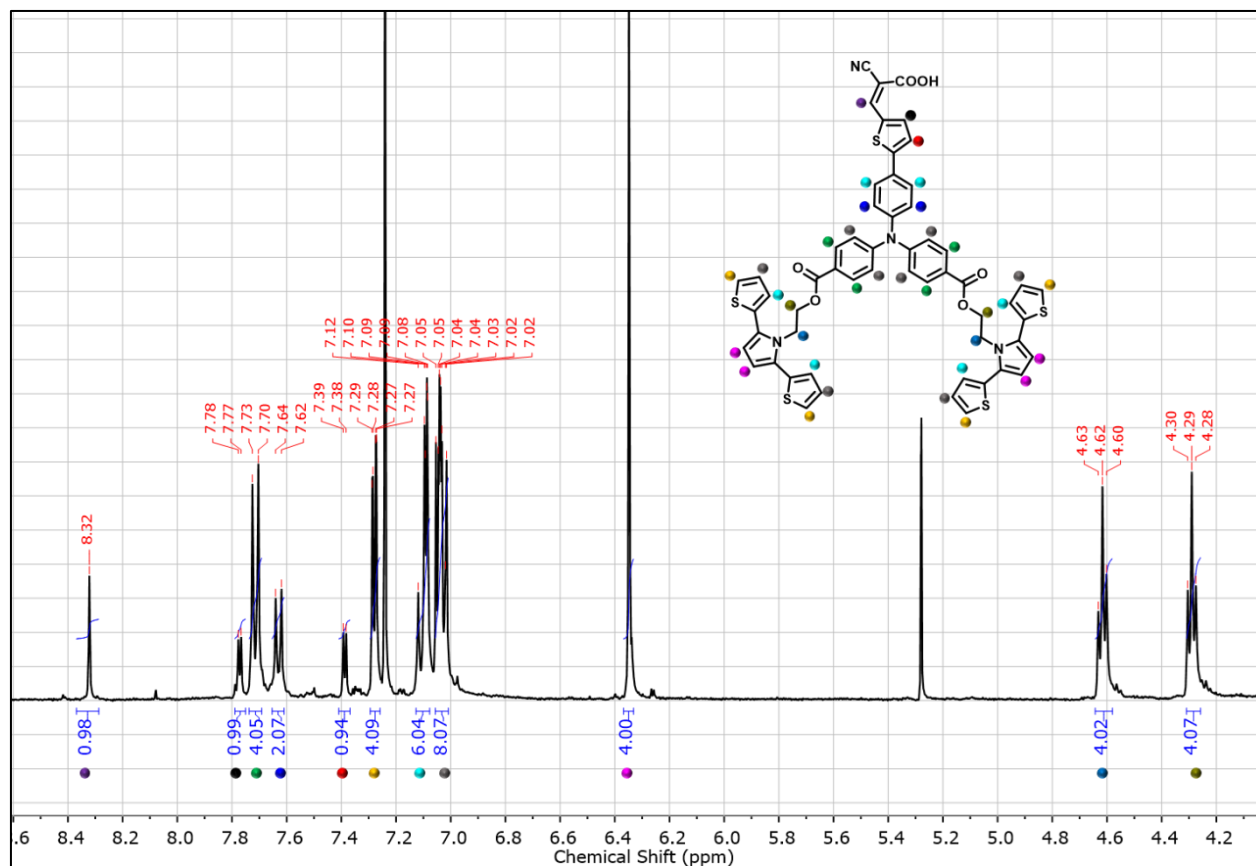


**Figure III-7:** NMR <sup>1</sup>H spectrum of the ADSNS dye in CDCl<sub>3</sub> with proton assignment.

### III.3.a.(ii) Optical and Theoretical Properties of the Dyes

The UV visible absorption spectrum in DCM (Figure III-8) for **ADCBZ** dye is characterized by a strong absorption band located at 444 nm ( $\epsilon = 34700 \text{ M}^{-1} \cdot \text{cm}^{-1}$ ) assigned to the ICT band. For **ADSNS**, the ICT absorption band is located at 440 nm ( $\epsilon = 25490 \text{ M}^{-1} \cdot \text{cm}^{-1}$ ). Compared to the corresponding value for **L1** dye lying at 432 nm ( $\epsilon = 23300 \text{ M}^{-1} \cdot \text{cm}^{-1}$ ), the ICT bands of the new dyes are slightly red-shifted due to the monomers substitution.

$$\lambda_{\text{max}}(\text{ADCBZ}) > \lambda_{\text{max}}(\text{ADSNS}) > \lambda_{\text{max}}(\text{L1})$$

In addition and as regard to **L1** dye, the molar extinction coefficients of **ADCBZ** and **ADSNS** are increased by a factor of 1.5 and 1.1 respectively.

$$\epsilon(\text{ADCBZ}) > \epsilon(\text{ADSNS}) > \epsilon(\text{L1})$$

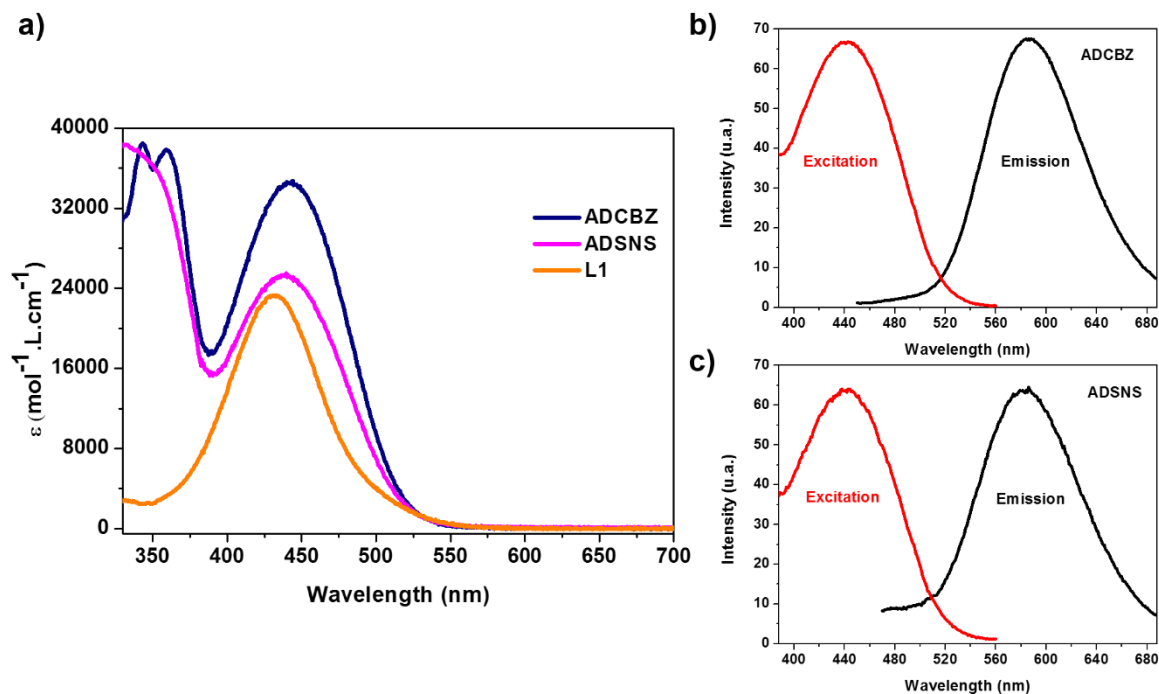


**Figure III-8:** (a) UV-Visible absorption spectra of ADCBZ, ADSNS and L1 dyes in DCM and (b) excitation and emission spectra of the two novel dyes in DCM.

Hence, with a high molar extinction coefficient and a higher wavelength, **ADCBZ** dye should ensure good light harvesting capacity in s-DSSC and should generate a high IPCE. Table III-1 presents the UV-vis data and the energy values for the different electronic and orbital levels calculated from experimental data.

When dyes are adsorbed on the TiO<sub>2</sub> surface the wavelength of maximum absorptions are 16 nm blue shifted with respect to those obtained in solution for **ADCBZ** and **ADSNS**. The blue shift is more pronounced compared to **L1** (8 nm) attributed to the H-type aggregate<sup>[30]</sup>.

The energy bandgap values, determined from the intercept (Figure III-8b and c) of the excitation and emission spectra of the dyes, are  $\Delta E_{0-0} = 2.40$  eV ( $\lambda = 518$  nm) and  $\Delta E_{0-0} = 2.44$  eV ( $\lambda = 510$  nm) for **ADCBZ** and **ADSNS** respectively, which are comparable to the bandgap of the **L1** reference dye,  $\Delta E_{0-0} = 2.35$  eV ( $\lambda = 530$  nm).

$$E_{0-0}(\mathbf{L1}) < E_{0-0}(\mathbf{ADCBZ}) < E_{0-0}(\mathbf{ADSNS})$$

The optical properties have also been investigated theoretically for equilibrium structures of dyes using DFT. The calculations show that the ICT bands which originate from the HOMO→LUMO single electronic excitation (or S<sub>0</sub>→S<sub>1</sub> transition) are found in the visible region at 444 nm, 440 nm and 432 nm for **ADCBZ**, **ADSNS** and **L1** respectively, details are provided in



Annex III-3. For both **ADCBZ** and **ADSNS** molecules the HOMO is centered on the triphenylamine core extended out to the ester side chains while the LUMO is predominantly localized on the acceptor part of the dye. The HOMO and LUMO orbitals show a good overlap on the  $\pi$ -conjugated bridge between acceptor and donor groups which suggests an efficient ICT during excitation of the dyes that allows for electron injection into  $\text{TiO}_2$ . This supports well that the maximum absorption wavelengths at 444 nm for **ADCBZ** and 439 nm for **ADSNS** dye are attributed to the HOMO-LUMO transitions of both dyes. The small red-shift of the ICT absorption of both dyes stems from the extension of the donor part yielding an extended HOMO-LUMO delocalization with respect to **L1**.

### III.3.a.(iii) Electrochemical Properties of Dyes

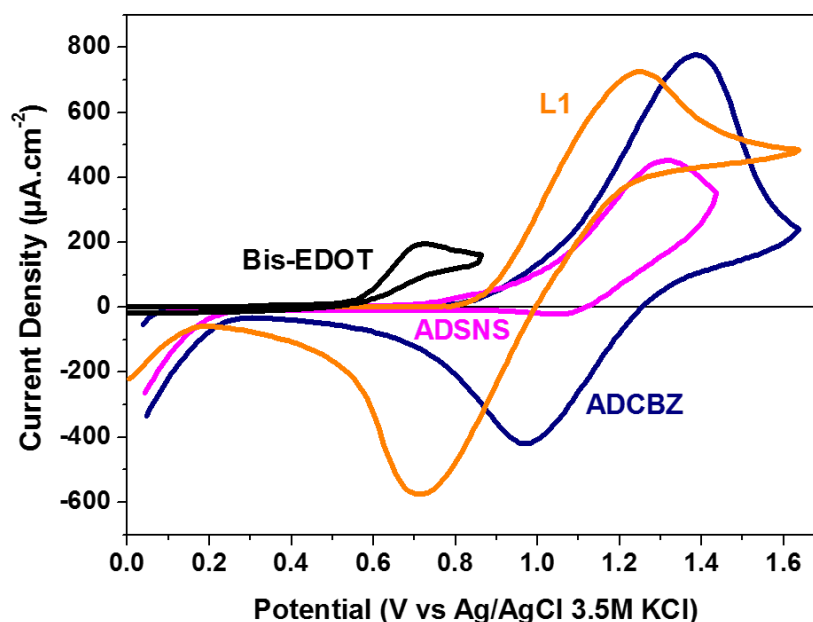


**Figure III-9:** Cyclic voltammograms of the ADCBZ, ADSNS and L1 dyes sensitized  $\text{TiO}_2$  photo-anode and of Bis-EDOT in organic electrolyte.

The CVs in organic medium displayed reversible redox behavior for all dyes (Figure III-9), where their onset oxidation potentials, ascribed to the oxidation of the donor group, are located at about 0.87 V, 0.82 V and 0.85 V vs. Ag/AgCl for **ADCBZ**, **ADSNS** and **L1**, respectively. The corresponding energy values in reference to vacuum calculated from the onset oxidation potentials, corresponds to  $E_{\text{HOMO}} = -5.52$  eV and  $E_{\text{HOMO}} = -5.47$  eV for **ADCBZ** and **ADSNS** respectively, a more negative level than that of the CB of PEDOT. As concerns the energy levels of the dyes' excited state, it is calculated by adding the energy  $\Delta E_{0-0}$  to the  $E_{\text{HOMO}}$  and is

estimated to be  $E_{\text{LUMO}} = -3.12$  eV for **ADCBZ** and  $E_{\text{LUMO}} = -3.03$  eV for **ADSNS**. These values indicate a favorable intramolecular charge separation resulting in an easy hole transfer from the dye to the HTM and an efficient electron injection from the excited dye to the conduction band of the  $\text{TiO}_2$ . All dyes display high oxidation potentials with respect to the onset of the oxidation potential of Bis-EDOT, therefore they are suitable for the *in-situ* PEP process.

Dye	$\lambda_{\text{max, abs}}$ (nm)	$\epsilon_{\text{max}}$ ( $\text{mol}^{-1} \cdot \text{L} \cdot \text{cm}^{-1}$ )	$\lambda_{\text{max, exc}}$ (nm)	$\lambda_{\text{max, em}}$ (nm)	$E_{\text{ox}}$ (V vs. Ag/AgCl)	HOMO (eV)	LUMO (eV)	$E_{0-0}$ (eV)
<b>ADCBZ</b>	444	34700	440	585	1.39	-5.52	-3.12	2.40
<b>ADSNS</b>	440	25490	441	584	1.32	-5.47	-3.03	2.44
<b>L1</b>	432	23300	448	622	1.25	-5.50	-3.15	2.35

**Table III-1:** Optical and electrochemical properties of ADCBZ, ADSNS, and L1 dyes.

### III. 3. b. *In-situ* PEP deposition of PEDOT on the Sensitized $\text{TiO}_2$

#### Photo-anodes

#### III.3.b.(i) *In-situ* PEP process

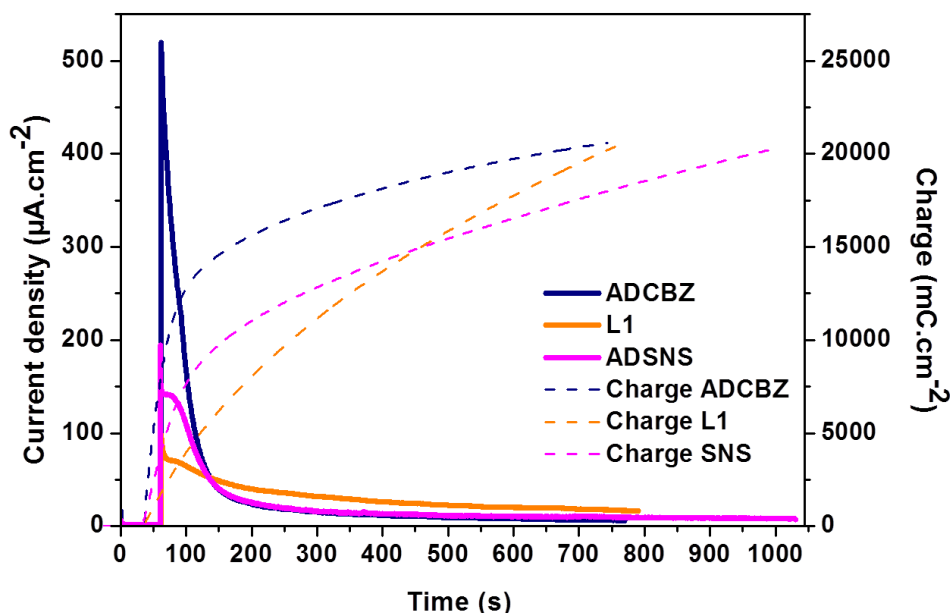


**Figure III-10:** Photocurrent variation (solid curves) and total polymerization charge (dotted curves) during the *in-situ* PEP process of Bis-EDOT in organic medium using organic dyes under a potential of 0.20 V vs. Ag/AgCl and 0.1 Sun.

The current-time obtained during the *in-situ* PEP of Bis-EDOT using the **ADCBZ**, **ADSNS** or **L1** are illustrated in Figure III-10. The current density transient measured for **ADCBZ** is relatively high compared to those measured for **ADSNS** and **L1** dyes, indicating very efficient electron transfer from Bis-EDOT monomer (or carbazole moiety) after oxidation to the dye and also from the dye to the TiO<sub>2</sub> nanoporous layer. Indeed, for both **ADCBZ** and **ADSNS** dyes, the first current density peak originates from the oxidation of each of the monomers linked to the dye (carbazole or SNS) and also from the oxidation of the Bis-EDOT monomer solubilized in electrolytic solution, followed by their coupling reactions following it. For the **L1** dye, the current is only due to the oxidation of the solubilized Bis-EDOT monomers oxidation. The current densities measured after 600 seconds for all dyes are stable and comparable indicating an efficient photo-electrochemical polymerization process. The amount of charge deposited is set at 20 mC.cm<sup>-2</sup>.

### III.3.b.(ii) Characterization of the Dye Sensitized TiO<sub>2</sub> Photo-anodes with and without HTM

The FTIR spectrum carried out on the new **ADCBZ** dye adsorbed on TiO<sub>2</sub> before HTM deposition (Figure III-11a) shows two strong bands at 725 cm<sup>-1</sup> and 751 cm<sup>-1</sup>, assigned to CH “out of plane” bending in unsubstituted carbazole<sup>[31]</sup>. The Figure III-11a represents also the spectrum from the same **ADCBZ** dye adsorbed on TiO<sub>2</sub> after HTM deposition by *in-situ* PEP. In this spectrum the band at 751 cm<sup>-1</sup> disappears whereas a strong band at about 810 cm<sup>-1</sup> is observed. This new strong “out of plane” bending peak at around 810 cm<sup>-1</sup> has been reported as a reliable marker certifying that the 3 and 6 positions of the carbazole moiety are substituted (coupling)<sup>[31]</sup>.

Similarly the FTIR spectrum of **ADSNS** displays a strong band below 700 cm<sup>-1</sup>, precisely at 693 cm<sup>-1</sup>, which refers to  $\alpha$ -H atoms of the thiophene moiety from the SNS structure (Figure III-11b) as reported by Otero *et al.*<sup>[14]</sup>. After PEDOT deposition, the spectrum shows the disappearance of this main characteristic peak at 693 cm<sup>-1</sup> whereas the peaks at 765 cm<sup>-1</sup> and 841 cm<sup>-1</sup> assigned to  $\beta$ -/ $\beta'$ -H atoms and  $\beta''$ -H atoms, are still present. These results support well that a copolymer is obtained from PEDOT chains combined with carbazole or SNS units leading to a HTM covalently linked to the dye as indicated in Figure III-11b.

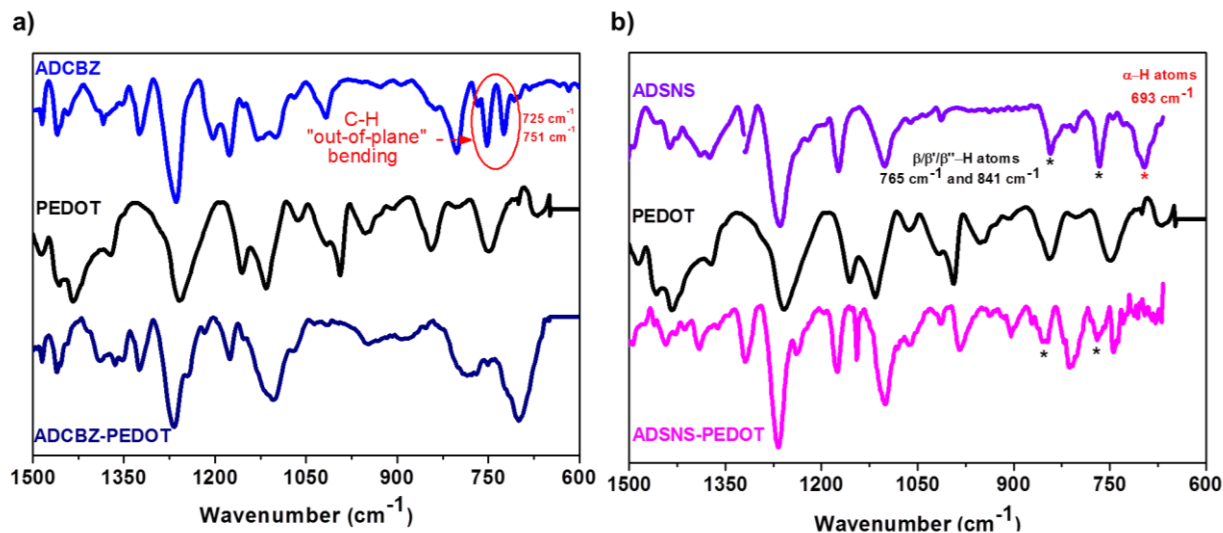


**Figure III-11:** Transmission FTIR spectra using the transmission of the substrate material as reference of (a) ADCBZ-PEDOT film and of (b) ADSNS-PEDOT film.

Furthermore, as clearly set out in the SEM images (Figure III-12) performed before and after *in-situ* PEP, the deposited polymer fills properly the pores of the dye anchored on the TiO<sub>2</sub> substrate.

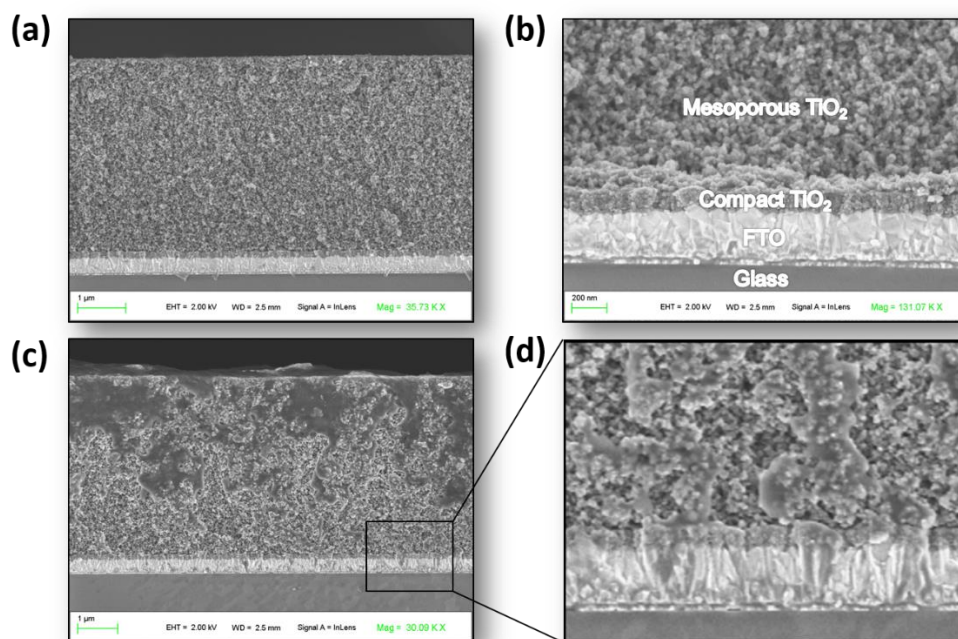


**Figure III-12:** Cross-sectional SEM views of the TiO<sub>2</sub> substrate supporting the ADCBZ dye before PEP (a) with 1 μm scale bar, (b) with 200 nm scale bar and after PEP (c) with 1 μm scale bar, (d) with magnification.

The electronic properties of deposited copolymer on dyed TiO<sub>2</sub> substrates were also investigated after the photo-oxidation using UV-vis-NIR measurements to further understand the copolymer electronic properties (Annex III-4). A broad absorption is observed between 600 nm and 1000 nm, for all sensitized TiO<sub>2</sub> photo-anodes with HTM, which belongs to the polaron and bipolaron states of the p-doped PEDOT co-polymer. The higher oxidation state of PEDOT co-polymer is observed for the two novel dyes where the NIR absorption is located at high wavelengths. This means that the PEDOT co-polymer is highly oxidized, in both cases, and may resulting in higher hole transport leading to good photocurrent in s-DSSC.

### III. 3. c. s-DSSCs devices performances

#### III.3.c.(i) I-V Characteristics

A thin gold layer used as counter-electrode was vapor deposited on the PEDOT film of the PEDOT-Dye/TiO<sub>2</sub>/FTO solid state electrode. The photovoltaic performances acquired under AM 1.5G full simulated sunlight for both **ADCBZ** and **ADSNS** based s-DSSCs compared to those of of **L1** based s-DSSC (Figure III-13a) are summarized in Table III-2.

Dye	V <sub>oc</sub> (V)	J <sub>sc</sub> (mA.cm <sup>-2</sup> )	FF (%)	Efficiency η (%)
<b>ADCBZ</b>	0.54	3.2	59	1.03
<b>ADSNS</b>	0.40	1.78	52	0.36
<b>L1</b>	0.43	3.70	57	0.91

**Table III-2:** Photovoltaic parameters of s-DSSCs based on ADCBZ, ADSNS and L1 dyes under the AM 1.5G illumination of the simulated sunlight (100mW/cm<sup>2</sup>)

The overall efficiency of the device based on **ADCBZ** dye yield up to η= 1.03 %, with J<sub>sc</sub>= 3.2 mA/cm<sup>2</sup>, V<sub>oc</sub>= 0.54 V and FF= 59 %. As regard **ADSNS**, the device is less performant yielding η= 0.36 %, J<sub>sc</sub>= 1.78 mA/cm<sup>2</sup>, V<sub>oc</sub>= 0.40 V and FF= 52 %. Our results point out a prominent improvement compared to those obtained in s-DSSCs reported previously by Houarner-Rassin who used pre-synthesized covalently wired Ru dye – P3OT<sup>[6]</sup> and obtained η= 0.16 %, J<sub>sc</sub>= 0.069 mA/cm<sup>2</sup>, V<sub>oc</sub>= 0.81 V, FF = 25 % or by Saito *et al.*<sup>[32]</sup> who used covalently wired Ru dye – HTM generated by PEP and obtained η= 0.26 %, J<sub>sc</sub>= 1.2 mA/cm<sup>2</sup>, V<sub>oc</sub>= 0.56 V, FF= 39 %. This improvement was expected from the concept of *in-situ* production of the PEDOT

covalently linked to the organic dye and clearly supports that the charge transfer processes were improved at TiO<sub>2</sub>/dye-HTM interface. Except for the photocurrent density, the photovoltaic parameters of **ADCBZ** based s-DSSC are slightly higher with respect to **L1** ( $\eta=0.91\%$ ) particularly the  $V_{oc}$  (0.43 V) and the FF (57 %). In fact, the photocurrent density, controlled by the light-harvesting and electron injection processes, led to 3.2 mA.cm<sup>-2</sup> for **ADCBZ** which is lower as regard to **L1** (3.7 mA.cm<sup>-2</sup>). For **ADSNS**, the device seems to be less efficient compared to **L1** and **ADCBZ** which is probably due its higher bandgap.

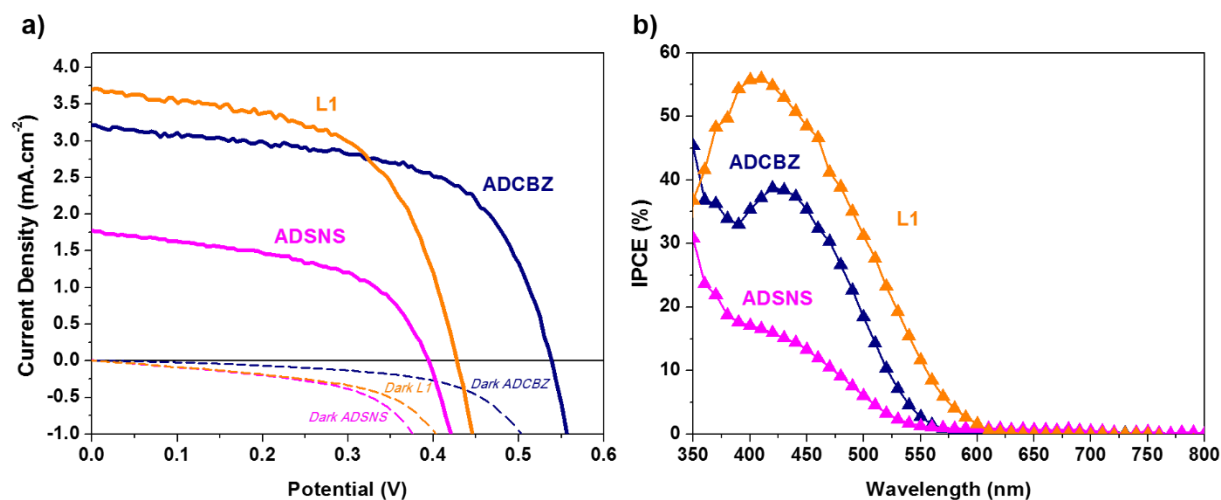


**Figure III-13:** (a) J-V characteristics of s-DSSCs based on ADCBZ, ADSNS and L1 dyes using PEDOT as HTM under the AM 1.5G illumination of the simulated sunlight (100mW/cm<sup>2</sup>). (b) IPCE spectra of the cells photosensitized by the new ADCBZ and ADSNS dyes and L1.

### III.3.c.(ii) IPCE

The IPCE spectra of dyes based s-DSSCs are illustrated in Figure III-13b. The IPCE of **ADCBZ** based s-DSSC exceeds 20 % in a spectral range from 400 to 500 nm with a maximum reaching 38 % at 420 nm which is consistent with its high absorption coefficient. The s-DSSC using **L1** dye exhibits the highest IPCE with a maximum of 56 % at 410 nm and correlates well with the photocurrent observed for this device ( $J_{sc}=3.7$  mA.cm<sup>2</sup>). s-DSSC based **ADSNS** has the lowest IPCE which does not exceed 20 % particularly owing to the low  $J_{sc}$ . The IPCE is also in agreement with the  $E_{0-0}$  of the individual dyes. The relatively low IPCE values for **ADCBZ** and **ADSNS** suggests that the electron injection from the excited state of this dye to the TiO<sub>2</sub> is probably not efficient inducing more electron recombination in the device.

### III.3.c.(iii) Photo-Induced Absorption Spectroscopy

PIA measurements are performed for the s-DSSCs based on each organic dye in order to qualitatively assess the electron injection and dye regeneration processes. The dyed photo-anode, in absence of HTM, is used as reference and PIA measurements are carried out both on the dyed photo-anode with and without HTM, under illumination as illustrated in Figure III-14. All three dyes should inject electrons in the CB of the TiO<sub>2</sub> and should become oxidized. This dye oxidized state is essentially measured in the range from 650 nm to 800 nm as an increase in absorbance (positive  $\Delta A$  signal). In the range of 500 to 600 nm, the negative  $\Delta A$  signal is attributed to the dye in ground state. For all three dyes, both signals (negative and positive) are observed. Therefore it can be considered that the injection process has taken place. In presence of PEDOT, we assume that the absorption contribution from PEDOT is similar for the three dyes. The absorption peak of **L1** dye at oxidized state is weaker of 72 % in presence of PEDOT (red curve, Figure III-14c) compared to the same absorption peak in absence of PEDOT (black curve, Figure III-14c). This means that the lifetime of the dye at oxidized state is at 72 % shorter than that of the dye's oxidized state when HTM is not present. Therefore, the **L1** dye regeneration by the PEDOT HTM is efficient. For **ADCBZ** and for **ADSNS** dyed photo-anode, the peak corresponding to its oxidized state absorption is respectively 39 % and 23 % lower than the peak corresponding its oxidized state absorption in absence of PEDOT. This indicates a less dye regeneration by HTM when **ADCBZ** sensitizer is considered and even less for **ADSNS**.

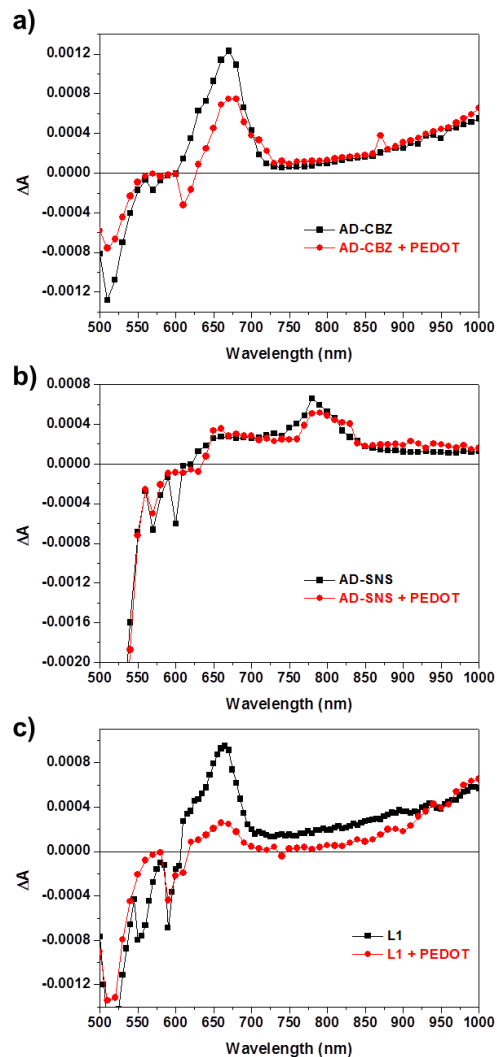


**Figure III-14:** PIA spectra of (a) ADCBZ, (b) ADSNS and (c) L1 dyes adsorbed at a nanostructured TiO<sub>2</sub> film without (black) and with (red) PEDOT.

These PIA results reveal that the dye regeneration process for the devices performances sensitized with **ADCBZ** and **ADSNS**, is not as efficiently as **L1** based s-DSSC which could be a possible reason of the low  $J_{sc}$ .

### **III. 3. d. Discussion**

The comparison of our results with those of Houarner-Rassin *et al.* and of Saito *et al.*, shows that the introduction of an organic dye covalently linked to the HTM is a powerful approach for s-DSSCs applications. The HTM formation through the PEP process allows providing a good pore filling and also an efficient electron transfer process between the dye and the mesoporous TiO<sub>2</sub> nanomaterial according to the high polymerization current. However, this is achieved under 0.2 V vs. Ag/AgCl which makes the charge separation process mandatory and irreversible since the recombination process is decreased by the applied bias. Indeed, the electron transfer from the oxidized monomer to the dye is followed by an irreversible chemical reaction (monomers coupling) and under these conditions the recombination process is prevented by the applied potential value. In the final s-DSSCs the long-lasting charge separation is key to the performance of solar cells<sup>[33]</sup>. In our case, the new design functionalized dye highlights the charge separation obtained by the covalent link with the HTM while decreasing the recombination losses occurring between the oxide semiconductor and the HTM. The photocurrent for **ADCBZ** and **ADSNS** are lower compared to **L1**, which can be explained by the configuration of the dye immobilized on the TiO<sub>2</sub> surface which is probably planar and not at a perpendicular angle to the surface<sup>[34]</sup>. Indeed, usually, carboxylic acid is used as anchoring group whereas alkyl groups linked to the dye, as bulky substituents, are generally used to avoid dye aggregation as well as other contact between the dye and the TiO<sub>2</sub> surface in order to prevent the recombination processes<sup>[34]</sup>. These synthesized new organic dyes contain the same anchoring group but also two ester groups which may be close to the surface and result in other supplementary binding sites to the TiO<sub>2</sub> surface. This may probably result in less rapid dye regeneration with respect to the electron injection from the oxidized dye to the TiO<sub>2</sub>. Hence an important recombination process at the TiO<sub>2</sub>/dye interfaces.



### III. 3. e. Impact of the s-DSSCs aging process on photovoltaic performances

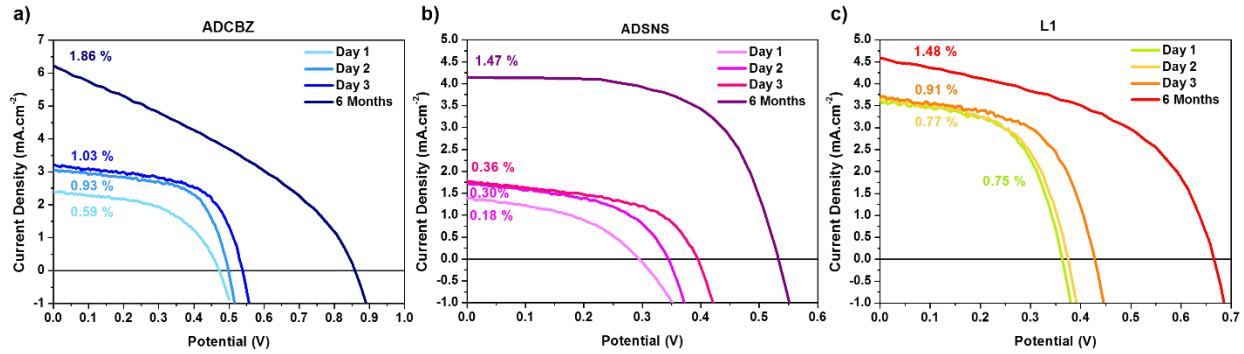


**Figure III-15:** J-V characteristics of s-DSSCs based on (a) ADCBZ, (b) ADSNS, and (c) L1 dyes after 1, 2, 3 days and 6 months under the AM 1.5G illumination of the simulated sunlight (100mW/cm<sup>2</sup>).

Dye	Aging time	V <sub>oc</sub> (V)	J <sub>sc</sub> (mA.cm <sup>-2</sup> )	FF (%)	Efficiency η (%)
ADCBZ	Day 1	0.47	2.41	52	0.59
	Day 2	0.50	3.03	61	0.93
	Day 3	0.54	3.20	59	1.03
	6 months	0.85	6.23	35	<b>1.86</b>
ADSNS	Day 1	0.30	1.39	44	0.18
	Day 2	0.35	1.73	50	0.30
	Day 3	0.40	1.78	52	0.36
	6 months	0.53	4.09	63	<b>1.37</b>
L1	Day 1	0.37	3.62	57	0.75
	Day 2	0.38	3.64	56	0.77
	Day 3	0.43	3.70	57	0.91
	6 months	0.66	4.60	48	<b>1.48</b>

**Table III-3:** Photovoltaic parameters of s-DSSCs based on ADCBZ, ADSNS and L1 dyes after 1, 2, 3 days and 6 months under the AM 1.5G illumination of the simulated sunlight (100mW/cm<sup>2</sup>).

For large scale applications, the s-DSSC must be stable in the long-term. Therefore we evaluate the impact of the obtained s-DSSCs aging process on the photovoltaic performances under a total ambient atmosphere (Figure III-15). After 3 days, the trend of each s-DSSC regardless of the dye is comparable. Indeed, in all cases, V<sub>oc</sub>, FF and J<sub>sc</sub> simultaneously increase with time inducing an

increase of the efficiency (Table III-3). These improvements are probably originating from the solvent provided from the *in-situ* PEP and from the additives solution leading to a better contact between the CE and the HTM is better resulting in a better charge transfer between both components and hence a decrease of charge recombination. Interestingly, after 6 months, the efficiencies of the different s-DSSCs further increase. In case of **L1**, the efficiency is 1.6 fold higher and reaches 1.48 %, where the  $V_{oc}$  is 1.5 fold increased (660 mV) and the  $J_{sc}$  is 1.2 fold higher (4.6 mA.cm<sup>-2</sup>). For **ADSNS**, both  $V_{oc}$  (1.3 fold) and  $J_{sc}$  (2.3 fold) are significantly improved with respect to those measured after 3 days, and the device yields an efficiency of 1.37 %. For **ADCBZ**, the efficiency is even improved compared to **ADSNS** and **L1** and reaches 1.86 % with an increase of both  $V_{oc}$  (1.6 fold) and  $J_{sc}$  (2 fold) photovoltaic parameters. This improvement could be attributed to the structural reorganization of the PEDOT conducting polymer induced by the solvent evaporation resulting in a better hopping transport within the polymer chains. This hypothesis will be verified through the measurements of conductivity of the HTM material in the near future as prospect.

### **III. 4. Conclusion**

In the present chapter, in order to solve interfacial recombination and pore filling issues that take place in s-DSSCs devices based on *in-situ* generated CP used as HTM, the objective of decreasing the energy barrier of the charge transfer between the dye and the HTM was successfully achieved. We developed a new strategy to obtain a covalent linkage between the dye and the HTM resulting in an elimination of the interface between these two components. The synthesis and characterization of two highly absorbing new metal-free organic dyes have been achieved: each one is covalently linked to a different electroactive monomer. The *in-situ* PEP processes, using any dye among the synthesized dyes, show moderate efficiencies when compared to that of the commercial pristine **L1** dye. When the resulting new dyes covalently linked to the HTM are introduced in s-DSSCs, the  $V_{oc}$  is, as high as, that of **L1** dye based s-DSSCs where the PEDOT CP is not linked to the dye. This indicates that the recombination process occurring at dye-HTM is minimize, as desired. The low  $J_{sc}$  is attributed to a possible interaction between the mesoporous TiO<sub>2</sub> surface and the ester function, inducing charge recombination at this interface. Switching this ester function by another function in the new

covalently linked dye-HTM will avoid this undesired interaction and may reducing recombination processes between electrons in the  $\text{TiO}_2$  with the holes of the oxidized dye, leading to an optimize final s-DSSC device.

### III. 5. References

- (1) Fukuri, N.; Masaki, N.; Kitamura, T.; Wada, Y.; Yanagida, S. *J. Phys. Chem. B* **2006**, *110* (50), 25251–25258.
- (2) Yanagida, S.; Yu, Y.; Manseki, K. *Acc. Chem. Res.* **2009**, *42* (11), 1827–1838.
- (3) Zhang, J.; Häggman, L.; Jouini, M.; Jarboui, A.; Boschloo, G.; Vlachopoulos, N.; Hagfeldt, A. *ChemPhysChem* **2014**, *15* (6), 1043–1047.
- (4) Chen, Z.; Tang, Y.; Yang, H.; Xia, Y.; Li, F.; Yi, T.; Huang, C. *J. Power Sources* **2007**, *171* (2), 990–998.
- (5) Houarner, C.; Blart, E.; Buvat, P.; Odobel, F. *Photochem. Photobiol. Sci. Off. J. Eur. Photochem. Assoc. Eur. Soc. Photobiol.* **2005**, *4* (2), 200–204.
- (6) Houarner-Rassin, C.; Blart, E.; Buvat, P.; Odobel, F. *Photochem. Photobiol. Sci.* **2008**, *7* (7), 789–793.
- (7) Kroeze, J. ?E.; Hirata, N.; Schmidt-Mende, L.; Orizu, C.; Ogier, S. ?D.; Carr, K.; Gr?tzel, M.; Durrant, J. ?R. *Adv. Funct. Mater.* **2006**, *16* (14), 1832–1838.
- (8) Krebs, F. C.; Biancardo, M. *Sol. Energy Mater. Sol. Cells* **2006**, *90* (2), 142–165.
- (9) Liu, X.; Cheng, Y.; Wang, L.; Cai, L.; Liu, B. *Phys. Chem. Chem. Phys.* **2012**, *14* (19), 7098–7103.
- (10) Tang, J.; Hua, J.; Wu, W.; Li, J.; Jin, Z.; Long, Y.; Tian, H. *Energy Environ. Sci.* **2010**, *3* (11), 1736–1745.
- (11) Venkateswararao, A.; Thomas, K. R. J.; Lee, C.-P.; Li, C.-T.; Ho, K.-C. *ACS Appl. Mater. Interfaces* **2014**, *6* (4), 2528–2539.
- (12) Ocakoglu, K.; Sogut, S.; Sarica, H.; Guloglu, P.; Erten-Ela, S. *Synth. Met.* **2013**, *174*, 24–32.
- (13) Sotzing, G. A.; Reddinger, J. L.; Katritzky, A. R.; Soloducho, J.; Musgrave, R.; Reynolds, J. R.; Steel, P. J. *Chem. Mater.* **1997**, *9* (7), 1578–1587.
- (14) Otero, T. F.; Carrasco, J.; Figueras, A.; Brillas, E. *J. Electroanal. Chem.* **1994**, *370* (1–2), 231–239.
- (15) Ferraris, J. P.; Skiles, G. D. *Polymer* **1987**, *28* (2), 179–182.
- (16) Ferraris, J. P.; Andrus, R. G.; Hrcir, D. C. *J Chem Soc Chem Commun* **1989**, No. 18, 1318–1320.
- (17) Tarkuc, S.; Sahmetlioglu, E.; Tanyeli, C.; Akhmedov, I.; Toppare, L. *Sens. Actuators B Chem.* **2007**, *121* (2), 622–628.
- (18) Yi?it, D.; Hac?o?lu, ?erife O.; G?il?, M.; Toppare, L. *New J Chem* **2015**, *39* (5), 3371–3379.
- (19) Cihaner, A.; Alg?, F. *J. Electroanal. Chem.* **2008**, *614* (1–2), 101–106.
- (20) Cihaner, A.; Algi, F. *Electrochimica Acta* **2008**, *53* (5), 2574–2578.
- (21) Chams, A.; Dupeyre, G.; Jouini, M.; Yassar, A.; Perruchot, C. *J. Electroanal. Chem.* **2013**, *708*, 20–30.
- (22) Yildiz, E.; Camurlu, P.; Tanyeli, C.; Akhmedov, I.; Toppare, L. *J. Electroanal. Chem.* **2008**, *612* (2), 247–256.
- (23) Camurlu, P.; Karagoren, N. *React. Funct. Polym.* **2013**, *73* (6), 847–853.
- (24) Houarner-Rassin, C.; Blart, E.; Buvat, P.; Odobel, F. *J. Photochem. Photobiol. Chem.* **2007**, *186* (2–3), 135–142.
- (25) Li, Z.; Ye, T.; Tang, S.; Wang, C.; Ma, D.; Li, Z. *J Mater Chem C* **2015**, *3* (9), 2016–2023.

- (26) Ghosh, K.; Masanta, G.; Chattopadhyay, A. P. *Eur. J. Org. Chem.* **2009**, 2009 (26), 4515–4524.
- (27) Suzuki, A. *J. Organomet. Chem.* **1999**, 576 (1–2), 147–168.
- (28) Merz, A.; Ellinger, F. *Synthesis* **1991**, 1991 (06), 462–464.
- (29) Amarnath, V.; Anthony, D. C.; Amarnath, K.; Valentine, W. M.; Wetterau, L. A.; Graham, D. G. *J. Org. Chem.* **1991**, 56 (24), 6924–6931.
- (30) Eisfeld, A.; Briggs, J. S. *Chem. Phys.* **2006**, 324 (2–3), 376–384.
- (31) Ambrose, J. F.; Carpenter, L. L.; Nelson, R. F. *J. Electrochem. Soc.* **1975**, 122 (7), 876–894.
- (32) Saito, Y.; Azechi, T.; Kitamura, T.; Hasegawa, Y.; Wada, Y.; Yanagida, S. *Coord. Chem. Rev.* **2004**, 248 (13–14), 1469–1478.
- (33) Moser, J.-E. *Nat. Mater.* **2005**, 4 (10), 723–724.
- (34) Koumura, N.; Wang, Z.-S.; Mori, S.; Miyashita, M.; Suzuki, E.; Hara, K. *J. Am. Chem. Soc.* **2006**, 128 (44), 14256–14257.

## **Chapter IV**

**Influence of the Nature of the Covalent Link**

**between the Dye and the HTM on s-DSSCs**

**Performances**

In the previous chapter, the new concept of covalently linked the dye to the *in-situ* generated co-polymer used as HTM, in order to remove the dye/HTM interface, was achieved successfully. Indeed, the resulting s-DSSCs have shown a faster charge transfer between the dye and the HTM inducing a decrease of charge recombination at the TiO<sub>2</sub>/HTM interface. Hence the V<sub>oc</sub> was improved. However this dye-HTM charge transfer was not optimal in view of the charge transfer occurring at TiO<sub>2</sub>/dye interface. Indeed, an important electron back transfer from TiO<sub>2</sub> to the oxidized dye, supported by a lower J<sub>sc</sub>, is observed. This is attributed to the more likely planar configuration of the dyes to the oxide surface inducing an unwanted additional binding site for the ester group provided from the covalent link between the TPA and the electroactive monomer. Therefore new alternatives must therefore be found, on dye's structure, to avoid the presence of an additional binding site that could adsorb onto the TiO<sub>2</sub> surface such as the ester group as presented in the previous chapter. In the present chapter, other novel dyes are designed by switching the ester group by another chemical function. Each of the new dyes is then introduced in s-DSSCs in order to enhance the short-circuit current density.

#### **IV. 1. Modification of the covalent link between the dye and the HTM**

One strategy is predominantly employed to increase the J<sub>sc</sub>: it consists to shift to more positive value the dye's ground state (HOMO) energy level, while maintaining in adequacy this dye HOMO level under the VB of the HTM, and the energy level of the dye's excited state (LUMO) above the TiO<sub>2</sub><sup>[1]</sup>. By tuning the HOMO level, while assuming that the LUMO level is fixed, the optical bandgap will narrow and hence the dye will absorb at higher wavelengths (see Figure IV-1). Knowing that the HOMO energy level is localized in the donor part of the dye's structure, different approaches have been proposed to modify the dye structure in order to

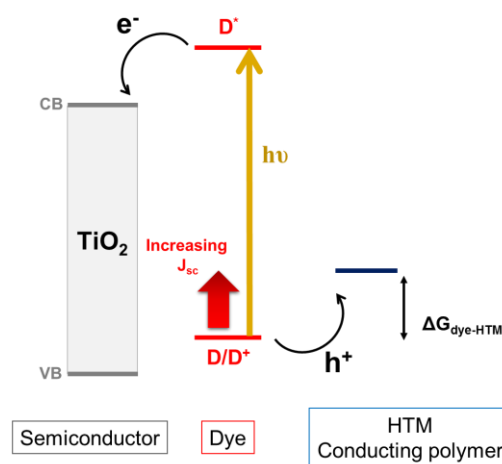


**Figure IV-1: Schematic diagram showing the strategy to enhance the photocurrent density in s-DSSC**

increase the HOMO energy level: (i) by the incorporation of an additional donor in the  $\pi$ -conjugated bridge, (ii) by the substitution of the TPA donor group and (iii) by the extension of the electron donating property in the donor group<sup>[2-4]</sup>.

#### **IV. 1. a. General context: extension of electron donating in the donor part**

The extension of the donor part in the D- $\pi$ -A organic dye structure was first introduced by Grätzel *et al.* who attached fluorene moieties on TPA core to prevent aggregation of the dyes and to reduce charge recombination processes<sup>[5]</sup>. As result, the HOMO level of TPA based dyes was systematically increased when adding fluorene moieties. Similarly Tarsang *et al.* tuned the electron donating part in order to shift the absorption ability of the dye to higher wavelengths<sup>[6]</sup>. Indeed, the addition of diphenylamine at para-position of TPA induced the positive shift of the HOMO energy level; hence a lower optical bandgap is obtained. Recently Yella and coworkers have investigated an organic dye structure combining the electron donating and hydrophobic properties of the fluorene compound and the alkoxy side chain leading to a performant DSSC<sup>[4]</sup>. Li *et al.* introduced an alkoxy chain in *para*-position of TPA (C213 dye)<sup>[7]</sup> causing a shift of the HOMO level from -5.5 eV (**L1** dye) to -5.09 eV. By increasing the length of the alkoxy side chain, the HOMO is quite at the same level<sup>[8]</sup>. When an aryl is substituted between the TPA and the alkoxy chain the HOMO level is shifted at -5.35 eV, less positive with respect to the C213 dye. This is due to the less donating mesomeric effect of the aryl group compared to the ether group which leads to a less electronic push.

In this present chapter, we report the syntheses of the new dyes by switching the ester covalent link of **ADCBZ** and **ADSNS** (see Chapter III) by another side chains that separate the TPA from the electroactive monomer. The strategy used for the synthesis corresponds to the one used in chapter III where the starting structural component corresponds to the **L1** pristine dye structure. The new side chains have the property to be (i) an electron donating group in order to shift the HOMO level to higher energy, (ii) the slight mesomeric effect of the new side chains will allow the energy HOMO level of the dye to stand below the VB of HTM. Knowing that the latter is located at about -5.2 eV for PEDOT, efficient dye regeneration is guaranteed. These new dyes are incorporated in the s-DSSCs and the photovoltaic performances are determined.



### IV. 1. b. Proposed organic dyes containing the electroactive monomer

The following four novel dyes were projected to be synthesized, two of them do not succeed. Nevertheless, discussion on synthesis methods are fully developed for furthering the synthesis of the two other dyes (see the section “results and discussions”). The D- $\pi$ -A framework for all these dyes follows the basic structure of **L1** dye. Each of the phenyl groups are para-substituted with a carbazole or SNS monomers (cf. chapter III) through a hydrocarbon chain of either (i) 3 carbon atoms or (ii) 4 carbon atoms containing an alkene function. Usually, C=C alkene group is introduced in the  $\pi$ -conjugated part to reduce the optical bandgap and to lead to a broader spectrum<sup>[9,10]</sup>. Here, the C=C alkene function gives an additional conjugated expansion in the donor part and should extend the absorption spectrum to the red region as reported by Liang *et al.*<sup>[11]</sup>. The number of carbon atoms between the TPA and the electroactive monomer is varied from 3 to 4 in order to investigate the influence of the chain length on the s-DSSCs performances.

#### IV.1.b.(i) Hydrocarbon chain with 3 carbon atoms

The two novel TPA based dyes containing electroactive monomer and holding the 3 carbon atoms alkene chain are namely **ADCBZ-1** ((Z)-3-(5-(4-(bis(4-((E)-3-(9H-carbazol-9-yl)prop-1-en-1-yl)phenyl)amino)phenyl)thiophen-2-yl)-2-cyanoacrylic acid) and **ADSNS-1** ((Z)-3-(5-(4-(bis(4-((E)-3-(2,5-di(thiophen-2-yl)-1H-pyrrol-1-yl)prop-1-en-1-yl)phenyl)amino)phenyl)thiophen-2-yl)-2-cyanoacrylic acid) (see Figure IV-2).

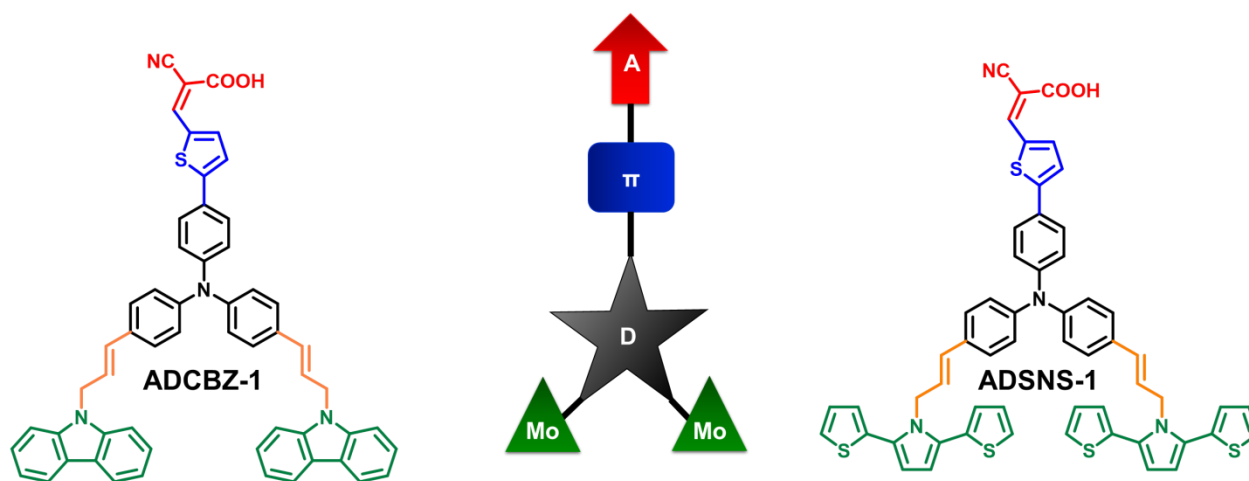


**Figure IV-2:** Molecular structure of the ADCBZ-1 and ADSNS-1 dyes covalently linked to the monomer through an alkene chain highlighted in orange.

#### IV.1.b.(ii) Hydrocarbon chain with 4 carbon atoms

Similarly, two other novel dyes have the same configuration as **ADCBZ-1** and **ADSNS-1** except that an additional carbon atom is incorporated in the covalent link between the TPA core and the electroactive monomer. They are named **ADCBZ-2** ((*Z*)-3-(5-(4-(bis(4-((*E*)-4-(9*H*-carbazol-9-yl)but-1-en-1-yl)phenyl)amino)phenyl)thiophen-2-yl)-2-cyanoacrylic acid) and **ADSNS-2** ((*Z*)-3-(5-(4-(bis(4-((*E*)-4-(2,5-di(thiophen-2-yl)-1*H*-pyrrol-1-yl)but-1-en-1-yl)phenyl)amino)phenyl)thiophen-2-yl)-2-cyanoacrylic acid) (see Figure IV-3).

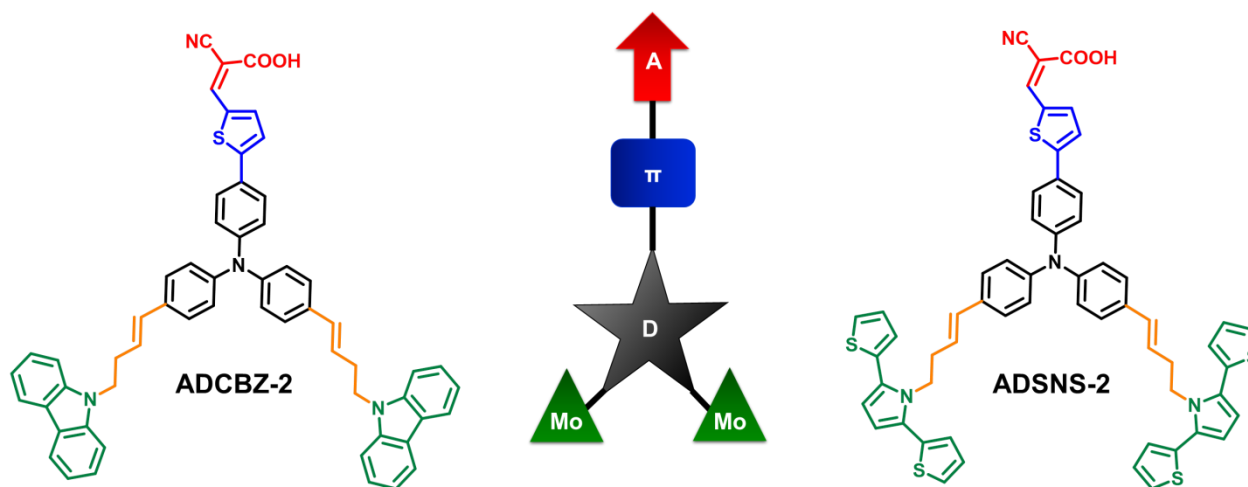


**Figure IV-3:** Molecular structure of the ADCBZ-2 and ADSNS-2 dyes covalently linked to the monomer through an alkene chain highlighted in orange.

The presence of the C=C double bond in the hydrocarbon chain linked to the N-functional group of the monomer does not affect the electronic properties of the monomer for this series of dyes.

**L1** pristine dye is employed as reference for results comparison.

## IV. 2. Experimental details

### IV. 2. a. Preparation of building blocks

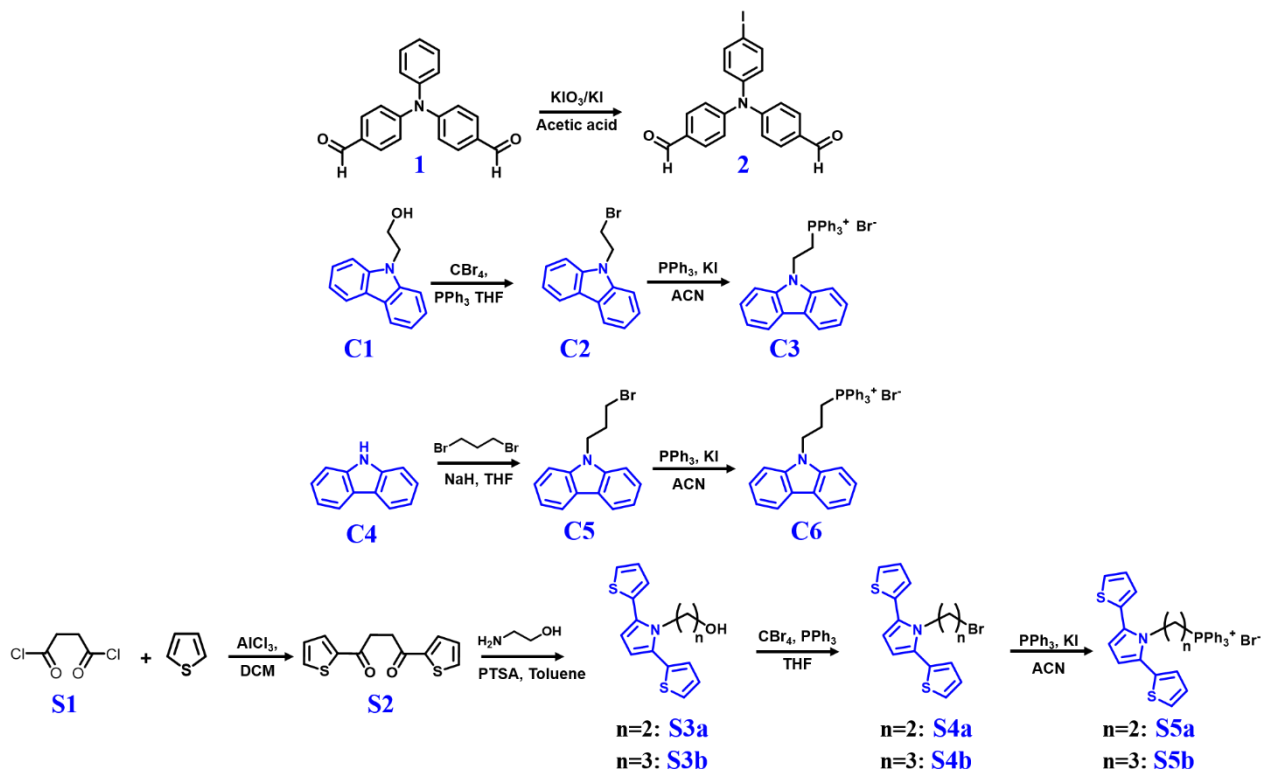


**Figure IV-4:** Synthetic route of the different building blocks required for the synthesis of the four new dyes.

The synthetic strategy to access **ADCBZ-1**, **ADSNS-1**, **ADCBZ-2** and **ADSNS-2** relies on the preparation of five building blocks: the 4,4'-(4-iodophenylazanediyl)dibenzaldehyde **2** and the phosphonium salts **C3**, **C6**, **S5a** and **S5b**.

- The product **2** is the common building block for all dyes synthesis, and its preparation is achieved by the iodination of the 4,4'-diformyltriphenylamine **1** following the same procedure as described in the chapter III.
- The intermediate phosphonium salt **C3** is obtained from the Appel reaction of the primary alcohol **C1** <sup>[12]</sup> that yields the bromide **C2** and subsequently the obtained **C2** reacts with the triphenylphosphine in order to get the desired phosphonium salt also known as Wittig reagent.

- The preparation of **C6** is based on the use of commercially available carbazole **C4** which reacts first with the sodium hydrate and subsequently with 1,3-dibromopropane by the nucleophilic substitution to give **C5** as described by Hattemer *et al.*<sup>[13]</sup>. Then **C5** is subjected to a nucleophilic substitution of the bromide by the triphenylphosphine resulting in the desired phosphonium salt **C6**.
- **S5a** and **S5b** have been obtained after four steps starting from the double Friedel-Crafts acylation on **S1** to get **S2** as described in Chapter III, followed by the Paal-Knorr reaction from the condensation of 1,4-dicarbonyl compound with 2-aminoethanol **A1** or 3-aminopropan-1-ol **A2** to give **S3a** and **S3b** respectively. In order to get the alkylbromide compound **S4a** and **S4b**, **S3a** and **S3b** are treated with carbon tetrabromide in presence of triphenylphosphine<sup>[14]</sup>. The final step follows the aforementioned procedure resulting in the desired Wittig reagents **S5a** and **S5b**.

#### **IV. 2. b. Preparation of ADCBZ-1, ADSNS-1, ADCBZ-2 and ADSNS-2 dyes**

The synthetic procedure of the four dyes is depicted in the Figure IV-5 and starts from the reaction between two intermediates:

- **2** + **C3** for **ADCBZ-1** synthesis
- **2** + **S5a** for **ADSNS-1** synthesis
- **2** + **C6** for **ADCBZ-2** synthesis
- **2** + **S5b** for **ADSNS-2** synthesis

These building blocks are coupled together through the well-known Wittig reaction. This reaction occurring between the aldehyde and the ylide, generated from phosphonium salt in presence of a strong base, leads to an alkene **8a**, **8b**, **8c**, and **8d**. Different base and solvent are tested in order to get a high reaction yield:

- Base: n-BuLi, t-BuOK, NaH
- Solvent : DCM, THF, DMF

Then, the Suzuki coupling reaction is implemented to get the compounds **9a**, **9b**, **9c**, and **9d**. The cyanoacrylic acid anchoring group is obtained by the Knoevenagel condensation reaction

between the aldehyde and cyanoacetic acid and should lead to **ADCBZ-1**, **ADSNS-1**, **ADCBZ-2** and **ADSNS-1** dyes.

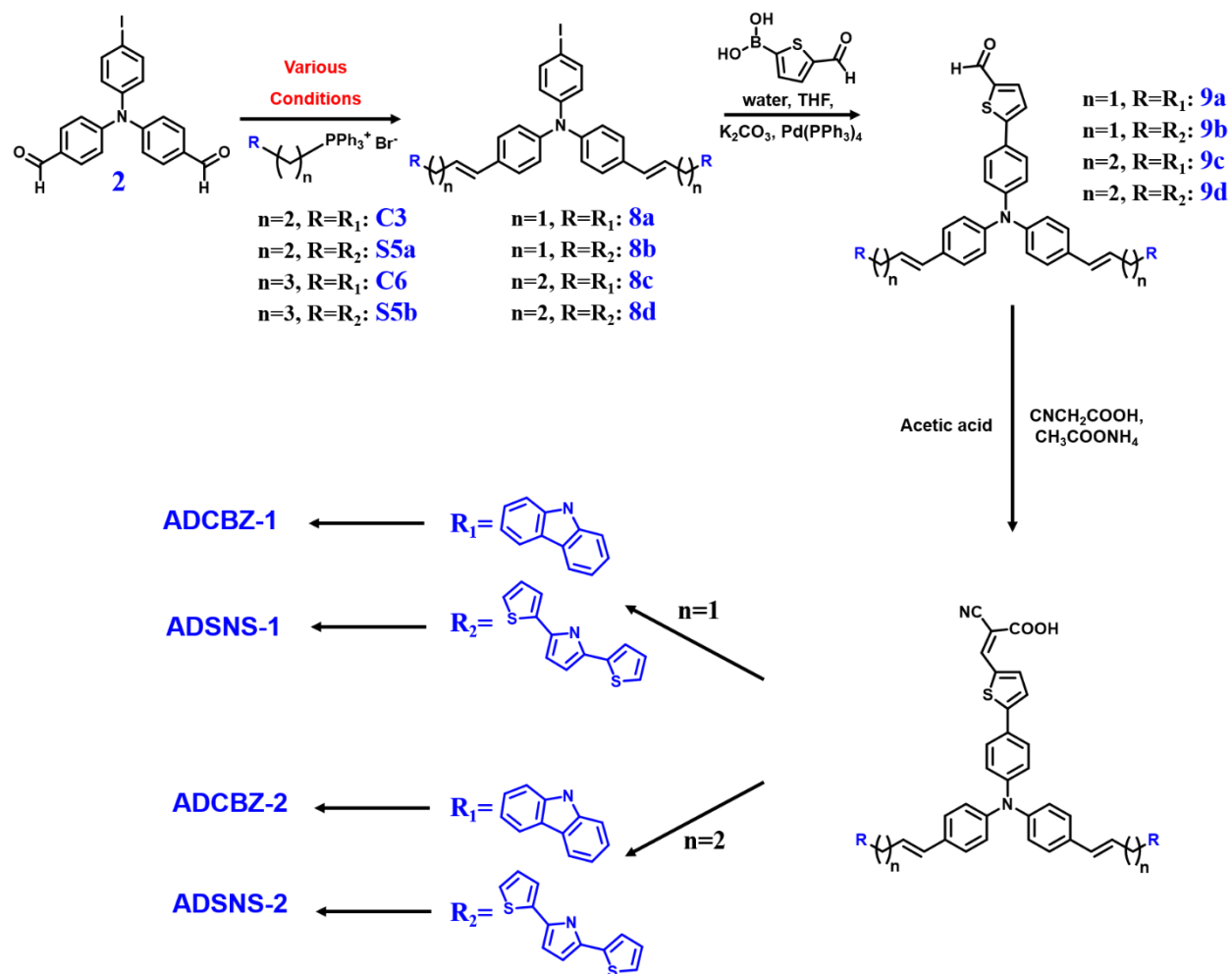


**Figure IV-5:** Synthetic route of ADCBZ-1, ADSNS-1, ADCBZ-2 and ADSNS-2 dyes

Further details on dyes syntheses (reagents and conditions) have been given in Annex IV-1.

### IV. 3. Results and Discussion

The synthesis of the four new dyes **ADCBZ-1**, **ADSNS-1**, **ADCBZ-2** and **ADSNS-2**, following the general synthetic route depicted in the Figure IV-5, was partially achieved. Indeed the preparation of **ADCBZ-1** and **ADSNS-1** dyes which involves in 6 and 7 steps respectively, has not succeeded since the olefination Wittig reaction between the di-aldehydes compound **2** and the phosphonium salt **C3** and **S5a** giving the alkene **8a** and **8b** respectively, did not completely

occur. Whereas, in the case of **ADCBZ-2** and **ADSNS-2** dyes, the Wittig reaction between the di-aldehydes compound **2** and the phosphonium salt **C6** and **S5b** was achieved successfully. The reaction limitation is attributed to the length of the N-substituted alkyl chain on the electroactive monomer **C3** and **S5a** which leads to direct elimination reaction of the alkyl chain supported by the nitrogen atom of the electroactive residue when the base is added at first (see the following section).

### **IV. 3. a. Dyes syntheses and physico-chemical characterization**

#### **IV.3.a.(i) Wittig olefination step: the “balance” between key step and limiting step**

- Synthesis disruption for ADCBZ-1 and ADSNS-1 dyes: role of the base and role of the order of the reactants addition :

The Wittig reaction was run in different conditions: by varying either the solvent or the base.

- *In dry THF with n-BuLi*

In the first attempt, the <sup>1</sup>H NMR of the resulting product shows an inseparable mixture between the alkene and the starting compound (see Annex IV-2). Indeed, two signals are observed in the aldehyde range, and the signals assigned to the protons of the resulting alkene are also observed. However, by integrating each peak, it seems that the reaction is a mono-olefination corresponding to the presence of an aldehyde in side of the TPA, and in the other side, the alkene chain is formed with a preferably *cis*- configuration. The other signal in the aldehyde range, corresponding to 20 % of the mixture, is the starting compound **2**. No signals related to the phosphonium salt are observed.

- *In dry DMF with n-BuLi*

In presence of DMF as solvent and n-BuLi as base, no reaction occurs (see Annex IV-3). After the purification by column chromatography, the alkene product is not present in the resulting crudes.

- *In dry DMF with NaH*

By changing the base, the resulting product is a mono-substituted Wittig product, with a high amount of the starting aldehyde compound **2** (> 50 %).

- In dry DCM with *t*-BuOK

Under these conditions, the resulting compound is the same as obtained at the first experimental procedure (dry THF + *n*-BuLi) except that the starting compound is always present at 30 % (Annex IV-4).

In all cases, the di-aldehyde starting compound is still present by varying the solvent and/or the base, and by increasing the reaction temperature. This indicates that the reaction, leading to the formation of ylide, is not completed. Taking into consideration these results, we investigate, exclusively, the reaction between the Wittig salt and the *t*-BuOK base. This reaction should lead to an ylide compound but in the NMR spectra, no chemical shifts can be assigned to the desired product (Annex IV-5). Actually, starting from compound **C3** and in the presence of a strong base, an elimination reaction takes place in preference to the olefination reaction.

The phosphorous  $^{31}\text{P}$  NMR is investigated (Figure IV-6) in order to understand the reaction mechanism occurring between the *t*-BuOK and the Wittig salt and to identify the resulting product.

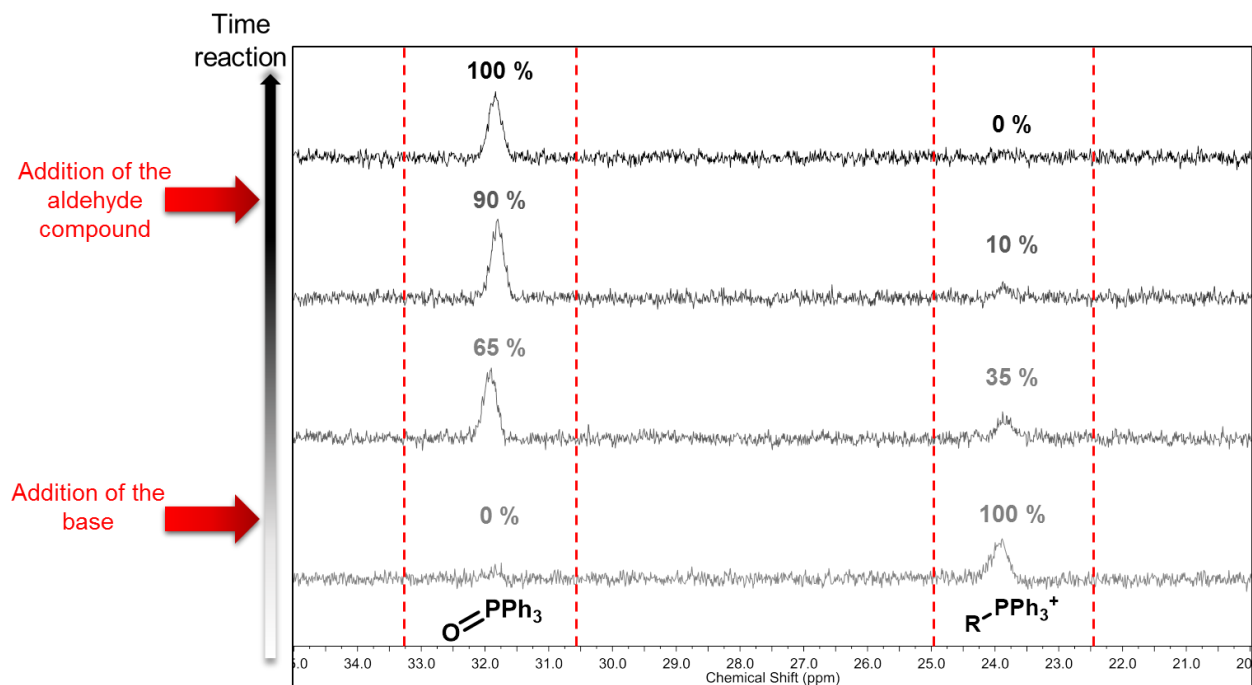


**Figure IV-6:** Wittig reaction follow-up, by  $^{31}\text{P}$  NMR.

The same elimination reaction described above on **C3** compound is also observed for the compound **S5a** in presence of the base. Therefore, the strong base will be added last in the next experiments.

- *Change of the reactant addition order in dry THF with t-BuOK*

The first attempt does not succeed, when the base is added last. But by changing the conditions (THF + t-BuOK) the desired product is obtained with only 15 % yield (Annex IV-6), which is not sufficient to pursue the next steps of the synthesis. As a consequence, we did not obtain the targeted new dyes and it was not possible to set up devices based on these new dyes. But these results show that at Wittig reaction step, in the dye synthesis procedures, the base must be added last.

➤ Synthesis of ADCBZ-2 and ADSNS-2 dye molecules :

The Wittig reaction between the aldehyde **2** and the intermediate compound **C6** or **S5b**, with an additional carbon in the N-substituted alkyl chain (n=3), is achieved under the optimal condition found previously *i.e.* with t-BuOK as base and dry THF as solvent. Moreover, the reaction is carried out by mixing first the phosphonium salt and the aldehyde compound together before the addition of the base.

When the base is added last, the reaction gives successfully the desired alkene compounds **8c** and **8d** confirmed by <sup>1</sup>H NMR (see Figure IV-7 and Figure IV-8) with a reaction yield of 27 % and 30 % respectively. Even though the reaction is achieved successfully, the reaction yield still remains low. An alternative route is already in progress which is the reaction between an organomagnesium TPA intermediate and the aldehyde of the electroactive monomer intermediate. But it will be not used in this thesis work. Nevertheless, the obtained products **8c** and **8d** were used to produce the targeted new dyes **ADCBZ-2** and **ADSNS-2**.



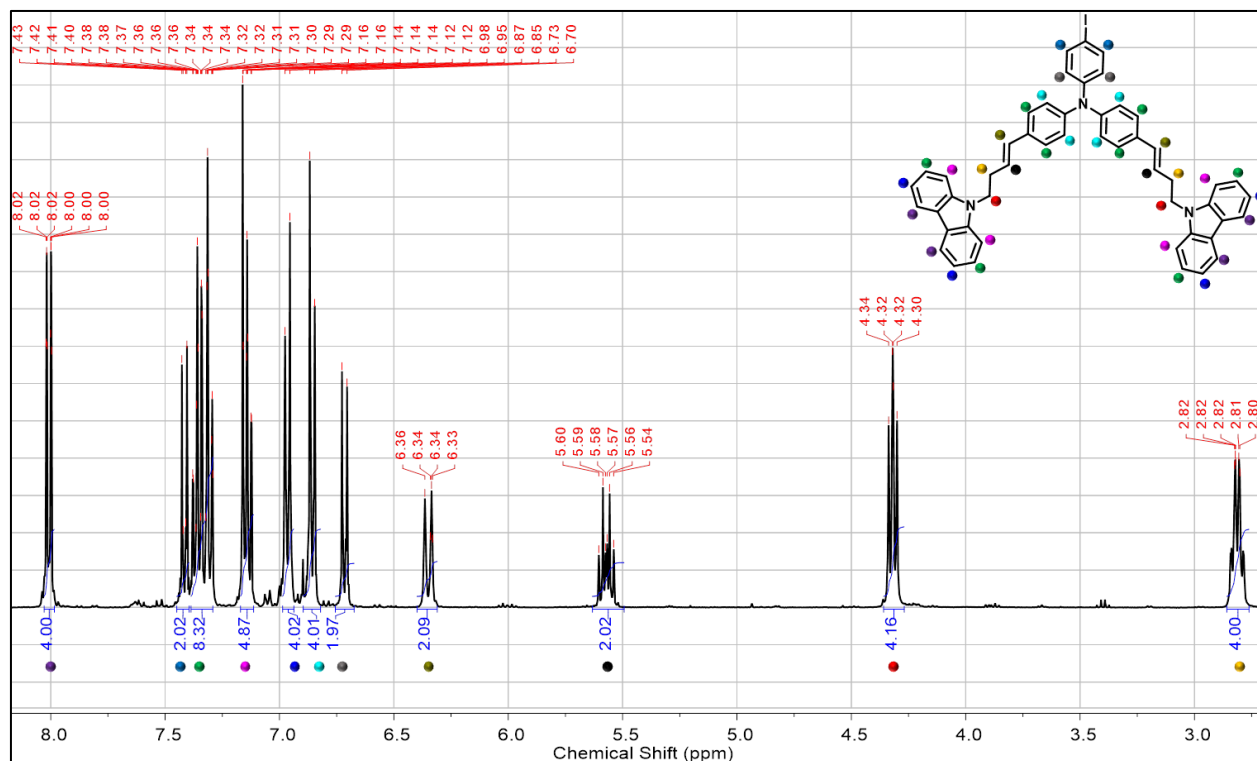


**Figure IV-7:** NMR <sup>1</sup>H spectrum of the alkene compound 8c after Wittig reaction in CDCl<sub>3</sub> with proton assignment.

For both compounds, the chemical shifts of the ethylenic protons are well defined in the range of 5.5-6.5 ppm. And interestingly, by determining the coupling constant, the *trans*-isomer is exclusively obtained when the base is added last. Indeed, among the resulting crudes, the *cis*-isomer is not identified in this synthesis compared to the products obtained in the previous syntheses when the base is added first.

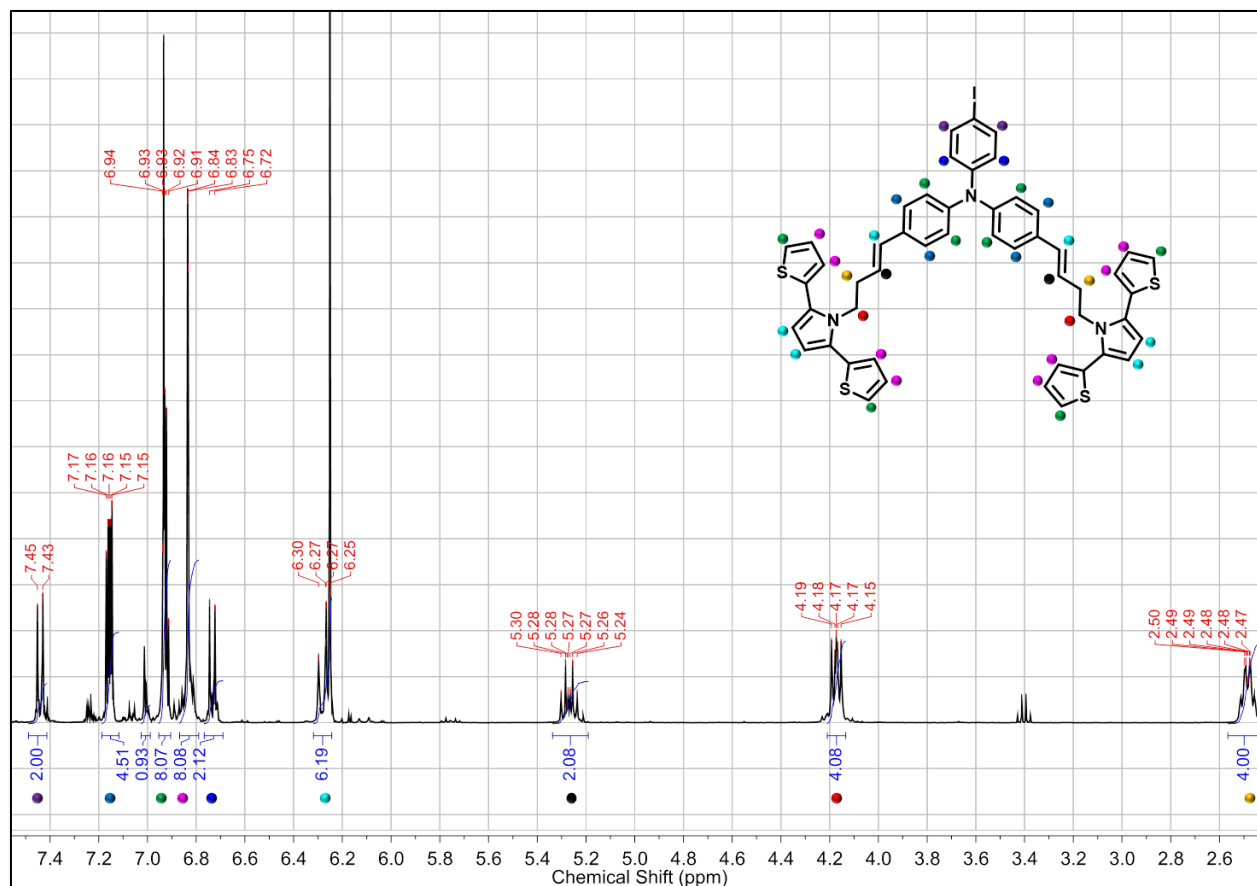


**Figure IV-8:** NMR <sup>1</sup>H spectrum of the alkene compound 8d after Wittig reaction in CDCl<sub>3</sub> with proton assignment.

Finally, the Suzuki reaction and the Knoevenagel condensation reaction yielded successfully the final product **ADCBZ-2** with an overall yield of 5 % after 6 steps and **ADSNS-2** with an overall yield of 4 % for 8 steps respectively. The final dyes structures are revealed by <sup>1</sup>H NMR (see Annex IV-7).

#### IV.3.a.(ii) ADCBZ-2 and ADSNS-2 dye molecules characterization

##### ➤ Optical and Theoretical Properties of the Dyes

As shown Figure IV-9, the absorption spectra in DCM for both **ADCBZ-2** and **ADSNS-2** dyes are characterized by a strong absorption maximum in the visible region at respectively 477 nm ( $\epsilon = 23315 \text{ M}^{-1} \cdot \text{cm}^{-1}$ ) and 470 nm ( $\epsilon = 21500 \text{ M}^{-1} \cdot \text{cm}^{-1}$ ) corresponding to the ICT band. Compared to the previous **ADCBZ** and **ADSNS** dyes (Chapter III) containing the ester, the switch from this latter by an alkene group decreases the  $\epsilon$ . However, employing this CH=CH conjugated group induces a bathochromic shift and also a broader spectrum. Similarly, compared to the ICT band of **L1** dye lying at 432 nm ( $\epsilon = 23300 \text{ M}^{-1} \cdot \text{cm}^{-1}$ ), the ICT bands of the new dyes are 30 nm

red-shifted due to the introduction of the electroactive substituents on the TPA core which is favorable for better dye light harvesting. Thus, the CH=CH substituent on TPA core is in favor in light harvesting.

$$\lambda_{\max}(\text{ADCBZ-2}) > \lambda_{\max}(\text{ADSNS-2}) > \lambda_{\max}(\text{L1})$$

However, the  $\epsilon$  of **L1** is comparable to that of **ADCBZ-2** and slightly higher than that of **ADSNS-2**.

$$\epsilon(\text{ADCBZ-2}) = \epsilon(\text{L1}) > \epsilon(\text{ADSNS-2})$$

Among the three dyes, **ADCBZ-2** exhibits the best molar absorption at higher absorption range which is desirable for light harvesting from the solar spectrum.

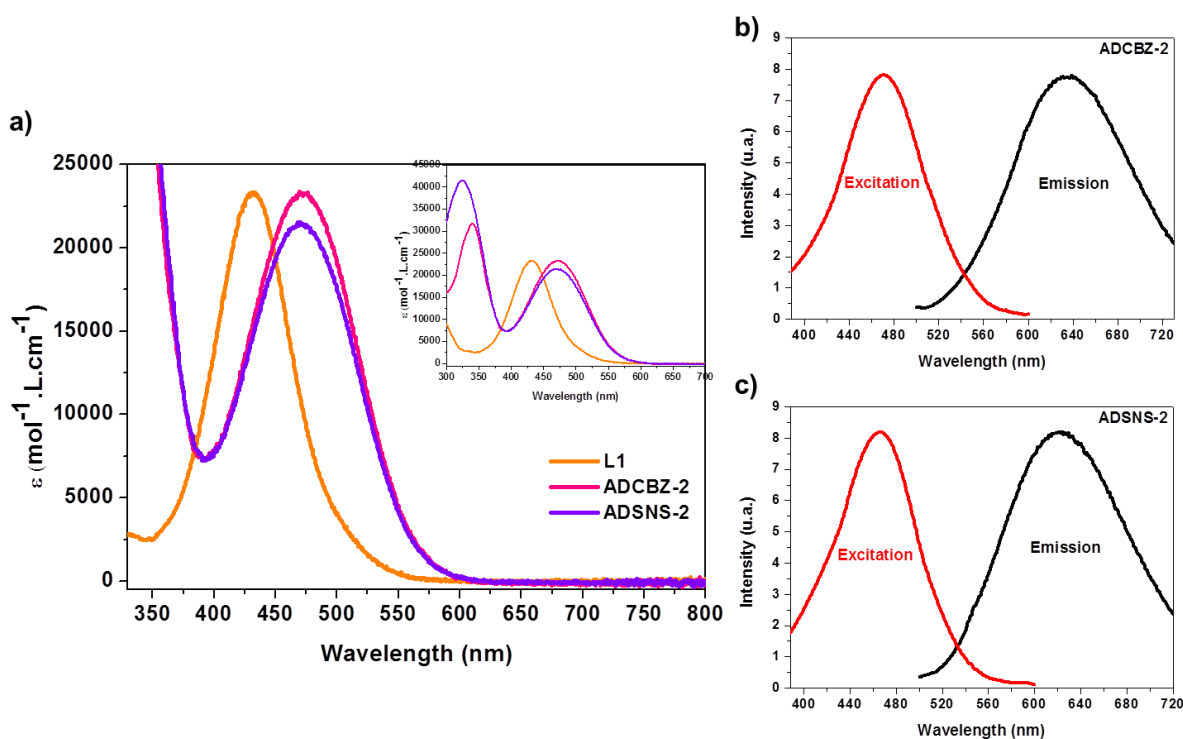


**Figure IV-9:** (a) UV-Visible absorption spectra of ADCBZ-2, ADSNS-2 and L1 dyes in DCM and (b) excitation and emission spectra of the two novel dyes in DCM.

The wavelength at maximum of the emission peak is not strongly affected by modifying the donor part of **ADCBZ-2** (635) nm for and of **ADSNS-2** (622 nm) with respect to **L1** (622 nm). However, the  $E_{0-0}$  of new dyes, determined from the intersection of the absorption and emission spectra are estimated to be 2.29 eV for **ADCBZ-2** and 2.33 eV for **ADSNS-2** which are low with respect to **L1** (2.35 eV) as well as those of **ADCBZ** (2.40 eV) and **ADSNS** (2.44 eV).

As expected, in the new dyes, the reduced bandgap is due to the enhancement of the electron donating ability resulting from the introduction of the C=C alkene group on the TPA core.

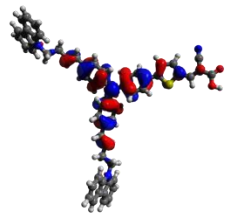
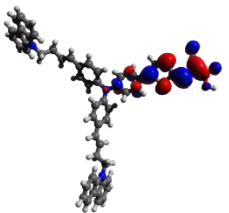
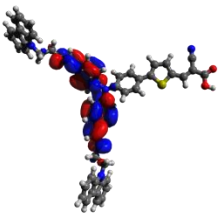
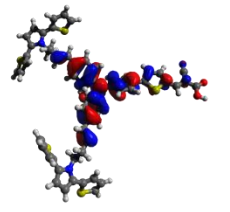
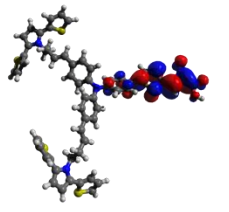
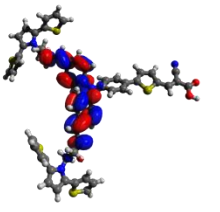
$$E_{0-0}(\text{ADCBZ-2}) < E_{0-0}(\text{ADSNS-2}) < E_{0-0}(\text{L1})$$

The optical and electrochemical data are listed in Table IV-1.

Dye	$\lambda_{\text{max, abs}}$ (nm)	$\epsilon_{\text{max}}$ ( $\text{mol}^{-1} \cdot \text{L} \cdot \text{cm}^{-1}$ )	$\lambda_{\text{max, exc}}$ (nm)	$\lambda_{\text{max, em}}$ (nm)	$E_{\text{ox}}$ (V vs. Ag/AgCl)	HOMO (eV)	LUMO (eV)	$E_{0-0}$ (eV)
<b>ADCBZ-2</b>	477	23315	470	635	0.67	-5.37	-3.08	2.29
<b>ADSNS-2</b>	470	21500	466	622	0.84	-5.24	-2.91	2.33
<b>L1</b>	432	23300	448	622	1.25	-5.50	-3.15	2.35

**Table IV-1:** Optical and electrochemical properties of ADCBZ, ADSNS, and L1 dyes.

The inset in Figure IV-9a, shows that in presence of an additional substituent in the donor part, a new absorption band appears in UV range attributed to the  $\pi \rightarrow \pi^*$  electron transition. From the calculated UV-Vis spectra, this band is mainly attributed to the HOMO  $\rightarrow$  LUMO+1 transition (see Table IV-2). The HOMO  $\rightarrow$  LUMO+1 orbital contribution is about 82 % for **ADCBZ-2** and 86 % for the same orbital contribution for **ADSNS-2**.

Dye	$\lambda_{\text{calc}}$ (nm) and Major contribution (%)	HOMO	LUMO	LUMO +1
ADCBZ-2	417 H $\rightarrow$ L(71%) 311 H $\rightarrow$ L+1(82%)			
ADSNS-2	415 H $\rightarrow$ L(72%) 311 H $\rightarrow$ L+1(86%)			

**Table IV-2:** Computed absorbance with their respective major contribution and HOMO, LUMO and LUMO +1 electron density distribution of ADCBZ-2 and ADSNS-2 dyes calculated from TD-DFT at the B3LYP level.

As regards the ICT band associated to the transition  $S_0 \rightarrow S_1$ , it is mainly attributed to the HOMO  $\rightarrow$  LUMO transition. The HOMO  $\rightarrow$  LUMO orbital contribution is about 71 % for **ADCBZ-2** and 72 % for **ADSNS-2**. The electron density distribution of the HOMO is centered on the TPA core and is delocalized till the side chains (see Table IV-2). At dye's excited state, the LUMO is delocalized across the  $\pi$ -linker propagated till the acceptor part leading to a good electronic charge transfer across the dye molecule from the donor part to the acceptor part. Therefore the excited electrons are efficiently injected into the  $\text{TiO}_2$  CB through the carboxylic group.

➤ Electrochemical Properties of Dyes

In Figure IV-10, **ADCBZ-2**, **ADSNS-2** and **L1** voltammograms show quasi-reversible redox processes and their oxidation potential are recorded at 0.67, 0.84 and 1.25 V vs. Ag/AgCl respectively. When compared to the CVs recorded for the dyes containing the ester group in the precedent chapter, we can conclude that the substitution of the ester to alkene group decreases significantly the oxidation potential of the two new dyes.

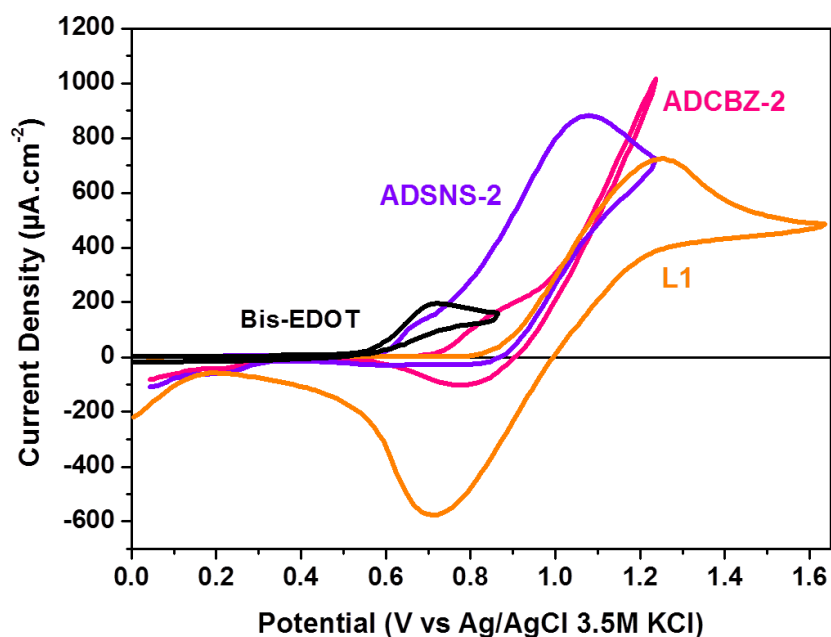


**Figure IV-10:** Cyclic voltammograms of the ADCBZ-2, ADSNS-2 and L1 dyes sensitized  $\text{TiO}_2$  photo-anode and of Bis-EDOT in organic electrolyte.

On the basis of the onset oxidation potentials of **ADCBZ-2** and **ADSNS-2** dyes determined at 0.72 and 0.59 V vs. Ag/AgCl respectively, the HOMO energy level is estimated to - 5.37 eV

and - 5.24 eV respectively. Thus, the objective of increasing the dye's ground state energy to more positive values is achieved. The calculated LUMO energy levels, from both the HOMO energy level and the  $E_{0-0}$ , for **ADCBZ-2** and for **ADSNS-2** are -3.08 eV and -2.91 eV respectively and they both lie above the CB of  $\text{TiO}_2$  providing sufficient driving force for electron injection in the CB. Regarding the HOMO energy level of each dye, it is more negative than the CB of PEDOT (-5.2 eV). Therefore these dyes can be used as sensitizers in s-DSSCs since the energy level of their frontiers orbitals match with the energy level of the CB of the electron transporting material  $\text{TiO}_2$  and the HTM (Figure IV-11).

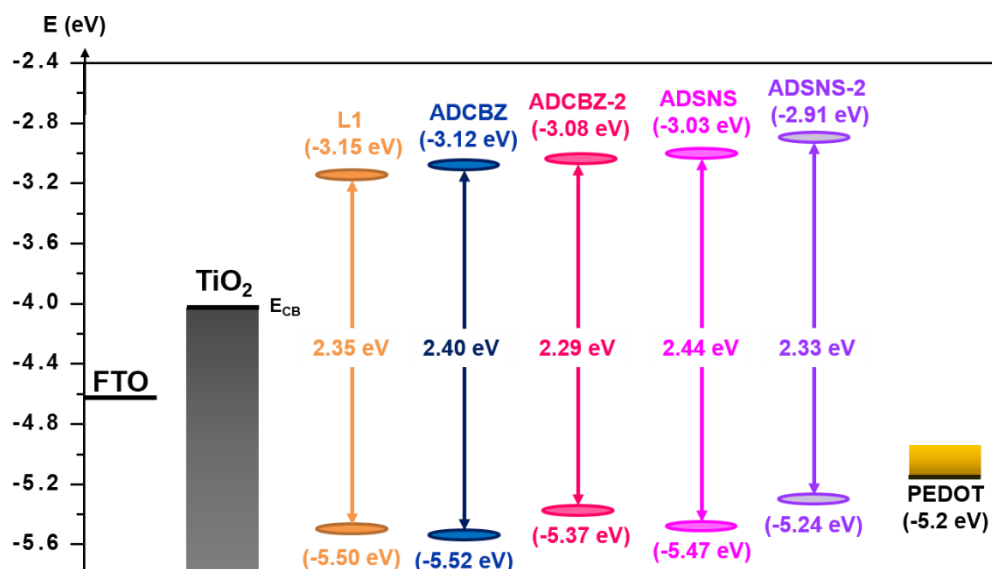


**Figure IV-11:** Energy levels diagram of the s-DSSC components determined from cyclic voltammetry and fluorescence measurements.

As the oxidation potential of dyes is more positive than the onset of the oxidation potential of Bis-EDOT, this monomer is suitable as precursor for the *in-situ* PEP process as monomer precursor.

### IV. 3. b. *In-situ* PEP deposition of PEDOT on the Sensitized $\text{TiO}_2$

#### Photo-anodes

##### IV.3.b.(i) *In-situ* PEP process

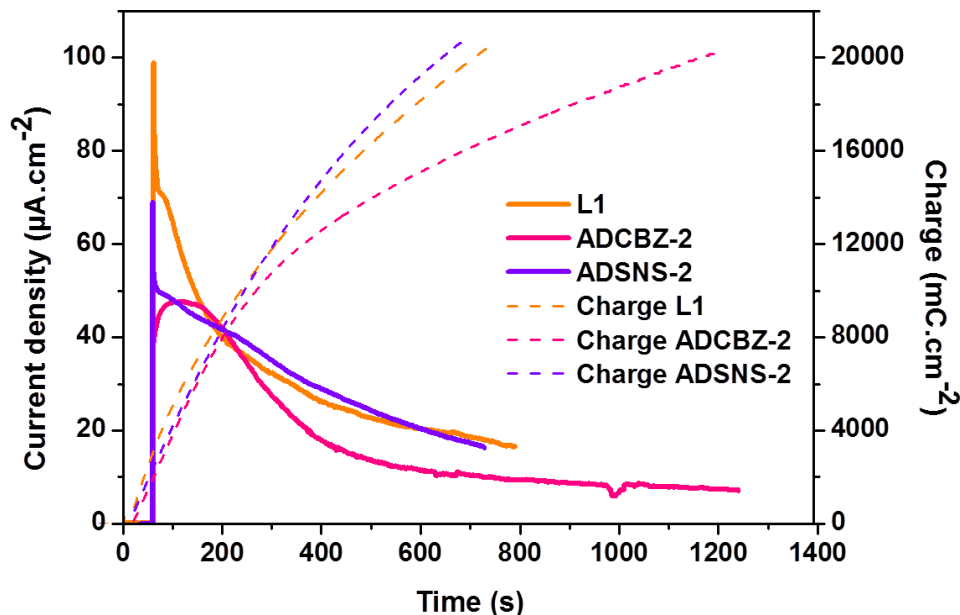


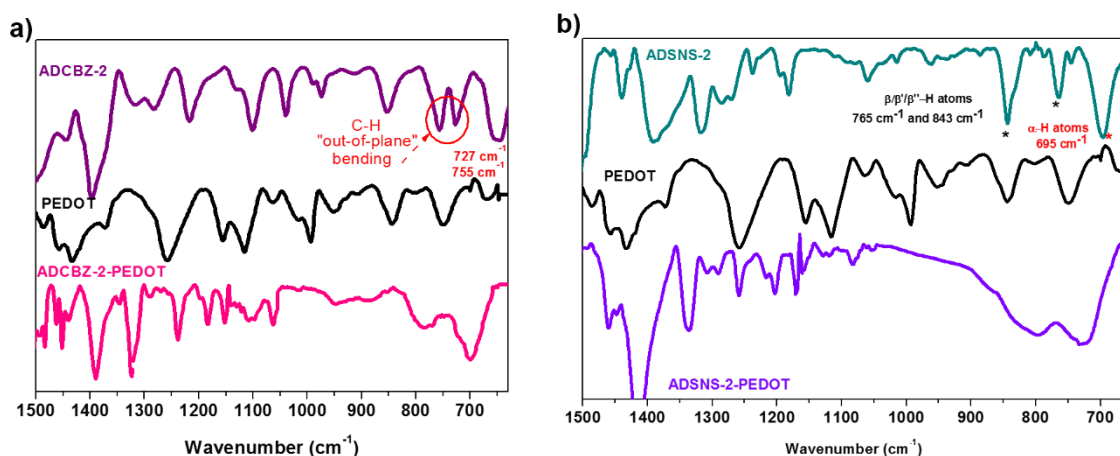
Figure IV-12: Photocurrent variation (solid curves) and total polymerization charge (dotted curves) during the *in-situ* PEP process of Bis-EDOT in organic medium using organic dyes under a potential of 0.20 V vs. Ag/AgCl and 0.1 Sun.

Figure IV-12 illustrates the chronoamperogram obtained during the *in-situ* PEP of Bis-EDOT using the **ADCBZ-2**, **ADSNS-2** or **L1** dye. The current density transient measured for **ADSNS-2** is similar to that obtained for **L1**, except that the nucleation step duration is very short, suggesting that this step occurs quickly than that observed with **L1**. However for **ADCBZ-2**, the nucleation process, which takes place in more than 200 s, is longer than that measured for **L1** dye (< 50 s), followed by the growth process where the current density decreases rapidly before reaching the current plateau. This current plateau is only observed for **ADCBZ-2** and seems to be stable ( $\approx 7\text{-}8 \mu\text{A}\cdot\text{cm}^{-2}$ ) indicating a more regular and homogeneous polymerization compared to **L1** and **ADSNS-2** where the current is continuously decreasing which indicates that the film is becoming more resistive with time deposition. Therefore the resulting polymer chains length must be shorter for **L1** and even more for **ADSNS-2** compared to **ADCBZ-2** where the polymer chains must be longer. The total charge deposited is set at  $20 \text{ mC}\cdot\text{cm}^{-2}$  and the corresponding durations are 1200 s, 790 s, and 730 s for **ADCBZ-2**, **L1**, and **ADSNS-2** dyes respectively.

#### IV.3.b.(ii) Characterization of the Dye Sensitized TiO<sub>2</sub> Photo-anodes with and without HTM layer

The FTIR spectra of the new dyes adsorbed on TiO<sub>2</sub> substrate are depicted in Figure 13. As observed for **ADCBZ** and **ADSNS** dyes, in Chapter III, the peaks attributed to CH “out of plane”

bending in carbazole, at  $727\text{ cm}^{-1}$  and  $755\text{ cm}^{-1}$ , are present as well as the peak at  $695\text{ cm}^{-1}$ , which refers to  $\alpha$ -CH of the thiophene moiety from the SNS structure. After PEDOT deposition, all these characteristic peaks, which refer to unsubstituted monomer, disappear. These observations are comparable to those done in FTIR of **ADCBZ** and **ADSNS**. They indicate undoubtedly the coupling reaction of the carbazole or SNS moiety in **ADCBZ-2** or **ADSNS-2** new dyes respectively with Bis-EDOT monomer and support the presence of the covalent link between the **ADCBZ-2** or **ADSNS-2** dye and the PEDOT polymer that will be used as HTM in the final device.



**Figure IV-13:** Transmission FTIR spectra using the transmission of the substrate material as reference of (a) ADCBZ-PEDOT film and of (b) ADSNS-PEDOT film.

### IV. 3. c. s-DSSCs devices performances

#### IV.3.c.(i) J-V Characteristics

Dye	$V_{oc}$ (V)	$J_{sc}$ ( $\text{mA}\cdot\text{cm}^{-2}$ )	FF (%)	Efficiency $\eta$ (%)
<b>ADCBZ-2</b>	0.47	5.0	51	1.2
<b>ADSNS-2</b>	0.48	4.1	46	0.91
<b>L1</b>	0.43	3.7	57	0.91
<b>ADCBZ</b>	0.54	3.2	59	1.03
<b>ADSNS</b>	0.40	1.8	52	0.36

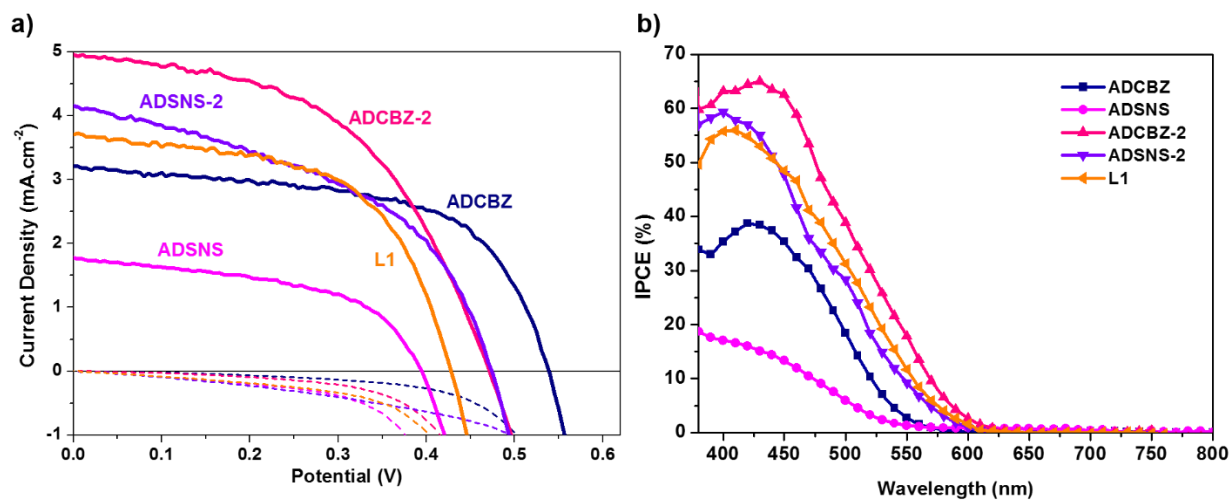
**Table IV-3:** Photovoltaic parameters of s-DSSCs based on ADCBZ, ADSNS and L1 dyes under the AM 1.5G illumination of the simulated sunlight ( $100\text{mW}/\text{cm}^2$ )



Figure IV-14a shows the comparison of the current density vs photovoltage (J-V) between the s-DSSCs based on each of the different organic dyes including the newly achieved **ADCBZ-2** and **ADSNS-2** based s-DSSCs. Their corresponding photovoltaic parameters are summarized in Table IV-3.

➤ ADCBZ-2 and ADSNS-2 vs. L1 based s-DSSCs:

The devices sensitized with **ADCBZ-2** or **ADSNS-2** dyes show an overall efficiency up to 1.2 % and 0.91 % respectively, and an improvement of the efficiency is achieved for **ADCBZ-2** compared to the device sensitized with **L1** (0.91 %). Moreover, the current density at short circuit conditions as well as the open circuit voltage obtained for s-DSSCs working with **ADCBZ-2** ( $J_{sc}= 5.0 \text{ mA}\cdot\text{cm}^{-2}$ ,  $V_{oc}= 470 \text{ mV}$ ) and **ADSNS-2** ( $J_{sc}= 4.1 \text{ mA}\cdot\text{cm}^{-2}$ ,  $V_{oc}= 480 \text{ mV}$ ) are significantly improved compared to **L1** ( $J_{sc}= 3.7 \text{ mA}\cdot\text{cm}^{-2}$ ,  $V_{oc}= 430 \text{ mV}$ ). The  $J_{sc}$  improvement with the new dyes, with respect to **L1**, is attributed to the positive shift of the HOMO energy level and also to the narrow bandgap  $E_{0-0}$ . As regards to the  $V_{oc}$ , it is increased in both devices based on **ADCBZ-2** and on **ADSNS-2** with respect to that based on **L1**. Clearly, the covalent linkage incorporated between the dye and the HTM led to a minimization of charge recombination at  $\text{TiO}_2/\text{HTM}$  interface as observed for **ADCBZ** and **ADSNS** based s-DSSCs.



**Figure IV-14:** (a) I-V characteristics of s-DSSCs based on ADCBZ-2, ADSNS-2 and L1 dyes compared to the characteristics of s-DSSCs based on ADCBZ and ADSNS measured under the AM 1.5G illumination ( $100\text{mW}/\text{cm}^2$ ). (b) IPCE spectra of the same cells.

➤ ADCBZ-2 and ADSNS-2 vs. ADCBZ and ADSNS based s-DSSCs:

The overall efficiencies of devices sensitized with **ADCBZ-2** or **ADSNS-2** dyes are effectively enhanced of respectively about 14 % and 60 % with respect to the efficiencies obtained with devices sensitized with their counterparts **ADCBZ** or **ADSNS** dyes. Regarding the  $J_{sc}$  for **ADCBZ-2** and **ADSNS-2**, it is increased by a factor of 1.6 and 2.3 respectively when a pairwise comparison is done. Therefore the objective of optimizing the  $J_{sc}$  by replacing the ester to an alkene covalent link is achieved. Hence the charge transfer between the HTM and the dye is increased and the recombination at  $TiO_2$ /dye interface is reduced.

#### IV.3.c.(ii) IPCE

The IPCE spectra illustrated in Figure IV-14b, show highest values of: 63 % at 430 nm for **ADCBZ-2**, 61 % at 420 nm for **ADSNS-2** and 56 % at 410 nm for **L1**. The resulting  $J_{sc}$  extracted from the IPCE are  $5.0 \text{ mA}\cdot\text{cm}^{-2}$  for **ADCBZ-2** and  $4.0 \text{ mA}\cdot\text{cm}^{-2}$  for **ADSNS-2**. These values are highly consistent with the  $J_{sc}$  obtained from J-V measurement. Moreover the order of  $J_{sc}$  extracted from IPCE measurements for whole dyes follows the same order obtained for  $J_{sc}$  values obtained from J-V measurements:

$$J_{sc,IPCE}(\text{ADCBZ-2}) > J_{sc,IPCE}(\text{ADSNS-2}) > J_{sc,IPCE}(\text{L1}) > J_{sc,IPCE}(\text{ADCBZ}) > J_{sc,IPCE}(\text{ADSNS})$$

The larger red photon collection is observed in IPCE spectra of the new dyes with respect to **L1**, **ADCBZ** and **ADSNS** dyes indicating an easiest light harvesting character of the two new dyes which may be the reason of  $J_{sc}$  improvement.

#### IV.3.c.(iii) Photo-Induced Absorption Spectroscopy

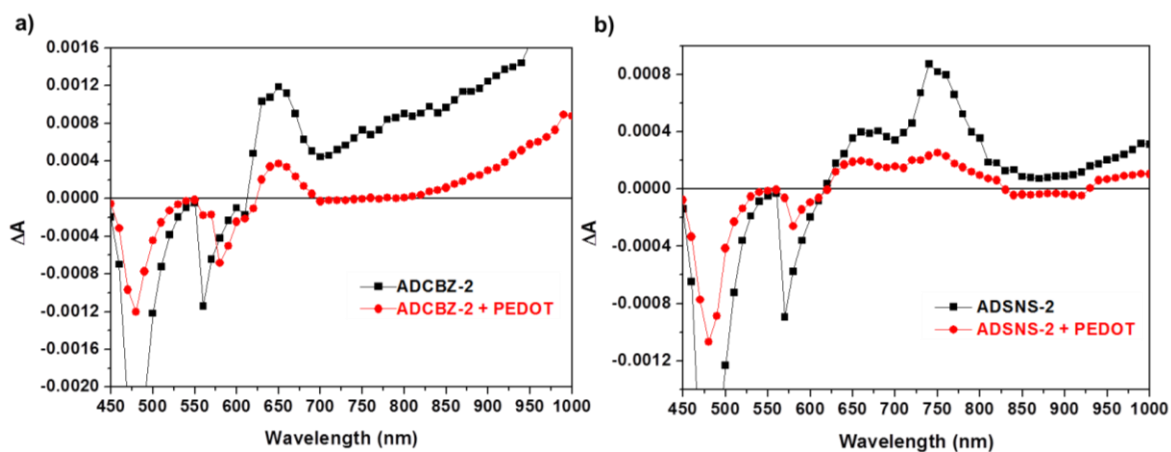


**Figure IV-15:** PIA spectra of (a) ADCBZ-2 and (b) ADSNS-2 adsorbed at a nanostructured  $TiO_2$  film without (black) and with (red) PEDOT.

As shown in Figure IV-15, in the absence of PEDOT (black curve) a positive peak is observed between 600 and 850 nm in the spectrum of TiO<sub>2</sub> sensitized with **ADCBZ-2** as well as in that of TiO<sub>2</sub> sensitized with **ADSNS-2**. This peak attributed to the light absorption of the oxidized dye. After the deposition of PEDOT (red curve), the positive peak significantly reduced which reveals that an efficient charge transfer occurs from the HTM to the dye. This decrease is more pronounced for these new dyes than that for **ADCBZ** and **ADSNS**. Therefore, the charge transfer is more effective for the s-DSSCs based on **ADCBZ-2** and **ADSNS-2** than that for the devices sensitized with **ADCBZ** or **ADSNS** resulting in a better photocurrent.

#### IV. 3. d. Impact of the s-DSSCs aging process on photovoltaic performances

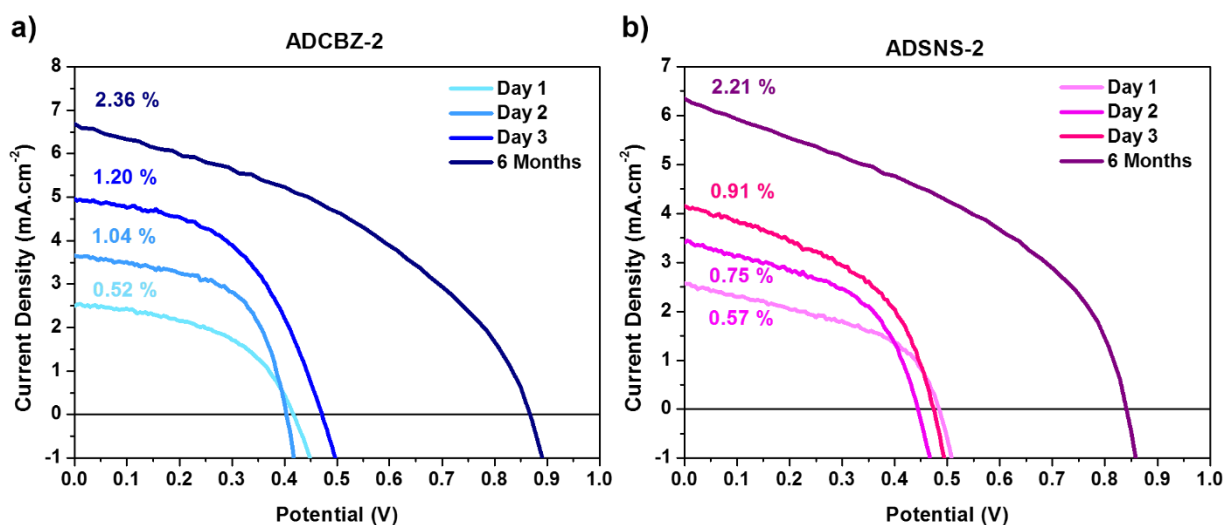


**Figure IV-16:** J-V characteristics of s-DSSCs based on (a) ADCBZ-2 and (b) ADSNS-2 after 1, 2, 3 days and 6 months under the AM 1.5G illumination of the simulated sunlight (100mW/cm<sup>2</sup>).

The aging process for the s-DSSCs sensitized with the new dyes has been checked (Figure IV-16). Similarly to **ADCBZ** and **ADSNS** dyes based s-DSSCs, reported in Chapter III, the photovoltaic parameters of devices based on **ADCBZ-2** and **ADSNS-2** increase with aging, mainly the  $V_{oc}$  and the  $J_{sc}$ . In both cases, the FF reaches an optimal value after 2 days and then decreases dramatically as observed for **ADCBZ** (cf. Chapter III). It can therefore be assumed that, as discussed in the Chapter III, the remaining solvent used for the preparation of the PEDOT CP and of additives, is the unique variable parameter which essentially contributes in this

s-DSSCs aging process. After 6 months, the efficiencies of both devices are two fold higher yielding to 2.36 % and 2.21 % for **ADCBZ-2** and **ADSNS-2** respectively. They are, thus, the two champion cells obtained from our new concept corresponding to link the organic dyes to the *in-situ* generated co-polymer used as HTM.

Dye	Aging time	V <sub>oc</sub> (V)	J <sub>sc</sub> (mA.cm <sup>-2</sup> )	FF (%)	Efficiency $\eta$ (%)
<b>ADCBZ-2</b>	Day 1	0.42	2.50	51	0.52
	Day 2	0.41	3.65	57	0.85
	Day 3	0.47	5.00	51	1.20
	6 months	0.86	6.71	41	<b>2.36</b>
<b>ADSNS-2</b>	Day 1	0.55	2.24	43	0.53
	Day 2	0.45	3.40	49	0.75
	Day 3	0.48	4.10	46	0.91
	6 months	0.85	6.32	41	<b>2.21</b>

**Table IV-4:** Photovoltaic parameters of s-DSSCs based on ADCBZ-2 and ADSNS-2 dyes after 1, 2, 3 days and 6 months under the AM 1.5G illumination of the simulated sunlight (100mW/cm<sup>2</sup>).

#### IV. 3. e. Discussion

In this Chapter, the comparison of our results obtained with the two novel dyes **ADCBZ-2** and **ADSNS-2** based s-DSSCs with respect to those obtained in the previous chapter with **ADCBZ** and **ADSNS** based s-DSSCs, clearly highlights the importance of the nature of the covalent link between the dye and the HTM. Indeed, the chemical structure of the novel dyes is similar to that of **ADCBZ** and **ADSNS** except that the ester is substituted by an alkene group. Whereas the length of the alkyl chain separating the HTM to the dye is comparable. This replacement is very useful to enhance the optical and electrochemical properties of dyes but it is further useful to increase the photovoltaic performances when it is introduced as sensitizer in the s-DSSCs. In fact, for dyes containing the ester group (**ADCBZ** and **ADSNS**), the possible planar configuration should induce a supplementary binding site. Under illumination, the electronic delocalization, from donor to acceptor within the dye, is disturbed by the ester which is probably adsorbed on TiO<sub>2</sub> surface and hence leads to an inefficient electron injection from the acceptor part of the oxidized dye into the TiO<sub>2</sub> CB, as developed in Chapter III, resulting in lower J<sub>sc</sub>. In the present

work, the presence of C=C alkene group within the covalent link in the new dyes introduces a structural rigidity and hence the dyes probably rely at perpendicular angle to the TiO<sub>2</sub> surface. Therefore, under illumination, the electronic delocalization, from donor to acceptor, within the dyes structure is optimal and does not interfere with the usual electron injection process from the oxidized dye acceptor into the TiO<sub>2</sub> CB. This optimization results in the increase of the J<sub>sc</sub> as desired.

#### **IV. 4. Conclusion**

The introduction of a covalent link between the dye and the HTM is a prominent factor to improve the s-DSSCs performances. In this Chapter, we just show that the nature of the covalent link between the dye and the HTM plays effectively a key role in the s-DSSCs performances. The switch from ester to alkene group led to more efficient s-DSSCs with an optimized photocurrent density J<sub>sc</sub>. As expected, the improvement is attributed to the introduction of the C=C alkene group in the novel dyes structure inducing the dyes (i) to absorb in higher wavelengths, (ii) to get a reduced bandgap and (iii) to have a lower oxidation potential. These conclusions are supported when compared with the first sensitizers **ADCBZ** and **ADSNS**. In addition, the absence of another binding site in the **ADCBZ-2** and **ADSNS-2** dyes chemical structure ensures a better electron transfer from the oxidized dye to the TiO<sub>2</sub> CB and the covalent link between the dye and the HTM ensures good dye regeneration and prevent any charge recombination between the TiO<sub>2</sub> and the HTM. The overall yields for devices sensitized with **ADCBZ-2** and **ADSNS-2** increase with aging and are, at present, at about 2.4 % and 2.2 % respectively. Therefore these organic dyes covalently linked to the electroactive monomer constitute promising candidates to make unprecedented s-DSSCs with optimized charge transfers.

## IV. 5. References

- (1) Hamann, T. W.; Jensen, R. A.; Martinson, A. B. F.; Van Ryswyk, H.; Hupp, J. T. *Energy Environ. Sci.* **2008**, *1* (1), 66.
- (2) He, J.; Liu, Y.; Gao, J.; Han, L. *Photochem Photobiol Sci* **2017**.
- (3) Cheng, M.; Yang, X.; Zhang, F.; Zhao, J.; Sun, L. *J. Phys. Chem. C* **2013**, *117* (18), 9076–9083.
- (4) Yella, A.; Humphry-Baker, R.; Curchod, B. F. E.; Ashari Astani, N.; Teuscher, J.; Polander, L. E.; Mathew, S.; Moser, J.-E.; Tavernelli, I.; Rothlisberger, U.; Grätzel, M.; Nazeeruddin, M. K.; Frey, J. *Chem. Mater.* **2013**, *25* (13), 2733–2739.
- (5) Kim, S.; Lee, J. K.; Kang, S. O.; Ko, J.; Yum, J.-H.; Fantacci, S.; De Angelis, F.; Di Censo, D.; Nazeeruddin, M. K.; Grätzel, M. *J. Am. Chem. Soc.* **2006**, *128* (51), 16701–16707.
- (6) Tarsang, R.; Promarak, V.; Sudyoardsuk, T.; Namuangruk, S.; Jungstittiwong, S. *J. Photochem. Photobiol. Chem.* **2014**, *273*, 8–16.
- (7) Li, R.; Lv, X.; Shi, D.; Zhou, D.; Cheng, Y.; Zhang, G.; Wang, P. *J. Phys. Chem. C* **2009**, *113* (17), 7469–7479.
- (8) Yu, Q.-Y.; Liao, J.-Y.; Zhou, S.-M.; Shen, Y.; Liu, J.-M.; Kuang, D.-B.; Su, C.-Y. *J. Phys. Chem. C* **2011**, *115* (44), 22002–22008.
- (9) Kitamura, T.; Ikeda, M.; Shigaki, K.; Inoue, T.; Anderson, N. A.; Ai, X.; Lian, T.; Yanagida, S. *Chem. Mater.* **2004**, *16* (9), 1806–1812.
- (10) Xu, W.; Peng, B.; Chen, J.; Liang, M.; Cai, F. *J. Phys. Chem. C* **2008**, *112* (3), 874–880.
- (11) Liang, M.; Xu, W.; Cai, F.; Chen, P.; Peng, B.; Chen, J.; Li, Z. *J. Phys. Chem. C* **2007**, *111* (11), 4465–4472.
- (12) Appel, R. *Angew. Chem. Int. Ed. Engl.* **1975**, *14* (12), 801–811.
- (13) Hattemer, E.; Zentel, R.; Mecher, E.; Meerholz, K. *Macromolecules* **2000**, *33* (6), 1972–1977.
- (14) Ignatenko, E. A.; Shklyayeva, E. V.; Abashev, G. G. *Russ. J. Org. Chem.* **2013**, *49* (9), 1379–1385.

## **Chapter V**

### **Modification of the Oxide Semiconductor in**

#### **s-DSSCs: Use of ZnO**

The interfacial charge transfers within s-DSSCs have been investigated and improved by the structural modification of the D- $\pi$ -A dye. Even though s-DSSCs based TiO<sub>2</sub> give tremendous efficiencies, the use of TiO<sub>2</sub> as n-type oxide semiconductor has some drawbacks such as the electron transport limitations within the TiO<sub>2</sub> layer, and the low abundance and even the scarcity of titanium ores. In the present chapter and for the first time in solid-state DSSCs based on *in-situ* produced CPs, we substitute TiO<sub>2</sub> by another semiconductor in order to optimize the charge transport process occurring within the n-type oxide semiconductor. Among the oxide semiconductors, ZnO is a promising candidate to TiO<sub>2</sub>, as it has a higher electronic mobility, compared to TiO<sub>2</sub>, with similar bandgap and similar energy-band structure (see Figure I-13, Chapter I). Therefore, we report the elaboration of a s-DSSC based on ZnO, as electron transport material, using CP as HTM produced by *in-situ* PEP. To the best of our knowledge, this is the first report where ZnO is employed as oxide semiconductor in s-DSSC based CP produced by *in-situ* PEP.

## **V. 1. Optimization of the Electron Transport Process within the Semiconductor**

The oxide semiconductor is a key component of the s-DSSC device since it is involved both in charge transfer and charge transport processes. Indeed, the oxide semiconductor collects electrons from the excited dye and these electrons diffuse toward the FTO, before reaching the cathode through the external circuit. The electrons diffusion within the oxide semiconductor occurs by multiple “trapping/detrapping” processes<sup>[1]</sup> (see Figure V-1a) as described in Chapter I. However these processes cause energy losses, taking place mainly in the bulk of the oxide nanoparticles, at grain boundaries and both at semiconductor/dye and semiconductor/electrolyte interfaces due to slow electron transport (see Figure V-1b)<sup>[2]</sup>. Indeed O’Regan and Durrant reported that for a conventional DSSC, more than 90 % of electrons are trapped in TiO<sub>2</sub> in spherical shape with a diameter of 20 nm, and less than 10 % are in the conduction band. Therefore several improvements have been brought to decrease the density of trap states and to increase the electron diffusion coefficient. Among them, the incident light intensity, the thickness of the mesoporous layer, the size and shape of particles, and the intercalation of Li<sup>+</sup> (from the additives) into TiO<sub>2</sub> are some factors<sup>[2]</sup>, which can potentially affect the electron diffusion through the TiO<sub>2</sub>



layer. Some authors have also developed new composite systems as photo-anodes mixing other oxide semiconductor, carbon nanotube or graphene to TiO<sub>2</sub> to improve the electron transport. The modification of the TiO<sub>2</sub> material by another n-type oxide semiconductor represents also an alternative photo-anode material.

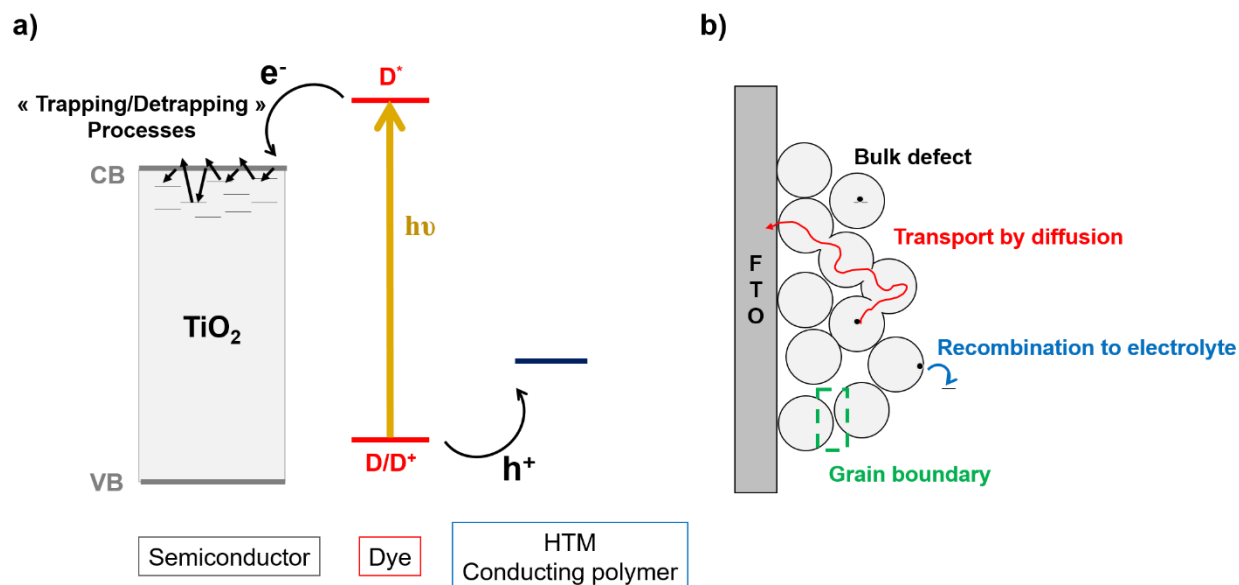


**Figure V-1:** Schematic diagram (a) of the trapping/detrapping processes in the TiO<sub>2</sub> electrode in s-DSSC and (b) of the electron transport by diffusion in the TiO<sub>2</sub> electrode reproduced from ref. [2].

### V. 1. a. General context

	ZnO	TiO <sub>2</sub>
<b>Crystal Structure</b>	Rocksalt, zinc blende, Wurtzite	Rutile, anatase, brookite
<b>Energy bandgap (eV)</b>	3.37	3.0-3.2
<b>Isoelectric point</b>	9	6 <sup>[3]</sup>
<b>Electron mobility (cm<sup>2</sup>.V.s<sup>-1</sup>)</b>	205-300 (bulk ZnO), 1000 (single nanowire)	0.1-4
<b>Electron diffusion coefficient (cm<sup>2</sup>.s<sup>-1</sup>)</b>	1.7 x 10 <sup>-4</sup> (nanospheres)	10 <sup>-8</sup> – 10 <sup>-4</sup> (nanospheres)
<b>Highest efficiency</b>	7.5 %	14.3 % <sup>[4-6]</sup>

**Table V-1:** Physical properties of ZnO and TiO<sub>2</sub> <sup>[1]</sup>.

It has been reported that the electron transport is faster in some oxide semiconductors than in TiO<sub>2</sub>, which should minimize the interfacial charge recombination and increase the charge collection efficiency, and finally may lead to higher device performances. SnO<sub>2</sub>, Nb<sub>2</sub>O<sub>5</sub>, and ZnO can be cited as promising alternative to TiO<sub>2</sub> oxide semiconductor. ZnO has attracted particular attention due to its different crystallization structures and attractive physical properties (see Table V-1). (i) Its electronic mobility is 100 to 1000 fold higher than that of TiO<sub>2</sub>; (ii) The bandgap (3.37 eV) and the energy-band structure are similar those of TiO<sub>2</sub>; (iii) Nanocrystalline ZnO can be prepared easily by different techniques which do not require a high temperature; (iv) Various nanostructures can be designed offering large specific area. These are some favorable properties to lead to a potentially efficient photo-anode for DSSCs.

Among the different morphologies, the one-dimensional ZnO nanostructures including nanowires (NW)<sup>[7]</sup>, nanorods (NR), nanotubes (NT) and nanotips (NTP) are, at present, the most suitable electron transporting material (ETM). Indeed they provide a direct charge pathway from the point of electron injection to the FTO substrate (see Figure V-2); they inhibit the recombination processes and also the density of trap states is decreased inducing a faster electron transport.

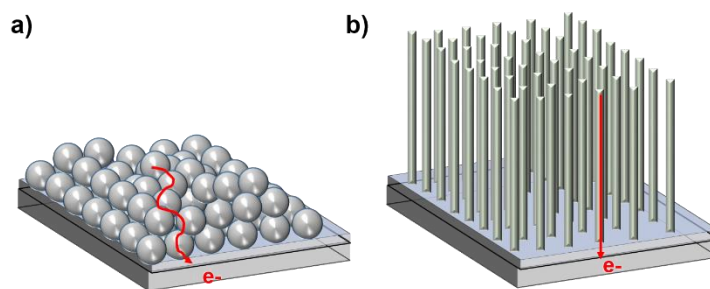


**Figure V-2:** Schematic representation of a photo-anode where the morphology of the mesoporous layer is (a) nanospheres or (b) nanotubes.

Moreover, the electron diffusion coefficient for these nanostructures are four order of magnitude higher ( $0.05\text{-}0.5\text{ cm}^2\cdot\text{V}\cdot\text{s}^{-1}$ ) than that of ZnO nanospheres. However Law *et al.* reported that the use of ZnO NW provides low surface area and a low light harvesting efficiency due to the inefficient dye loading which limits the overall efficiency of the DSSC<sup>[8]</sup>. The surface area can be improved by combining different morphologies with or without combination with other different materials<sup>[9-11]</sup>. In contrast to ZnO NW, ZnO NT offer large surface area owing to their hollow cavity structure and their high porosity<sup>[12]</sup>. However the introduction of ZnO NT in DSSCs shows

relatively lower devices efficiencies ( $< 4.7\%$ )<sup>[13]</sup> when compared to DSSCs based ZnO NW ( $5.2\%$ )<sup>[14]</sup>. This is explained by high electron back transfer from the CB of ZnO to the electrolyte. Recently some authors have proposed to include a layer of plasmonic gold NPs in DSSC as blocking layer at ZnO/dye interface to prevent this recombination process and the obtained yield was  $6.0\%$ <sup>[13]</sup>. Regarding ZnO nanotips, the efficiency of the DSSC increases with the length of the tips due to the larger surface area and the present measured efficiency is  $1.4\%$ <sup>[15]</sup> when Zn foil is used as substrate.

ZnO NR are the most widely used as photo-anode in DSSCs and in s-DSSCs and can be easily synthesized by various techniques such as by chemical vapor deposition (metal organic chemical vapor deposition)<sup>[16]</sup>, by solution processes (sol-gel method, polyol hydrolysis), by electrochemical deposition, and by physical method. Until now, the s-DSSCs based ZnO nanorods have shown promising improvement. Indeed, Boucharef *et al.* achieved a s-DSSC based on ZnO NR using spiro-OMeTAD with  $0.5\%$  efficiency<sup>[17]</sup>. They spotlight the use of ethyl cellulose in the ZnO paste formulation that improve the porosity of the mesoporous ZnO layer and hence the dye loading. The performance was further improved ( $> 0.61\%$ ) by using an organic dye instead of Ru dye<sup>[18]</sup>. Similarly, a s-DSSC based ZnO NR was developed with P3HT conducting polymer as HTM<sup>[19]</sup>. The authors found an overall efficiency of  $0.13\%$ . In all these works, the efficiencies are below the highest efficiency achieved for s-DSSC based on ZnO which is reported to be  $1.7\%$ <sup>[20]</sup>. The efficiency is low when compared to similar devices based on TiO<sub>2</sub>. This limitation can be explained by a relative instability of this oxide semiconductor in the presence of the acidic protons provided from the carboxylic acid group in the acceptor part of the dye structure. In the presence of a solvent, during the sensitization step, the protons of the dye can cause the dissolution of ZnO leading to the formation of Zn<sup>2+</sup>/dye agglomerates<sup>[21]</sup> and may precipitate within the pores of the ZnO film<sup>[2]</sup> as blocking layer. Therefore an insulating layer stands in the ZnO film and a low amount of active dyes is deposited on the ZnO surface inducing a low electron injection from the photo-excited dye in the ZnO CB and a high charge recombination within the s-DSSCs. The instability of ZnO with respect to TiO<sub>2</sub> in acidic medium is attributed to the high isoelectric point of ZnO compared to TiO<sub>2</sub> (see Table V-1). The agglomerates are thus detrimental to the performance of an all ZnO-based DSSCs.

In this present chapter, we proposed to develop a stable ZnO photo-anode instead of TiO<sub>2</sub> in s-DSSCs, and our aim is to enhance the charge transport within the electron transporting material layer and to improve the overall efficiency of the device. We propose to use the procedure we used previously with TiO<sub>2</sub> based s-DSSCs to produce new s-DSSCs based on CP as HTM. The CP will be produced by *in-situ* PEP directly on the dye modified ZnO substrate.

At present, and to the best of our knowledge, no report has been done on ZnO based s-DSSCs using CP as HTM generated by *in-situ* PEP.

### **V. 1. b. s-DSSCs based ZnO using Conducting Polymers generated by *in-situ* PEP**

In order to understand the effect of the new oxide semiconductor on the device efficiency, our initial approach consist in producing a s-DSSC based on ZnO with the same components used for the elaboration of the s-DSSCs based on TiO<sub>2</sub>. This strategy will allow an easy and better comparison. Therefore the targeted ZnO based s-DSSC device will be composed of:

- The FTO substrate with the same sheet resistance (15 Ω/sq)
- The configuration of the photo-anode will be the same, comprising a blocking layer and a mesoporous layer with the same thicknesses and only TiO<sub>2</sub> is replaced by ZnO. An attempt is made without blocking layer.
- An efficient organic dye that gave a high efficiency in s-DSSC based on TiO<sub>2</sub>
- The same PEDOT CP generated by *in-situ* PEP used as HTM with the same deposited total charge
- The same metallic counter electrode

Regarding the photo-anode and taking into consideration the effect of the different ZnO morphologies on the electronic transport, the nanorods are incorporated in the mesoporous layer. Simultaneously, we investigate the effect of the ZnO blocking layer (BL) varying several parameters.

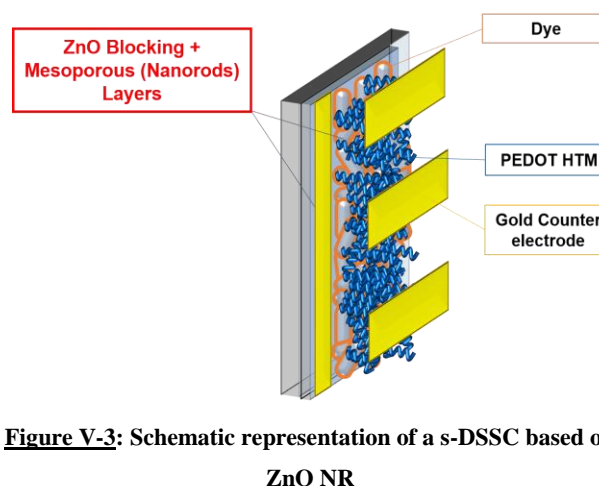


**Figure V-3:** Schematic representation of a s-DSSC based on ZnO NR

The blocking layer is a dense layer of the semiconductor deposited directly on the FTO substrate avoiding any contact between the FTO and the HTM on the one hand, and between the FTO and the dye, on the other hand. These two interfaces are responsible for the recombination of charges which are the cause of the current losses of the cells. When these two parameters are decreased, it is possible to improve the efficiency of the devices.

The BL is prepared by varying different parameters as outlined below:

- the absence vs. the presence of the BL
- the variation of the technical procedure: sol-gel and spray pyrolysis
- the number of successive layers deposited during the preparation of the BL: 1 or 3 layers
- the influence of the substrate size during the preparation of the BL: (i) in single electrode (1 x 1), (ii) in 4 twin electrodes (2 x 2).

In order to evaluate the effect of these parameters, we relied on the electrochemical measurements.

Two other important parameters are also investigated which correspond to the effect of dye adsorption time (4 min, 2 h, 18 h) on cell performances which is a critical step in the implementation of the s-DSSC based ZnO. The effect of the  $\text{Li}^+$  concentration providing from additives is also studied.

## **V. 2. Elaboration of ZnO Photo-anode**

The implementation of ZnO photo-anode was achieved in three steps: the etching process, the blocking layer preparation and the mesoporous layer preparation. For the etching process, the procedure is the same as described in chapter II.

### **V. 2. a. Preparation of ZnO blocking layer**

The blocking layer is prepared by sol-gel method and by spray pyrolysis process using for both a precursor solution.

#### **V.2.a.(i) Spin coating process**

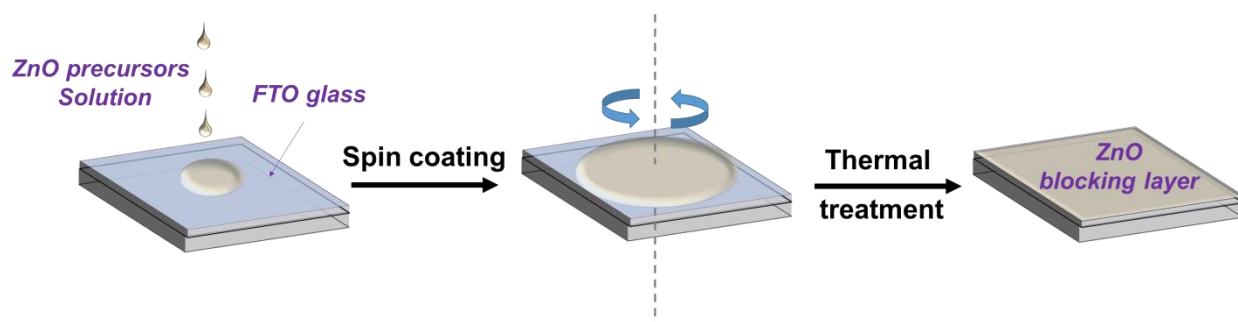


**Figure V-4:** Schematic representation of spin-coating technique on FTO substrate.

ZnO blocking layer is achieved by sol-gel method and uniformly deposited as thin film on the FTO substrate by means of spin-coater followed by a thermal treatment (Figure V-4). The sol-gel method follows the colloidal processing route involving a colloidal suspension (sol) containing zinc acetate dehydrate salt that acts as precursor dissolved in organic solvent. The sol is prepared following the procedure developed by Liu *et al.*<sup>[22]</sup>. Indeed, the authors developed a simple route to make an efficient BL resulting in a performant DSSCs. Briefly, zinc acetate dehydrate (0.2 M and 0.6 M) is added into 10 mL of absolute ethanol. The mixture is under stirring at 50 °C for 10 min until the solution forms a white emulsion. Then, diethanolamine (DEA) is added into the emulsion which becomes promptly transparent. The solution is kept under stirring for 10 min more. The sol is found to be stable and clear without any precipitate or turbidity. The DEA is added following the molar ratio 1:1 (DEA/Zinc acetate dehydrate).

The procedure was optimized in order to get a similar thickness as obtained for TiO<sub>2</sub> based s-DSSCs *i.e.* ≈100 nm. Therefore for a precursor concentration of 0.2 M, three layers are required whereas for a precursor concentration of 0.6 M, one layer is suitable. The solution is spin-coated under 3000 rpm for 30 s, on FTO substrates: (1 x 1) and (2 x 2) with a volume of 25μL and 100μL respectively. The coating films are dried at 50 °C for 5 min, and then sintered at 300 °C for 20 min after each deposited layer.

### V.2.a.(ii) Spray pyrolysis process

ZnO BL is prepared with the method reported by Memarian *et al.*<sup>[4]</sup> who demonstrated an efficient BL using spray pyrolysis method. Using this procedure, they found an unprecedented DSSC efficiency of 7.5 % in liquid electrolyte based DSSC. The ZnO solution precursor contains 0.24 M of zinc acetate dehydrate in 16 mL methanol/water (2:1, v/v). The substrates are arranged on a hot plate, and then the spray pyrolysis process is carried out following the protocol described below:

Monitoring temperature	Heating time (min)
RT → 150 °C	5 min
150 °C → 250 °C	20 min
<b>SPRAY PYROLYSIS</b>	
250 °C → 450 °C	30 min

**Table V-2:** Temperature and time conditions during the spray pyrolysis process.

After spray pyrolysis, the substrates are annealed at 450°C for 30 min which is the optimal temperature to make a well-connected network between ZnO aggregates for an efficient electron transport and hence for an improvement of  $J_{sc}$ <sup>[4]</sup>.

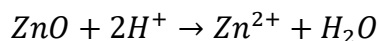
### **V. 2. b. Preparation of ZnO mesoporous layer**

The doctor-blade method initially developed for preparation of TiO<sub>2</sub> photo-anodes based DSSCs, has also been adopted to construct ZnO mesoporous films. Contrary to TiO<sub>2</sub> paste composed of commercial nanoparticles, ZnO paste is home-made, provided from the collaboration<sup>[23]</sup>. ZnO paste is prepared from a colloidal mixture of ZnO nanorods powder and ethylcellulose in ethanol. ZnO NR powder was synthesized by hydrolysis in polyol medium technique. The rod-like nanoparticles size is given at 35 nm and at 110 nm for the diameter and the length respectively. The effect of the size and shape was investigated by the group of Pauporté who found that ZnO NR, of 35 nm in diameter, based DSSC yield the best efficiency<sup>[23,24]</sup>. Once the ZnO paste was doctor-bladed on FTO/ZnO BL substrates, the photo-anodes are sintered in order to remove the organic compounds and to improve the ZnO crystallinity using a gradual sintering procedure: 250 °C for 10 min, 300 °C for 10 min, 350 °C for 10 min, 390 °C for 2 min and 410 °C for half of an hour in air atmosphere. The heating temperature is achieved at 410 °C which was determined as the best temperature leading to the best DSSCs performances<sup>[25]</sup>.

### **V. 2. c. Sensitization Step: Dye Adsorption**

The commercially available D35 dye is used in this work. It is solubilized in ethanol at  $C = 0.2$  mM. The FTO/ZnO electrodes are immersed in the dye bath overnight as made for FTO/TiO<sub>2</sub> in the other chapters.

The sensitization of ZnO is known to be a critical step due to the presence of acidic proton providing from the anchoring group which cause the dissolution of ZnO:



Therefore the effect of dye adsorption time on cell performances is investigated. The FTO/ZnO electrodes are immersed in the dye bath for 4 min, 2h and 18h.

#### **V. 2. d. *In-situ* PEP process and additives**

The *in-situ* PEP process was carried out by chronoamperometry (see the experimental section in chapter II) in organic medium using Bis-EDOT as monomer precursor and a total charge of 20 mC.cm<sup>-2</sup> is deposited. After polymerization, the *in-situ* generated PEDOT films are spin coated with 50 µL of an ionic liquid additives containing tBP:LiTFSI (5:1) in acetonitrile. Quintana *et al.* have shown that the Li<sup>+</sup> ions shift the conduction band of the ZnO to more negative potential whereas opposite behavior is found for TiO<sub>2</sub> [26]. Therefore, in order to study the influence of the Li<sup>+</sup> ions on cell performances, the concentration of LiTFSI is decreased 10 fold and a s-DSSC is implemented without LiTFSI.

#### **V. 2. e. Characterizations and s-DSSC performances**

The surface morphology of ZnO compact blocking layer is characterized by SEM, the film conductivity is evaluated by cyclic voltammetry (CV) using the same conditions as described in chapter II, and the thickness is determined both by SEM and by profilometer. Similarly, the mesoporous layer is characterized by SEM, profilometer and XRD in order to evaluate the crystalline structure of ZnO as well as the porosity of the mesoporous film. s-DSSCs are assembled following the procedure detailed in the previous chapters. The photovoltaic performances of s-DSSCs are determined from the I-V curves.

### **V. 3. Results and Discussion**

Several parameters have been varied during the preparation of the s-DSSC based ZnO and are listed in the Table V-3.



Component	Parameter	Condition	Electrode	Deposited layer			
Photo-anode	Without blocking layer						
	With blocking layer				Spin coating	1 x 1	1 and 3 layers
						2 x 2	1 and 3 layers
					Spray pyrolysis		
Dye	Adsorption time	4 min					
		2 h					
		18 h					
Additives	LiTFSI concentration	0.05 M					
		0.005 M					
		No LiTFSI					

**Table V-3:** Experimental conditions that have been varied during the preparation of the s-DSSCs based on ZnO.

### V. 3. a. Electrochemical characterization of the ZnO blocking layer

The resulting FTO substrates in presence of BL obtained by different methods and conditions are characterized electrochemically in order to evaluate their blocking effectiveness, and are compared to the pristine FTO substrate.

#### V.3.a.(i) Blocking layer by spin coating vs. spray pyrolysis

The Figure V-5 shows the voltammograms obtained for these two substrates in comparison with FTO substrate. Almost no current is measured for the substrate having the BL prepared by spin coating while an important current is measured for the substrate with a BL prepared by spray pyrolysis. This clearly indicates that the BL deposited by spin coating does not allow any charge transfer in the studied potential range, indicating a complete blocking property, whereas for BL deposited by spray pyrolysis, the electrode obtained is conductive. Therefore, in our conditions, the spin coating method is more efficient than spray pyrolysis and will be exclusively used for subsequent experiments.

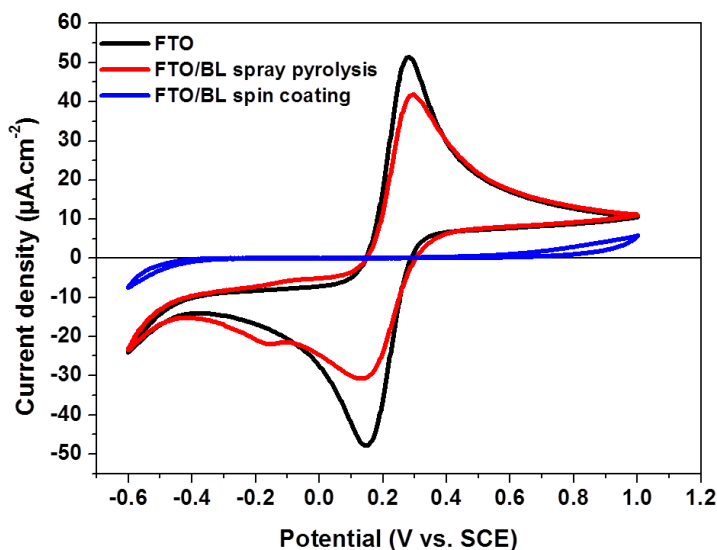


**Figure V-5:** Cyclic voltammograms of the pristine FTO electrode (black) compared to FTO/BL prepared by either spray pyrolysis (red) or by spin coating (blue).

### V.3.a.(ii) Blocking layer by spin coating: 1 layer vs. 3 layers

When the amount of precursors is constant, the electrodes fabricated using 1 layer and 3 layers shows CV with no significant current when compared to the CV obtained for pristine FTO electrode (Figure V-6).

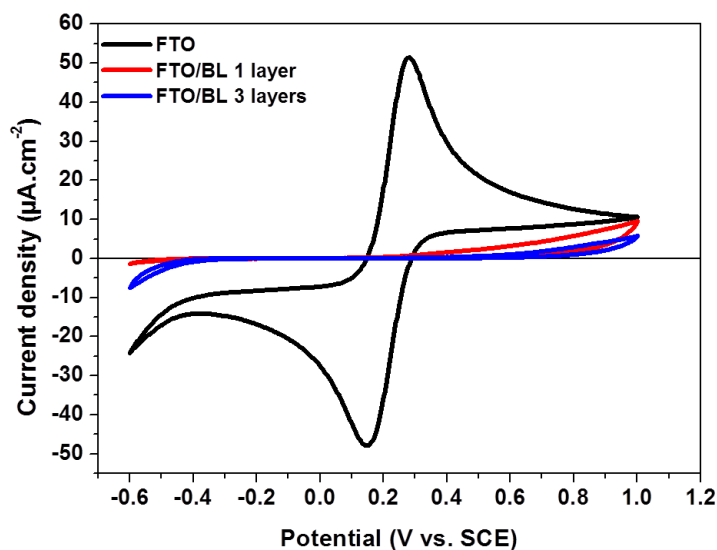


**Figure V-6:** Cyclic voltammograms of the pristine FTO electrode (black) compared to FTO/BL prepared by spin coating with 1 layer (red) or 3 layers (blue).

This supports that the BL of the two substrates constitutes efficient barrier to prevent charge transfer. However, a closer look suggests that the resulting substrate with 3 deposited layers is

more resistive than the substrate with 1 deposited layer. Therefore, the substrate with 3 deposited layers prepared by spin coating method is more effective and will be applied for the preparation of all the following experiments.

### V.3.a.(iii) Influence of the substrate size by spin coating: 3 layers on (1 x 1) and (2 x 2) electrodes

According to the CV measurements illustrated in the Figure V-7, the electrodes obtained after BL deposition on small area (1 x 1) or of large area (2 x 2) substrates, are all resistive indicating blocking ability as shown in the inset and one is completely resistive. However, the CV of (1 x 1) electrode shows a large plateau in the entire potential domain explored, whereas, the CV of (2x2) shows a leakage current at the limits of the potential domain.

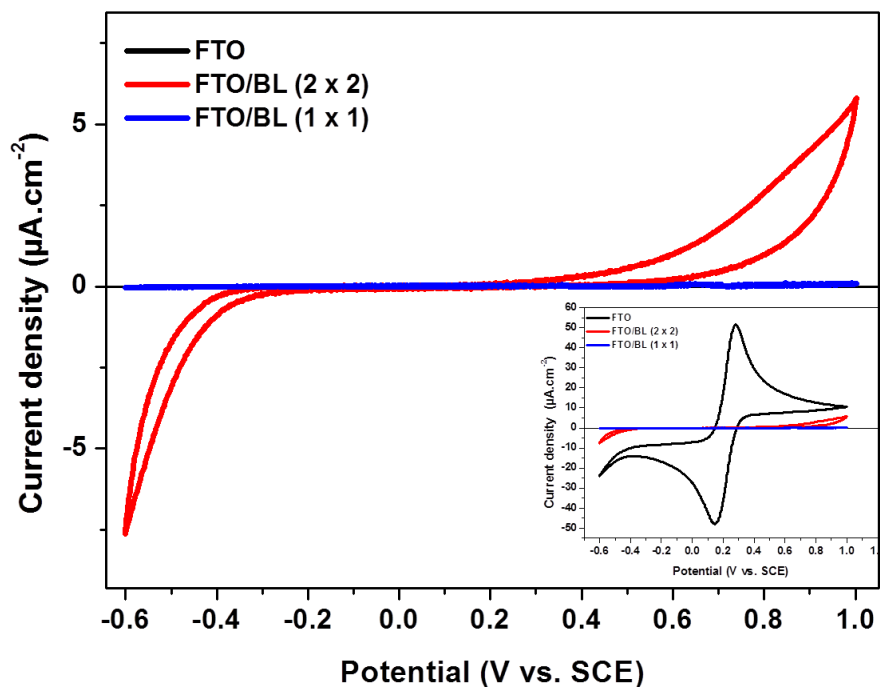
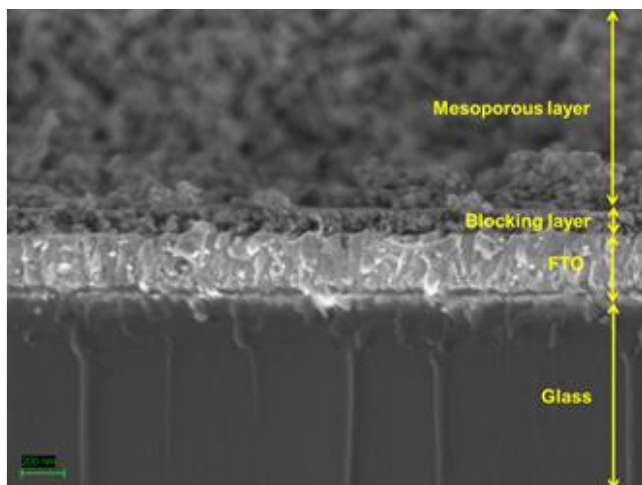


**Figure V-7:** Cyclic voltammograms FTO/BL prepared by spin coating on individual (blue) and (2 x 2) (red) substrates compared to (inset) the pristine FTO electrode (black).

Therefore for the blocking layer preparation, (i) 3 layers will be deposited by (ii) spin coating method on (iii) individual electrode which should minimize charge recombination at FTO/dye and at FTO/HTM interfaces of the *s*-DSSC.

### V. 3. b. Structural characterization of ZnO blocking layer and ZnO mesoporous layer

#### V.3.b.(i) Thicknesses and morphologies determination of blocking and mesoporous layers by SEM



The cross sectional SEM view, in Figure V-8, clearly shows two different layers on the top the FTO glass substrate: the blocking layer as compact layer and the mesoporous layer of ZnO nanorods. The structure is relatively comparable to the obtained photo-anode obtained for TiO<sub>2</sub>. For both layers, the morphology and the thickness are determined.

**Figure V-8:** Cross-sectional SEM view of ZnO (blocking layer + mesoporous layer) deposited on FTO substrate

#### ➤ Blocking layer analysis

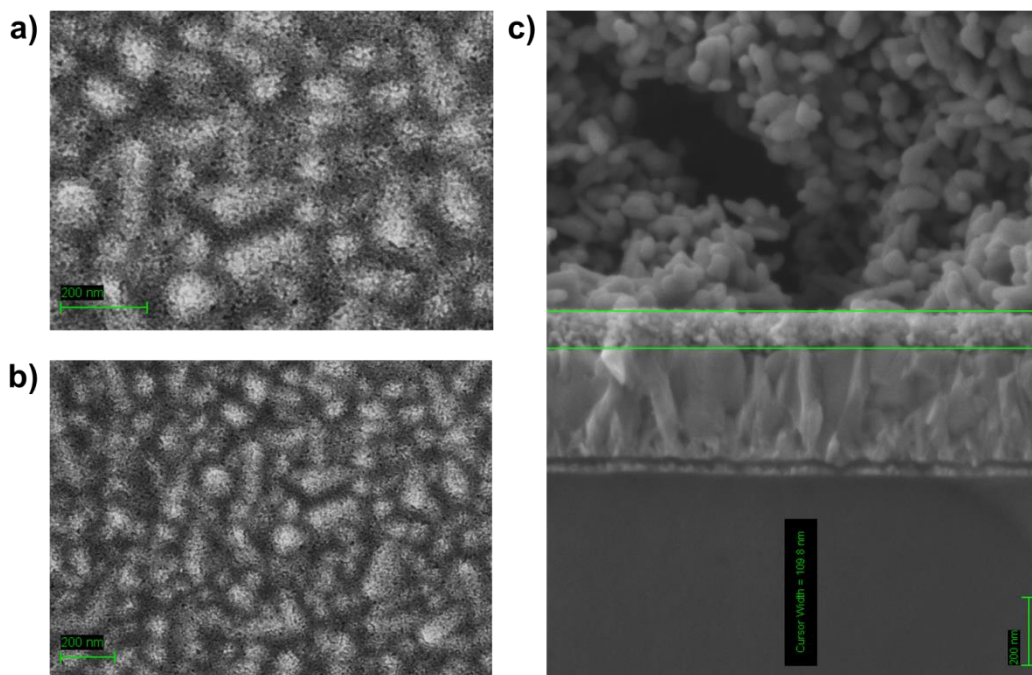


**Figure V-9:** Surface SEM images of ZnO blocking layer coated on FTO electrode with (a) and without (b) magnification. (c) Cross sectional SEM image of ZnO photo-anode and the BL thickness is measured at 110 nm.

Figure V-9 shows SEM images of ZnO BL spin coated on FTO substrate. Clearly, with magnification, a thin ZnO layer composed of small nanoparticles is observed on the FTO substrate. Particles size is estimated to be approximately 15 nm in diameter. From the cross-section SEM view, the BL is uniformly flat and homogeneous without any cracks, and the thickness is estimated to be approximately 110 nm.

➤ Mesoporous layer analysis

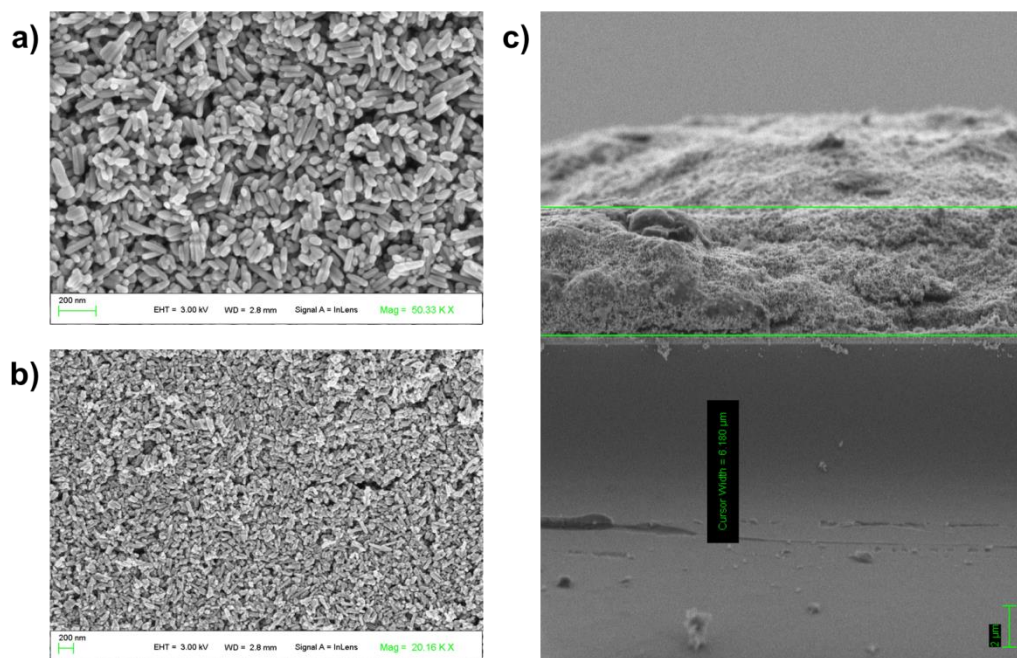


**Figure V-10:** Surface SEM images of ZnO mesoporous layer coated on FTO electrode with (a) and without (b) magnification. (c) Cross sectional SEM image of ZnO photo-anode and the mesoporous layer thickness is around 6 μm.

The SEM images of ZnO mesoporous surface show that nanoparticles are rod-shape with uniform size (Figure V-10). As expected, the average diameter of rods is 35 nm and the length is estimated to be around 100 nm. Interestingly, the ZnO film is conveniently porous owing to the use of ethyl cellulose as polymeric additive which induces a suitable porous ZnO electrode. As shown in the cross-sectional SEM image, the doctor bladed film is quite flat but the average thickness is around 6.1 μm which is comparable to that obtained for TiO<sub>2</sub>. Note that thickness of this layer is controlled by the tape thickness.

These SEM analyzes thus confirm that the obtained photo-anode is adequate, with an ideal configuration and with similar thicknesses as obtained for TiO<sub>2</sub>, for the BL and the mesoporous

layer. However additional characterization is required to evaluate the structure crystallinity and the pore size of the film. This is done by XRD.

### V.3.b.(ii) Pore size and crystalline structure determination of the mesoporous layer by XRD

The XRD pattern of the mesoporous film is shown in Figure V-11a. The resulting peaks, are intense and perfectly match with the zincite mineral reference pattern (JCPDS 01-073-8765). Indeed the zincite mineral have the hexagonal wurtzite crystalline structure (P63mc space group)<sup>[27]</sup> with the divalent cation in tetrahedral coordination with oxygen, and each oxygen in tetrahedral coordination to four divalent cations. The comparison of this diagram with that of the reference pattern shows that the (100) plane (Figure V-11b) appears to be the preferential crystallographic orientation since the intensity of this peak at 31.5 ° is greater than the theoretical intensity. The diffraction features for SnO<sub>2</sub> from FTO are marked by asterisk.

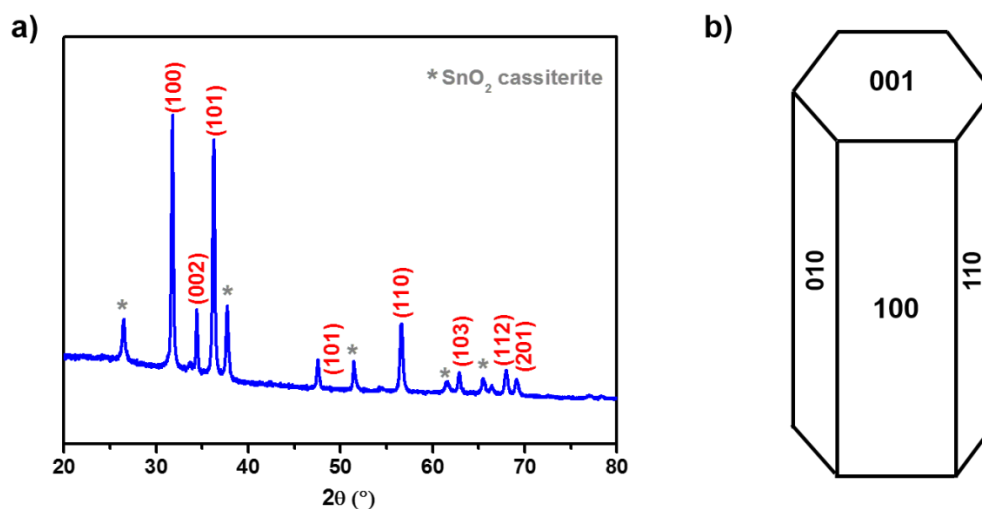


**Figure V-11:** (a) X-Ray diffraction pattern of ZnO mesoporous layer with the associated plane and (b) illustration of a zincite crystal with the corresponding plane.

Complementary measurements are carried out, at the low diffraction angles, in order to estimate the pore size of the mesoporous layer of ZnO. The pore size is in average of 20 nm slightly lower than that obtained for TiO<sub>2</sub>.

These low diffraction angles measurements also allow the determination of the crystallite size for both BL and mesoporous layers: 18 nm and 40 nm in diameter are found for crystallite within the

blocking layer and the mesoporous layer respectively. These values are in good agreement with SEM analyzes.

### V. 3. c. Characterization of D35 dye sensitized ZnO photo-anode

The redox behavior of D35 dye adsorbed on ZnO substrate is studied for the different dye adsorption time corresponding to 4 min, 2h, and 18h and compared to D35 adsorbed on TiO<sub>2</sub> substrate. In the Figure V-12, all CVs of these different substrates are presented and display a reversible redox behavior.

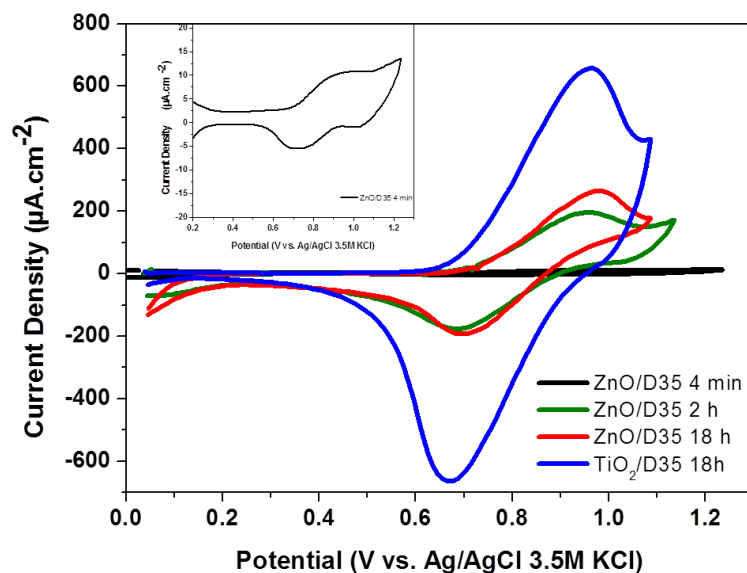


**Figure V-12:** Cyclic voltammograms of the D35 dye sensitized ZnO photo-anode for 4 min (black), 2h (green), 18h (red) and cyclic voltammograms of the D35 dye sensitized TiO<sub>2</sub> photo-anode (bleu).

For the same dye adsorption time of 18h, the current density of D35 adsorbed on ZnO, is much lower than that of D35 adsorbed on TiO<sub>2</sub> substrate. The low current density must be due to the less amount of adsorbed dye onto the ZnO surface caused by the deterioration of the latter by H<sup>+</sup> during dye loading process. Conversely, TiO<sub>2</sub> based photo-anodes is insensitive to a prolonged dye adsorption time, due to its higher chemical stability. This is highly consistent with the calculated dye concentration, after desorption (see Table V-4).

The amount of adsorbed dye molecules decreases continuously as the adsorption time decreases. Indeed for an adsorption time of 4 min, few dye molecules are present, showing almost no current density in the voltammogram. Interestingly, for a dye adsorption time of 2h, the CV behavior of the dyed photo-anode is almost the same as for a dye adsorption of 18h. This

indicates that the surface coverage is comparable for dye immersion duration of 2h and 18h which is consistent with the calculated D35 dye concentration after desorption.

Adsorption time	D35 concentration on ZnO calculated after desorption ( $\text{mol.L}^{-1}$ )
4 min	0.009
2 h	0.039
18 h	0.045

**Table V-4:** Calculated D35 concentration after desorption with 0.1 M KOH in methanol determined from UV-Vis spectra

The D35 dye oxidation potential differs upon the oxide semiconductor on which it is adsorbed, as well as the time of adsorption. When  $\text{TiO}_2$  is used, the oxidation potential is 0.96 V vs. Ag/AgCl whereas for the same adsorption time on ZnO, the determined  $E_{\text{ox}}$  is slightly higher 0.98 V vs. Ag/AgCl. However the  $E_{\text{ox}}$  decreases continuously as the adsorption time decreases, (0.95V and 0.93V for 2 h and 4 min respectively). However the onset of the oxidation potential remains the same for D35 adsorbed on ZnO whatever the sensitization time ( $E_{\text{onset,ox}} = 0.72$  V vs Ag/AgCl). The corresponding energy value in reference to vacuum calculated from the onset oxidation potentials, corresponds to  $E_{\text{HOMO}} = -5.37$  eV. From the  $E_{0-0}$  calculated in the chapter II which is reported to be at 2.18 eV, the LUMO level can be determined,  $E_{\text{LUMO}} = -3.19$  eV.

We can thus describe the energy level diagram of D35 dye as well as that of ZnO and PEDOT (Figure V-13).

According to the voltammograms, the oxidation potential of D35 matches with the onset of the oxidation potential of Bis-EDOT (0.57 V vs Ag/AgCl) and not with the  $E_{\text{onset,ox}}$  of EDOT (1.21 V vs Ag/AgCl). Finally, the convenient dye-monomer pair, for the *in-situ* PEP process, is D35 – Bis-EDOT.

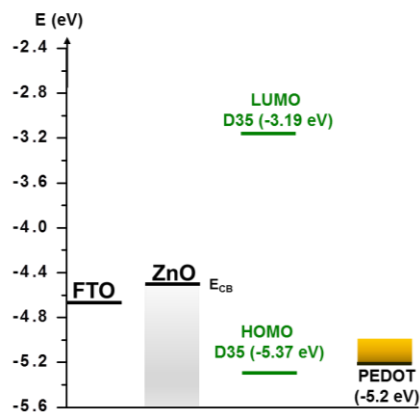


**Figure V-13:** Energy band diagram of s-DSSC based on ZnO using D35 as sensitizer.



### V. 3. d. In-situ PEP using D35 organic dye in organic medium

The *in-situ* PEP is performed using the dyed ZnO photo-anodes in presence of BL with different adsorption time (Figure V-14). During the *in-situ* PEP on FTO/ZnO/D35 for any adsorption time, the resulting chronoamperograms follow the typical current transient curve (monomer oxidation, nucleation and growth processes). However, for an adsorption time of 4 min the current polymerization is instantly decreased to reach the current plateau of  $2 \mu\text{A}\cdot\text{cm}^{-2}$  and hence only a few amount of CP is deposited with a total charge of  $6 \text{mC}\cdot\text{cm}^{-2}$ . The low current is provided from the low amount of dye molecules adsorbed on ZnO surface which is not sufficient to oxidize the monomers in solution. For an adsorption time of 2h and 18h, the polymerization occurs for both within 23 min and the behavior seems to be similar to that obtained for D35 adsorbed on  $\text{TiO}_2$  photo-anode under the same conditions (cf. Chapter II). The *in-situ* PEP process is therefore suitable and leads to stable current on ZnO photo-anode. Therefore, the optimal adsorption time that will be used to set up ZnO based photo-anodes corresponds to either 18h or 2h.

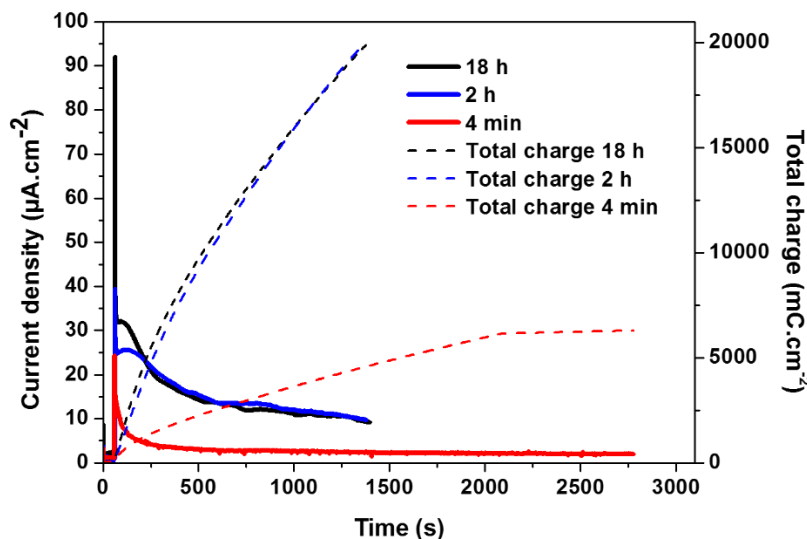


**Figure V-14:** Photocurrent variation (solid curves) and total polymerization charge (dotted curves) during the *in-situ* PEP process of Bis-EDOT in organic medium using D35 dye adsorbed on ZnO substrate with BL at different time under a potential of 0.20 V vs. Ag/AgCl and 0.1 Sun.

The ZnO photo-anodes without BL are also tested in order to study the role and the necessity of the ZnO BL in the final s-DSSC device. As shown in Figure V-15, for a 4 min adsorption time, it took at least 1h to produce a polymer and the total charge amounts to  $5 \text{mC}\cdot\text{cm}^{-2}$ . Whereas for an adsorption time of 2h, total charges of  $9 \text{mC}\cdot\text{cm}^{-2}$  was obtained and for an adsorption time of 18h

the total charge was  $13 \text{ mC.cm}^{-2}$ . However in none of these three cases, a total charge of  $20 \text{ mC.cm}^{-2}$  is deposited on the electrode surface. This was not the case when the blocking layer is present. Therefore the presence of blocking layer is required to ensure an efficient *in-situ* PEP process.

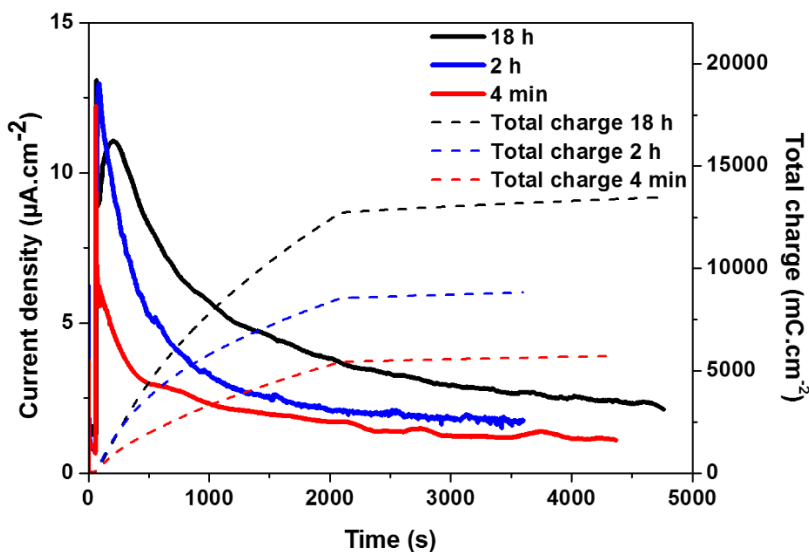


**Figure V-15:** Photocurrent variation (solid curves) and total polymerization charge (dotted curves) during the *in-situ* PEP process of Bis-EDOT in organic medium using D35 dye adsorbed on ZnO substrate without BL at different time under a potential of 0.20 V vs. Ag/AgCl and 0.1 Sun.

### V. 3. e. SEM characterization of FTO/ZnO/D35/PEDOT photo-electrode

After achieving the *in-situ* PEP process, the FTO/ZnO/D35/PEDOT photo-electrode is characterized by SEM.

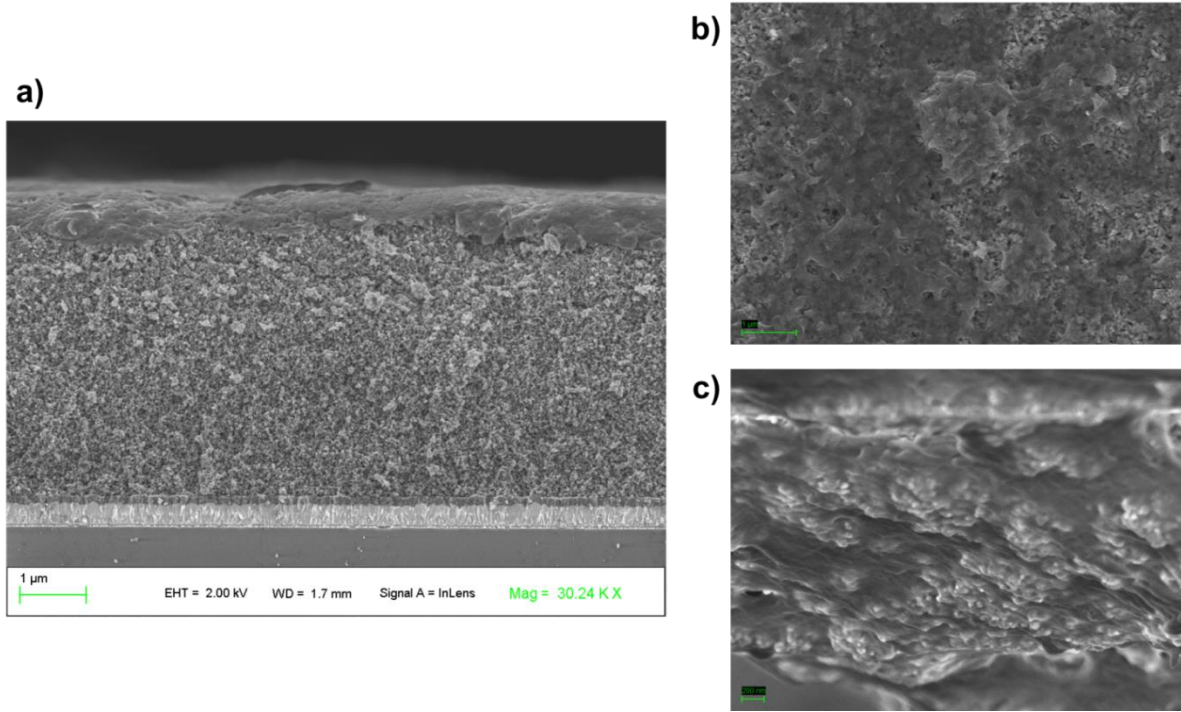


**Figure V-16:** (a) Cross-sectional SEM image and surface SEM images surface of FTO/ZnO/D35/PEDOT photo-electrode (b) with magnification (c) with tilt angle.

As illustrated in the Figure V-16, the CP is well deposited on the dyed photo-anode. However, the polymer is only observed mainly on the top of the ZnO mesoporous layer but not within the pores compared to the SEM images of TiO<sub>2</sub> photo-anode obtained after *in-situ* PEP.

### V. 3. f. ZnO based s-DSSCs devices performances

Presence of blocking layer	Aging Time	V <sub>oc</sub> (V)	J <sub>sc</sub> (mA.cm <sup>-2</sup> )	FF (%)	Efficiency $\eta$ (%)
No BL	1 Day				
	15 Days	0.29	$2.9 \times 10^{-5}$	23	0.00
With BL	1 Day	0.09	7.09	33	0.22
	15 Days	0.23	6.87	39	0.62

**Table V-4:** Photovoltaic parameters of s-DSSCs based on ZnO sensitized with D35 dye under the AM 1.5G illumination of the simulated sunlight (100mW/cm<sup>2</sup>).

After metallic gold counter-electrode deposition, the complete s-DSSCs based ZnO are obtained. However, for most of samples the gold evaporation was not succeeded leading to inefficient s-DSSCs with a counter electrode of a thickness of less than 20 nm, due to the inappropriate

deposition conditions. Therefore, we report exclusively the photovoltaic performances of operational s-DSSCs: (i) with and without BL, for an (ii) adsorption time of 18h, with (iii)  $20 \text{ mC.cm}^{-2}$  of PEDOT total charge and, (iv) in presence of 0.05 M of LiTFSI. The photovoltaic parameters are listed in the Table V-4.

As indicated in the Table V-4, the photovoltaic parameters cannot be obtained for s-DSSCs without BL after 1 day. But after 15 days, a  $V_{oc}$  of 290 mV and a very low  $J_{sc}$  are measured, leading to an efficiency of 0 %. By contrast, in presence of BL, an efficiency of 0.22 % is reached at first which is higher to that obtained by Lee at al.<sup>[19]</sup> who reported a ZnO NR based s-DSSC using P3HT as HTM yielding to 0.13 % efficiency. They found a  $J_{sc}$  value of less than  $1 \text{ mA.cm}^{-2}$  whereas in our case the  $J_{sc}$  is seven times higher. Therefore, in our s-DSSCs, the electron injection processes from D35 dye to ZnO and from the HTM to the dye are more efficient. However the  $V_{oc}$  is low (0.09 V) which means that some recombination takes place probably due to the remaining solvents. Indeed when the same s-DSSCs is characterized after 15 days (Figure V-17) the  $V_{oc}$  is 2.5 fold higher (0.23 V) and the FF is also increased resulting in an overall efficiency of 0.62 %. This overall efficiency is relatively high with respect to ZnO based s-DSSCs produced until now and knowing that the maximum efficiency is of 1.7 % obtained for s-DSSCs based on CuSCN used as HTM. Therefore the production of the CP by *in-situ* PEP is promising for ZnO based s-DSSC and the presence of BL is required in this type of s-DSSC.

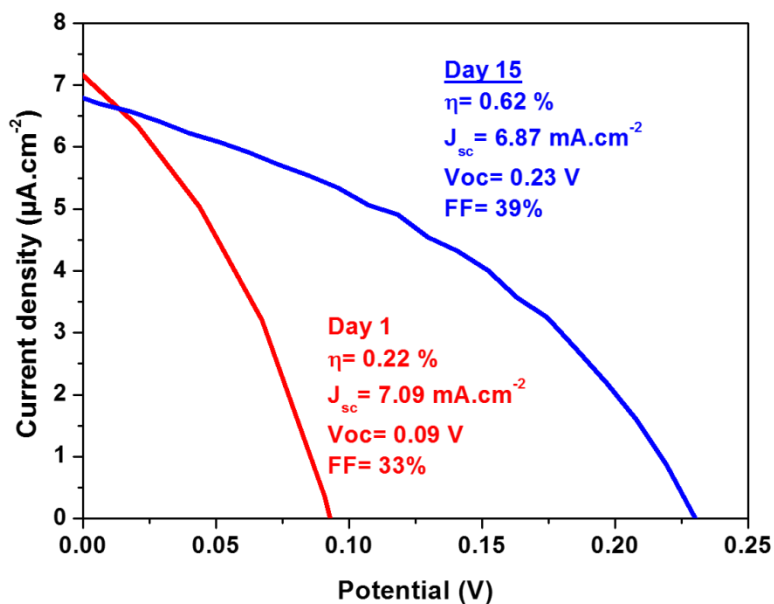


**Figure V-17:** Photovoltaic Parameters of s-DSSCs based ZnO with BL measured after 1 and 15 days, illuminated at  $100 \text{ mW cm}^{-2}$  (AM 1.5G)

### V. 3. g. Discussions

As seen earlier, in the second Chapter, for TiO<sub>2</sub>, the *in-situ* PEP process is a highly effective method allowing the HTM to fill the pores of the semiconductor material. Concerning the dyed ZnO photo-anode in presence of blocking layer using the suited spin coating method, the *in-situ* PEP process is achieved successfully. However without blocking layer, the *in-situ* PEP process took more than 1h to produce a small amount of polymer where the total charge does not exceed 13 mC.cm<sup>-2</sup>. This ineffective *in-situ* PEP may originate from two main steps:

- The adsorption step: the dissolution of ZnO results in the formation of agglomerates of Zn<sup>2+</sup> and dyes molecules. These agglomerates can fill the ZnO mesopores and can potentially block the diffusion and the access of monomers during the *in-situ* PEP process.
- The *in-situ* PEP step itself: to the partial dissolution of ZnO originating from acidity resulting from the protons released during the polymerization process

Thus, the resulting HTM is not or weakly present within the ZnO mesoporous layer as highlighted from SEM analyses. The resulting overall efficiencies of devices based on ZnO ( $\eta=0.62\%$ , with  $J_{sc}=6.9\text{ mA}\cdot\text{cm}^{-2}$ ,  $V_{oc}=0.23$  and  $FF=39\%$ ) are lower to those obtained with their analogues based on TiO<sub>2</sub>. Indeed, for TiO<sub>2</sub> based s-DSSC using the same dye (D35) and the same HTM (PEDOT) generated by *in-situ* PEP from the same monomer precursor (Bis-EDOT) in organic medium, the overall yield is 4.60 % with  $J_{sc}=8.2\text{ mA}\cdot\text{cm}^{-2}$ ,  $V_{oc}=0.83\text{ V}$  and  $FF=68\%$ . According to the low value of the  $V_{oc}$ , obtained with ZnO based devices, this decrease can be explained by an important charge recombination processes within the cell due to the poor pore filling when compared to the  $V_{oc}$  obtained with TiO<sub>2</sub> based device. The relative comparable high  $J_{sc}$  current obtained with ZnO based devices compared to the  $J_{sc}$  obtained with TiO<sub>2</sub> based devices is probably due to the higher mobility within ZnO nanomaterial as regard to the mobility within TiO<sub>2</sub> nanomaterial.

## V. 4. Conclusion

In this Chapter, we developed for the first time, a ZnO based s-DSSC using a HTM generated by *in-situ* PEP. For the ZnO based s-DSSCs studied, we demonstrated that the *in-situ* PEP process can be carried out using the dye modified ZnO substrates as deposition electrode, but this *in-situ* PEP process is not as effective to allow the HTM to fill the ZnO mesopores. Indeed the HTM seems to be mainly deposited on the top of the dyed ZnO photo-anode. Nevertheless, when the resulting FTO/ZnO/D35/PEDOT photo-electrodes are used in devices, the s-DSSCs show undisclosed and promising photovoltaic performances. Setting up this type of targeted s-DSSC devices based on ZnO, which are stable over time, largely cost-effective and very environmentally friendly as regard to other type of s-DSSCs, is essential. Therefore, the optimization of this type of ZnO based s-DSSCs is of major interest and must be continuing first by improving the pore filling, the ZnO the surface and the ZnO/HTM interface. A high improvement potential can be done at these levels to obtain highly efficient ZnO based s-DSSCs using CP as HTM obtained by *in-situ* PEP.

## V. 5. References

- (1) Zhang, Q.; Dandeneau, C. S.; Zhou, X.; Cao, G. *Adv. Mater.* **2009**, *21* (41), 4087–4108.
- (2) Hagfeldt, A.; Boschloo, G.; Sun, L.; Kloo, L.; Pettersson, H. *Chem. Rev.* **2010**, *110* (11), 6595–6663.
- (3) Vittal, R.; Ho, K.-C. *Renew. Sustain. Energy Rev.* **2017**, *70*, 920–935.
- (4) Memarian, N.; Concina, I.; Braga, A.; Rozati, S. M.; Vomiero, A.; Sberveglieri, G. *Angew. Chem. Int. Ed.* **2011**, *50* (51), 12321–12325.
- (5) Kakiage, K.; Aoyama, Y.; Yano, T.; Oya, K.; Fujisawa, J.; Hanaya, M. *Chem Commun* **2015**, *51* (88), 15894–15897.
- (6) Hao, Y.; Yang, W.; Zhang, L.; Jiang, R.; Mijangos, E.; Saygili, Y.; Hammarström, L.; Hagfeldt, A.; Boschloo, G. *Nat. Commun.* **2016**, *7*, 13934.
- (7) Barpuzary, D.; Patra, A. S.; Vaghasiya, J. V.; Solanki, B. G.; Soni, S. S.; Qureshi, M. *ACS Appl. Mater. Interfaces* **2014**, *6* (15), 12629–12639.
- (8) Law, M.; Greene, L. E.; Johnson, J. C.; Saykally, R.; Yang, P. *Nat. Mater.* **2005**, *4* (6), 455–459.
- (9) Chen, L.-Y.; Yin, Y.-T. *Nanoscale* **2013**, *5* (5), 1777.
- (10) Yang, Y.; Zhao, J.; Cui, C.; Zhang, Y.; Hu, H.; Xu, L.; Pan, J.; Li, C.; Tang, W. *Electrochimica Acta* **2016**, *196*, 348–356.
- (11) Kang, X.; Jia, C.; Wan, Z.; Zhuang, J.; Feng, J. *RSC Adv* **2015**, *5* (22), 16678–16683.
- (12) Martinson, A. B. F.; Goñes, M. S.; Fabregat-Santiago, F.; Bisquert, J.; Pellin, M. J.; Hupp, J. T. *J. Phys. Chem. A* **2009**, *113* (16), 4015–4021.
- (13) Abd-Ellah, M.; Moghimi, N.; Zhang, L.; Thomas, J. P.; McGillivray, D.; Srivastava, S.; Leung, K. T. *Nanoscale* **2016**, *8* (3), 1658–1664.
- (14) McCune, M.; Zhang, W.; Deng, Y. *Nano Lett.* **2012**, *12* (7), 3656–3662.
- (15) Yang, Z.; Xu, T.; Ito, Y.; Welp, U.; Kwok, W. K. *J. Phys. Chem. C* **2009**, *113* (47), 20521–20526.
- (16) Galoppini, E.; Rochford, J.; Chen, H.; Saraf, G.; Lu, Y.; Hagfeldt, A.; Boschloo, G. *J. Phys. Chem. B* **2006**, *110* (33), 16159–16161.
- (17) Boucharef, M.; Di Bin, C.; Boumaza, M. S.; Colas, M.; Snaith, H. J.; Ratier, B.; Bouclé, J. *Nanotechnology* **2010**, *21* (20), 205203.
- (18) Schlur, L.; Carton, A.; Lévêque, P.; Guillon, D.; Pourroy, G. *J. Phys. Chem. C* **2013**, *117* (6), 2993–3001.
- (19) Lee, T.-H.; Sue, H.-J.; Cheng, X. *Nanoscale Res. Lett.* **2011**, *6* (1), 517.
- (20) Desai, U. V.; Xu, C.; Wu, J.; Gao, D. *Nanotechnology* **2012**, *23* (20), 205401.
- (21) Warnan, J.; Guerin, V.-M.; Anne, F. B.; Pellegrin, Y.; Blart, E.; Jacquemin, D.; Pauporté, T.; Odobel, F. *J. Phys. Chem. C* **2013**, *117* (17), 8652–8660.
- (22) Liu, Y.; Sun, X.; Tai, Q.; Hu, H.; Chen, B.; Huang, N.; Sebo, B.; Zhao, X. *J. Power Sources* **2011**, *196* (1), 475–481.
- (23) Hosni, M.; Kusumawati, Y.; Farhat, S.; Jouini, N.; Pauporté, T. *J. Phys. Chem. C* **2014**, *118* (30), 16791–16798.
- (24) Hosni, M.; Kusumawati, Y.; Farhat, S.; Jouini, N.; Ivansyah, A. L.; Martoprawiro, M. A.; Pauporté, T. *ACS Appl. Mater. Interfaces* **2015**, *7* (3), 1568–1577.
- (25) Guerin, V. M.; Magne, C.; Pauporté, T.; Le Bahers, T.; Rathousky, J. *ACS Appl. Mater. Interfaces* **2010**, *2* (12), 3677–3685.

- (26) Quintana, M.; Marinado, T.; Nonomura, K.; Boschloo, G.; Hagfeldt, A. *J. Photochem. Photobiol. Chem.* **2009**, *202* (2–3), 159–163.
- (27) Kihara, K.; Donnay, G. *Can. Mineral.* **1985**, *23*, 647–654.



---

---

## General Conclusion and Perspectives

---

---

In this thesis work, several solid-state dye-sensitized solar cells based on conducting polymer used as HTM have been developed in order to improve the photovoltaic performances of these devices according to the two following criteria: by optimizing the interfacial charge transfer processes within the s-DSSC, and by optimizing the charge transport within the n-type oxide semiconductor. To reach these goals, each component that constitutes the device was varied in order to investigate their effect on the device's performances. The analytical study is carried out by varying one component (*i.e.* sensitizer and the oxide semiconductor) of the device at a time. Simultaneously, the effect of the *in-situ* PEP on the resulting CP used as HTM was investigated. The *in-situ* PEP was performed in two different media (organic and aqueous) and using two different monomer precursors when possible (Bis-EDOT and EDOT).

In **Chapter II**, a series of commercially available organic dyes have been systematically investigated as sensitizers in s-DSSCs, in order to determine the best fragments of these dyes structures, *i.e.* donor, linker, and acceptor units, that have an efficient contribution on the *in-situ* PEP process to produce the CP both in organic and in aqueous media and hence on the performances of the s-DSSCs. The studied dyes **L1**, **D35**, **LEG4**, **RK1**, **BA504** and **BA741**, share the same TPA core, as donor, in their D- $\pi$ -A configuration, but are differentiated by their conjugated bridge, their acceptor and their supplementary donor (if any) moieties imbedded on the TPA. When used for *in-situ* PEP process, the **D35** dye shows high *in-situ* PEP efficiency; whereas by switching only the thiophene residue used as the  $\pi$ -conjugated bridge in **D35** dye by another  $\pi$ -conjugated bridge in the dye structure of LEG4, the corresponding *in-situ* PEP shows lower polymerization reaction yield. Regarding the s-DSSCs performances of the obtained s-DSSCs, **D35** based s-DSSC shows exceptional good and stable photovoltaic performances whatever the medium and the monomer used for the *in-situ* PEP. Therefore, in seeking the promising organic dye structure which may improve both the *in-situ* PEP yield and the s-DSSC efficiency, we concluded that the best fragments are determined to be: (i) the cyanoacrylic acid as anchoring group, (ii) the thiophene as  $\pi$ -conjugated bridge and (iii) the additional donating residues on the TPA core.

The thesis work is continued on the optimization of the interfacial charge transfer processes which are done both at (i) the dye/HTM level and at (ii) the dye/semiconductor level. The dye/HTM interface has been completely removed through the development of a new concept of covalently linking the dye to the *in-situ* generated co-polymer used as HTM as presented in the **Chapter III**. Indeed, based on the results obtained in **Chapter II**, the structure of the commercial **L1** pristine dye was used as starting building block to design two novel dyes, **ADCBZ** and **ADSNS**, each of them have the particularity to hold an electroactive monomer as pendant group on the TPA core. The interface was removed by the fact that the electro-active monomer, covalently linked to the dye is co-polymerized by *in-situ* PEP with a second monomer solubilized in the electrolytic solution. The resulting co-polymer, used as HTM, was demonstrated to be covalently linked to the dye. The resulting s-DSSCs based on each of these two novel dyes have shown fast charge transfer between the dye and the HTM inducing a decrease of charge recombination at the TiO<sub>2</sub>/HTM interface. Hence the V<sub>oc</sub> was improved. However the chemical function used to link the TPA to the electro-active monomer plays a key role in the s-DSSCs performances, when the *in-situ* PEP resulting dye linked CP is used as HTM in the device. Indeed, the presence of the ester group used as covalent link in the new dye induced a supplementary binding site of the dye on TiO<sub>2</sub> surface during the adsorption step, which negatively impacted the charge transfer at TiO<sub>2</sub>/dye interface supported by a lower J<sub>sc</sub>: a main issue in s-DSSC devices.

Consequently the **Chapter IV**, was dedicated to study the effect of switching the nature of this covalent link from ester to alkene. Therefore, two other novel organic dyes **ADCBZ-2** and **ADSNS-2**, the structural configuration of which are the same as the two previous one except the ester group linker which has been exchanged by the C=C alkene group. As expected, when these novel dyes used as sensitizers in s-DSSCs, good performances have been obtained owing to the introduction of the C=C alkene group in the novel dyes structure inducing the dyes (i) to absorb in higher wavelengths, (ii) to get a reduced bandgap and (iii) to have a lower oxidation potential: three benefits that contributes to the optimized photocurrent density J<sub>sc</sub>, and consequently to higher s-DSSCs efficiency.

From the sets of results of the two chapters, we concluded that the introduction of a covalent link between the dye and the HTM is a prominent factor to improve the s-DSSCs performances. We also concluded that the nature of covalent link between the dye and the HTM if any, must be

neutral as regard to the possible interaction with the semiconducting oxide supporting the dye/HTM component. Among the four novel dyes: **ADCBZ**, **ADSNS**, **ADCBZ-2** and **ADSNS-2**, the two latter gave the best and promising efficiencies of 2.4 % for **ADCBZ-2** and 2.2 % for **ADSNS-2**.

This series of organic dyes covalently linked to the electroactive monomer constitutes promising candidates to achieve unprecedented s-DSSCs with optimized charge transfers.

The TiO<sub>2</sub> semiconducting oxide is the most widely used material in DSSCs, but due to its low abundance and to the scarcity of titanium ores, other semiconductors based DSSCs are progressively emerging and ZnO is the most promising semiconductor alternative. Therefore, and for the first time, we developed s-DSSCs based on ZnO semiconductor using CP used as HTM and produced by *in-situ* PEP. The ZnO based s-DSSC achieved in **Chapter V** is based on **D35** dye, the most efficient one found in our study and the CP used the PEDOT produced from Bis-EDOT which shows also the best performances when used as HTM. The optimal conditions to produce ZnO photo-anode are determined and the resulting s-DSSC device based on **D35** dye as photosensitizer and PEDOT as HTM led to a high overall efficiency of 0.62 % taking into consideration that the record efficiency achieved in ZnO based s-DSSC corresponds to 1.7 %. This first result obtained is the first unique and promising for this type of s-DSSCs based on CP generated by *in-situ* PEP. Nevertheless, in view of the  $V_{oc}$  value, the optimization of this type of ZnO based s-DSSCs is of major interest and will be done in two steps: first the adsorption step must be optimized and second the *in-situ* PEP must be done in conditions that avoid the ZnO dissolution during both processes and hence the poor pore filling may be improved. For future prospects, some directions are planned to add co-adsorbent during the adsorption step in order to protect the ZnO from the protons released when *in-situ* PEP occurs.

Although the four novel dyes synthesized have shown very interesting physicochemical and electrochemical properties and have also shown a conversion efficiency up to 2 % when used as HTM linked sensitizers in solar cells. The photovoltaic parameters ( $V_{oc}$ ,  $J_{sc}$ , and FF) can be further improved. Therefore, for future prospects, we proposed to modify either (i) the  $\pi$ -conjugated bridge between the TPA core and the cyanoacrylic acceptor in order to enlarge the light dye absorption to NIR region; (ii) the nature of the covalent link between the electroactive monomer and the TPA core probably by using an alkyl link instead of conjugated link, which

may avoid totally the water solvent and the protons to reach the semiconducting surface; (iii) the electroactive monomer for better conducting properties of the HTM.

Regarding the interesting results obtained with aging process which is in opposition to the classical DSSCs aging processes, the origin of this is not yet well understood and there is a high potential to improve these s-DSSCs based on CP produced by *in-situ* PEP.